P. ten Houte de Lange

Dawn Aerospace Mk-III Spaceplane Aerothermodynamic Analysis

Dawn Aerospace Mk-III Spaceplane Aerothermodynamic Analysis

By

P. ten Houte de Lange

in partial fulfilment of the requirements for the degree of

Master of Science
in Aerospace Engineering

at the Delft University of Technology,
to be defended publicly on Thursday April 29, 2022 at 10:00 AM.

Supervisor:	Ir. M. C. Naeije	TU Delft
	Ir. T. R. Knop	Dawn Aerospace
Thesis committee:	Dr. Ir. E. J. O. Schrama	TU Delft (Chair)
	Dr. Ir. M. F. M. Hoogreef	TU Delft (External Examiner)
	Dr. Ir. F. F. J. Schrijer	TU Delft

This thesis is confidential and cannot be made public until April 29, 2024.

An electronic version of this thesis is available at http://repository.tudelft.nl/.

Abstract

Dawn Aerospace is developing a horizontal take-off and landing two stage to orbit partially-reusable launcher concept. The re-usable first stage spaceplane operates on a return to launch site trajectory and integrates into the existing airspace, flying as an UAV. For any re-entry vehicle the design needs to account for aerothermodynamic behaviour around the vehicle, to ensure the structure can survive the re-entry temperatures. The unique mission of the Mk-III means the thermal design considerations are unique and provide a new engineering challenge and research topic.

This thesis investigates the aerothermodynamic behaviour of the Mk-III flow and structure. A loosely coupled model was created for this purpose, which couples engineering methods to predict the aerothermodynamics and the thermal behaviour of the structure. The coupling is done by transferring the external skin temperature and convective heat flux between the two simulations.

The primary research question for this thesis is “What thermal protection systems have potential to be implemented on the Dawn Aerospace Mk-III spaceplane for a range of different design trajectories.” Two thermal protection systems (TPS) and material choices have been identified as potential solutions. The first is a fully titanium structure, which can handle the temperature experienced by the Mk-III for all trajectories at every point along the vehicle. The second is a combined titanium and BMI CF structure with an insulation layer on the BMI CF. The titanium is required for the temperatures experienced on the vehicle’s leading edges, while the BMI CF has been identified as suitable in areas away from the leading edge if protected by an insulation TPS. A benefit this option produces is that the insulation layer can be changed in thickness to lighten the vehicle for lower design trajectories, therefore creating different vehicles for different trajectories. However, combining a metal with a composite could pose manufacturing issues such as cost for different manufacturing processes and joining problems. This thesis could not properly trade-off between these two options due to it being outside the scope of this thesis and due to limitations in detailed structural knowledge.

These two material choices were chosen from four materials analysed in the thesis and four different TPS. Other TPS were not suitable at decreasing the structural temperature for the Mk-III mission or had an unjustifiable weight penalty. The other material choices would have been suitable in certain situations but were heavier than the current proposed options and might have required a TPS.

This thesis provides valuable insight in what suitable material and TPS choices could be for the Mk-III mission. It also shows that for any future material and TPS choice to be made, a comprehensive structural analysis is required. Mass is a key trade-off parameter between the two proposed solutions and a better structural analysis is required for any further trade-off.

Preface

Having worked towards obtaining my master's degree at the TU Delft for almost 3 years I am happy to be able to complete this thesis and continue with the next chapter of my life. This project has been really enjoyable and I hope I can continue the research in the future as I continue working on the Mk-III for Dawn Aerospace. So, thanks Dawn Aerospace for giving me the opportunity (and freedom) to do this thesis. Even though it was the plan from the point we started working together, I am thankful we could still do it even though Dawn Aerospace has been focusing on internal growth rather than thesis students. Tobi Knop, our update sessions were always randomly timed but I think that worked out perfectly. Also, thanks to all my colleagues, particularly Bertil Oving and Andreas Fischer, for your constant reminder that I should finish and get back to working full time.

Marc Naeije, you once said you didn't need to be acknowledged so I will surely not do that. I hope you enjoyed working together as I did and enjoyed the topic. As from the very start you are still invited to come by Dawn Aerospace at some point and look at our operation. I also want to thank Ferry for helping share his thoughts on the thesis at various stages.

As I was writing this thesis my biggest problem was commas. So, I very much appreciate my proof-readers, Mirjam Bertrand and Pieter van Dongen. Thanks for reading through all of the report. Will Austin, you are the best! (Written without a choice) Thanks you for the more detailed read and trying to find mistakes in my content and I hope I fulfilled your requests. Also, thanks to all the people who offered to proofread my report but struggled to find the time. I would have done the same, maybe not even offered so I appreciate the thought. Lastly, I have been talking about the various thesis (problems) to Alma van Oudheusden and flatmates, so thanks to them for listening.

I hope everyone enjoys reading this.

Philip ten Houte de Lange
Delft, April 2022

Contents

Nomenclature

α	Absorption constant	[-]
α	Thermal diffusivity	$[\mathrm{m}^2/\mathrm{s}]$
β	Approximation of coefficient of thermal expansion	[-]
$\dot{Q}$	Heat transfer rate	$[\mathrm{W}]$
$\epsilon_{1,2,3}$	Fraction of molecules dissociated/atoms ionized	[-]
$\frac{\epsilon_n}{k}$	Electronic energy	$[\mathrm{K}]$
$\frac{hv}{k}$	Vibrational constant	[-]
γ	Specific heat ratio	[-]
Λ	Leading edge sweep angle	$[\mathrm{deg}]$
λ	Mean free path of molecule	[-]
$\left(\frac{du}{dx}\right)_{x=0}$	Stagnation velocity gradient	$[1/\mathrm{s}]$
Bi	Biot number	[-]
Gr	Grashof number	[-]
Nu	Nusselt number	[-]
Pr	Prandtl number	[-]
Re_t	Transition Reynolds number	[-]
Re_x	Reynolds number	[-]
St	Stanton number	[-]
μ	Dynamic viscosity	$[\mathrm{kg}/\mathrm{ms}]$
ρ	Density	$[\mathrm{kg}/\mathrm{m}^3]$
ρ	Reflection constant	[-]
σ	Stefan-Boltzmann constant	$5.670374 \cdot 10^{-8}$ $[\mathrm{W}/\mathrm{m}^2\mathrm{K}^4]$
$\sum n_i$	Number densities of the atmospheric gas components	[-]
θ	Angle between the flow and tangent of surface	[-]
ε	Emissivity constant	[-]
A	Area	$[\mathrm{m}^2]$
A	Reactant components in chemical reaction	[-]

a	Speed of sound	$[\mathrm{m/s}]$
a	Stoichiometric reaction coefficients of reactants	[-]
B	Product components in chemical reaction	[-]
b	Stoichiometric reaction coefficients of products	[-]
c	Specific heat capacity	$[\mathrm{J/kgK}]$
C_f	Local skin friction coefficient	[-]
C_m	Laminar to turbulent transition coefficient	[-]
C_p	Specific heat at constant pressure per mole	$[\mathrm{J/molK}]$
c_p	Specific heat at constant pressure	$[\mathrm{J/kgK}]$
C_v	Specific heat at constant volume per mole	$[\mathrm{J/molK}]$
$C_{1,2,3}$	Coefficient for free convection	[-]
E	Internal energy per mole	$[\mathrm{J/mol}]$
F	Dimensionless view factor	[-]
F	Empirical factor	[-]
g	Gravitational acceleration	$[\mathrm{m/s^2}]$
g_n	Electronic degeneracy	[-]
H	Enthalpy per mole	$[\mathrm{J/mol}]$
H	Geopotential altitude	$[\mathrm{km}]$
h	Altitude	$[\mathrm{m}]$
h	Specific enthalpy	$[\mathrm{J/kg}]$
h_{conv}	Convective heat transfer coefficient	$[\mathrm{W/m^2K}$ - free convection or $\mathrm{kg/m^2s}$ - forced convection]
H_s	Scale height	7050 $[\mathrm{m}]$
k	Boltzmann constant	$1.38065 \cdot 10^{-23}$ $[\mathrm{m^2kg/s^2K}]$
k	Conductive heat transfer coefficient	$[\mathrm{W/m^2K}]$
K_c	Chemical equilibrium constant for concentration units	[-]
K_p	Chemical equilibrium constant for pressure units	[-]
L	Characteristic length	$[\mathrm{m}]$
L	Thickness	$[\mathrm{m}]$
$\dot{m}$	Mass flow rate	$[\mathrm{kg/s}]$

M	Mach number	[-]
M	Mass	[kg]
M	Mean molecular weight	[kg/mol]
M_0	Reference molar mass	0.029 [kg/mol]
N_0	Avogadro number	$6.0221409 \cdot 10^{23}$ [molecules/mol]
p	Pressure	[Pa]
Q	Heat transfer	[J]
Q	Partition functions	[-]
q	Dynamic pressure	[Pa]
q	Heat transfer flux	[W/m^2]
R	Distance	[m]
R	Radius	[m]
R	Universal gas constant	8.314463 [J/molK]
r	Recovery factor	[-]
r_0	Effective radius of Earth	[km]
S_{ij}	Collision cross section of particle i with particle j	[-]
T	Temperature	[Ks]
t	Time	[s]
V	Velocity	[m/s]
x	Mole fraction	[-]
x, y, z	Distance along surface	[m]
x, y, z	Distance in cartesian coordinate system	[m]
Z	Compressibility factor	[-]
Z	Geometric altitude	[km]

Subscripts

0	Reference
1	State before the shock wave or Surface 1
2	State after the shock wave or Surface 2
∞	Free stream

c	Per unit concentration
d	Diffusion
i	i^{th} element
L	Local
n	Molecular collisions
p	Per unit pressure
r	Recovery
$r+v$	Rotational and vibrational
st	Stagnation
$t+e$	Translation and electronic excitation
w	Wall

Superscript

$*$	Eckert’s reference enthalpy

Acronyms

Al	Aluminium
BMI CF	Bismaleimide carbon fibre
GUI	Graphical user interface
LEO	Low Earth orbit
Mk-III	Dawn Aerospace Mk-III spaceplane
SiC CF	Silicon carbide carbon fibre
SQ	Sub-research-question
Ti	Titanium
TPS	Thermal protection system(s)
UAV	Unmanned aerial vehicle

1. Introduction

Getting to space is a never-ending problem engineers face when designing new launch vehicles. How do we get into space efficiently, cheaply and reliably? The conventional method of launching to orbit is using a multiple-stage, vertical take-off rocket. Partial re-usability of traditional rockets has been demonstrated recently by vertically landing used rocket stages. Even though challenging to design them, rockets are cheap to develop (compared to alternatives) which has made them a popular choice for an expensive transport system. Alternative methods and concepts of launching to space have also been developed. One proven alternative are spaceplanes which are rockets designed with plane features capable of reaching space to deliver a payload, for example the Space Shuttle. Although for the ascent these planes do not contribute hugely to performance, they do have benefits for the descent. Most notably they are capable of operating and behaving like a conventional aircraft, allowing horizontal landing, reducing re-entry loads (structural and thermal) and greater manoeuvrability.

Over the years there have been a number of spaceplane projects having reached various development stages. These concepts involve various launch methods such as a rocket booster, air-launch from an aircraft or horizontal launching. Variability in concepts is also caused by the various missions for which the spaceplanes are designed. For example, the Space Shuttle Orbiter is designed for orbital re-entry whereas the X-34 was designed for air-launch suborbital ascent and descent. Dawn Aerospace is developing one such spaceplane concept for launching small satellites into Low Earth Orbit (Dawn Aerospace, 2021b). The concept is a two stage to orbit horizontal take-off and landing partially-reusable unmanned launch vehicle. The first stage is designed to be a reusable spaceplane and the second stage a conventional rocket.

When vehicles travel at supersonic speeds, the kinetic energy of the flow is converted into thermal energy. This means that the flow around the vehicle is heated which, with time and temperature gradient, is transferred to the vehicle itself. Orbital vehicles must fly at high speeds to achieve the velocity required to deliver payloads into orbit, which causes high velocities upon re-entry. Therefore, due to these high speeds, both the thermal loads and heat transfer must be accounted for in the vehicle's design. Depending on the re-entry origin a space vehicle can have massively varying thermal load requirements. Vehicles entering from orbit traditionally have a maximum speed between Mach 20 and 25 (Young & Crippen, 2011), while a sub-orbital vehicle reaching the Karman line might only reach maximum speeds of Mach ~3. Design for a thermal protection system (TPS) of any space vehicle therefore highly depends on the mission.

This thesis assesses possible TPS for the Dawn Aerospace Mk-III spaceplane. The TPS will be evaluated for a range of trajectories which provide an understanding if there are limitations to particular trajectories. Four material choices will be evaluated for their aerothermodynamic behaviour; two composites and two metals. One of these materials will be identified for evaluating extending the trajectory operating range on by means of a TPS. The TPS investigated are active cooling system by means of internal coolant flow, radiative cooling, insulation and heat sink. These evaluations should provide a baseline for future TPS studies that are then developed alongside the Mk-III spaceplane design. This paragraph has been neatly formulated into research objective, primary research question and sub-research questions (SQ) that are the basis of this thesis.

Research objective: *To assess possible thermal protection system for a two stage to orbit horizontal take-off and landing launch vehicle’s reusable first stage spaceplane aimed at launching small satellites into orbit integrated with airspace as an unmanned aerial vehicle by using full or segmented 3D transient numerical simulation using engineering methods within a flow-structure coupled environment with the aim of identifying a reusable, maintenance free and light weight thermal management systems suitable for suborbital flight.*

Primary research question: *What thermal protection systems have potential to be implemented on the Dawn Aerospace Mk-III spaceplane for a range of different design trajectories.*

- **SQ 1:** *What material choices would be suitable to implement on the Mk-III spaceplane for the range of different design trajectories.*
  - **SQ 1.1:** *Are there suitable composite structures that can handle the thermal protection system performance?*
  - **SQ 1.2:** *Are there suitable metallic structures that can handle the thermal protection system performance?*
- **SQ 2:** *How can a thermal protection system extend the trajectory operating range of a structural material choice from sub-question 1?*
  - **SQ 2.1:** *Could the residual pressurant from the oxidizer and fuel tanks be used as an effective active thermal protection system on the internal surface of the vehicle's skin structure?*
  - **SQ 2.2:** *Can an external coating to change the vehicle's radiative properties be added to the structure as an effective thermal protection system?*
  - **SQ 2.3:** *Can an insulative layer be added to external surface of the structure as an effective thermal protection system?*
  - **SQ 2.4:** *Can a heat sink, by means of material thickness, be added to the structure as an effective thermal protection system?*

The report has been set up to allow the reader to understand the process and decisions of the thermodynamic analysis of the Mk-III spaceplane. Therefore, first Dawn Aerospace and the Mk-III project is introduced to provide an overview of why this thesis is important and what it can provide to the scientific community. Next there is some background information given that should allow the reader to refresh their knowledge of thermodynamics and explain any underlying principles. Based on that knowledge the model and underlying equations are explained and presented, alongside the decisions why the model was set up in this particular way. Having created the model, it was validated against primarily X-15 data and also X-34 flight and simulation data. The model was then used to show the results of the different TPS and provide answers to the research questions. Lastly the model was analysed in a sensitivity study to evaluate how sensitive the model is to various input parameters.

1.1. Dawn Aerospace

Dawn Aerospace is a start-up company formed in 2018 aimed at becoming part of and changing the space market. Located in both the Netherlands and New Zealand, Dawn Aerospace have grown to more than 60 full time employees working on both launch vehicle development and in-space propulsion. The goal is to provide products for complete transportation of your satellite. This vision comes in three different areas that Dawn Aerospace calls "Deliver, Position and Return" (Dawn Aerospace, 2021b). Deliver describes launch platforms aimed at providing a reusable and flexible options to orbit. Position describes the in-space propulsion products aimed at using green propellants to provide quick manoeuvring capabilities for satellites in space. Dawn Aerospace uses non-toxic chemical propellants with high thrust levels alongside 3D printing manufacturing, to provide high manoeuvrability to CubeSats and small satellites. Lastly, return is aimed at the recovery or de-orbiting of the satellites after their useful lifetime in space.

This thesis will contribute to the “Deliver” aspect of the Dawn Aerospace transportation system goals. The Deliver project of Dawn Aerospace has the goal "Fly to space, twice a day" (Dawn Aerospace, 2021b). The goal is realised by implementing a spaceplane into a two stage to orbit partially-reusable horizontal take-off and landing system. This concept creates a sustainable and reusable option for flight, as well as flexible launch options compared to conventional rocket launches. The spaceplane is able to achieve this due to its capability to integrate with the existing aviation infrastructure and airspace. The first vehicle of Dawn Aerospace, the Mk-I, was designed as a subsonic Unmanned Aerial Vehicle (UAV) for initial rocket engine development. Its successor, the Mk-II Aurora Figure 1.1, has started flight testing in 2021 with supersonic suborbital space flight capabilities with a maximum altitude of 110 km and a 4 kg payload capability (Dawn Aerospace, 2021b). The Mk-II Aurora is a technology demonstrator for the successor, the Mk-III, operating as a horizontal take-off and landing UAV. The Mk-III is the full-scale prototype of the launch platform project capable of flying faster, higher and carrying a second stage. This vehicle will be the primary vehicle of interest for thesis and will be discussed further in Chapter 2.

Figure 1.1. The Mk-II Aurora (Dawn Aerospace, 2021b)

2. MK-III

The Dawn Aerospace Mk-III (from here on called the Mk-III) will be a two stage to orbit partially-reusable horizontal take-off and landing launch vehicle, capable of launching small satellites into a Low Earth Orbit (LEO) (Dawn Aerospace, 2021a). The first stage of the Mk-III will be a spaceplane further developed from the Dawn Aerospace Mk-II Aurora, launched on a suborbital trajectory where it releases the second stage containing the payload. This second stage, designed as a conventional second stage rocket, will deliver the payload into LEO. In this concept only the spaceplane is reusable and the second stage will burn up upon re-entry after delivering the payload into orbit.

This chapter describes the unique Mk-III mission and trajectory, including that it doesn't achieve a cruise speed. The spaceplane is a suborbital vehicle and the mission is to achieve horizontal take-off and landing at the same landing site. This uniqueness allows for opportunities in the TPS design of the Mk-III that have not been implemented before in such an application. The Mk-III is currently in the conceptual design phase meaning some aspects of the Mk-III are already known, whereas others are still open for design choices (priv. comm. Tobias Knop). This chapter will explain the known, unknown and assumed design choices to ensure applicability of the thesis.

2.1. Mk-III mission and features

The Mk-III mission is the most developed and known part of the project and addresses the 'Deliver' goal of Dawn Aerospace's vision. It is based on implementing the infrastructure and method of operating from the well-established aerospace industry to space flight, with the goal to provide a flexible and cost-effective launch service to deliver small satellites into LEO (Dawn Aerospace, 2021a).

The spaceplane is where the aerospace industry and Mk-III are integrated. The key aspects of the spaceplane that help realise the mission are (Dawn Aerospace, 2021a)

- Flying within the existing airspace: The spaceplane can fly like an aircraft. Therefore, it is capable of operating as a UAV within the existing airspace. Conventional rockets require closed off airspace because of launch failure probability and debris, thereby greatly disturbing air/sea/land traffic. Integration of the spaceplane and operating it as an UAV means that launch opportunities should be more flexibly obtainable. This also flows into the design of a staging mechanism where debris cannot be created as this would require airspace closure.
- Horizontal take-off and landing: Vertical take-off rockets require special infrastructure (launch pads) whereas runways for aircraft already exist across the world. Making use of the great number of horizontal launch sites makes the Dawn Aerospace concept vastly more flexible in launch locations and opportunities without the need for new infrastructure. Capabilities such as bringing the launch vehicle to the customer can be achieved with this concept, re-inventing how the space industry operates.
- Take-off and landing at the same landing site: Movement and recovery costs of having the spaceplane land at a different site can be avoided by designing the spaceplane to return to the launch site. Being roughly the same size as a business jet, returning the spaceplane by land would be logistically challenging and costly. Using a spaceplane concept allows for the vehicle to glide back to the launch site without the use of additional fuel (Haex, 2020).
- Controlled re-entry: A spaceplane is capable of a controlled re-entry allowing aspects such as controlled thermal loads, structural loads and re-entry manoeuvrers to be adjusted during flight. It ties in with the re-usability aspect of the spaceplane as well as integrating within the airspace.
- Re-usable twice a day: This addresses the low cost and flexibility aspect of the spaceplane concept. The aircraft model has high re-usability and low maintenance meaning many operation cycles are possible before requiring maintenance. Higher turn around between flights and not requiring a new vehicle every flight will flow down into lower launch costs for the customer. The ‘fly twice a day’ goal describes the aim that Dawn Aerospace wants to operate the spaceplane like an aircraft.

A single-stage-to-orbit provides significant challenges that have not yet been achieved with the available technology. Therefore, for the Mk-III a two stage to orbit system is conceptualized where the second stage operates like a conventional rocket second stage. This two-stage concept also means that return of the spaceplane to the launch site is realizable. Upon delivery of the payload the second stage will burn up in the atmosphere to, like the spaceplane, not disturb the commercial airspace by debris. Figure 2.1 (Dawn Aerospace, 2021b) shows the Mk-III mission profile.

To allow widespread use and flexible flying capabilities the Mk-III is developed as a UAV, operating using a rocket engine with a mixture of kerosene and hydrogen peroxide for propellants, which is the same as the Mk-II (priv. comm. Tobias Knop). The Mk-II demonstrates and tests the spaceplane capabilities for the Mk-III project. The Mk-II itself does not have sufficient payload performance for a second stage but can carry a small payload. From a thermodynamic viewpoint the Mk-III spaceplane is the vehicle of interest because the spaceplane will experience significant aero-heating loads during re-entry. The spaceplane also needs to be capable of experiencing these loads repeatedly without maintenance in between flights. The second stage however burns up upon re-entry. Although not yet fully defined, this thesis assumes the second stage only experiences aerodynamic loading during the descent into the atmosphere, as the second stage will be inside the spaceplane for ascent. During re-entry from LEO the aero-heating loads are of magnitudes larger compared to that of the spaceplane, as the velocity will be significantly greater (near orbital velocity compared to Section 2.2). This means the first and second stage require different thermal analyses and therefore this thesis will only focus on the first-stage spaceplane.

2.2. Trajectory

In collaboration with the TU Delft, Dawn Aerospace has run two trajectory optimization studies based on the Mk-III mission. Haex (2020) performed trajectory optimization using a cost model and Sonneveld (2021) performed trajectory simulations evaluating aerodynamic performance. Both these thesis projects resulted in a range of potential trajectories for various vehicle properties, payload capabilities and payload orbits.

The Mk-III cost optimized trajectory (Haex, 2020) based the price of the vehicle on solely the dry mass of the vehicle launching the payload to a polar orbit. Within this model different spaceplane return methods were evaluated. Firstly, an aeroturn was evaluated, here the spaceplane's aerodynamics were used to turn the vehicle to the launch site after re-entry into the atmosphere. Secondly, a boostback was initiated at spaceplane burnout after staging with the second stage to reduce the horizontal velocity of the spaceplane during coast and re-entry. Both these return mechanisms were modelled specifically for this thesis using four cases of varying payload mass and final orbit altitude. The payload capacity was set to 150 and 250 kg and the orbit was set to 400 and 600 km altitude. These parameters allow a spread in potential first stage trajectories based on the exact payload carried and target orbit.

The aerodynamic trajectory simulations (Sonneveld, 2021) modelled trajectories as a method of comparing the performance of different vehicle properties. The properties adjusted were aerodynamic properties, engine performance, launch location, mass and efficiency parameters. Sonneveld (2021) model used a payload mass of 250 kg and a target orbit of 600 km similar to the trajectories from Haex (2020).

To compare the large number of trajectories obtained from Haex (2020) and Sonneveld (2021), the metrics maximum trajectory velocity (and Mach number) and maximum trajectory altitude were used. Figure 2.2 plots these metrics against one another, ordering them into their types of trajectories. Though not displayed on the figure, it was found that generally the larger the payload mass and higher the target orbit, the higher the maximum altitude and velocity of the spaceplane. A noticeable difference between the two trajectory simulations is that Sonneveld (2021) trajectories are of similar magnitude to those from Haex (2020) but have less spread in the trajectory performance metrics. This is attributed to the smaller effect of changes in the vehicle's performance parameters, such as aerodynamic efficiency, compared to the change in Haex (2020) trajectories from payload mass and orbit altitude. Also, Sonneveld's (2021) trajectories for the same target payload and target orbit have lower maximum altitude and velocity compared to Haex's (2020) trajectories.

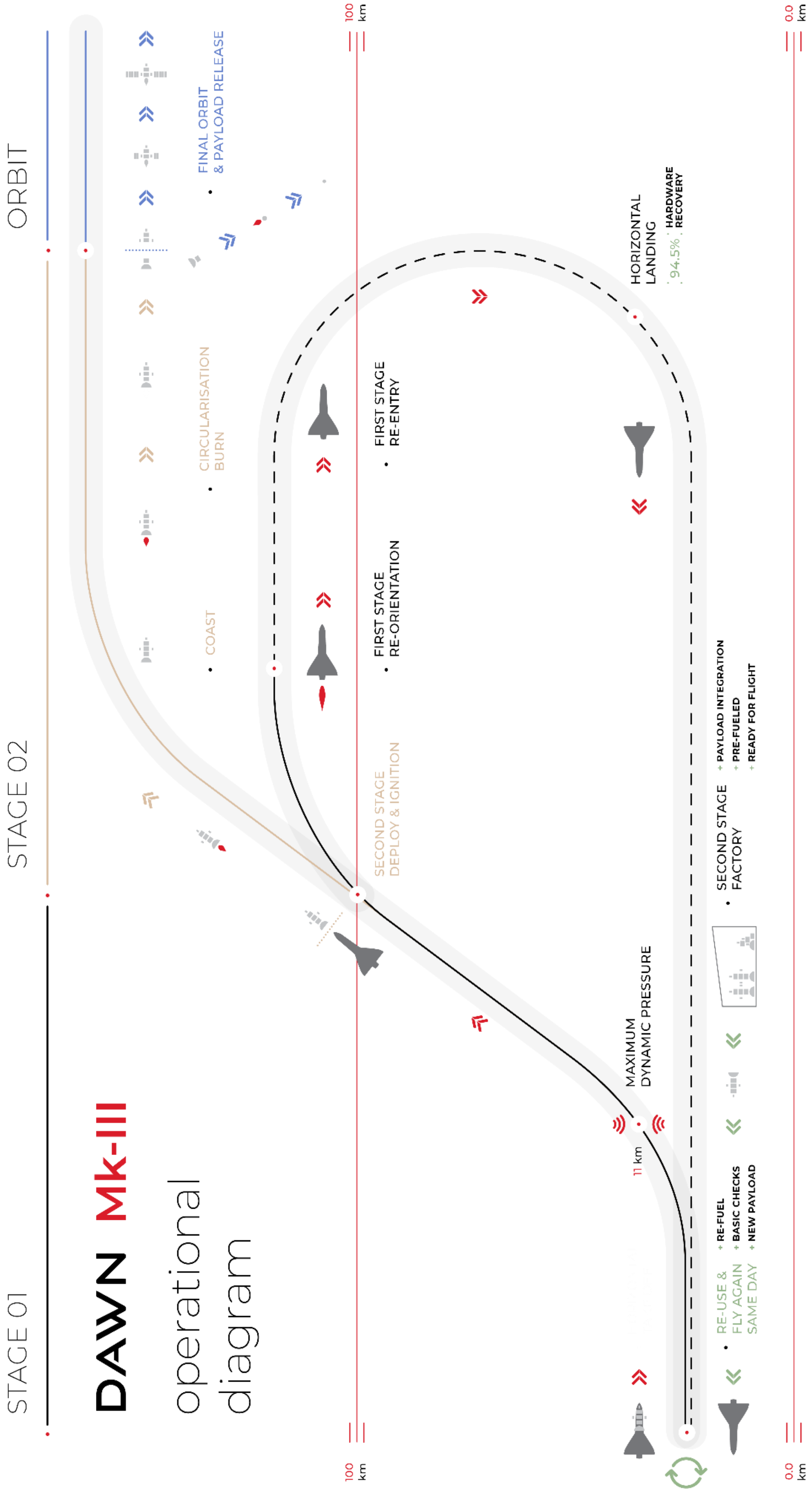

Figure 2.1. Mk-III mission profile (Dawn Aerospace, 2021b)

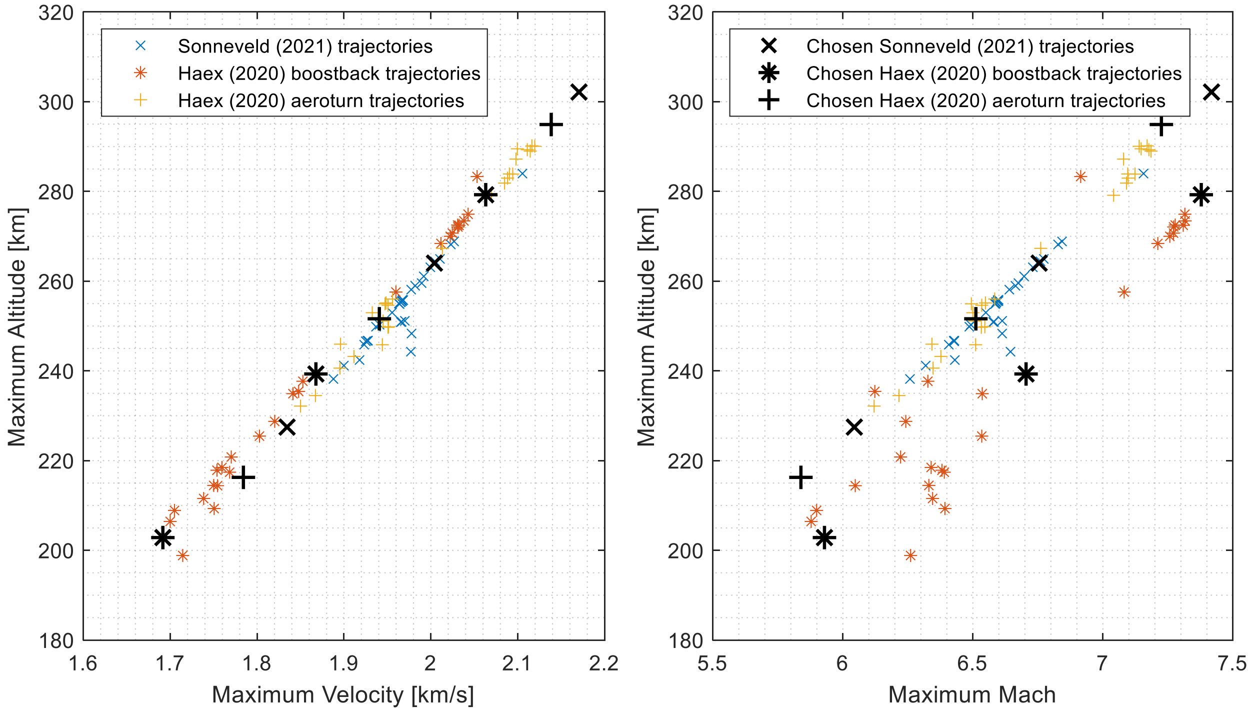

Figure 2.2. Mk-III spaceplane trajectories from Haex (2020) and Sonneveld (2021) showing the trajectories maximum velocity and Mach number against the maximum altitude.

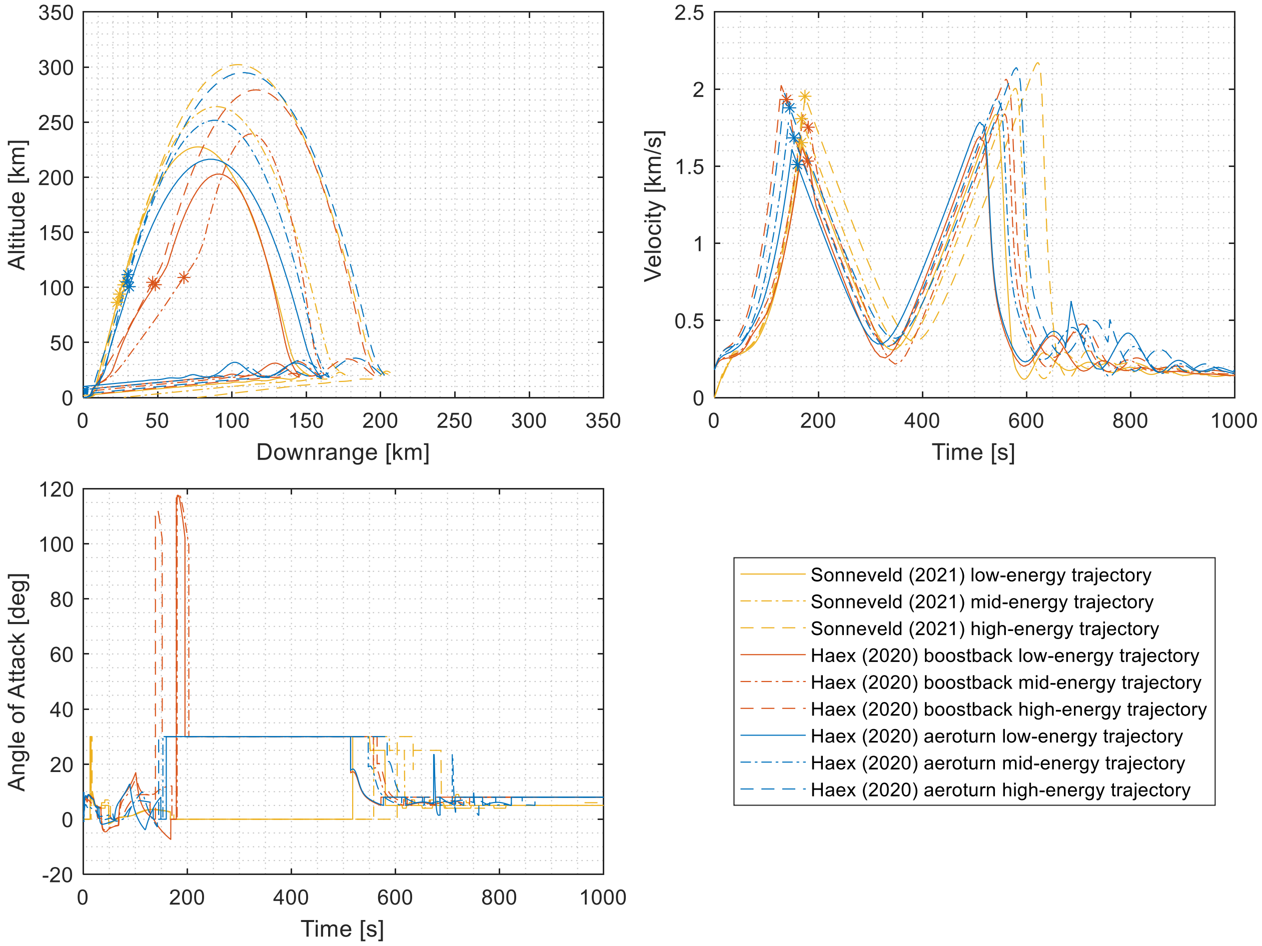

Figure 2.3. Mk-III spaceplane chosen trajectories to analyse from this thesis from Haex (2020) and Sonneveld (2021). Asterix indicates staging with second stage.

Within Haex’s (2020) trajectories the boostback also has a lower maximum altitude and velocity compared to the same aeroturn case. This difference is caused by the boostback having a shallower spaceplane ascent trajectory compared to the aeroturn and Sonneveld’s (2021) trajectories. The shallower ascent and thereby higher horizontal velocity given to the second stage results in less vertical velocity and lower first stage altitudes. This effect is also seen in the maximum Mach number vs maximum altitude graph in Figure 2.2, where the boostback trajectories do not follow the near perfect linear correlation that the other two types of trajectories follow. The boostback maximum Mach number is achieved during ascent rather than re-entry as for the other trajectories, caused by the decrease in horizontal velocity after staging.

A trajectory selection covering the trajectory range has been created because analysing all trajectories will not help answer the research questions better. These chosen trajectories are marked in Figure 2.2 and take into consideration the two different thesis projects from which the trajectories originate (Haex, 2020; Sonneveld, 2021) and the variation within these projects. The selection of these trajectories was based on the research question, obtaining as large and as evenly as possible spread of trajectories. The performance metrics of trajectories, maximum altitude and velocity, were used to aid this decision.

Figure 2.3 shows the chosen trajectories in more detail. Rather than analysing only the maximum parameters of a trajectory, the real simulations will use the entire transient trajectory. Hence Figure 2.3 shows the three aspects of the trajectory required in the model for this thesis: altitude, velocity and angle of attack. The altitude against downrange graph shows that the Haex (2020) aeroturn and Sonneveld (2021) trajectories both follow a similar steep ascent path and that Haex (2020) boostback trajectories follow a shallower ascent until after staging. Secondly this graph clearly shows immediately after re-entry, even before some small skipping re-entry is completed, all trajectories except a few of the Sonneveld (2021) trajectories, return to the launch site. This inability to return to the launch site is ignored for this thesis given that it is a trajectory and vehicle design issue and does not appear to affect the thermodynamic dependent portions of the trajectory when compared to the Haex (2020) trajectories. Notably Sonneveld (2021) doesn’t appear to have a large altitude skipping re-entry whereas the Haex (2020) trajectories do show this. This difference appears to be the primary reason for the Sonneveld (2021) trajectories not reaching the launch site on return. The skipping is induced by choosing angle of attacks for the spaceplane, which was controlled by inputs for the Sonneveld (2021) trajectories and by optimization for the Haex (2020) trajectories. Therefore, in future trajectories the return can be modified by changing the low velocity re-entry angle of attack.

The velocity graph Figure 2.3 re-iterates that the skipping behaviour is primarily induced by the Haex (2020) trajectories and less so by the Sonneveld (2021) trajectories. The velocity graph also shows that the Haex (2020) and Sonneveld (2021) simulations use different starting conditions. The velocity from Sonneveld (2021) simulations start at 0 km/s whereas those from Haex (2020) start at roughly 0.2 km/s. This can be attributed to Haex (2020) assuming take-off has already occurred and accounting for take-off by means of mass calculations. Sonneveld (2021) on the other hand uses simple equations to model the take-off and effect it has on the vehicle. These decisions are based on their thesis research questions where Sonneveld (2021) is specifically investigating the aerodynamic behaviour and effect along the entire trajectory, whereas Haex (2020) is investigating the vehicle around a cost perspective.

The angle of attack graph in Figure 2.3 shows that, except during coasting, all trajectories have some large variations and changes in their angle of attack. This is primarily true for the Haex (2020) trajectories as this uses an optimizer to dictate the angle of attack, whereas Sonneveld (2021) inputs the angles of attack in a more controlled manner. The Haex (2020) boostback trajectory spikes after staging, which is to turn the aircraft around and provide the boost for decreasing the horizontal velocity. The simulation will not be set up to handle these extreme angles of attack, so these will be decreased to 30 degrees under the assumption that at this stage the thermal loads are non-significant.

2.3. Shape

The Mk-III spaceplane is currently in the design phase, and the final shape of the vehicle has not been finalised (priv. comm. Tobias Knop). The Mk-II has been developed as a prototype for the Mk-III spaceplane and has already delivered key findings for the design of the Mk-III spaceplane. Due to the lack of Mk-III shape knowledge, the Mk-II vehicle shape will be used as a baseline. The shape of the vehicle can be seen in Figure 2.4. It is imported into the simulator via a Parasolid file containing the external surface of the vehicle which, in conjunction with the selected material properties, defines the vehicles shape, internal and external.

The two thesis' conducted on the Mk-III didn't require an exact model of the vehicle shape (Haex, 2020; Sonneveld, 2021) as is required for an aerothermal analysis. The aerothermal analysis requires knowledge of the external shape and internal structure of the vehicle to calculate surface angles, with respect to the flow and to calculate the heat propagation through the structure. The trajectory calculations in the theses primarily requires knowledge of the shape for aerodynamic modelling. For both theses the X-34 aerodynamic data was used due to the completeness of this available data and state of the Mk-II at the time of starting these projects (Haex, 2020; Sonneveld, 2021). Haex (2020) also calculated vehicle sizing based on simplified shape assumptions and based on the fuel and oxidizer volumes required to reach orbit. These were subsequently used to calculate vehicle mass and were fed into the trajectory simulations. The aerodynamic models and mass therefore are not actually directly input into the aerothermal analysis, but indirectly affect it though the trajectory.

Because the Mk-III has a different mission to the Mk-II, it must therefore be larger in size to launch a second stage and carry a payload. The scaling of the Mk-II shape to the Mk-III size was done based on Haex's (2020) results, who alongside trajectory simulations, investigated the required size of the vehicle for each trajectory. The results from Haex (2020) increased the vehicle size to 22.5 m in length, which was deemed an appropriate first estimate of the Mk-III vehicle size to conduct the aerothermal analysis. Dawn Aerospace does not believe the shape and size described in this chapter will be the final version of the Mk-III but for the purposes of this thesis will allow adequately accurate results and conclusions to be drawn from (priv. comm. Tobias Knop). The aerothermal analysis from this thesis is one of the inputs that will help make more detailed shape and sizing decisions.

Figure 2.4. Dawn Aerospace Mk-II Aurora spaceplane

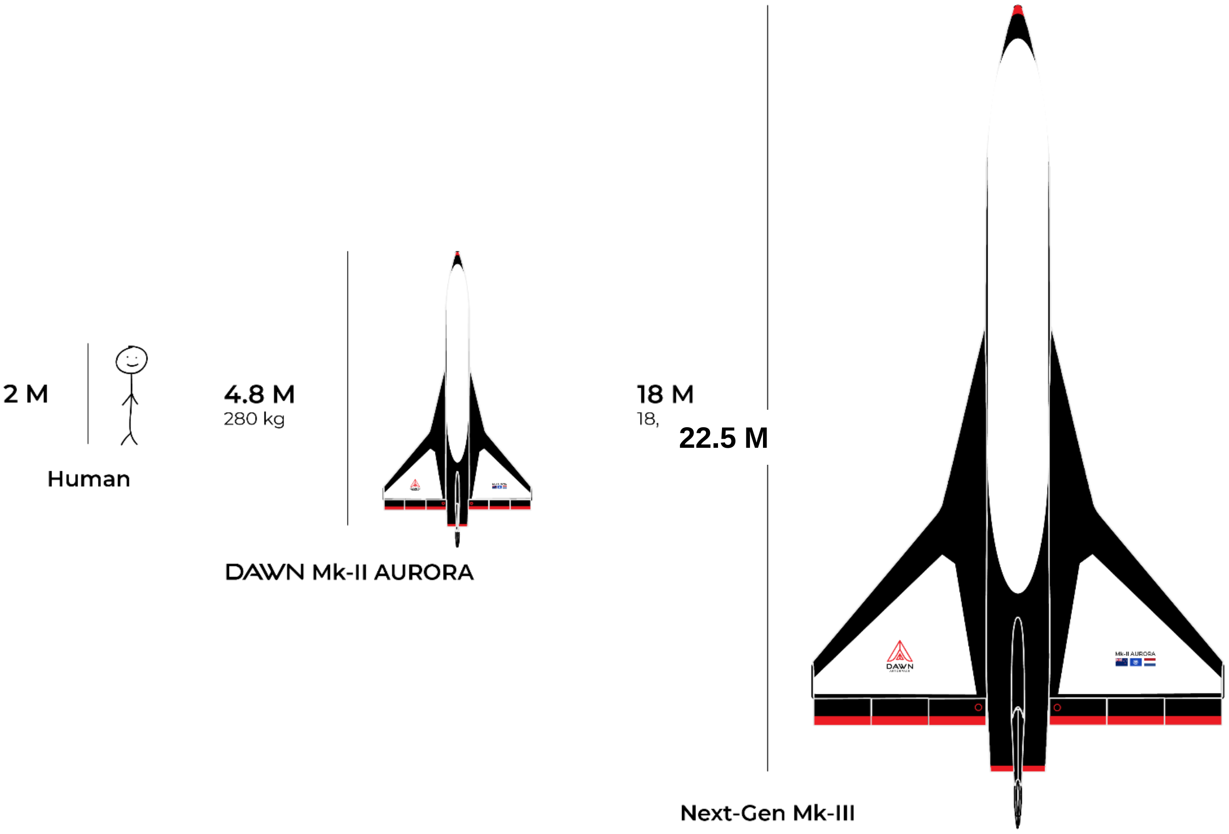

Figure 2.5. Mk-II Aurora and Mk-III size difference – modified from published picture (Dawn Aerospace, 2021b)

2.4. Materials and structure

Like the shape, the Mk-III material and internal structure are still under conceptual development. The aim of the thesis is to provide insight into suitable thermodynamic protection systems of which material choice is a key part. However, the thesis is not aimed at providing a directly applicable solution, due to the design of the Mk-III not being sufficiently developed as of undertaking this thesis. The research questions have therefore been formulated to provide knowledge of the thermal behaviour of various materials, with wide ranging materials and protection systems that have potential of suiting the spaceplane's structural needs. With guidance from Dawn Aerospace, two composite materials, bismaleimide carbon fibre (BMI CF) and silicon carbide carbon fibre (SiC CF), and two metal materials, titanium and aluminium, were selected to suit the needs of this thesis. The properties of these materials were extracted from GRANTA EduPack (Granta Design Limited, 2020) and are displayed in Table 2.1. These material choices vary widely in terms of their density, strength, operational temperature, thermal conductivity and specific heat capacity, allowing the investigation into the effect of these material properties.

No structural analysis had been conducted into the Mk-III prior to this research. For this thesis a simple structural calculation was conducted to calculate the skin thickness of each material, based on the yield strength, ignoring any effect an internal structure might have and only considering the bending stress along the wing. This calculation allows the effect of yield strength of the different materials to be accounted for, resulting in a fairer comparison of materials. The calculation used a wing loading distribution extracted from the Mk-II wing, to calculate the loading, which could be used to calculate the stresses in the material for different material thicknesses. A safety factor of 2 was applied on the stress to account for the conceptual state of the design including internal structure, stress concentrations and skin buckling. Table 2.1 shows the results of these calculations and the resultant mass per surface unit area and specific heat capacity per surface unit area. It is important to realise that this is just a rough approximation that is only valid for this thesis. Further structural design and analysis will be required in future to provide more accurate structural information.

Table 2.1. Material properties (Granta Design Limited, 2020).

Material	BMI CF		SiC CF		Titanium		Aluminium	
	In-plane	Out-of-plane	In-plane	Out-of-plane	In-plane	Out-of-plane	In-plane	Out-of-plane
Density $[\mathrm{kg/m^3}]$	1540		2600		4600		2920	
Max temperature $[\mathrm{K}]$	523		1373		1773		880	
Thermal conductivity $[\mathrm{W/mK}]$	2.425	0.725	20	7	7.6		117.5	
Specific heat capacity $[\mathrm{J/kgK}]$	945		630		560		935	
Yield Strength $[\mathrm{MPa}]$	507	32	363	225	1040		380	
Thermal expansion coefficient $[\mu\varepsilon/\mathrm{K}]$	11.85	23.85	5.2	2.8	9.1		22.4	
Minimum thickness $[\mathrm{m}]$	0.00238		0.003332		0.00115		0.00315	
Mass/unit area $[\mathrm{kg/m^2}]$	3.67		8.66		5.29		9.20	
Specific heat capacity per unit area $[\mathrm{J/m^2K}]$	3464		5458		2962		8600	

The material thicknesses displayed in Table 2.1 are applied to the entire vehicle under the assumption that the entire vehicle requires the same material thickness. In reality the different locations of the vehicles required different material thicknesses, such as the fuselage and wing or leading edge and central sections of the wing. The assumption that the entire vehicle is constructed of a single material doesn't have to apply, as there may be thermal and mass requirements that make the leading edge require a different material to the other portions of the vehicle. This assumption is however in line with the assumption that there is no internal structure, which also has an effect on the stresses in the vehicle's external skin. Applying a variable material thickness would also require more detailed structural analysis which falls outside the scope of this thesis.

The presence of an internal structure has been omitted for calculating the vehicle skin temperature, however it will also be omitted within the thermodynamic simulation. The X-15 (Reed & Watts, 1961) shows the effect of spars on the temperature distribution, showing the localized heat sink effects it causes. It stresses that there are large temperature differences between the unsupported and supported skin temperatures. However, the effect of the spar's heat sink capability appears locally, meaning it will only have a positive thermodynamic effect on the material capabilities, though a negative effect by the thermally induced stresses. Because of the uncertainty associated with the Mk-III and the thereby associated thermodynamically positive effect, an internal structure can provide a heat sink; it is neglected in this thesis.

In Table 2.1, the BMI CF and SiC CF materials both show an in- and out-of-plane material property for the thermal conductivity, yield strength and thermal expansion coefficient. These properties are there due to the anisotropic properties caused by the fibres in the composite. It is assumed that the fibres are layered so that the material properties in the in-plane direction are constant. The properties of the in-plane direction are affected by the fibres, where thermal and structural loads make use of the fibres. For the out-of-plane direction, the matrix primarily transfers the loads and hence the material properties are different. This is particularly obvious for the yield strength, where the BMI CF material is more than an order of magnitude stronger in the in-plane direction, compared to the out-of-plane direction. For most calculations the in-plane material properties are used, but both properties are input into the simulations to accurately model the material thermal behaviour in the surface's normal direction.

2.5. Requirements

There are several requirements for the Mk-III mission. Many of them are already taken into account in the trajectory optimization (Haex, 2020) and do not apply to the thermal analysis itself.

Thermal Requirements

- The Mk-III spaceplane shall be designed to withstand and operate under the aero-thermal loads experienced by the design trajectory
- The Mk-III spaceplane shall have a non-ablative heat shield
- The Mk-III spaceplane shall not require extensive maintenance after each flight
- The Mk-III spaceplane shall not require additional maintenance on the TPS beyond the maintenance schedule of the whole spaceplane

Trajectory Dependent Requirements

- The Mk-III spaceplane shall carry a second stage and payload during ascent
- The Mk-III spaceplane shall be large enough to fit the second stage and payload within the structure
- The Mk-III spaceplane shall deploy the second stage and payload in space
- The Mk-III spaceplane shall take off and land horizontally on a runway
- The Mk-III spaceplane shall land on the same runway as it took off from
- The Mk-III spaceplane shall be able to be flown within the existing aerospace flight space
- The Mk-III spaceplane shall be an UAV
- The Mk-III spaceplane shall withstand the trajectory's external loads
- The Mk-III spaceplane shall use a rocket engine as its propulsion
- The Mk-III spaceplane shall use kerosene as fuel
- The Mk-III spaceplane shall use hydrogen peroxide as oxidizer

3. Background

To understand the models and decisions used in this thesis it is crucial to have an understanding of the fundamentals of thermodynamics. This chapter will cover types of heat transfer, the non-dimensional numbers used for the models and how to use these different elements of heat transfer join to define the thermodynamic behaviour.

3.1. Thermal models

Heat transfer is the transfer of thermal energy from one medium to another medium of lower temperature (Zandbergen, 2020). The amount of energy transfer is often either expressed as a total energy transfer over a period of time, an energy transfer per unit of time, or as the amount of energy per unit time and per unit area (flux). The heat flux is most often used as a unit of energy transfer as it decouples the medium or element size from the unit of energy, making it suitable for comparison with other bodies. Equation 3.1 (Zandbergen, 2020) shows the relationship between the heat transfer rate (amount of energy transfer per unit time) and the heat flux.

$$\dot{Q} = qA \tag{3.1}$$

Where

$\dot{Q}$ is the heat transfer rate $[\mathrm{W}]$
q is the heat transfer flux $[\mathrm{W/m^2}]$
A is the area $[\mathrm{m^2}]$

Heat transfer can occur by a number of different means of energy transport (Zandbergen, 2020). These include conduction, radiation and convective heat transfer. As well as transferring heat, a medium can also absorb energy. This absorption can either cause an increase in the internal energy of the medium, or cause a phase change or structural change to the medium. Both of these changes have an effect on the heat transferred to and from the medium.

3.1.1. Conduction

Conduction is a method of thermal energy transfer occurring through a medium due to a temperature gradient (Zandbergen, 2020). It is caused by the interaction of particles within solids, liquids and gases where one particle transfers energy to the next. The heat flux caused by conduction can be defined according to Fourier's law for thermal conduction, as shown in Eq. 3.2 (Connor, 2021; Zandbergen, 2020). Even though conduction occurs in all media, solids, liquids and gases, it is neglected in almost all liquid and gas analyses (Moran, Shapiro, Boettner, & Bailey, 2010). The generally lower thermal conductivity constant (k) of gasses and liquids, compared to solids, means these media are dominated by other modes of heat transfer, such as convection. The difference's primary cause is the intermolecular spacing between particles in the medium.

$$q = -k\nabla T \tag{3.2}$$

Where

k is the conductive heat transfer coefficient $[\mathrm{W/m^2K}]$
T is the temperature $[\mathrm{K}]$

The thermal conductivity constant shown in Eq. 3.2 is true for an isentropic medium. Particularly in certain composites, the thermal behaviour is not isentropic due to fibre orientation and the difference in thermal conductivities of the fibre, matrix and composite layers. In this case Eq. 3.2 can be redefined by the thermal conductivity constant in the x, y and z direction, as shown in Eq. 3.3 (Connor, 2021).

$$q = -k_x\frac{\partial T}{\partial x} - k_y\frac{\partial T}{\partial y} - k_z\frac{\partial T}{\partial z} \tag{3.3}$$

Where

x, y, z are distance along cartesian coordinate system $[\mathrm{m}]$

3.1.2. Radiation

Radiation is a form of heat transfer caused by a medium emitting/absorbing electromagnetic radiation (Zandbergen, 2020). A perfectly radiating medium is modelled as a black body, where the intensity of the radiation emitted follows Planck's law (Culham, 2016). Planck's law models the intensity of radiation (energy emitted) per electromagnetic radiation frequency/wavelength, which is dependent on the body’s temperature. For purposes of thermodynamics the intensity, as a function of frequency/wavelength, is of negligible importance. Stefan Boltzmann's law computes the radiative heat flux emitted by a black body into a hemisphere, as shown in Eq. 3.4 (Culham, 2016), neglecting any wavelength/frequency dependencies. In reality a perfectly radiating black body rarely exists and a body is characterised as a diffuse grey body. This type of body assumes the radiation properties are both independent of direction and wavelength. Because a body is not a perfect emitter, an emissivity constant (ε, value between 0 and 1) is defined to quantify the body's imperfectness compared to a black body, as shown in Eq. 3.5 (Zandbergen, 2020).

$$q_{\text{blackbody}} = \sigma T^4 \tag{3.4}$$

$$q_{\text{diffgreybody}} = \varepsilon \sigma T^4 \tag{3.5}$$

Where

σ is the Stefan–Boltzmann constant ($5.670374 \cdot 10^{-8}$ $[\mathrm{W/m^2K^4}]$)
ε is the emissivity constant

Alongside emitting radiation, a body can also absorb, reflect or transmit radiation originating from other media (Culham, 2016). Absorption (α) is where the energy entering the media is transferred to a different type of energy, usually internal energy/heat. Reflection (ρ) is where the electromagnetic radiation 'bounces' off the surface, never causing any heat transfer to the medium. Transmission (τ) is where the electromagnetic radiation travels through the medium without transferring energy to the particles themselves. For materials that might be evaluated in this thesis, the transmitted radiation will be neglected as only a small portion of the wavelengths will be likely to travel through the type of materials (Zandbergen, 2020). The incoming radiation can therefore either be absorbed or reflected as shown in Eq. 3.6. Because the media are modelled as a diffuse grey body the reflected radiation will scatter similarly to the emitted radiation (in a hemisphere). It will however be different to the emitted radiation as it will contain the same amount of energy as the incoming radiation. Kirchhoff’s law states that for a material in thermodynamic equilibrium the absorption constant is equal to the emissivity constant, as shown in Eq. 3.7. This thermodynamic equilibrium state is assumed in other studies like that of the Space Shuttle (Ko, Quinn, Gong, Schuster, & Gonzales, 1982) and therefore will be assumed for this thesis as well.

$$1 = \alpha + \rho \tag{3.6}$$

$$\varepsilon = \alpha \tag{3.7}$$

Where

α is the absorption constant
ρ is the reflection constant

A diffuse surface radiates energy from the surface spread over a hemisphere around the surface. For a receiving surface, only a portion of the radiated energy is received, unless the receiving surface covers the entire hemisphere from the original surface. To account for this effect a view factor is used to quantify the portion of radiation that leaves surface A and arrives at surface B(Zandbergen, 2020; Culham, 2016). The view factor is dependent on the distance, angle and area of the two surfaces as shown in Figure 3.1 and quantified by Eq. 3.8. Depending on the shape of the surfaces, simplifications to this equation can be made to help with computational cost, however in this thesis the software used covers these calculations.

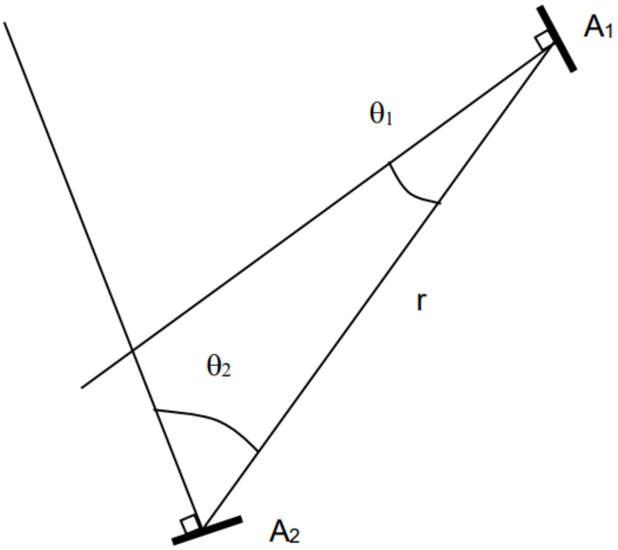

Figure 3.1. Radiation View Factor (Zandbergen, 2020)

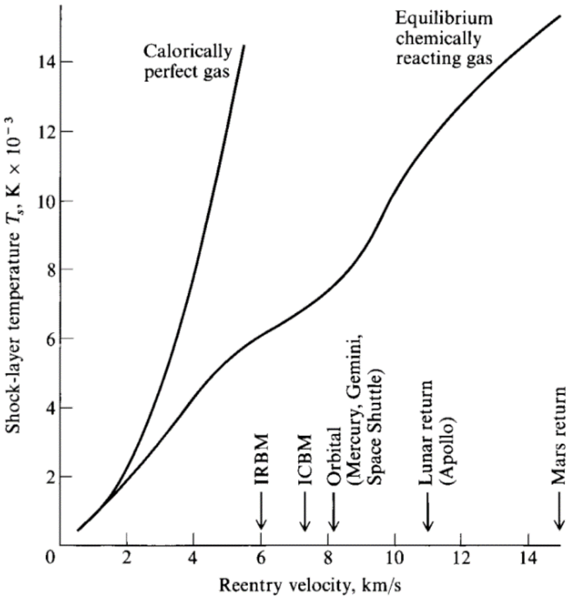

Figure 3.2. Shock layer temperature for a calorically perfect gas and an equilibrium chemically reacting gas (Anderson, 2006)

$$A_1 F_{1\to 2} = A_2 F_{2\to 1} = \int_{A_1} \int_{A_2} \frac{\cos(\theta_1)\cos(\theta_2)}{\pi R_{12}^2} dA_2 dA_1 \tag{3.8}$$

Where

A is the element area $[\mathrm{m}^2]$
F is the dimensionless view factor
θ is the angle between the flow and tangent of surface $[\mathrm{deg}]$
R_{12} is the distance between two surfaces $[\mathrm{m}]$

3.1.3. Convection

Convection is heat transfer caused by the movement of a fluid (Zandbergen, 2020). This movement transports fluid particles which each carry a quantity of internal energy, hence energy is transferred. For this thesis the convective heat transfer within the air (fluid) is not of importance but the heat transfer of air to the body can be predicted using Newton’s law of cooling. Newton's law of cooling states that the heat loss of a body is proportional to the difference in temperatures between the body and its surroundings while under the effects of a flowing fluid, as shown in Eq. 3.9. The convective heat transfer coefficient (h) includes the effects of the fluid flow pattern near the surface, the fluid properties and the geometry of the surface.

$$q_{\mathrm{conv}} = h_{\mathrm{conv}}(T_r - T_w) \tag{3.9}$$

Where

h_{conv} is the convective heat transfer coefficient $[\mathrm{W/m^2K}]$
T_r and T_w are the reference and wall specific temperatures respectively $[\mathrm{K}]$

Equation 3.9 is only partially true because in high temperature (and high pressure) air the specific heat of the flow does not remain constant. This means that the use of enthalpy is more appropriate for the calculation of convective heat transfer (Spruijt & Zandbergen, 1996), as shown in Eq. 3.10. The use of enthalpy is better able to capture the change in specific heat, which according to Spruijt & Zandbergen (1996) is required for flow faster than Mach 6. This justification is also shown by Figure 3.2 where the calorically perfect gas has a constant specific heat and the equilibrium chemically reacting gas accounts for the specific heat change. The Mk-III's trajectory, shown in Figure 2.3, shows that either temperature or enthalpy could be used for modelling but, because there are still uncertainties in the Mk-III trajectory design, enthalpy is chosen to suit potential future needs.

$$q_{\text{conv}} = h_{\text{conv}}(h_r - h_w) \tag{3.10}$$

Where

h_{conv} is the convective heat transfer coefficient $[\text{kg/m}^2\text{s}]$
h_r and h_w are the reference and wall specific enthalpy respectively $[\text{J/kg}]$

3.1.4. Absorption

A medium can also act as a heat sink, absorbing energy and storing it in the form of internal energy (Zandbergen, 2020). This stored energy increases the medium's temperature causing a change in the amount of energy being transferred to its surroundings. Hence the material's temperature, particularly in comparison to its surrounding, is an important value. Unlike for heat transfer when storing energy, a unit of joule is used rather than a heat flux. This is because mass is a factor in the amount of energy absorbable per unit temperature, as shown in Eq. 3.11 (Zandbergen, 2020). This equation can be related to the amount of energy per unit time by taking the derivative with respect to time, as shown in Eq. 3.12 (Zandbergen, 2020). In these equations it is assumed that the mass of the medium/element remains constant.

$$Q = Mc\Delta T \tag{3.11}$$

$$\dot{Q} = Mc\frac{\partial T}{\partial t} \tag{3.12}$$

Where

Q is the heat transfer $[\text{J}]$
M is the mass $[\text{kg}]$
c is the specific heat capacity $[\text{J/kgK}]$
t is the time $[s]$

When a material changes its internal energy there is potential for a phase change to occur. For this thesis a phase change could potentially occur in a TPS that relies on cooling fluid. A phase change of this nature could result in clogging of the cooling system and hence is not a desirable phenomenon. Phase change could also occur in a structural part of the spaceplane. However, this will lead to negative structural effects likely resulting in failure. Therefore, phase change will not be modelled in this thesis but, whether they may occur will be checked.

3.2. Non-dimensional numbers

For aerodynamics and thermodynamics, important behaviours of the flow are non-dimensionalized into a few dimensionless numbers. These numbers can inform the user about the type of flow expected, allow the analysis to be simplified, and allows easier comparisons without being dependent on geometry.

3.2.1. Reynolds number

The Reynolds number (Re) is a dimensionless number that represents the ratio of the inertial forces relative to the viscous forces in a fluid (Zandbergen, 2020). Equation 3.13 shows the formulation for the Reynolds number at a distance x from the stagnation point. For the Reynolds number of a vehicle, the characteristic length of the vehicle would be used in place of x (which is the mean aerodynamic chord of the vehicle's main wing for this thesis). A frequent use of the Reynolds number is as a measure of whether the flow is laminar or turbulent, which is an important consideration in convective heat transfer. Laminar flow heat fluxes are generally lower than those caused by turbulent flow, due to the larger amount of mixing in the boundary layer of the turbulent flow. The Reynolds number is also often used to approximate boundary layer properties for simple geometries. This allows for a relatively simple analysis of the boundary layer with by joining complex behaviours into one value.

$$\mathrm{Re_x} = \frac{\rho V x}{\mu} \tag{3.13}$$

Where

Re is the Reynolds number
ρ is the density $[\mathrm{kg/m^3}]$
V is the velocity $[\mathrm{m/s}]$
x is the distance along surface $[\mathrm{m}]$
μ is the dynamic viscosity $[\mathrm{kg/ms}]$

3.2.2. Biot number

The Biot number (Bi) is a dimensionless number used in thermal analyses to define the resistance of heat transfer inside the material, compared to the resistance of heat transfer at the material's surface (Adrian, 2007). Defined according to Eq. 3.14, the Biot number accounts for the fluid conductivity, the material thickness and material conductivity to allow an informed decision whether the material can be considered thermally thin or thermally thick. In a thermally thin material, it can be assumed that a uniform temperature distribution exists normal to the surface. Thereby, instead of splitting up the material into elements in the direction normal to the surface, a single element can be used. Otherwise, if the material is considered thermally thick, the material requires to be split into elements to solve the internal heat gradient present. Duarte, Silva, & Castro (2009) and Simsek, Kuran, Ak, & Uslu (2016) define a thermally thin material as a material that has a Biot number of less than 0.1.

$$\mathrm{Bi} = \frac{h_{\mathrm{conv}}}{k} L \tag{3.14}$$

Where

Bi is the Biot number
L is the material thickness $[\mathrm{m}]$

3.2.3. Nusselt and Stanton number

The Nusselt (Nu) and Stanton numbers (St) are two dimensionless numbers that can be used to calculate the convection heat transfer coefficient (Zandbergen, 2020) of a flowing fluid. The Stanton number defines the amount of heat transfer of a fluid by means of convection, compared to the total heat contained within the fluid flow, as shown in Eq. 3.15 (Zandbergen, 2020). The definition of the Stanton number can change depending on whether enthalpy or temperature is used to define the convection heat transfer. For this thesis, enthalpy is used. The Nusselt number compares the heat transfer of a fluid by convection and conduction. For this thesis the Stanton number will be used because of the use of enthalpy in the convective heat transfer (Quinn, 2000). The Nusselt number, as shown in Eq. 3.16, is however useful for the prediction of free convection. Convection within the context of aerodynamic heating almost always references forced convection, but some convection, such as that internal to the structure, can be considered free convection. For the free convection, temperature is used rather than enthalpy, as in Eq. 3.9, hence the Nusselt number can be used.

$$\mathrm{St} = \frac{h_{\mathrm{conv}}}{\rho V} \tag{3.15}$$

$$\mathrm{Nu} = \frac{h_{\mathrm{conv}} L}{k} \tag{3.16}$$

Where

St is the Stanton number
Nu is the Nusselt number
L is the characteristic length $[\mathrm{m}]$

3.2.4. Prandtl number

The Prandtl number (Pr) is a dimensionless number that compares the momentum transfer between the flow and the wall relative to the heat transfer between the flow and the wall (Zandbergen, 2020). The true formulation of the Prandtl number is given by Eq. 3.17, though it is often approximated for gasses by a rougher approximation of the Prandtl number as given by Eq. 3.18 (Zandbergen, 2020).

This thesis however uses an alternative method described in Section 5.1.1 because this accounts for dissociation within the air.

$$\mathrm{Pr} = \frac{c_p \mu}{k} \tag{3.17}$$

$$\mathrm{Pr} \approx \frac{4\gamma}{9\gamma - 5} \tag{3.18}$$

Where

Pr is the Prandtl number
c_p is the specific heat at constant pressure $[\mathrm{J/kgK}]$
γ is the specific heat ratio

3.2.5. Grashof number

The Grashof number (Gr) is a dimensionless number that describes the ratio of buoyancy to viscous forces of a fluid (Sommers, 2012). Hence it is an important number in the use of free convection as the driving factor is the buoyancy of warm and colder fluids. Equations 3.19 and 3.20 show the formulation of the Grashof number (Ko, Quinn, & Gong, 1988).

$$\mathrm{Gr} = \frac{g\beta(T_\infty - T_w)L^3\rho^3}{\mu^3} \tag{3.19}$$

$$\beta = \frac{2}{T_w + T_\infty} \tag{3.20}$$

Where

Gr is the Grashof number
g is the gravitational acceleration $[\mathrm{m}/s^2]$
β is the approximation of coefficient of thermal expansion

3.3. Defining thermal energy balance

Once all the components of heat transfer are known, a thermal energy balance equation can be set up. For this a fictional control volume is used in which energy can be stored and transferred in/out across its boundaries. For the thermodynamics that will be taking place for the Mk-III, the control volume will be an element within the structure. Therefore, there are three cases to consider.

- Element exposed to the external flow
- Element within the structure only surrounded by other structural elements
- Element exposed to the internal void of the spacecraft

Each of these three types of elements will have different combinations of convective, radiative and/or conductive heat transfer going in and out of the control volume boundaries, as well as an assigned mass capable of absorbing energy. The heat flux for each of these methods is defined by the material properties and calculated from the flow conditions. Because the spaceplane is travelling through an ever-changing trajectory the thermodynamic condition is transient. This means that the energy equation calculates the change in temperature for a control volume over a period of time, rather than calculating the steady state of the control volume.

3.4. Initial Predictions Based on Standard Graphs

For a space vehicle to re-enter safely, the vehicle travels through a ‘re-entry corridor’, an example of which is shown in Figure 3.3 (Mooij, 2019). Such a corridor takes into considerations limitations of the vehicle, including structural and thermal limits, creating altitude versus velocity limits of where the vehicle can fly. Figure 3.3 shows an example of a re-entry corridor that accounts multiple vehicle limits. The altitude versus velocity graphs can be used to gain an initial understanding of various vehicle metrics. Figure 3.4 is an example of this for the Hopper (Pezzella G. , Martini, Roncioni, Kauffmann, & Tomatis, 2008) where from the altitude and velocity, the vehicle’s Mach and Reynold’s number can be calculated along the trajectory. In Figure 3.5 (Hansen, 1958) an approximation of the stagnation temperature at different altitudes and velocities is shown. These types of graphs help inform initial design decisions based on simplified models. Figure 3.5 (Hansen, 1958) allows the Mk-III stagnation temperature to be approximated at 2000 [K] which will be used to help identify potential materials for the vehicle.

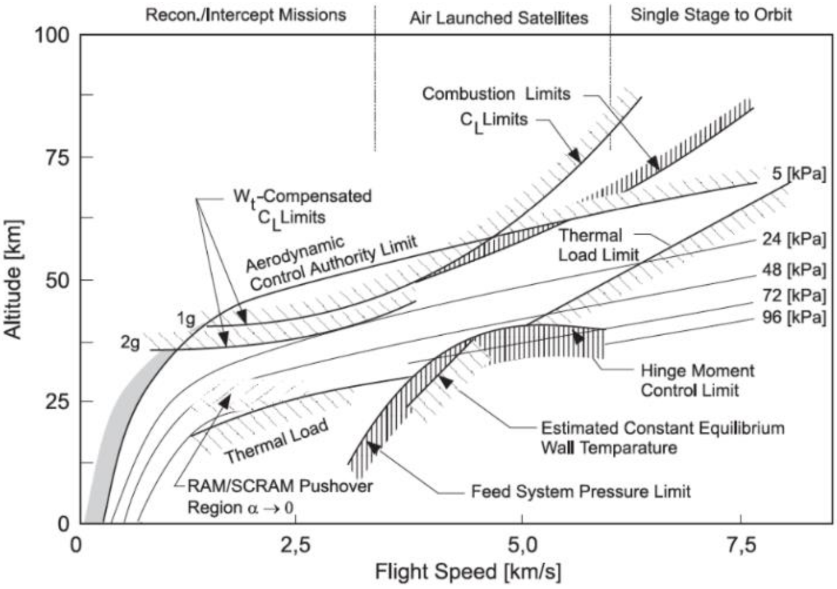

Figure 3.3. Example of a re-entry corridor (Mooij, 2019)

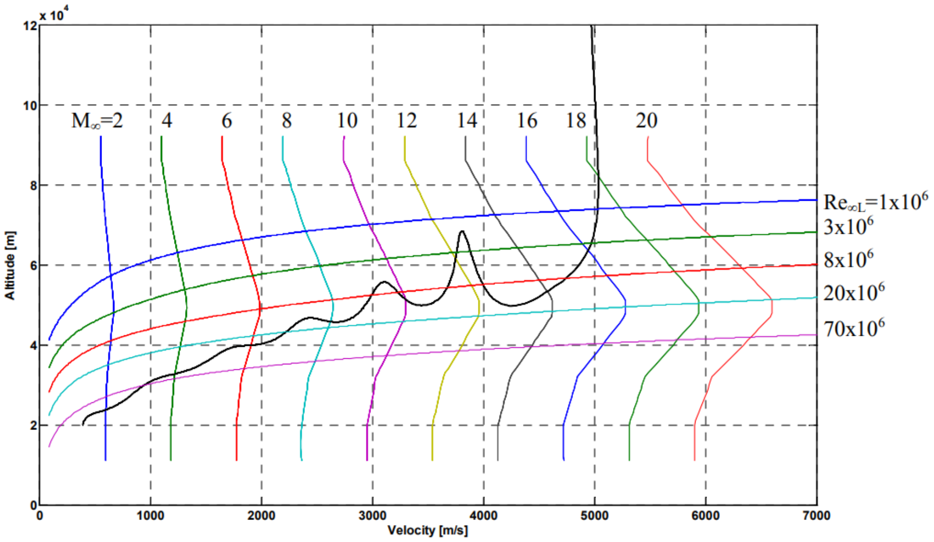

Figure 3.4. Reynolds number and Mach number against altitude and velocity for the Hopper (Pezzella et al. 2008)

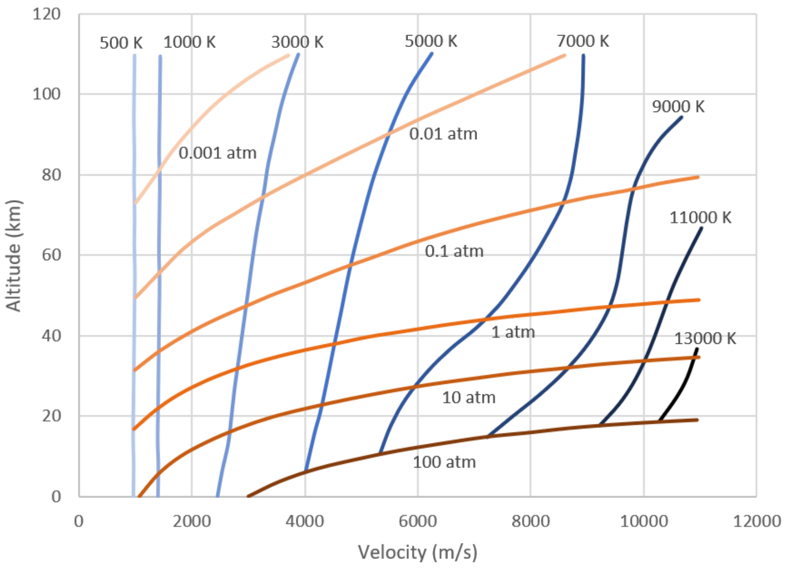

Figure 3.5. Stagnation Temperature Approximation at Different Altitudes and Velocities (Hansen, 1958)

4. Model

Thermal modelling is a complex analysis that requires modelling both the fluid flow and the thermodynamics of the structure. This thermal behaviour is ever changing due to the constantly changing state of the vehicle as it flies along the trajectory. The combination of these aspects means that the modelling of the aerothermal behaviour of the Mk-III vehicle is not trivial and requires a transient coupled structural and fluid thermal model along the entire trajectory. This chapter will discuss firstly the tools for the flow and structural thermal modelling. The chapter will then continue to discuss how and why the model has been built to combine the separated thermal fields that are coupled to each other. Lastly the configuration of the vehicle within these models will be discussed.

4.1. Tools

4.1.1. Flow modelling

The first identifiable problem is the modelling of the thermal behaviour of the flow around the Mk-III. Due to the changing spaceplane temperature and trajectory conditions this flow field is continuously changing, causing differencing heat flow to the spaceplane's structure. The prediction of this heat flow can be done by either wind tunnel testing or numerical calculations, or engineering method calculations (Simsek et al., 2016). Each of these methods have their own advantages and disadvantages such as accuracy, cost, time and complexity. Use of engineering methods is chosen for this thesis to model the thermal behaviour of the flow field around the Mk-III. This method is expected to be sufficiently accurate for this thesis and the fastest option. The method suits the stage of conceptual development of the Mk-III best out of the three options. Chapter 5 will display all the engineering methods used to achieve an accurate model of the flow.

The numerical methods choice does not exclude the usage of either of the other methods in future studies, in particular numerical methods. Combining this tool with more accurate, yet more expensive and less accessible models, means that results can be calibrated to gain the most out of accuracy and coverage in terms of trajectory and plane surface. An example of this is for the Hopper (Pezzella et al., 2008) and will be discussed further in Section 4.4.

These engineering methods have been implemented into a MATLAB program. The rational for using MATLAB is primarily due suitability for the analysis and easy accessibility. MATLAB has a toolbox that is able to connect with ANSYS APDL, the program used for the structural modelling, which will be a key feature of this simulation. The author also already had familiarity with the program which is an additional benefit over other options.

4.1.2. Structural modelling

The thermal modelling of the structure is the heat transfer to, from and within the structure. The convective heat transfer to the structure is already calculated by the flow modelling however, the structural thermal model accounts for the time element in the simulation taking the heat flux and integrating it over time. Due to the primary mode of heat transfer in the structure being conduction, and the convection and radiation can be seen as incoming energy, the equations are significantly easier compared to those for modelling flow (Simsek et al., 2016). For this reason, the simulation is left to already existing programs so as to not recreate the work many others have already done. For this thesis ANSYS APDL is used to model the structural thermal behaviour for the following reasons. Firstly, ANSYS APDL can be coupled to MATLAB and has potential to be coupled to ANSYS numerical flow simulation tools in the future. Secondly, ANSYS has the capability of complex composite structure definitions which allows for the anisotropic properties of the materials to be modelled. Lastly the author's familiarity with the program will aid simulation design. The complex shape means defining a composite structure from a CAD file would be complicated without an existing program designed to do so. ANSYS has a package called ACP (pre) designed to define composite structures for the use of its programs, including ANSYS APDL.

4.2. Coupling

Section 4.1 gives a brief overview of the tools used to calculate the flow and structural simulation however, these models both require to be solved at the same time. Due to them requiring different tools, solving them at the same time becomes a difficult task. One solution for this is to loosely couple the simulations (Barth & Longo, 2010). This means that the simulations are coupled via their input and output but are solved separately. The output of the flow model, and input of the structural model, is a convective heat flux, split into the components convective heat transfer coefficient and near wall temperature. The output of the structural model and input of the flow model, is the wall temperature. Chapters 3 and 5 explains how these inputs and outputs are used and created in the calculations.

Figure 4.1 shows the loosely coupled simulation process in a schematic diagram. It shows both the time loop and required input and output of both the flow and structural simulations, as well as the overall input files required to define the model. Section 4.3 will describe the process of defining these input files. What Figure 4.1 shows that only small pieces of information are being transferred into and between models. The complexity of the calculations is mainly within the flow (and partially structural) model. Caution was taken when creating the coupled environment to ensure ANSYS and MATLAB interacted correctly. This coupling complexity is caused both by the sensitivity of the connection and the fact that ANSYS APDL is an old language which ANSYS has built their own GUI to ease user interaction. This GUI however does not interact with MATLAB or other languages. Therefore, the ANSYS APDL program language needs to be processed and evaluated for interactive use.

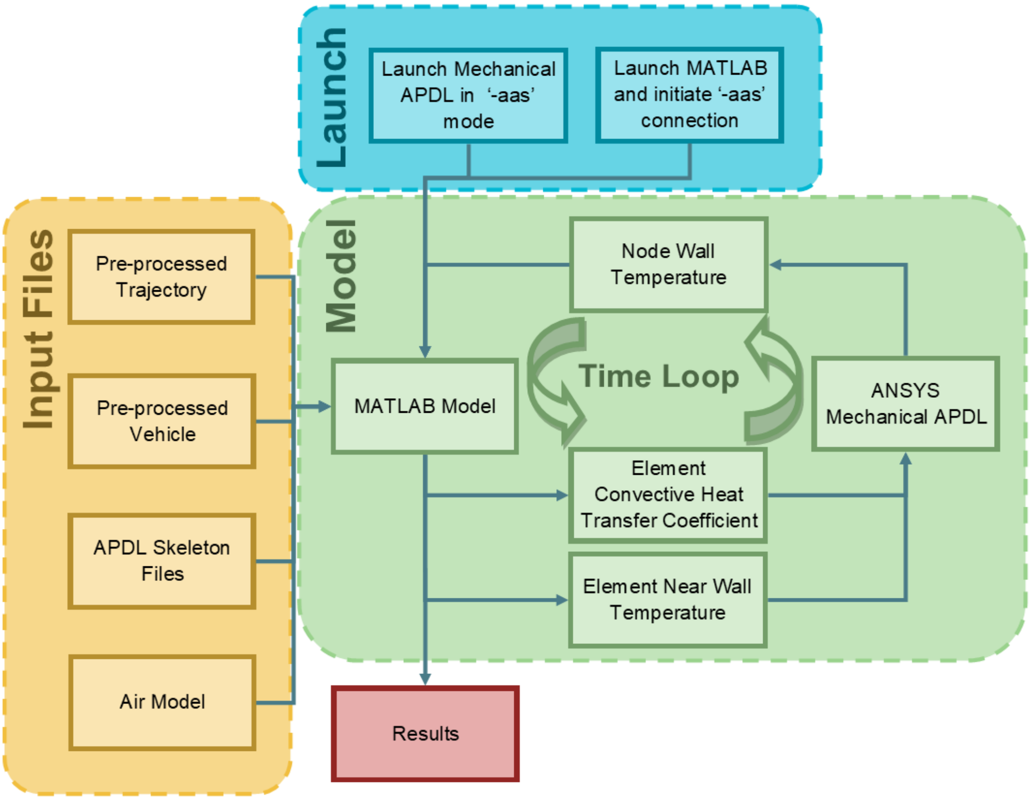

Figure 4.1. Aerothermodynamic model schematic diagram of the time simulation

A notable difference between what has been discussed in Chapter 3 and what is shown in Figure 4.1 is the use of convective heat transfer coefficient and near wall temperature, rather than importing a flux or using enthalpy. The reasoning behind importing a temperature into ANSYS APDL rather than an enthalpy is due to ANSYS APDL being a structural analysis working with material temperatures. However, using temperature does not affect the heat flux as enthalpy has been used in the flow calculations and temperature is used as an alternative definition for flux. Conversely, a convective flux heat transfer was also not used due to better convergence being observed, using the convective heat transfer coefficient. Using flux meant that the model did not change the incoming convective heat flux to the surface as the surface was changing temperature, which it did over time due to the heat flux itself. Defining the flux by a convective heat transfer coefficient and near wall temperature allows Eq. 3.10 to be used to account for the changing wall temperature. These inputs means that a smaller time step and iteration steps within a single time step are not required to provide sufficient accuracy of the model, hence improving simulation time. However, this method does not account for the change in both the convective heat transfer coefficient and near wall temperature due to the wall temperature, whose effect will be further discussed in Section 5.2.

4.3. Pre-simulation

The calculations taking place inside the simulation loop are described in detail in Section 4.2. For these calculations to take place, three main groups of information are required.

- Air model – explained in Section 5.1.1, allows the look-up of air properties based on enthalpy/temperature and pressure
- Trajectory – Time dependent trajectory data of velocity, altitude and angle of attack. As shown in Section 5.1.2, a number of the pre and post shock flow conditions are independent of the vehicle. Therefore, together with the air model, a trajectory pre-processing tool can pre calculate the pre-shock and post-shock air conditions.
- Vehicle – For the flow calculation, this only includes the relationship between the vehicle mesh node and elements of the external surface and the normal direction of the external elements. For the flow and structural model, different levels of detail are required in the vehicle model. The flow model requires information on the external vehicle's nodes and elements of the vehicle whereas the structural model requires only locations of the nodes of the vehicle and how the vehicle joins together.

Once the above information is known the engineering methods can be applied to calculate the convective heat transfer coefficient and the near wall or recovery temperature using an input external surface temperature.

The method of communication between MATLAB and ANSYS is through the use of input files generated in MATLAB and then imported into ANSYS. MATLAB creates this input file based on a “skeleton input file” alongside information of convective heat flux and vehicle temperature. Within a simulation the only information in an input file that changes is the convective heat flux (or components thereof) and the temperature of the vehicle. Between different simulations, the definition of the vehicle might change which means 90% of the skeleton file would change and hence a new skeleton file is created. A change in the trajectory would not cause a change in the APDL skeleton file as this only affects flow calculations. The flow of the skeleton files and particularly the unique vehicle skeleton file is visualized in Figure 4.2.

Figure 4.2 shows an overview of the flow of information for creating the input files for the thermodynamic model. Notably, two primary groups of information are required for the simulation: the vehicle information and the trajectory information. These two key groups are separate input, meaning that if one changes the other does not also have to be modified. The vehicle pre-processing is a vastly more involved process due to the work required for ANSYS defining the composite structure, but also due to the information of processing this information for the use in MATLAB. A most notable portion of this work is to extract external vehicle element information such as the normal direction of the surface. The trajectory processing on the other hand requires significantly less work. Separating these two processes means combinations of vehicle and trajectory can be created without additional workload. The other input information remains the same, independent on the particular trajectory and vehicle case studied. Only if there is a change in the model will some of these files change.

4.4. Configuration

As well as knowing the tools and method of modelling, to start modelling we need to know what portion of the vehicle or trajectory will be analysed. The term used within this thesis to describe which part of the vehicle or trajectory is analysed, is the configuration of the analysis. This term does not refer to for example the angle of the control surfaces or the specific trajectory time analysed.

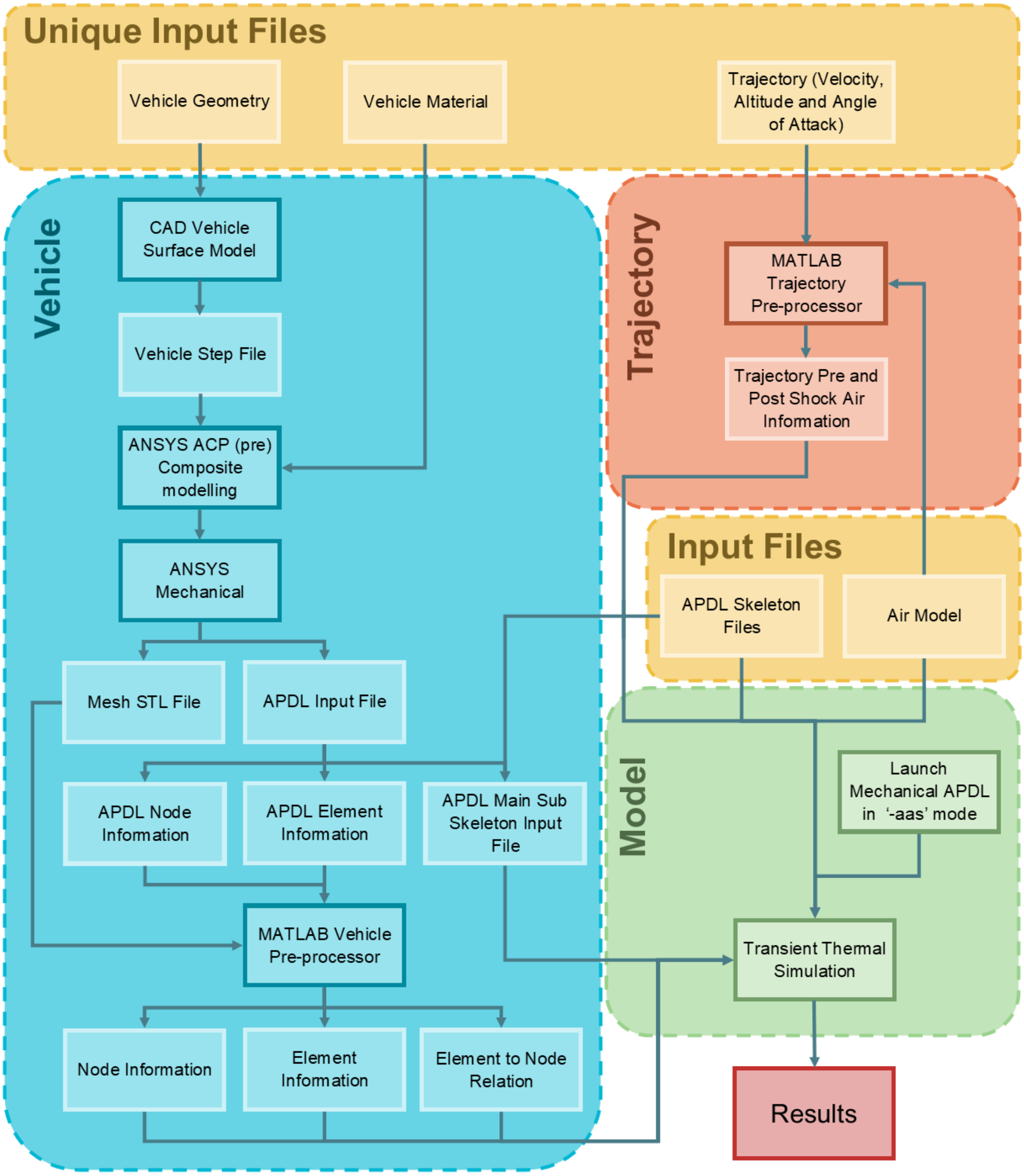

Figure 4.2. Aerothermodynamic model schematic diagram input file structure

There are four configurations that spaceplanes in literature have used which are a combination of 2D vehicle cross section, 3D vehicle (or section thereof), full transient trajectory or single time trajectory point (Barth, 2008; Gong, Quinn, & Ko, 1982; Ko et al., 1982; Pezzella et al., 2008; Husain, Jamshed, & Qureshi, 2012). Which method is used is dependent primarily on the tools used and the decade in which the research was conducted. As has been discussed, the chosen engineering methods are quick in its calculation, meaning that it is suitable to accompany this with a 3D full vehicle transient trajectory analysis, which has been chosen for this thesis. This configuration gives the best overview of the temperature the entire vehicle experiences at any stage in the trajectory. The validation of this is given in Chapter 6.

5. Engineering models

The use of engineering models is widely used within the conceptual and preliminary analysis of spaceplanes. Engineering methods approximate the flow and heating conditions based on empirical and theoretical equations, to best predict the aerodynamic heating that a spaceplane or hypersonic vehicle might experience. There are numerous approaches to solving aerodynamic heating by the use of engineering models, which vary in both complexity and in the different heat transfer aspects they account for. Generally, engineering methods solve the one dimensional thermodynamic equations (normal to the plane's surface) (Quinn, 2000; Duarte et al., 2009; Simsek et al., 2016) and represent the plane's geometry by simplified shapes. By evaluating the heat transfer one dimensionally, the fundamental equations are significantly simplified while providing a reasonable approximation for most surfaces. However, such equations cannot account for three-dimensional effects such as shock wave interactions. Most of the engineering methods covered in this thesis will be modelled under some shape simplification assumptions. An example is the wing surface aft of the leading edge can be modelled as a flat plate flow. This simplifies the equations and allows basic verification of methods while being appropriate approximations of the true flow around a significant portion of the airfoil.

This chapter will primarily focus on the modelling of the flow using engineering methods. Section 4.2 has cover the linking between the flow results to the results of analysing the thermal behaviour in the structure. The chapter will start with determining the flow conditions around the surfaces being analysed (pressure, temperature, etc). Next these flow conditions will be further processed and used to predict the convective heat transfer coefficient. Convective heat transfer to the surface has already been explained in Section 3.1.3 to represent the amount of heat flux going into the plane. All other heat transfer methods (radiative and conduction) depend only on the temperatures and material properties so do not require the empirical flow calculations as the external flow and convective heat transfer does.

5.1. Local flow conditions

The engineering methods for predicting the flow used in aerodynamic heating is generally split into two parts. Firstly, the flow field is calculated using inviscid models to approximate the flow field outside the boundary layer. Once these conditions are known, assumptions are made to model the boundary layer, thereby modelling the viscous behaviour (Anderson, 2006; Duarte et al., 2009). This separation is important as it splits the complexity of the boundary layer and the calculation of the surrounding flow field. This section discusses the inviscid flow conditions. The next section will continue the discussion for the modelling of boundary layer flow using these local flow conditions at the boundary layer edge.

The boundary layer calculation can be separated into two distinct regions. The first is the stagnation point (and surrounding leading edge) and the second is the boundary layer away from the leading edge (Quinn, 2000). In the stagnation point most of the heating occurs due to the deceleration of the flow to zero velocity. On non-leading edge portions of the vehicle, most of the heating is caused by the viscous deceleration of the flow within the boundary layer.

5.1.1. Flow conditions and their relation to enthalpy

For a large number of equations defined within this chapter, local properties of air are required. Generally, air properties can be defined by two parameters, which normally are a combination of pressure and either temperature or enthalpy. Enthalpy is a more appropriate property to define the flow field compared to temperature, due to the changing specific heat at high temperatures, as explained in Section 3.1.3. Although the flow energy is measured in enthalpy the vehicle’s energy is measured in temperature. Therefore, a method for transforming between these parameters is required (Hansen, 1958). In addition to these parameters there are other thermodynamic and transport properties needed for the inviscid and boundary layer analysis, which is why Appendix A.1 describes the approximation of the following parameters from a known pressure and temperature.

- Compressibility factor (Z)
- Dimensionless enthalpy per mole $\left(\frac{ZH}{RT}\right)$
- Dimensionless specific heat at constant pressure $\left(\frac{ZC_p}{R}\right)$
- Ratio of specific heat (γ)
- Dynamic viscosity (μ)
- Coefficient of thermal conductivity (k)
- Prandtl number (Pr)

The transformation from temperature to enthalpy at a known pressure is a long sequence of equations split into simple steps. However, the opposite transformation becomes increasingly more complex using this method as the equations are not easily reversibly solved. Therefore, the method in Appendix A.1 will be implemented in a way to create a look-up table. This look-up table will allow the transformation of thermodynamic properties both ways, and means that calculation processes for transforming properties is required during the analysis. Appendix A.1 shows and explains the steps taken and equations used to calculate the air properties and create the look-up tables.

5.1.2. Stagnation point

The earlier comparison of using enthalpy or temperature for convective heat transfer is also applicable to the prediction of the flow. Across a shock wave the pressure, velocity, enthalpy and other flow properties change considerably and must be accounted when calculating flow conditions at the stagnation point. For the calculation of the properties after the shock wave it is assumed that the free stream state is known (as they are defined by the trajectory, *i.e.* altitude and velocity) and that at the leading edge there is a normal isentropic shock wave. The process of calculating the air properties after the shock wave is by iterative process (Moeckel, 1957). The first step is to use Eq. 5.1 and 5.2 using an initially guess of $\mathrm{V}_2/\mathrm{V}_1$. Next the state behind and in front of the shock wave can be used to estimate the density behind and in front of the shock wave. For this the ideal gas relation can be used as shown in Eq. 5.3, where a compressibility factor is included to account for high temperature effects where dissociation causes the number of moles to change compared to the undissociated air. Lastly the ratio $\mathrm{V}_2/\mathrm{V}_1$ should be updated according to Eq. 5.4 and iterated until convergence.

$$\frac{\frac{p_2}{p_1}-1}{\gamma_1 M_1^2} = 1-\frac{V_2}{V_1} \tag{5.1}$$

$$\frac{\frac{h_2}{h_1}-1}{\frac{\gamma_1-1}{2}M_1^2} = 1-\left(\frac{V_2}{V_1}\right)^2 \tag{5.2}$$

$$\frac{p}{\rho} = \frac{ZRT}{M_0} \tag{5.3}$$

$$\frac{\rho_2}{\rho_1} = \frac{V_1}{V_2} \tag{5.4}$$

Where

M is the Mach number

Having calculated the flow conditions behind the shock wave the solution can now be used to calculate the flow conditions at the stagnation point (Quinn, 2000). The flow condition firstly requires the calculation of the Mach number behind the shock wave. This is calculated by the use of Eq. 5.5 where the input can be obtained by using the lookup tables produced from Section 5.1.1. The stagnation point values of pressure, temperature and density can then be calculated by using Eq. 5.6 to 5.8 (Quinn, 2000; Duarte et al., 2009; Simsek et al., 2016). In Eq. 5.8 the values of pressure, compression factor and temperature can be either those relative to the wall/stagnation point or relative to just behind the shock wave. In the case of the stagnation temperature this value should be used to calculate the stagnation enthalpy with the use of the lookup tables.

$$M_2 = \sqrt{\gamma \frac{p_2}{\rho_2}} = \sqrt{\gamma Z_2 R T_2} \tag{5.5}$$

$$p_{st} = p_2 \left(1 + \frac{\gamma_2 - 1}{2} M_2^2\right)^{\frac{\gamma_2}{\gamma_2 - 1}} \tag{5.6}$$

$$T_{st} = T_2 \left(1 + \frac{\gamma_2 - 1}{2} M_2^2\right) \tag{5.7}$$

$$\rho = \frac{p M_0}{Z R T} \tag{5.8}$$

A shock wave is only formed in front of the leading edge when the spaceplane is in supersonic/hypersonic free stream flight. When the plane is flying subsonic the free stream conditions replace the supersonic/hypersonic conditions after the shock wave in Eq. 5.5 to 5.8.

5.1.3. Flow prediction over the remainder body

The non-stagnation point regions of the vehicle are also important from an aerothermodynamic point of view as there can also be substantial heat transfer along the remainder of the body (sometimes even more than at the leading edge). Even if the heat transfer is lower in these regions, it is important to analyse them as they might be capable of different materials choices and lighter structures compared to the material in the leading edge regions. Similarly to the prediction at the stagnation point, the inviscid flow field can be calculated. One of the most crucial steps in calculating the heat flux over the non-leading edge regions is the prediction of the pressure distribution along the surface, which is then used to map out the velocity and temperature locally. For this either modified Newtonian method or inviscid CFD is used in literature reports (Simsek et al., 2016; Duarte et al., 2009; Quinn, 2000). Inviscid CFD is considered to be more accurate as it accounts for more complex shock effects compared to the modified Newtonian method. The modified Newtonian method on the other hand is quicker and has been shown to provide acceptable predictions of the flow field for many cases.

The modified Newtonian method is an approximate method for predicting the pressure distribution over a hypersonic body, using the known properties at the stagnation point (Anderson, 2006). The modified Newtonian method, as defined by Eq. 5.9, generally uses the maximum value of the pressure coefficient evaluated at a stagnation point behind a normal shock wave as defined by Eq. 5.10. The method is known to be more accurate for blunt-nosed bodies and is more accurate for higher hypersonic speeds. This is caused by the underlying assumption of the modified Newtonian method becoming increasingly similar to the true flow. The fact that the modified Newtonian method is a less accurate fit for subsonic and low supersonic flow is generally justified due to the lower heating rates at these lower speeds (Duarte et al., 2009). This lower heating rate with high error causes a low heating rate error in the overall trajectory and thereby is neglected. By deeming this error negligible the modified Newtonian method is able to be implemented and thereby method continuity and simplicity is kept across the entire speed range.

$$C_p = C_{p_{max}} \sin^2 \theta \tag{5.9}$$

$$C_{p_{max}} = \frac{p_{0L} - p_\infty}{q} \tag{5.10}$$

Where

q is the dynamic pressure [Pa]

Once the coefficient of pressure is transformed into a local pressure using the rearranged Eq. 5.10 the value can be used to estimate the local Mach number. This is done using an equation similar to Eq. 5.6 as shown in Eq. 5.11 (Quinn, 2000). This local Mach number can be used in Eq. 5.12 to calculate the local temperature at the edge of the boundary layer. As has been done at the stagnation point, these local temperatures and pressures can be used in the look up table to calculate the flow enthalpy at the edge of the boundary layer.

$$M_L = \sqrt{\left(\left(\frac{p_{st}}{p_L}\right)^{\frac{\gamma-1}{\gamma}} - 1\right)\frac{2}{\gamma - 1}} \tag{5.11}$$

$$T_L = \frac{T_{st}}{1 + \frac{\gamma - 1}{2} M_L^2} \tag{5.12}$$

5.2. Convective heat transfer

Knowing the inviscid local flow conditions is the first step into determining the heat flux from aerodynamic heating. The next is to use engineering models to model the boundary layer and the enthalpy/temperature distributions that exist within it. The section will cover the various aspects of modelling the boundary layer and calculating the resulting convective heat transfer flux.

5.2.1. Laminar-to-turbulent transition

Before modelling the boundary layer, it is important to understand the basic concepts driving the engineering methods modelling the heat transfer in the boundary layer and how the flow conditions in the boundary layer effect this. The viscous effects in the boundary layer and the wall temperature cause a temperature/enthalpy gradient to occur at the surface of the vehicle. Figure 5.1 (Anderson, 2006) shows one such possible temperature distribution in the boundary layer. This gradient is a result of the heat transfer to the surface and is in correlation with the amount of heat transfer as shown in the formulation of convective heat transfer in Section 3.1.3. From basic aerodynamics it is known that there are two types of boundary layers; laminar and turbulent (ignoring transition region). For turbulent boundary layer there exists more mixing of energy from the free-stream in the boundary layer, causing higher gradients of properties closer to the surface compared to a laminar boundary layer. Therefore, it can be understood that to accurately predict the heat transfer due to aerodynamics, the laminar to turbulent regions of the flow must be predicted. The transition Reynolds number is a value widely used to predict when the transition from laminar to turbulent flow occurs. However, this number is dependent on a large number of flow variables making an accurate prediction of when transition occurs is a complex process. Additionally, it is known that a transition from laminar to turbulent flow does not occur instantly but is defined, where the turbulent behaviour is more dominant, as shown in Figure 5.2 (Schlichting & Gersten, 2016). In most analyses the definition of transition is between the dominantly laminar and dominantly turbulent regions.

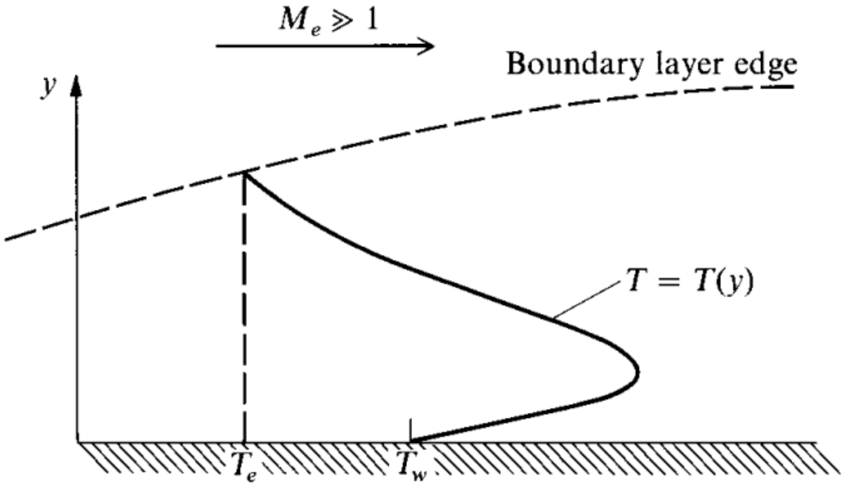

Figure 5.1. Example of a temperature profile within the boundary layer (Anderson, 2006)

Having understood the importance of predicting the Reynolds number, an appropriate equation to calculate it can be selected. The Space Shuttle assumed that transition occurred at a local Reynolds number of $5 \cdot 10^5$ (Gong et al., 1982). However, when modelling high speed flow, the effect of Mach number is one that cannot be ignored in the transition criteria. Quinn (2000), Simsek et al. (2016) and

Duarte et al. (2009) uses Eq. 5.13 to define the point at which the flow is laminar and turbulent, accounting for both the Reynolds number effect as well as Mach number effect. Table 5.1 shows the input values for Eq. 5.13 depending on the part modelled. (Quinn, 2000) does state that features, such as surface roughness and shock interaction, that cause premature transition are not accounted for in this model. There are many more models to predict the transition point however, this particular NASA model is used for high-speed aircraft, thereby very applicable for the Mk-III.

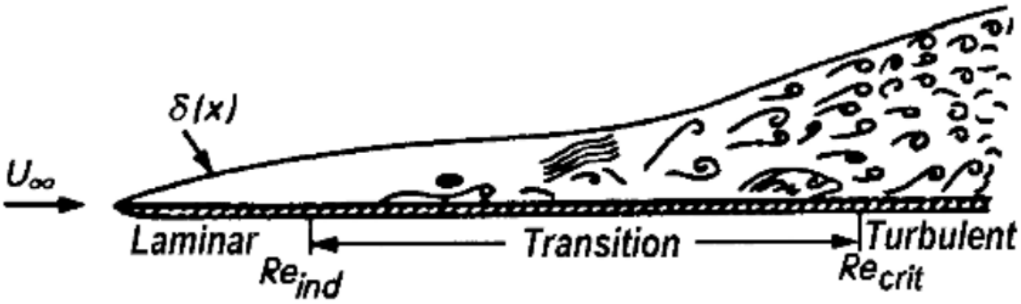

Figure 5.2. Laminar to turbulent transition representation (Schlichting & Gersten, 2016)

$$\log_{10}(\mathrm{Re_L}) > \log_{10}(\mathrm{Re_t}) + C_M M_L \qquad 5.13$$

Where

$\mathrm{Re_t}$ is the transition Reynolds number

C_M is the laminar to turbulent transition coefficient

Table 5.1. Laminar-to-turbulent transition recommended model values

	$\log_{10}(Re_t)$	C_M
Fuselage	5.5	0.2
Wing – no sweep	5.5	0.2
Wing – with sweep	5.5	0.1

5.2.2. Recovery enthalpy

As has been explained and shown in Figure 5.1, in the boundary layer a temperature/enthalpy gradient occurs due to the viscous effects heating the flow in the boundary layer. As can be seen in this figure the boundary layer edge temperature is not used to define the temperature gradient and therefore is not the value used when calculating the convective heat transfer. To account for this temperature profile in the boundary layer, the recovery enthalpy (also known as the adiabatic wall enthalpy) is defined. This is an enthalpy measurement used to represent the case where there is an adiabatic wall condition (*i.e.* no heat transfer to the wall). Equation 5.14 shows the equation for the recovery enthalpy (Quinn, 2000). Unlike the similar equation for the recovery temperature, the recovery enthalpy cannot be rearranged for a compressible flow into an equation of the Mach number and specific heat ratio due to the varying flow properties at high temperatures. It should be noted that within the boundary layer it is assumed that the flow is incompressible. In Quinn (2000) they also use the gravitational conversion factor and mechanical equivalent of heat, however this is because of their use of imperial units. For SI units this is not required but the user should be aware of the difference.

$$h_r = h_L + r\frac{V_L^2}{2} \qquad 5.14$$

Where

r is the recovery factor

Equation 5.14 holds for the laminar and turbulent flow across plane and for three-dimensional and two-dimensional leading edges without sweep. The difference between laminar and turbulent flow is accounted for by the convective heat transfer coefficient itself. To Eq. 5.14 another term is added to account for the sweep of the wing in the two-dimensional leading edge case, according to Eq. 5.15.

$$h_r = h_L + \frac{V_L^2}{2} + 0.855\frac{V_\infty^2 \sin^2(\Lambda)}{2} \qquad 5.15$$

Where

Λ is the leading edge sweep angle [deg]

The unknown in these equations is the recovery factor, r. For leading edge (stagnation point) calculations the recovery factor is equal to 1, as has already been input into Eq. 5.15. For the laminar and turbulent cases across an assumed flat plate (as will be the case with the remainder of the plane's analysis) the recovery factor is given by Eq. 5.16 and 5.17 respectively. This is an approximation but is widely used due to the good correlation with experimental data as the Prandtl number follows the same trends as the recovery factor. Only at extremely high temperatures, not expected within this analysis, will the recovery factor cause an error of sufficiently large amount using these equations (Anderson, 2006).

$$r = \sqrt{\mathrm{Pr_w}} \qquad 5.16$$

$$r = \sqrt[3]{\mathrm{Pr_w}} \qquad 5.17$$

5.2.3. Eckert's reference enthalpy

Having the equations for the local flow enthalpy, recovery enthalpy and the wall enthalpy gives insightful information about the boundary. But this doesn't provide information about the distribution within the boundary layer and at what enthalpy the flow properties should be evaluated. The Eckert's reference enthalpy is a calculated value, used in calculating the convective heat transfer coefficient that represents the enthalpy distribution in the boundary layer (Anderson, 2006). Although it is simple model, as shown in Eq. 5.18, it is able to provide an enthalpy value about which flow properties can be calculated to allow an accurate prediction of the convective heat transfer coefficient. This equation is used extensively in literature and therefore will also be applied when using engineering methods for the thermal analysis of the Mk-III (Quinn, 2000; Quinn & Gong, 1990; Anderson, 2006). In the literature reviewed that did not use Eckert's Reference Enthalpy, the Eckert's Reference Temperature was used which has an identical formulation but then using temperature instead (Simsek et al., 2016; Duarte et al., 2009; Spruijt & Zandbergen, 1996).

$$h^* = h_L + 0.5(h_w - h_L) + 0.22(h_r - h_L) \qquad 5.18$$

5.2.4. Variable or constant entropy

Entropy is a topic not often covered in modelling of thermodynamics in literature though the underlying assumptions within these models do account for entropy. Quinn (2000) states that a variable entropy flow occurs around bodies with blunt leading edges and noses. The paper states that the constant entropy situation only occurs for bodies with a sharp leading edge or nose. Variable entropy methods therefore appears at first glance to be more for the initial analysis of the Mk-III, as both the nose and leading edges are assumed to be blunt. This method however introduces complexities into the prediction of the convective heat transfer coefficient, because the momentum boundary layer thickness is required to be calculated and integrated. Because of this added complexity many aircraft surfaces are approximated with shapes where the constant entropy method provides a good result and representation of the flow (Quinn, 2000). Because other methods (Duarte, Silva, & Castro, 2009; Anderson, 2006) evaluate variable entropy cases with constant entropy models, this will also be implemented into the engineering methods for the Mk-III to limit the complexity of the model while still retaining an appropriately accurate model.

5.2.5. Convection heat transfer coefficient for stagnation point

For the stagnation point, the heat transfer coefficient can be predicted using the Fay and Riddell or Beckwith equations. These equations are simplified in Quinn (2000) using the assumption that Lewis number is 1.0 (which relates to no diffusion of air elements (Anderson, 2006)) and Prandtl number is 0.71. This is a large assumption given that dissociation is accounted for in the calculation of the flow properties. However, no method investigated accounts for the dissociation within heat transfer coefficient calculations (Anderson, 2006; Spruijt & Zandbergen, 1996; Duarte et al., 2009). The Fay and Riddle equation is shown in Eq. 5.19 which is used for the three-dimensional stagnation point. The Beckwith equation as shown in Eq. 5.20 is used for the two-dimensional stagnation point with or without sweep. The reason that the three-dimensional case has higher heating is explained in Anderson (2006), there the flow is more 'relieved' and can move to more dimensions, hence the boundary layer thickness is smaller and therefore the heat transfer gradient is larger. These equations have been validated against X-15 flight data showing good correlation. The X-15 is a different aircraft; however, it does have a comparable trajectory to the Mk-III spaceplane. The velocity gradient in these equations is approximated by Eq. 5.21 (Anderson, 2006; Quinn, 2000), which is a widely used approximation within literature.

$$h_{\text{conv}} = 0.94(\rho_{st}\mu_{st})^{0.4}(\rho_w\mu_w)^{0.1}\sqrt{\left(\frac{du}{dx}\right)_{x=0}} \tag{5.19}$$

$$h_{\text{conv}} = 0.704(\rho_{st}\mu_{st})^{0.44}(\rho_w\mu_w)^{0.06}\sqrt{\left(\frac{du}{dx}\right)_{x=0}} \tag{5.20}$$

$$\left(\frac{du}{dx}\right)_{x=0} = \frac{1}{R}\sqrt{\frac{2(p_{st}-p_1)g}{\rho_{st}}} \tag{5.21}$$

Where

$\left(\frac{du}{dx}\right)_{x=0}$ is the stagnation velocity gradient [$1/s$]

R is the leading edge radius [m]

5.2.6. Convection heat transfer coefficient for laminar flow

For both the laminar and turbulent flows over the main section of the aircraft structure, a simplification is made: the behaviour can be predicted as the behaviour over a flat plate. This means that surfaces such as the wing surface is approximated by the flow over a flat plate, greatly simplifying any analysis and allowing comparison with well documented reference cases. The equation governing the heat transfer coefficient is by the use of Stanton number and the Blasium skin friction formula (Quinn, 2000). This allows for the final Eq. 5.22 to be formalized. Any variable indicated with a star is evaluated at the reference enthalpy as has been calculated by Section 5.2.3 using the calculation of thermodynamic and transport properties explained in Section 5.1.1. The F in the equation is an empirical factor that is used in Eq. 5.22 and 5.23. Over the wing this is assumed to be 1 as the flat plate assumption is a good approximation. However, over a conical section the factors used are 1.73 and 1.15 for laminar and turbulent flows respectively. This allows this equation to also be applied to the fuselage as this represents a more conical shape.

$$h_{\text{conv}} = (F)0.332\sqrt{\frac{\rho^*\mu^*V_L}{x}}(Pr_x)^{-0.6} \tag{5.22}$$

Where

F is the empirical factor

5.2.7. Convection heat transfer coefficient for turbulent flow

The turbulent flow convective heat transfer coefficient is calculated using the van Driest method (Quinn, 2000). This method defines the convection heat transfer coefficient as per Eq. 5.23. The skin friction theory of van Driest calculates the turbulent flow skin friction over a flat plate using Eq. 5.24 with input Eq. 5.25 and 5.26. Unlike the laminar flow coefficient, the reference enthalpy is not used in this analysis. This is because the van Driest method does account for it but within the equation, rather than by the use of Eckert's reference enthalpy. The van Driest method is also used for the Space Shuttle (Ko et al., 1988) and shown as the turbulent convective heat transfer coefficient calculation in Quinn (2000).

$$h_{\text{conv}} = (F)\frac{C_f \rho_L V_L}{2(Pr_w)^{0.4}} \quad 5.23$$

$$\frac{0.242}{A\sqrt{C_f}\sqrt{\frac{h_w}{h_L}}}\left[\sin^{-1}\left(\frac{A-\frac{B}{2A}}{\sqrt{\left(\frac{B}{2A}\right)^2+1}}\right)+\sin^{-1}\left(\frac{\frac{B}{2A}}{\sqrt{\left(\frac{B}{2A}\right)^2+1}}\right)\right]-0.41-\log_{10}\left(\mathrm{Re_L}C_f\right) + 0.76\log_{10}\left(\frac{h_w}{h_L}\right)=0 \quad 5.24$$

$$A = \sqrt{\frac{\frac{\gamma-1}{2}M_L^2}{\frac{h_w}{h_L}}} \quad 5.25$$

$$B = \frac{1+\frac{\gamma-1}{2}M_L^2}{h_w/h_L} - 1.0 \quad 5.26$$

Where

C_f is the Local skin friction coefficient

5.2.8. Convection over leading edge

Between the stagnation point and the flatter sections of the body is the leading edge portion of the structure. In this region, neither the convective heat transfer coefficient approximations for the stagnation point nor laminar/turbulent flow over a flat plate are capable of describing the heat transfer coefficient. To approximate the heat transfer in this region a simple yet effective formulation is used, which is to approximate the heat transfer to a fraction of the stagnation point heat transfer, depending on the angle from the stagnation point. Quinn (2000) uses Figure 5.3 to predict the heat transfer flux relative to the stagnation point heat transfer flux. The θ_s is the angle between the stagnation point surface and the angle of the surface/element currently analysed. This method is generally conceived accurate up to a value of 70 deg from the stagnation surface angle, after which the flow moves to flat portions of the vehicle and flat plate methods should be used. This Figure 5.3 is a very similar method to a method described in Anderson (2006) except that this accounts for Mach number whereas the method in Anderson (2006) does not. This is shown in Figure 5.3 to cause discrepancies at higher angles.

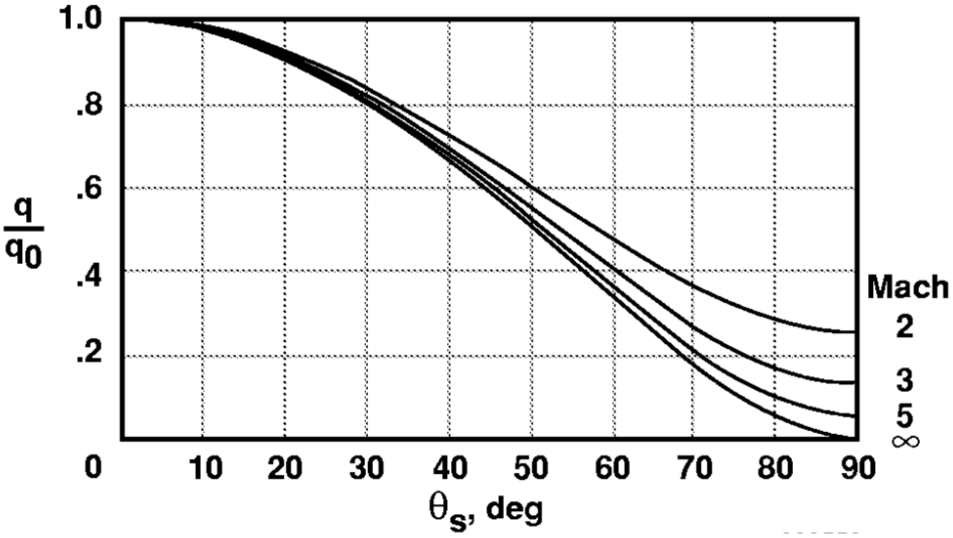

Figure 5.3. Leading edge convective heat transfer compared to stagnation point convective heat transfer (Quinn, 2000)

5.3. Internal convective cooling

As well as convection on the external skin of the vehicle, one of the research questions investigates the use of an active cooling system by running the oxidizer and fuel tank pressurant along the inside structure of the vehicle. This type of active cooling produces a flow of cold fluid on the interior of the vehicle that can remove the energy coming from the external flow through the structure. Because this is a scenario of flow providing heat transfer from a solid surface, convective heat transfer equations apply. This section will provide an overview of the calculations and assumptions associated with modelling this type of cooling.

To calculate the convective heat transfer, first the state of the flow coming into the internal structure of the vehicle should be known. This will be different to the state of the pressurant in the pressurant tanks and the fuel and oxidizer tanks. The pressurant tank is a high-pressure storage tank which stores the pressurant until it is required to pressurize the fuel and oxidizer tanks. The fuel and oxidizer tanks both have different low pressures to suit the needs of the rocket engine. The state of the fuel and oxidizer tank pressurant is calculated based on the state of the pressurant in the pressurant tank, using the conservation of enthalpy. The state in the tanks can then be used to calculate the total mass of pressurant to fully pressurize the fuel and oxidizer tanks once empty of fuel and oxidizer. Next, the state of the pressurant used as coolant (the point at which it would enter the structure) can be calculated based on the state the engine requires the fuel and oxidizer in and using the conservation of enthalpy. This state has a lower pressure than the tanks due to the losses associated with valves and pipes. This coolant pressurant pressure is then also used in the tanks to calculate the amount of pressurant left in the fuel and oxidizer tanks after being fully drained for cooling purposes. The pressurant mass available for active cooling is the difference between the initial pressurant mass in the tank and the pressurant mass left in the tank at cooling pressures. Therefore, this calculation results in a total mass of available pressurant for cooling purposes, the pressure, temperature and other state properties at the point which it exits the system to cool the structure.

The goal of the active cooling investigation in this thesis is to provide a recommendation whether this type of TPS has potential for the Mk-III. For this reason, a simplified model is used that calculates the heat flux a cooling system could create. For this calculation it is assumed that a cooling system can be designed to meet these demands. The calculation uses Eq. 5.27 to calculate the amount of energy absorbable by the coolant. The mass flow rate is calculated by the total amount of coolant available divided by the amount of time the coolant system is operating for. The specific heat at constant pressure is obtained from NIST (2021) and the change in temperature is a design parameter. By using the surface area of the vehicle, a heat flux on the internal surface of the vehicle can be calculated according to Eq. 3.1. This heat flux can be applied to the model on the internal surface of the vehicle during the time at which the cooling system is active.

$$\dot{Q} = \dot{m} c_p \Delta T \qquad 5.27$$

Where

$\dot{m}$ is the mass flow rate $[\mathrm{kg/s}]$

5.4. Atmospheric models

The Mk-III trajectory takes the spaceplane through an altitude range of 0 to 300 km during the ascent and descent. This large altitude range means that the spaceplane is flying through a change in atmospheric properties that has an influence on both aerodynamic loading as well as the thermal loads entering the structure. Through the years various atmospheric models have been developed to describe and predict the properties that distinguish the atmosphere. There are two distinct types of atmospheric models; standard atmospheric models which are only altitude dependent and reference atmospheric models which are dependent on both position and time (Mooij, 2019). For this thesis standard atmospheric models will be implemented because the trajectory does not account for the effect of Earth's surface position nor time. The Mk-III mission is not sufficiently defined to know which airport will be used for operations so any positional variations would only be an estimate (priv. comm. Tobias Knop). Therefore, the additional complexity of a reference atmospheric model does not make sense unless it is also accounted for in the trajectory. There are two standard atmospheric models that are widely used and referenced; Exponential atmosphere model and the US76 Standard Atmosphere (Mooij, 2019). Due to the atmospheric models primarily being able to be used in pre-simulation tools for processing the trajectory, the more calculation intensive model, US76 Standard Atmosphere, will be used for the thesis as it is a better representation of the Earth's atmosphere. Appendix A.2 explains the US76 standard atmospheric model.

6. Validation

The model explained in Chapters 4 and 5 was validated against known flight and reference model data. The air model was checked against the original models (Hansen, 1958). The X-15 and X-34 could be used to validate the model itself (Hassain & Qureshi, 2013; Banner, Kuhl, & Quinn, 1962; Riley & Kleb, 1998). However, a key problem for validating this model is to find representable vehicles with trajectories from which all information required is known. Information such as trajectory, vehicle geometry and material properties are publicly accessible for the X-15, however for other vehicles it is not publicly accessible. Key information such as material properties or structural thicknesses are not publicly accessible for a vehicle such as the X-34, making a transient thermal analysis inaccurate with incorrect assumptions. In these cases, if the data is available, a cold wall analysis can validate a part of the model without accounting for the transient behaviour thereby mitigating any unknown vehicle properties.

6.1. Air model

The air model is a key component of the model, making the validation of the results a requirement for validating the entire model. At almost all calculation steps outlined in Sections 5.1 and 5.2 one or more air properties are required. For a number of these steps the calculation is repeated for each of the mesh elements, making the air property calculation a large section of the model. In addition, due to the transient nature of this problem any calculation builds upon the results of the previous time step, creating a cumulative effect on any error. An error in the air model can therefore have a significant effect on the outcome of the analysis.

As noted in Section 5.1.1 the air model itself already has an error associated with it. This error is in the order of a few percent. The air model error is largest at lower temperatures but due to the heat transfer being lower at these temperatures, caused by lower speeds, this has less of an influence on the overall heat load compared to the high temperature error. Even though the air model has an error, this is far less than the error associated with any current trajectory from the Mk-III. The trajectories for the X-15 and X-34 used for validation in this chapter are well known from flight data, but the Mk-III does not have any flight data and therefore the trajectory is only an approximation. In addition to this known error, any air property is inherently uncertain due to the constantly changing atmosphere. Therefore, the errors introduced into the model by the air model are negligible for the purpose of this thesis.

Figure 6.1 show the results of various air properties as a function of temperature and pressure. The results modelled are displayed against the reference data (Hansen, 1958). Although the equations in Hansen (1958) capture the complex air property effect, Figure 6.1 shows that the reference data in Hansen (1958) does not provide sufficient resolution. Therefore, the equations are remodelled to a suitable resolution for the thermal model. The reference data matches well against the remodelled equations as shown in Figure 6.1. This means that the equations are properly executed and that the remodelled data can be used for the thermal model.

The air property data is used in the model by way of look-up tables. To ensure that the errors of the look-up method are suitable, a check was carried out against extracting the data from the air model itself. Table 6.1 shows the results of this analysis. All air properties except density have an error that is negligible compared to the error of the model itself. However, the density interpolation results show an error in the order of 10 to 100 %, which is unacceptable for the thermal analysis. This large error can be explained by the density variations with temperature and density shown in Figure 6.2. The density changes in order of magnitude over the range of temperatures and densities modelled in this analysis. Both the linear interpolation and spline interpolation cannot capture these changes with the resolution of the current data set. Therefore, density will be calculated not by a look-up table but by the use of Eq. 5.3. This equation uses the pressure, temperature and compressibility which are all either trajectory values or values with low interpolation error.

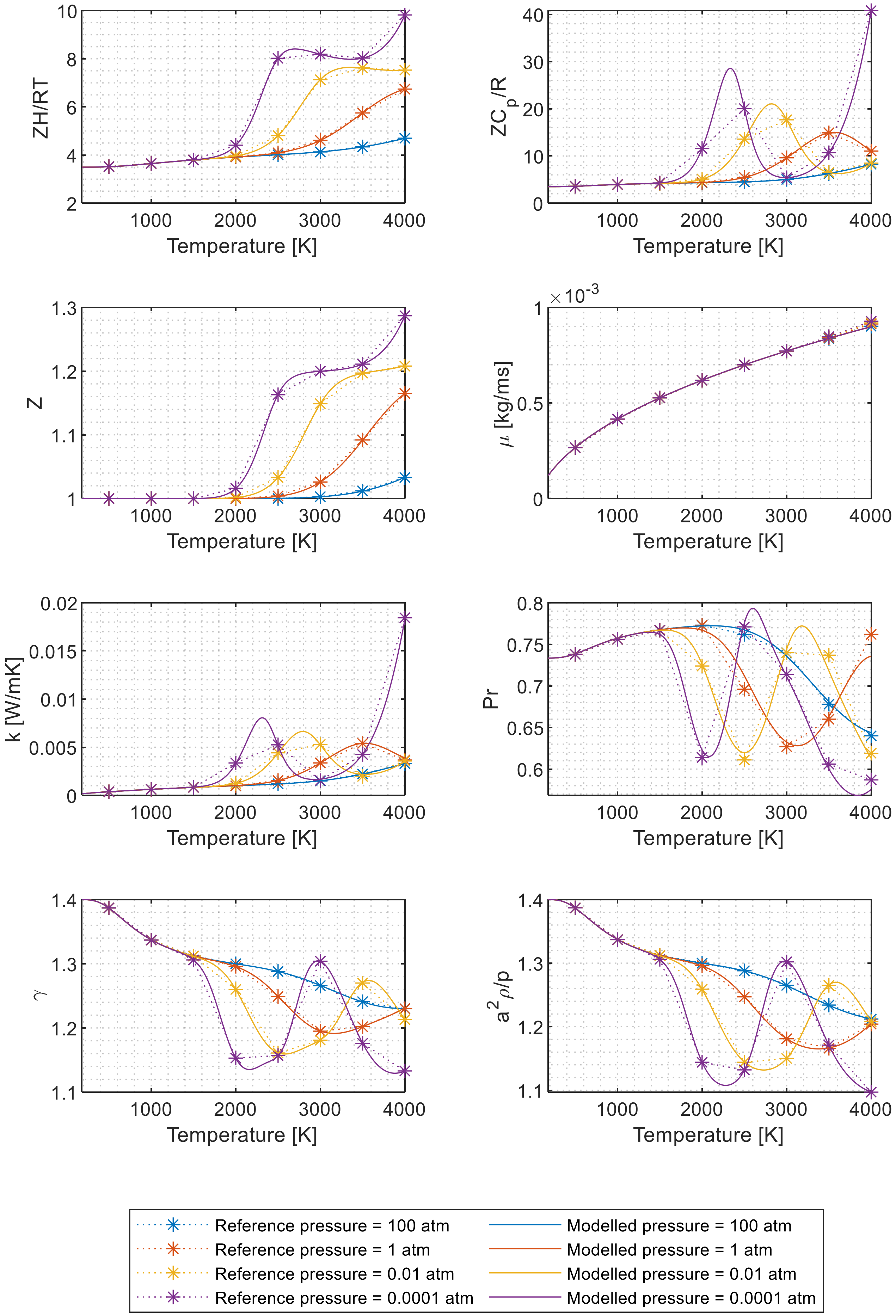

Figure 6.1. Air model validation displaying air properties against pressure and temperature (Hansen, 1958)

Table 6.1. Air model interpolation errors

	Linear Interpolation			Spline Interpolation		
	Minimum	Mean	Maximum	Minimum	Mean	Maximum
Enthalpy	0.044%	0.096%	0.111%	0.102%	0.103%	0.103%
Specific heat ratio	-0.017%	0.000%	0.007%	-0.002%	0.000%	0.002%
Density	-86.781%	-0.091%	28.988%	-122.4163%	-0.091%	38.620%
Prandtl number	-0.025%	0.000%	0.021%	0.000%	0.000%	0.000%
Dynamic Viscosity	-0.010%	0.001%	0.021%	-0.025%	0.000%	0.016%
Conductivity	-0.004%	0.131%	0.291%	0.148%	0.149%	0.149%
Compressibility	-0.020%	-0.002%	0.002%	0.000%	0.000%	0.000%
Speed of sound	-0.010%	0.000%	0.009%	-0.001%	0.000%	0.001%

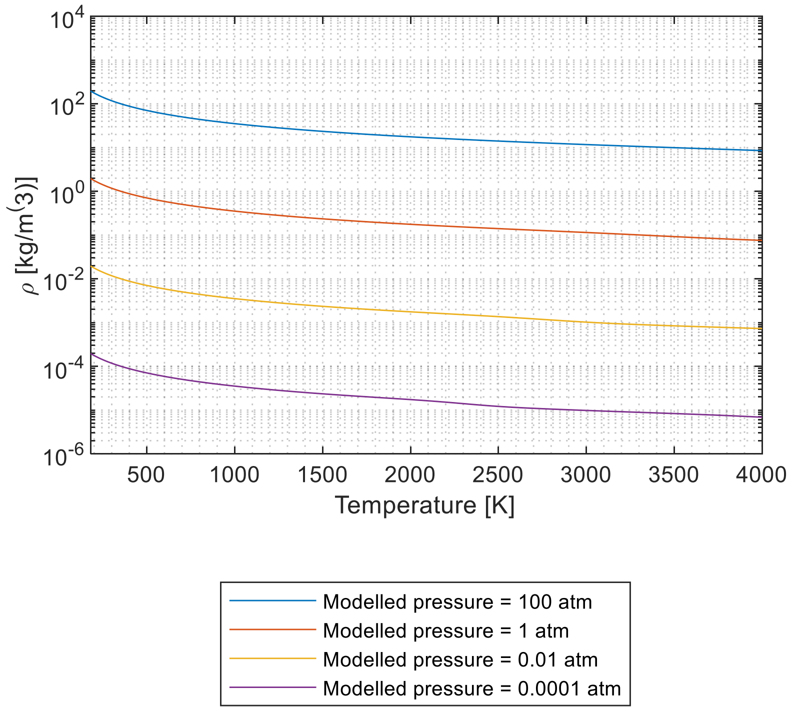

Figure 6.2. Air model density variations with pressure and temperature

6.2. X-34 cold wall stagnation point

The X-34 is a vehicle whose specific internal geometry information is not publicly accessible. This information includes material thicknesses and material properties. For this reason, a transient hot wall thermal validation analysis is not possible. However due to the trajectory being known, a cold wall thermal analysis can be conducted. For the X-34 cold wall heat flux at the stagnation point for two trajectories, shown in Figure 6.3, has been modelled (Riley & Kleb, 1998), which can be compared to the thermal model from this thesis where the wall conditions are kept cold. Figure 6.4 compares the results and shows that there is a good match between the reference and modelled heat flux.

The cold wall heat flux validation carried out on the X-34 trajectories does not fully validate the thermal model. It does however validate a portion of the model. Particular aspects of the model that it validates are the air model, shock layer model and stagnation point heat flux Eq. 5.5, 5.6, 5.19 and 5.21.

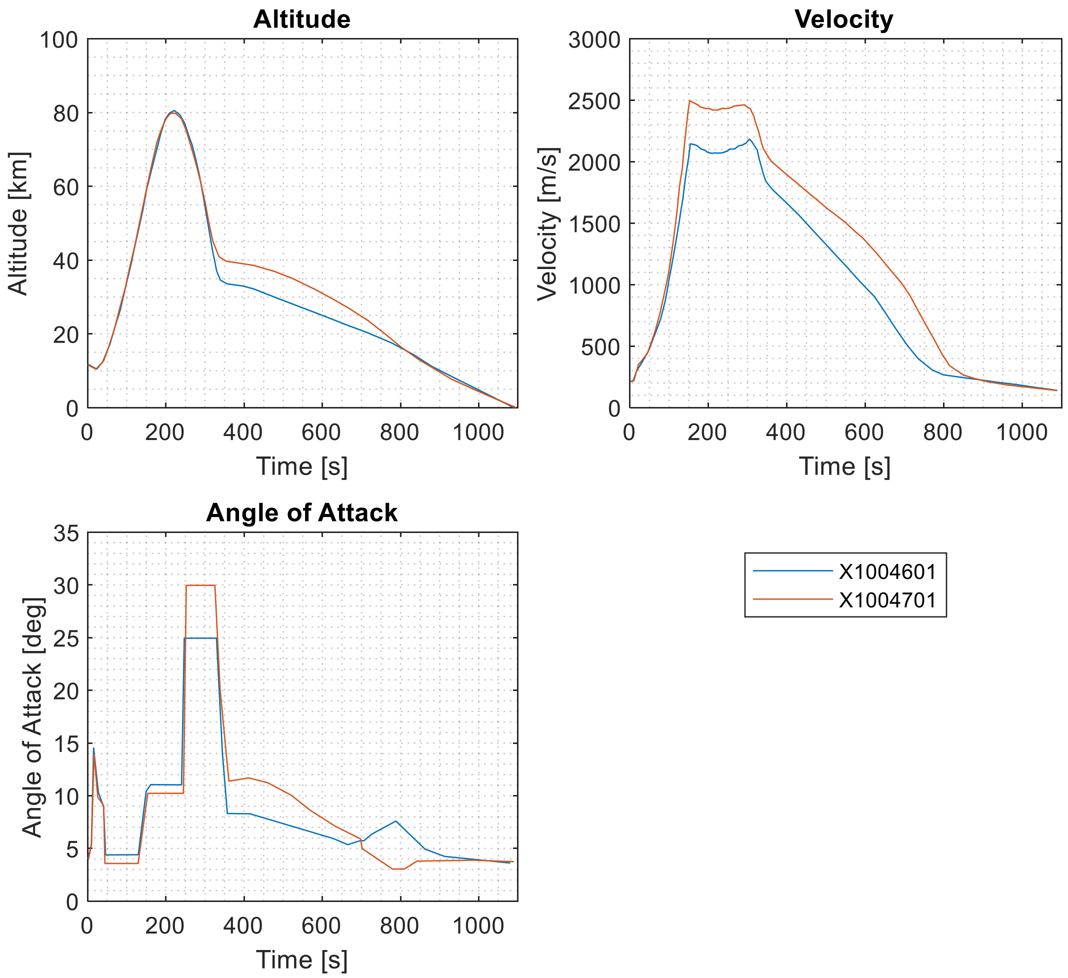

Figure 6.3. X-34 Validation trajectories of two trajectories (one in red, the other in blue) (Riley & Kleb, 1998)

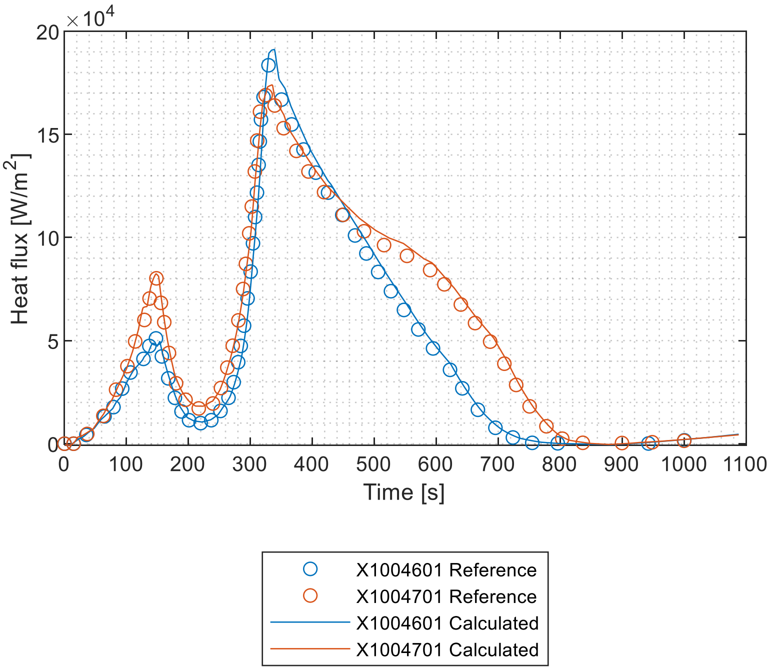

Figure 6.4. X-34 cold wall stagnation point validation for 2 trajectories (Riley & Kleb, 1998)

6.3. X-15

The X-15 has a suitable amount of publicly available data from which a thermal model can be validated. As described in Section 6.3.1, the X-15 has a similar design flight path shape though its design velocity and altitude are slightly lower than that of the Mk-III. Nonetheless, it is a vehicle that in terms of the trajectory is one of the closest matching vehicles to the proposed Mk-III. The validation from the X-15 can be split into two validation locations. The first is the wing at mid-span, for which there are two trajectories of which there is transient thermal data available over a number of locations along the wing's chord. The second is the fuselage for which there is a single trajectory and location available to validate against. Figure 6.5 shows the three X-15 validation trajectories (Hassain & Qureshi, 2013; Banner, Kuhl, & Quinn, 1962).

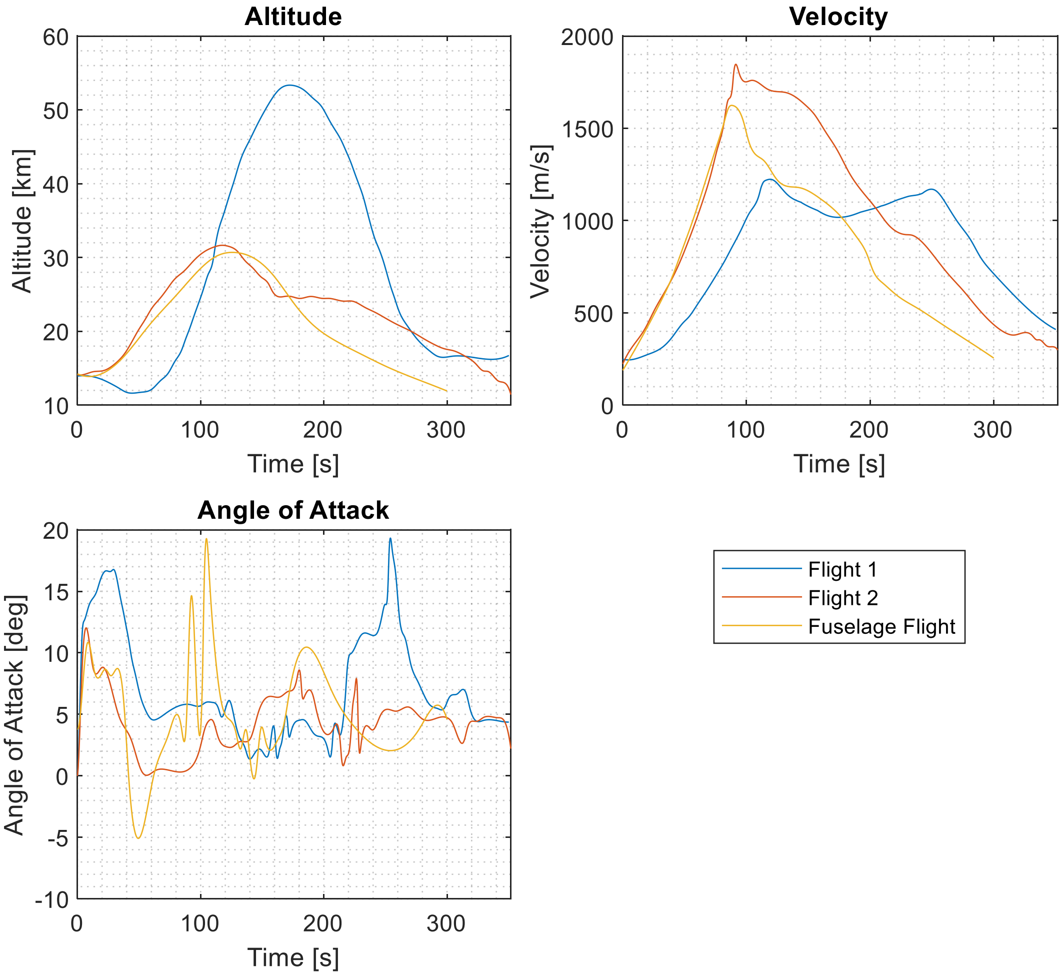

Figure 6.5. X-15 validation trajectories (Hassain & Qureshi, 2013; Banner, Kuhl, & Quinn, 1962).

6.3.1. X-15 wing

The two X-15 wing validation trajectories, labelled flights 1 and 2 in Figure 6.5, are different to each other from an aerothermal standpoint. Flight 1 follows a trajectory that is closer to what will be expected for the Mk-III where a parabola like shape is flown and a high altitude is reached. Flight 2 remains at a lower altitude but reaches closer to the maximum velocity expected for the Mk-III. Because of this combination, both these trajectories can show valuable insights into how the models used behave and will perform for the Mk-III analysis.

Figure 6.6 to Figure 6.11 show the results of various model inputs compared to the reference flight data for both flights. To start with, these figures show a good match in the temperature trends seen in both flights. Flight 1 has two increases in temperature caused by the ascent and re-entry portion of the flight. Flight 2, remains lower in the atmosphere and therefore doesn't re-enter the atmosphere causing a single temperature peak.

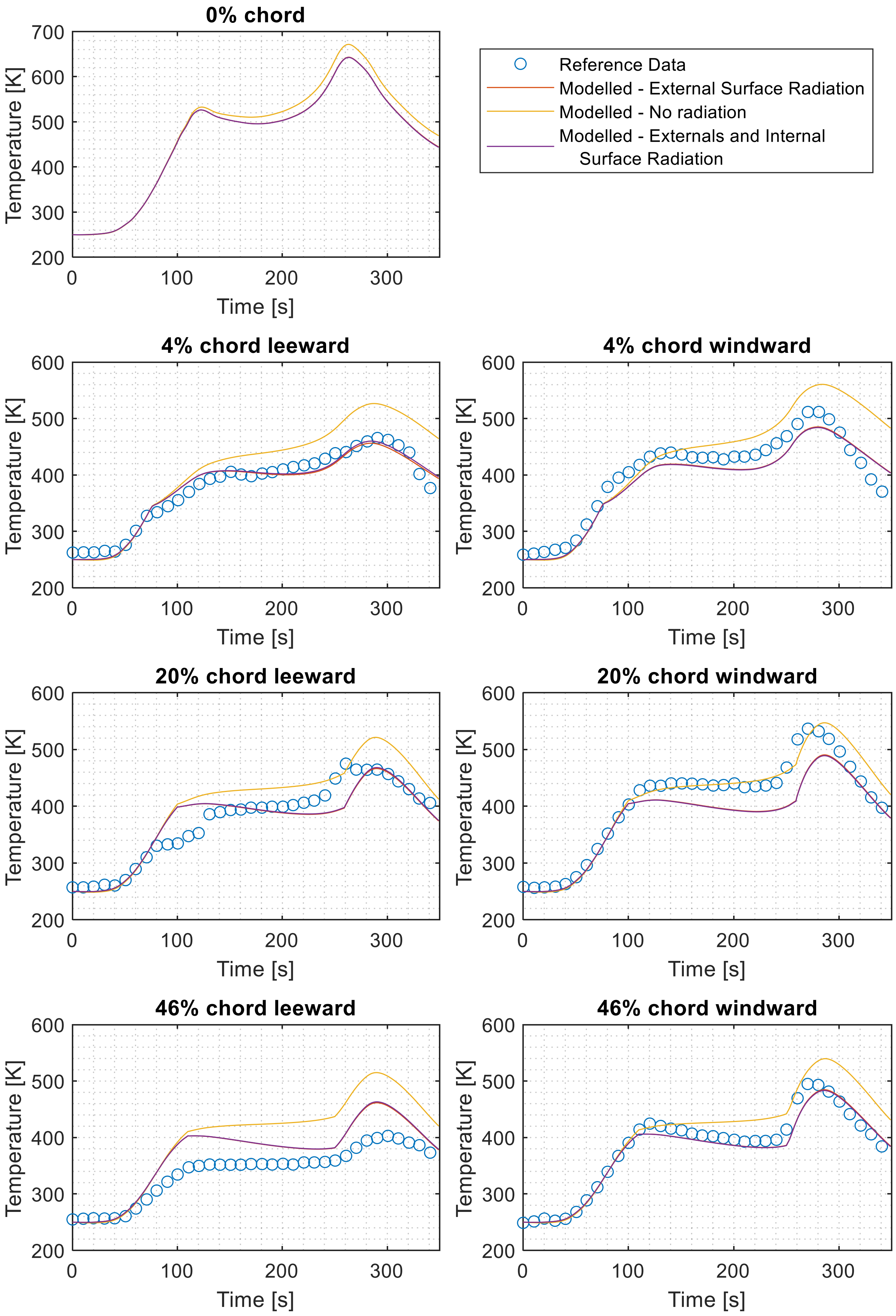

Figure 6.6. X-15 flight 1 validation investigating the influence of radiation

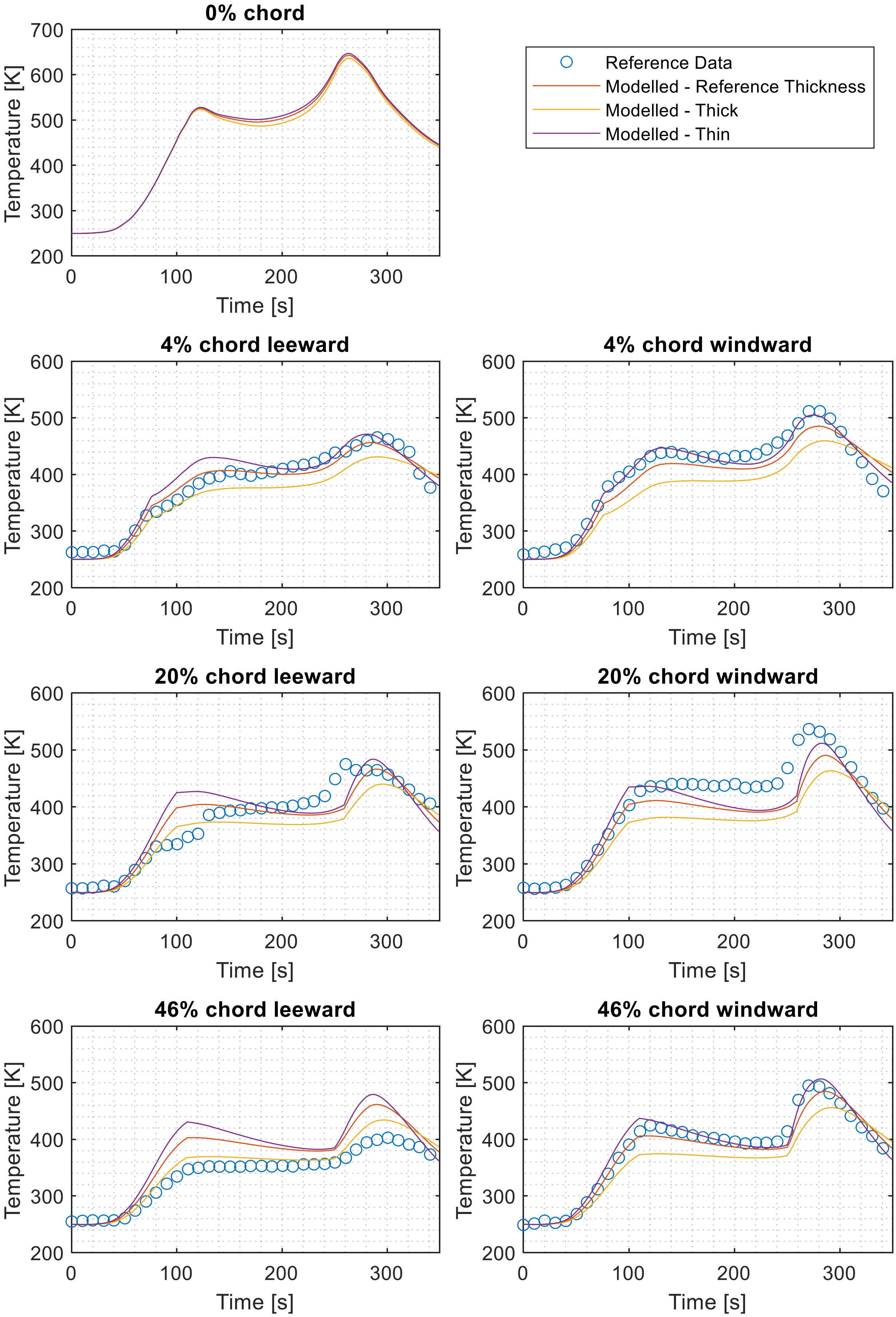

Figure 6.7. X-15 flight 1 validation investigating the influence of skin thickness

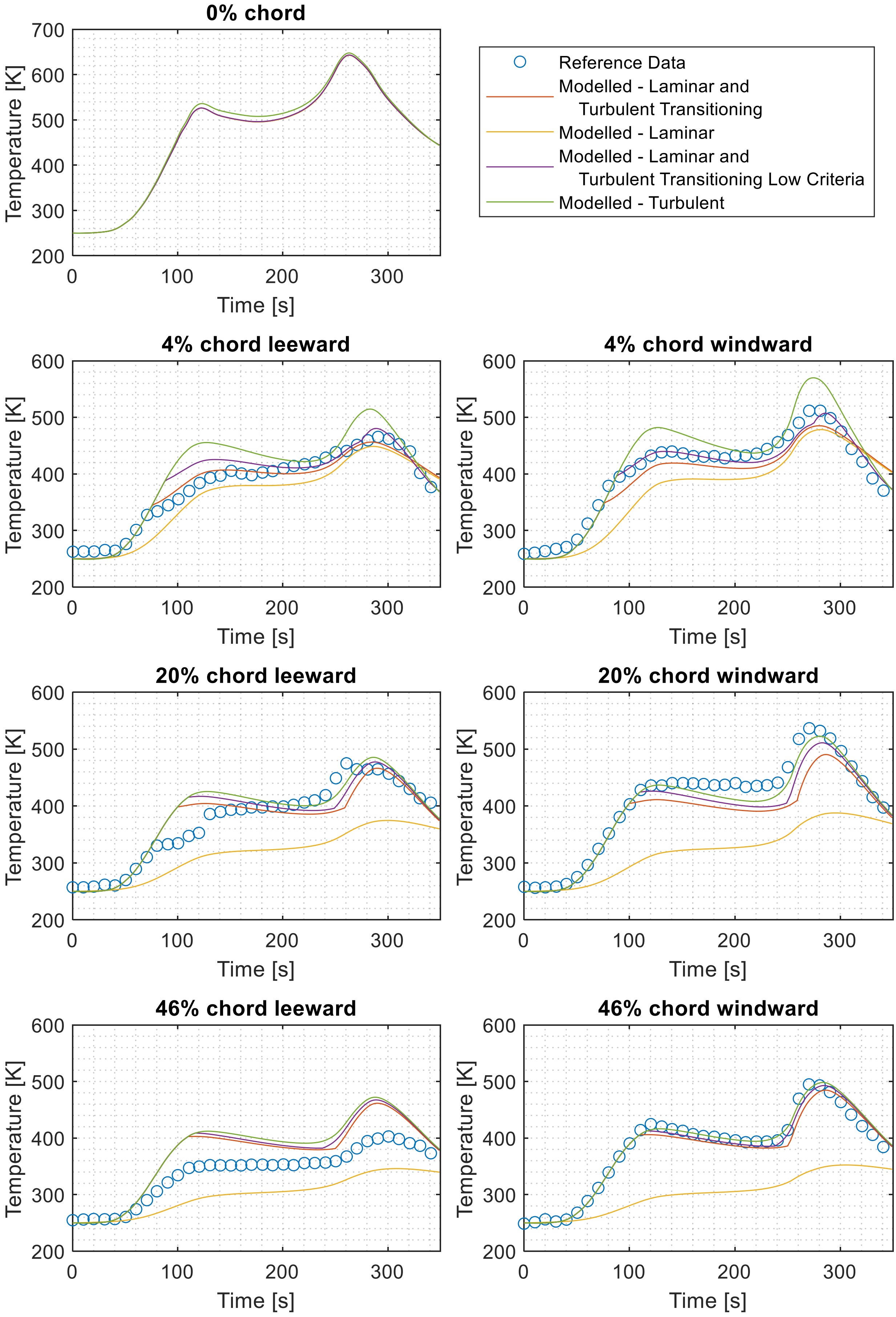

Figure 6.8. X-15 flight 1 validation investigating the influence of turbulence

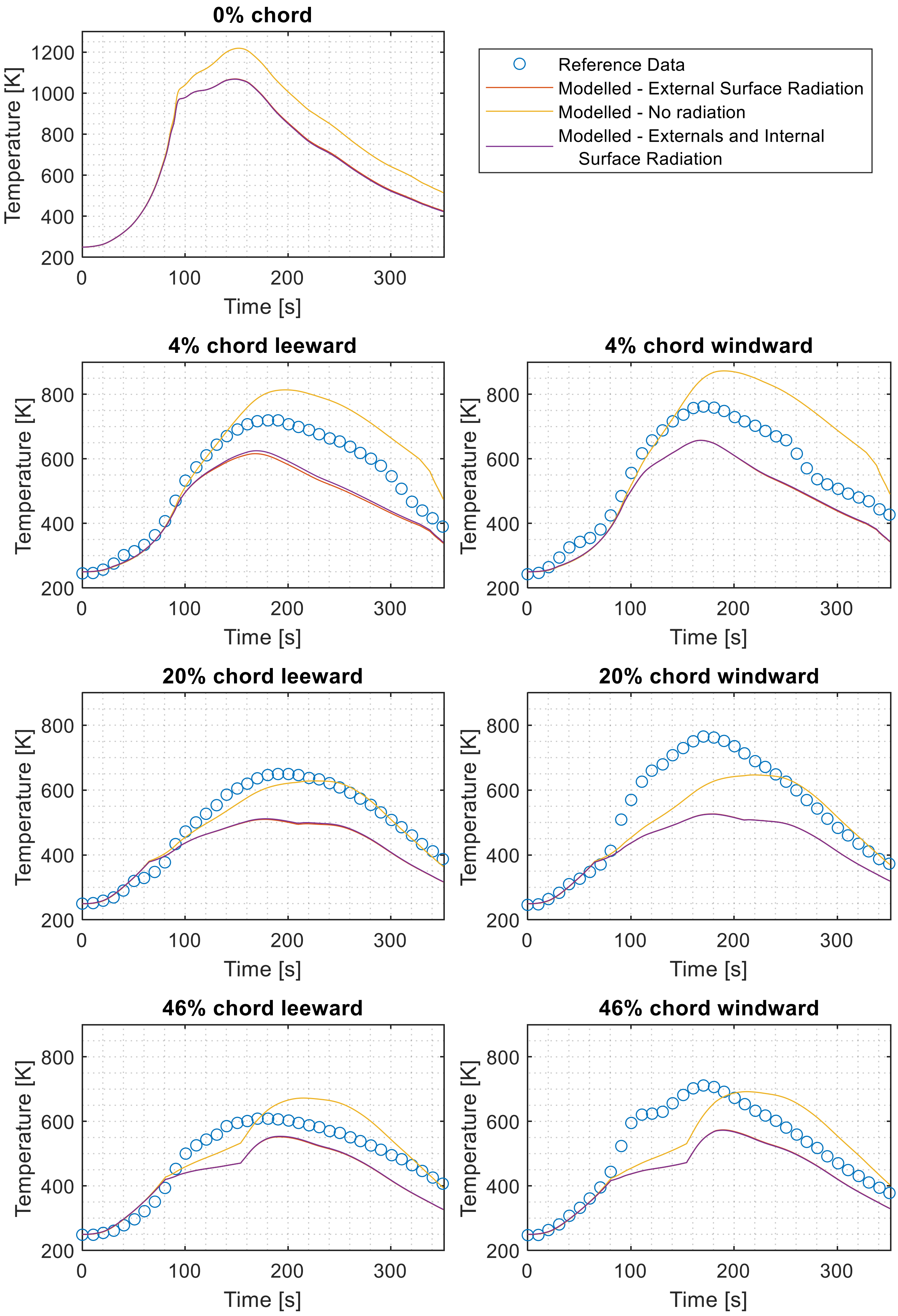

Figure 6.9. X-15 flight 2 validation investigating the influence of radiation

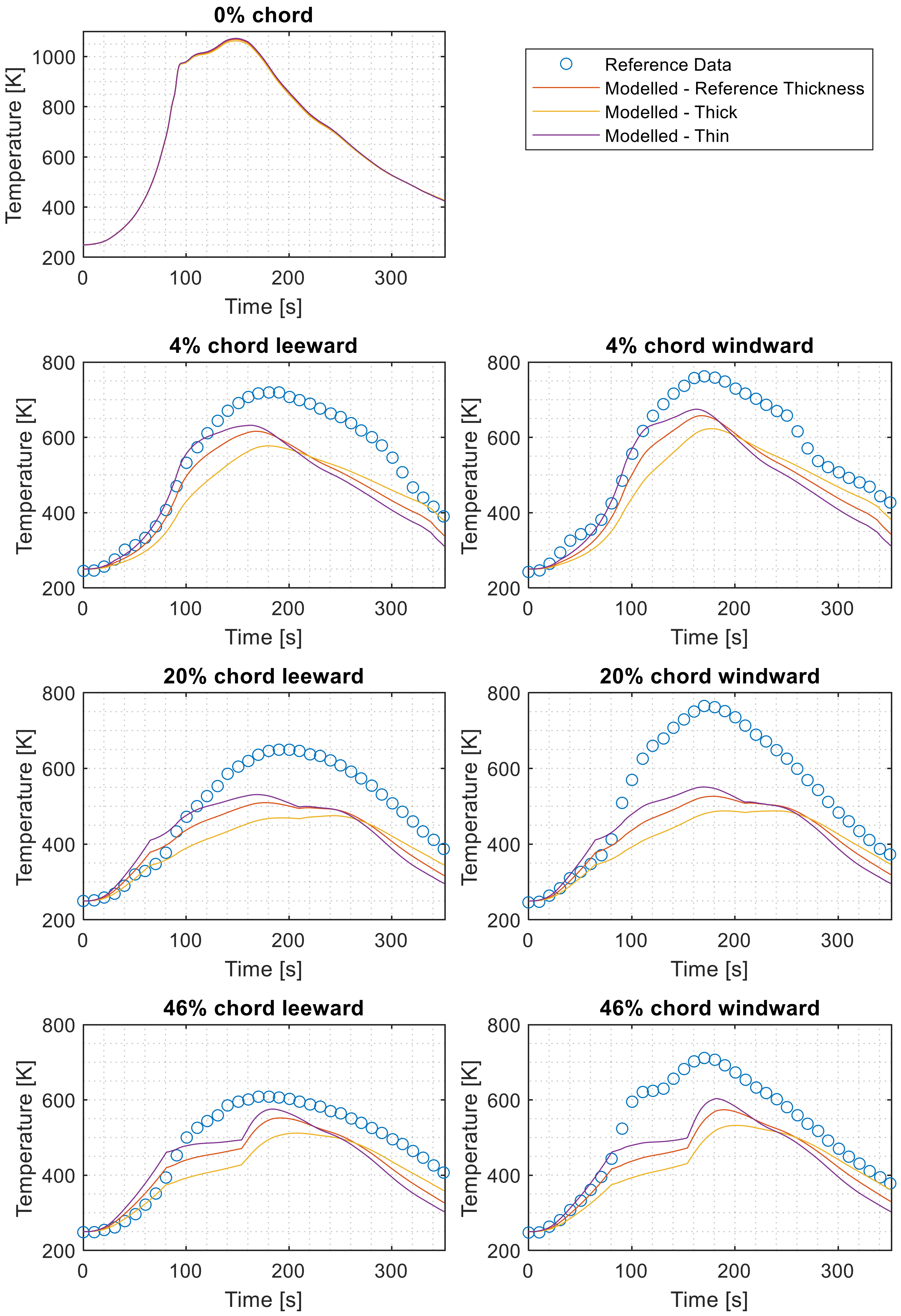

Figure 6.10. X-15 flight 2 validation investigating the influence of skin thickness

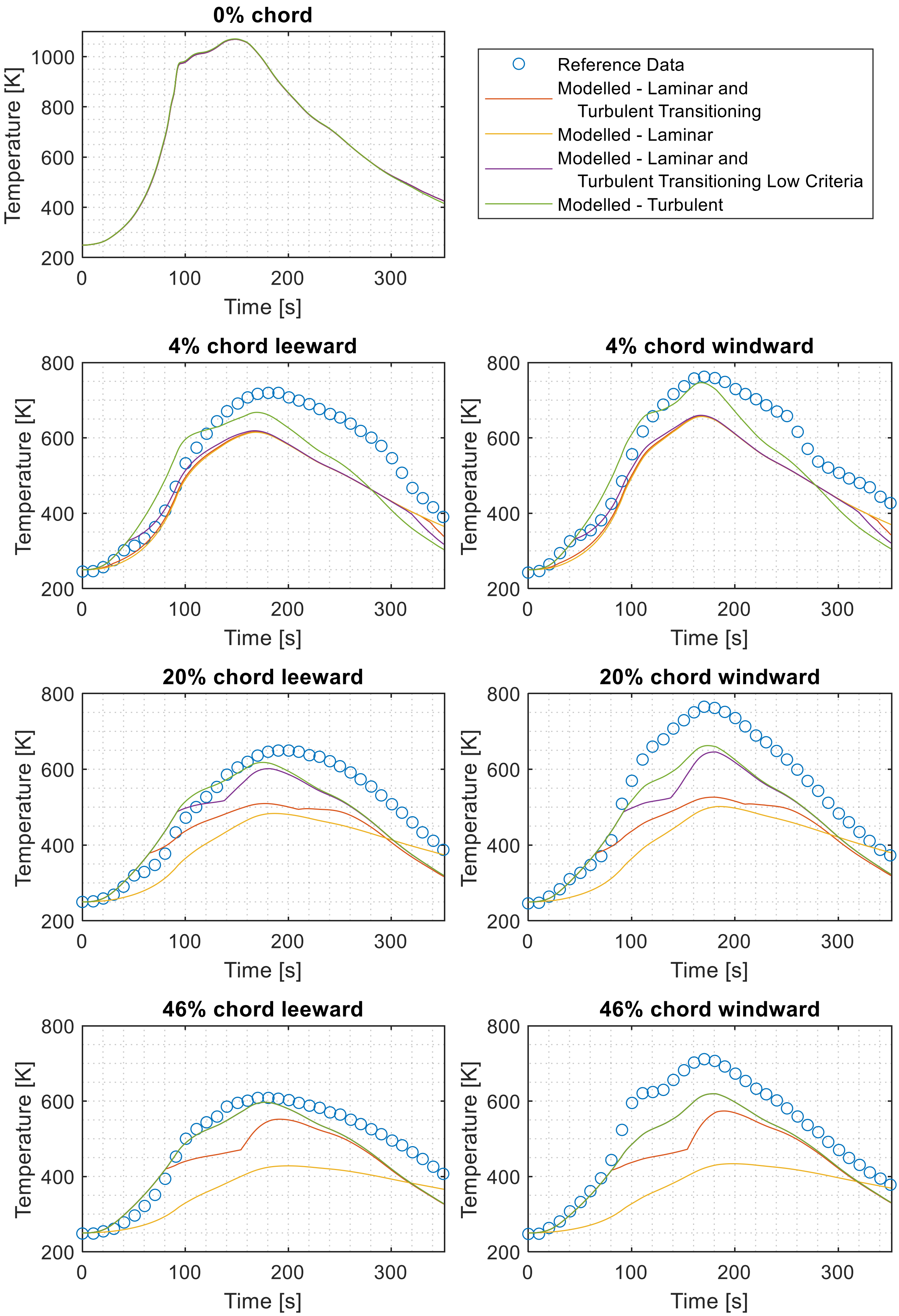

Figure 6.11. X-15 flight 2 validation investigating the influence of turbulence

Figure 6.6 and Figure 6.9 show the application of radiation models to different surfaces for flights 1 and 2 respectively. What this demonstrates is that radiation is an important aspect to consider in the model, as it changes the maximum temperature by as much as 200 $[\mathrm{K}]$. Primarily flight 1 shows that the exclusion of all radiation overestimates the maximum surface temperature. The radiation of the external skin to the atmosphere and surroundings will therefore be included in all future models. The radiation of the internal surfaces, radiating within the enclosed space and therefore only radiating to other internal skin elements, does not require to be included in the model. It is a negligible effect because its inclusion does not affect the temperature of the wing above the error of the model itself, which will be covered in Section 6.4. This can be explained by the temperatures of the internal skin being relatively close to one another compared to the temperature of the external skin and atmosphere.

Figure 6.7 and Figure 6.10 show the effect of changing the skin thickness for flights 1 and 2 respectively. The reference data defines a particular skin thickness for the wing location modelled. Reed & Watts (1961) states that the skin thickness of the wing is between 0.04 and 0.088 inches which allows the effect of skin thickness on the thermal behaviour of the X-15 to be visualized. As expected, a thinner skin has a more rapid change in temperature. This is because for the exact same conditions, *i.e.* same heat flux, there is less material to absorb the energy so the temperature of the material will rise. Both flights therefore show that the thinner the skin, the more rapid the temperature rises but also the quicker it cools, leading to both the highest overall temperature and lowest final temperature.

As explained in Sections 5.2.6 and 5.2.7, whether the flow is laminar or turbulent defines which equations are used to solve the convective heat flux. Figure 6.8 and Figure 6.11 show the results of allowing the model explained in Section 5.2.1 to determine turbulence transition and compares it to fully turbulent and fully laminar conditions. The reference data (Hassain & Qureshi, 2013) has used a C_M value of 0.2 even though the X-15 wing is a swept wing. Therefore, the simulation was repeated with the lower turbulence criteria of C_M 0.1 to model what is proposed by Quinn (2000), Simsek et al. (2016) and Duarte et al. (2009). What the figures show is that whether the flow is locally turbulent or laminar has an impact on the transient temperature profile. For both flights the low turbulent transition criteria fit better to the reference data. In particular for flight 2 the fully turbulent case is an even better fit to the reference data compared to low turbulent transition criteria.

Having identified the importance of turbulence prediction, Figure 6.12 shows the Reynolds number and turbulent transition Reynolds number for flights 1 and 2. The first apparent difference between flights 1 and 2 is that the flight Reynolds number for flight 1 has a parabolic shape to it. This can be explained by the parabolic shape of the flight's trajectory and therefore its altitude profile. Because of this, the point of transition between the laminar and turbulent domain is almost at the same point in time for both the C_M values. On the other hand, for flight 2 the change from C_M of 0.2 to 0.1 causes a much larger portion of the wing to be turbulent for a longer period of the flight. This is also seen in Figure 6.8 and Figure 6.11 where the lower C_M value has a much larger impact on the maximum temperature, compared to the higher C_M for flight 2 than for flight 1. This therefore shows that the proposed value of C_M equal to 0.1 for a swept wing produces a better prediction of the thermal behaviour of the vehicle and will be used for the subsequent simulations of the Mk-III.

6.3.2. X-15 fuselage

The fuselage is validated with flight data from a single trajectory. Less information about the vehicle and thermocouples are also known for this flight test. In particular the material thickness of that location and the exact location of measurement are unknown. Reed & Watts (1961) states that the material thickness of the fuselage is between 0.05 and 0.136 inches thick, providing a minimum and maximum material thickness for which this validation can be performed. Additionally, the exact thermocouple location is not stated within the flight data report. However, two potential locations have been identified as the two thermocouple this data belongs to.

Figure 6.13 shows the influence of skin thickness on the transient thermal behaviour of the X-15 fuselage. A first glance at this data shows that a similar trend experienced by the X-15 wing data is experienced by the fuselage data, *i.e.* a thinner structure causes quicker temperature changes. What can be presumed from this data is that at the validation location the X-15 fuselage is at 0.05 inches. This is because both the trend and the temperature magnitude of the thin modelled fuselage match that of the flight data very well.

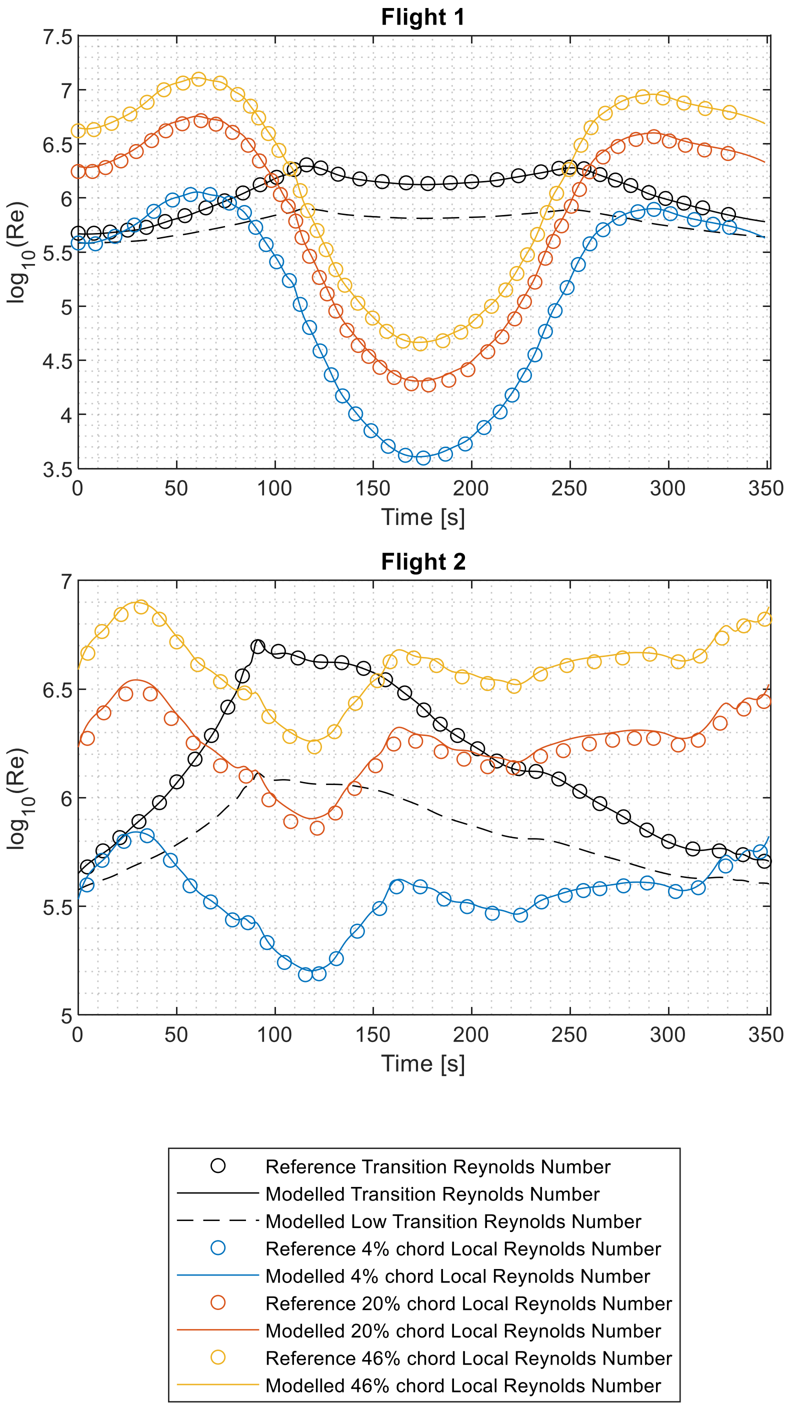

Figure 6.12. X-15 wing validation flights Reynolds number

Figure 6.14 shows the modelled data where only laminar or turbulent models are used. When a transitioning model for turbulence is used, the fuselage is fully turbulent at the thermocouple location which is why it is not displayed. It is clear that at this particular location along the fuselage the flow is turbulent. Due to there being no transition at this location, this figure doesn't give insight into the validity of the turbulence transition model.

Figure 6.13 and Figure 6.14 show the results of the modelled and flight data. Both figures show that the thermocouple location at 2.2 $[\mathrm{m}]$ results in a lower skin temperature. This is because the Reynolds number at the 2.2 $[\mathrm{m}]$ location is higher causing a slightly lower heat flux. Because there is no transition between laminar and turbulent flow at this location the change in Reynolds number has this effect. A fully laminar location would result in the same effect. A transitioning location would cause the transition at a further downstream location to occur earlier due to the higher Reynold's number, meaning it will be in the turbulent regime for longer and hence likely experience more heat flux. Even though there is a difference in temperature between the two locations, both match up with the flight data for the accuracy required and expected from an engineering methods model.

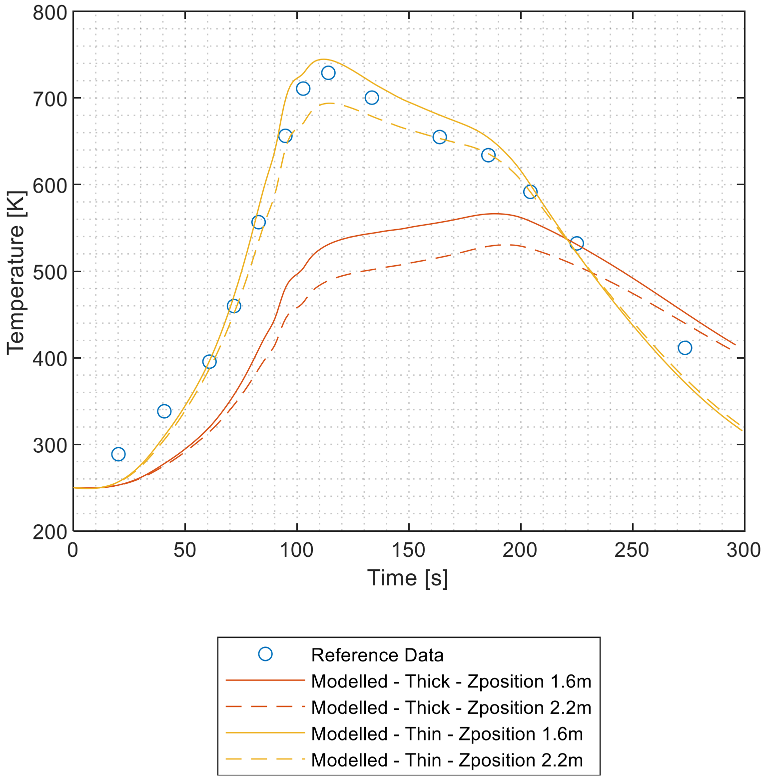

Figure 6.13. X-15 fuselage flight validation influence of skin thickness

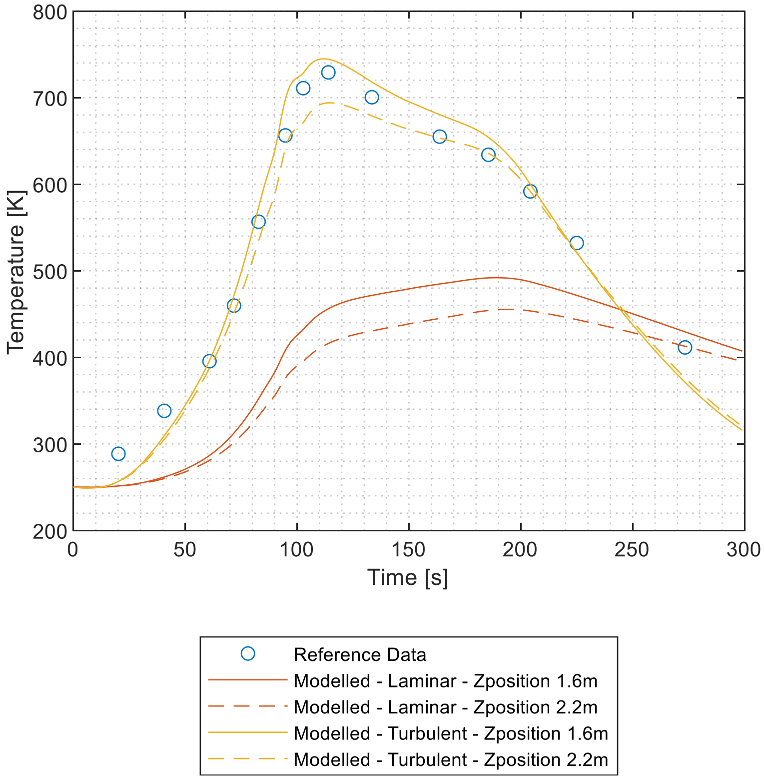

Figure 6.14. X-15 fuselage flight validation influence of turbulence

6.4. Model Accuracy

The model validation in this chapter can be used to investigate the uncertainty of the model. Table 6.2 and Table 6.3 show the difference in maximum temperature of the models and the flight data for the X-15 wing and fuselage. For the wing there are six locations along the wing for which the model and flight data can be compared, whereas for the fuselage there is a single thermocouple. The conclusion of previous validation is that external radiation needs to be accounted for, but internal radiation can be neglected, and that the Quinn (2000), Simsek et al. (2016) and Duarte et al. (2009) proposed turbulence criteria should be used. Table 6.2 confirms this by having the lowest difference between the model and flight data maximum temperature compared to all other settings, except for flight 2 where the fully turbulent model would be a slightly better fit to the flight data. Table 6.3 confirms that the fuselage is likely on the thin end of the fuselage skin thickness limits and that the flow is fully turbulent at the measured location.

Table 6.2. Difference between maximum temperature of models and reference data for X-15 wing validation

Flight 1								
			Leeward			Windward		
Thickness	Radiation	Turbulence	4%	20%	46%	4%	20%	46%
Reference	External	High criteria	-9 [K]	-9 [K]	59 [K]	-26 [K]	-46 [K]	-10 [K]
Reference	No	High criteria	61 [K]	46 [K]	112 [K]	49 [K]	10 [K]	45 [K]
Reference	External & Internal	High criteria	-5 [K]	-7 [K]	60 [K]	-28 [K]	-48 [K]	-12 [K]
Thick	External	High criteria	-34 [K]	-35 [K]	31 [K]	-52 [K]	-73 [K]	-39 [K]
Thin	External	High criteria	6 [K]	9 [K]	76 [K]	-7 [K]	-25 [K]	12 [K]
Reference	External	Laminar	-17 [K]	-100 [K]	-57 [K]	-33 [K]	-149 [K]	-142 [K]
Reference	External	Low criteria	15 [K]	2 [K]	65 [K]	-4 [K]	-25 [K]	-2 [K]
Reference	External	Turbulent	49 [K]	11 [K]	69 [K]	58 [K]	-14 [K]	3 [K]
Flight 2								
			Leeward			Windward		
Thickness	Radiation	Turbulence	4%	20%	46%	4%	20%	46%
Reference	External	High criteria	-103 [K]	-140 [K]	-57 [K]	-105 [K]	-239 [K]	-138 [K]
Reference	No	High criteria	95 [K]	-21 [K]	64 [K]	111 [K]	-118 [K]	-19 [K]
Reference	External & Internal	High criteria	-94 [K]	-138 [K]	-55 [K]	-105 [K]	-239 [K]	-139 [K]
Thick	External	High criteria	-142 [K]	-174 [K]	-97 [K]	-139 [K]	-277 [K]	-179 [K]
Thin	External	High criteria	-87 [K]	-119 [K]	-33 [K]	-87 [K]	-214 [K]	-108 [K]
Reference	External	Laminar	-105 [K]	-166 [K]	-180 [K]	-106 [K]	-263 [K]	-278 [K]
Reference	External	Low criteria	-101 [K]	-48 [K]	-12 [K]	-102 [K]	-119 [K]	-92 [K]
Reference	External	Turbulent	-52 [K]	-31 [K]	-12 [K]	-16 [K]	-102 [K]	-92 [K]

Overall, the data shows that the error of the model can exceed 100 [K] depending on the flight trajectory. Primarily the problem with this is that the models underestimate the temperatures, meaning it is not a conservative model. The models used are engineering models based on empirical data, meaning that their accuracy was never expected to be as good as flight testing or a CFD model. The errors introduced by the model were discussed to be acceptable for answering the research questions and achieving the aim of this thesis.

Table 6.3. Difference between maximum temperature of models and reference data for X-15 fuselage validation

Thickness	Turbulence	Location	
		Z 1.6m	Z 2.2m
Thick	Transitioning	-163 [K]	-199 [K]
Thin	Transitioning	16 [K]	-35 [K]
Thin	Laminar	-237 [K]	-274 [K]
Thin	Turbulent	16 [K]	-35 [K]

7. Results

This section presents the results of the research question analyses and explains their effect on the TPS. Firstly, a convergence study will be described, which was conducted to ensure the results of the analysis were sufficiently accurate to answer the research questions. Then, the four material choices for sub-research-question 1 are individually evaluated and then a comparison is made between the materials. Lastly, for a chosen material the four different TPS were applied in varying degrees to allow the analysis of their effectiveness in light of the Mk-III mission. To analyse these questions, the temperature profiles at different vehicle locations are extracted from all the simulation results. Figure 7.1 shows these locations visually.

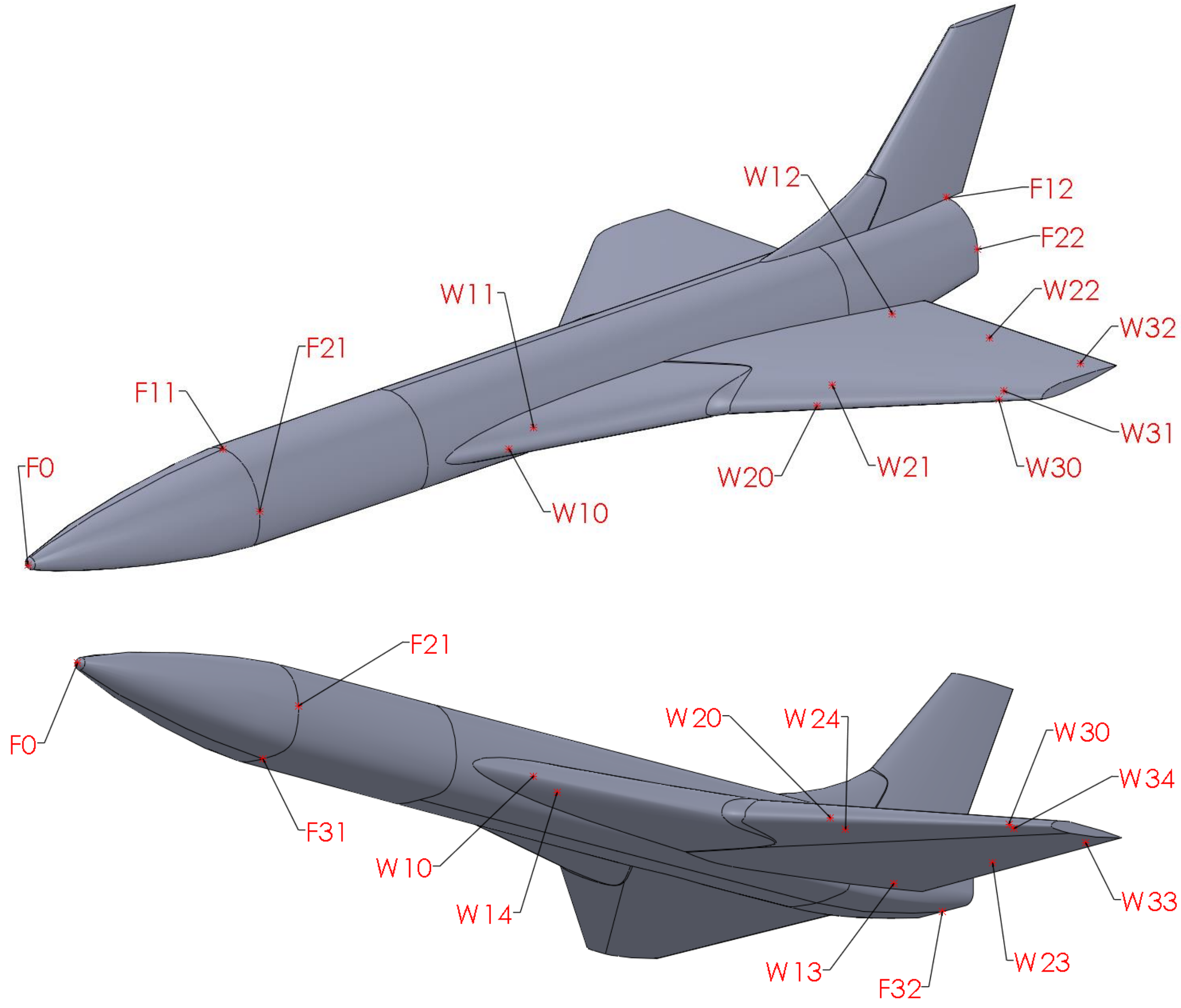

Figure 7.1. Mk-III vehicle locations that are plotted and analysed.

7.1. Convergence study

Prior to producing any analysable results, the simulation first needs to be checked to ensure the required and expected accuracy of the model is achieved by the model itself. This does not mean that the model equation accuracy is questioned but investigates the error introduced by components such as the time step or mesh. There are three components of the model that were subjected to a convergence study; the number of skin layers in the normal direction of the skin, the refinement of the mesh and the time step. This section will explain the results of this convergence study.

7.1.1. Number of layers

The first convergence study was the number of mesh layers in the normal direction of the skin, as shown in Figure 7.2. Three different layer setups were used, all of which summed up to the material thickness calculated in Section 2.4; these were 2, 5 and 10 layers. Only two different materials were tested within this convergence study; BMI CF and aluminium. These materials were chosen due to their thermal conductivity being the minimum and maximum of the range of materials investigated.

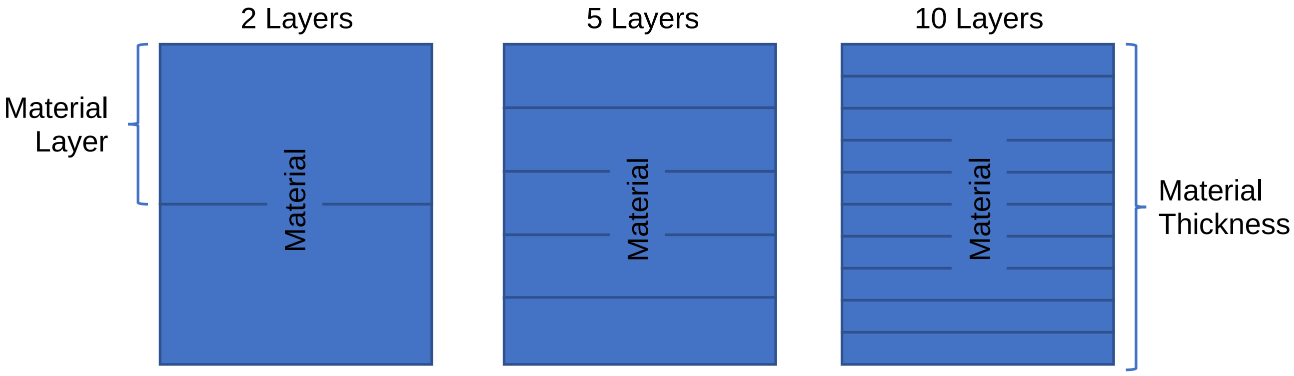

Figure 7.2. Structural skin layers

The convergence study for BMI CF was conducted using a time step size of 10 $[s]$ and with a mesh setup of mesh spacing of 100 mm and 15° curvature limit. Sonneveld's (2021) mid-energy trajectory was used as the trajectory for this study. Figure 7.3 shows the temperature profile along the trajectory for a few chosen vehicle locations. These locations are chosen as they are representable of the temperature profiles along the entire vehicle. The figure does not visually show the 10 layer result due to overlapping of lines and near similar results. Figure 7.3 shows that the number of layers does not influence the external skin temperature results significantly as the error of which falls well within the error of the model. Table 7.1 shows the simulation time for the different meshes. These results show that there is only a small difference between the simulation time of 2 and 5 layers and that the simulation time almost doubles from 5 layers to 10 layers. The similar simulation time between 2 and 5 layers is caused by the number of vehicle mesh elements and nodes being the same on the external vehicle skin for all the meshes. Therefore, the convective heat flux calculation still requires the same number of calculations, regardless of the number of layers the internal structure consists of. The difference in simulation time is therefore solely due to the difference in simulation time of the structural model, which is why the simulation time increases more rapidly from 5 to 10 layers.

Table 7.1. Simulation time for BMI CF number of layers convergence study

Layers	Mesh size $[\mathrm{no.\,nodes}]$	Simulation time $[\mathrm{hrs}]$
2	130668	5.7
5	261336	6.4
10	479116	10.7

The convergence study for aluminium was conducted using a time step size of 5 $[s]$ and a mesh setup with a mesh spacing of 100 mm and 5° curvature limit. Sonneveld's (2021) mid-energy trajectory was used as the trajectory for this study. From Figure 7.4 and Table 7.2 the same conclusions can be drawn as for the BMI CF simulations. This means that the effect of thermal conductivity does not significantly affect the external skin temperature due to the thin structure.

Table 7.2. Simulation time for aluminium number of layers convergence study

Layers	Mesh size $[\mathrm{no.\,nodes}]$	Simulation time $[\mathrm{hrs}]$
2	385131	21.0
5	770262	28.3
10	1412147	53.5

5 Layers in the normal direction of the skin was chosen for any future simulation. The choice was firstly based on the insignificant effect of the number of layers on the external skin temperature. However, choosing to use 5 layers in the normal direction rather than 2, which could save up to 25%

simulation time, is because it allows for future analysis of the temperature gradient within the material. This temperature gradient could help inform decisions on TPS as well as allow potential future use in stress calculations that include the thermal stresses from material expansion. The stress calculation would be out of the scope of this thesis but that does not exclude the results to be imported whenever it does take place.

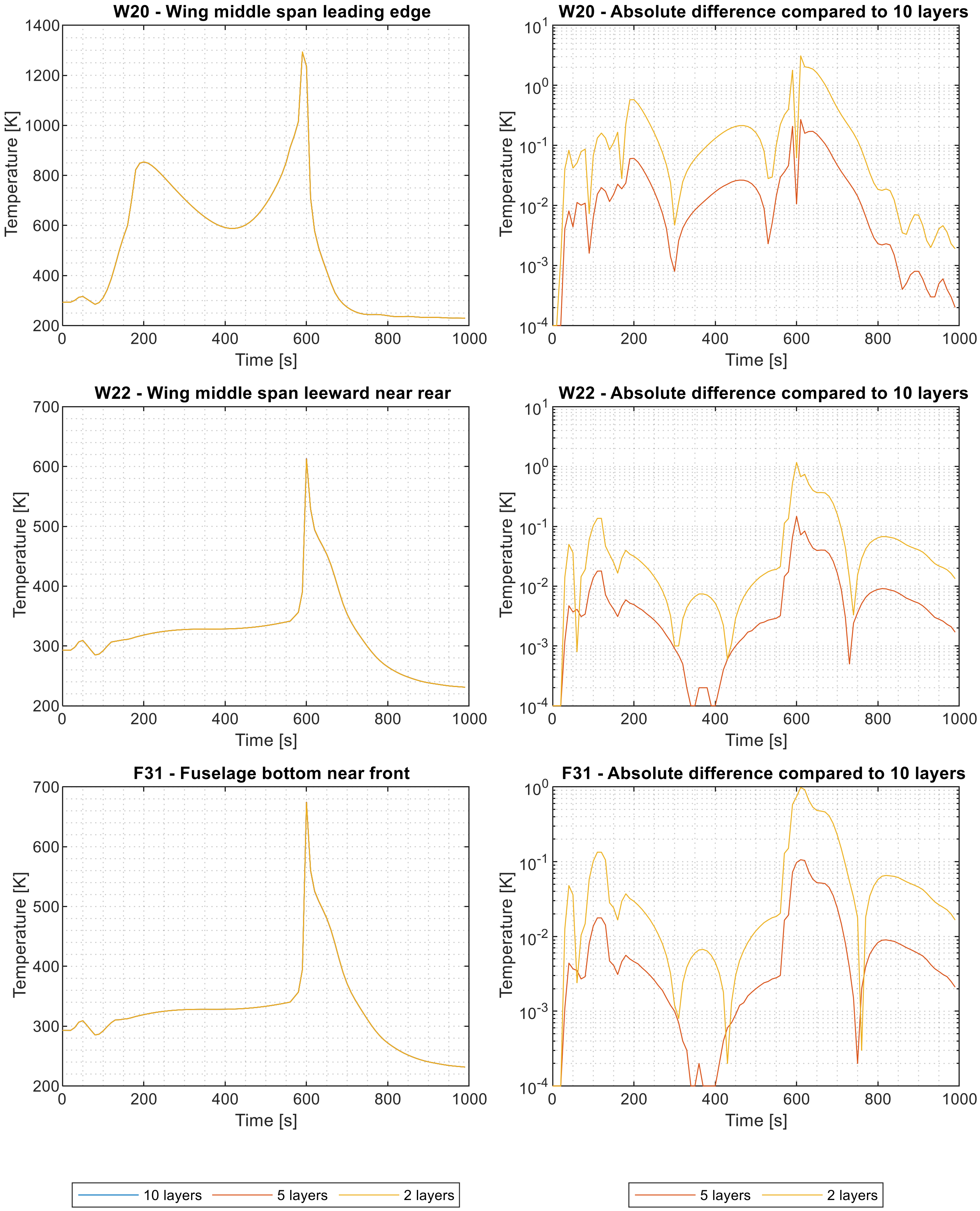

Figure 7.3. BMI CF number of layer convergence study results selection showing transient temperature and the transient difference compared to 10 layers

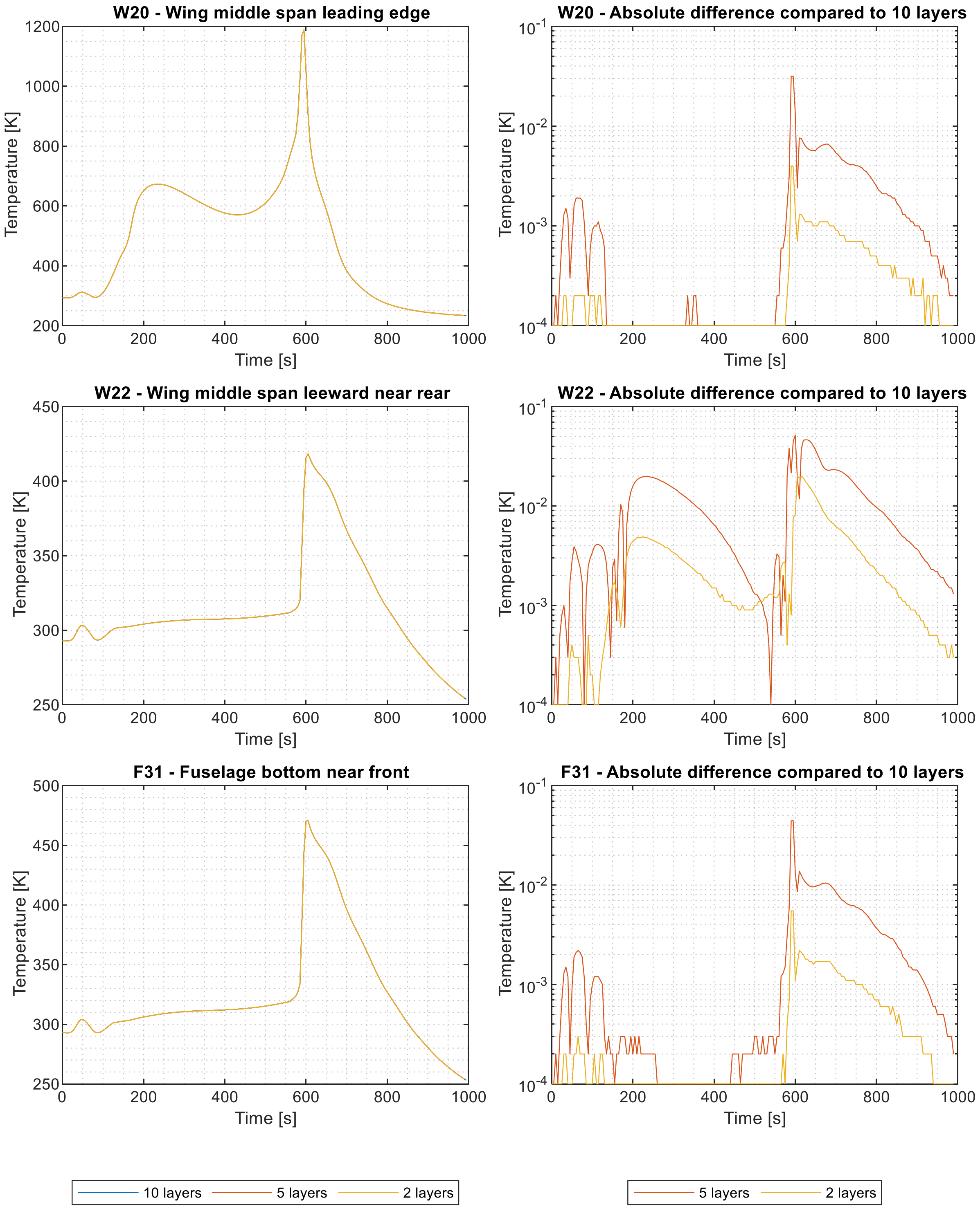

Figure 7.4. Aluminium number of layer convergence study results selection showing transient temperature and the transient difference compared to 10 layers

7.1.2. Mesh refinement

The second convergence study investigated the vehicle mesh as well, particularly investigating the mesh size of the external vehicle shape. Together with the number of layers in the normal direction of the surface it creates and determines the mesh size. For this study again the Sonneveld's (2021) mid-energy trajectory was used as the trajectory, the time step along the trajectory was set at 10 [s] and the number of mesh layers was set to 5. This study only used BMI CF given that it primarily influences the resolution of the convective heat transfer. The two parameters used to influence the surface mesh are mesh spacing and curvature limit. The mesh spacing parameter primarily influences the mesh of the flatter sections of the fuselage and wing, whereas the curvature limit parameter has a large influence on the leading edges and any high curvature surfaces. In the study the maximum mesh spacing was set to 100 and 50 mm and the curvature limit was set to 5, 10 and 15°.

Figure 7.5 shows the results of this study for a number of selected locations along the wing and fuselage that best showcase the variety of results observed over the whole vehicle. Particularly the 100/10, 100/15 and 50/15 meshes show results with temperature differences compared to the most accurate case exceeding 100 K. The error the mesh introduces should be well below the model error so that it is a negligible source of error, which would not be the case for these meshes.

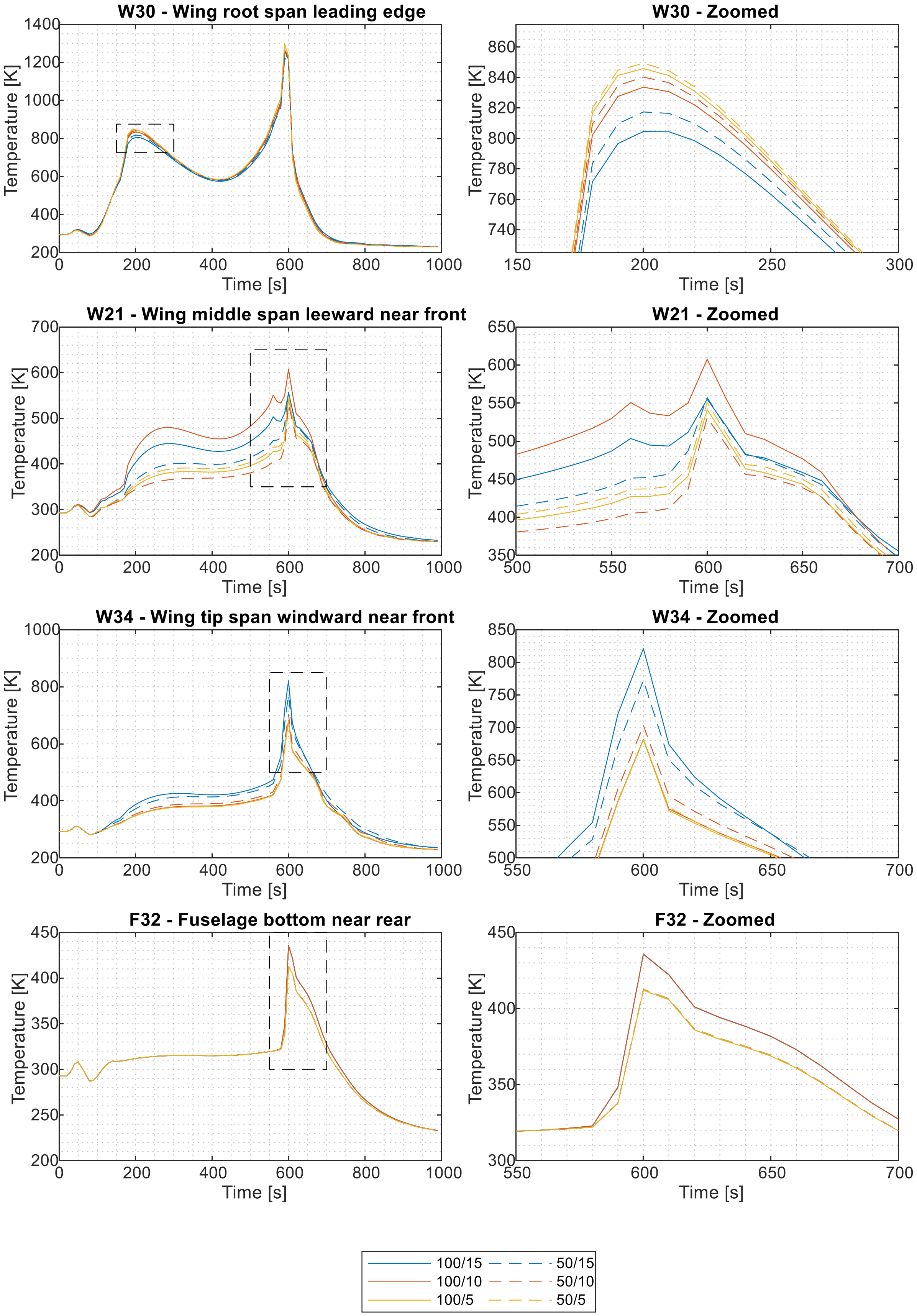

Figure 7.5. BMI CF external vehicle surface mesh convergence study results selection showing transient temperature a zoomed section of the transient temperature.

As well as the accuracy of the results, simulation time was minimized to prevent thesis delays. Table 7.3 shows the simulation time for all simulations done during the mesh refinement study. The simulation time aspect must also account for the time step convergence study as this also has an influence on the simulation time. As will be explained in Section 7.1.3, the simulation time will double with respect to the simulation time shown in Table 7.3 due to the time step change. This means that the 50/5 mesh would take too long to simulate and allow a sufficient number of results to be completed within the thesis.

Table 7.3. Simulation time for BMI CF mesh refinement convergence study

Mesh spacing	Curvature limit [°]	Mesh size $[\mathrm{no.\,nodes}]$	Simulation time $[\mathrm{hrs}]$
50	5	1120074	26.3
50	10	734892	17.5
50	15	663384	16.6
100	5	769362	17.3
100	10	347502	8.0
100	15	261336	6.4

Too large a simulation time is also the argument when considering that the curvature limit or mesh spacing could be decreased further than done in this study. If this happens, based on Table 7.3, the mesh size would be similar if not larger than the 50/5 mesh. This would mean that this category of mesh would also produce simulation times too large for this thesis and were therefore not conducted.

Figure 7.5 shows that the 100/5 mesh overall produces results closer to the most accurate mesh modelled, the 50/5 mesh, compared to the 50/10 mesh. The simulation time of these two meshes are indistinguishable meaning that temperature error is the deciding factor. Therefore the 100/5 mesh will be used for answering the research questions.

7.1.3. Time step

Lastly the time step used to step along the transient trajectory was investigated. For this thesis only a constant time step was used because working in collaboration with Dawn Aerospace has allowed access to resources. What this means is that Dawn Aerospace did not require a simulation optimized for running time, but rather the time to integrate a variable time step simulator was used for investigating the research questions. What this does not mean is that it is reasonable to design a simulation that requires one week of simulation time, but that the gains possible with a variable time step simulator were not required to make this thesis sufficiently accurate and fit within the framework of the thesis. Therefore, the investigation into a suitable time step was limited to testing suitable constant times steps. For the study 5 mesh layers, a mesh spacing of 100 mm and 15° curvature limit was used along with the Sonneveld's (2021) mid-energy trajectory. Again, this study was only done using the BMI CF material as it relates to the accuracy of the convective heat transfer at any one time along the trajectory.

Figure 7.6 shows the results of the time step convergence study for a number of selected locations along the wing and fuselage that best showcase the variety of results observed over the whole vehicle. This figure shows that the 10 and 20 $[\mathrm{s}]$ time steps can produce an error of more than 100 K with peak temperature offsets along the trajectory of 10 s or more. Therefore, these time steps do not provide sufficient accuracy for the model, so that the time step does not introduce negligible errors relative to the error of the model. The 2 $[\mathrm{s}]$ and 5 $[\mathrm{s}]$ time steps both show very similar results with acceptable model errors with the 2 $[\mathrm{s}]$ time step result showing smoother curves. The 2 $[\mathrm{s}]$ time step simulation takes more than two times the simulation time compared to the 5 $[\mathrm{s}]$ time step simulation, as shown in Table 7.4. Together with the decision in Section 7.1.2 the simulation time would therefore be unpractical. Therefore the 5 $[\mathrm{s}]$ time step will be used for this thesis. It can be noted that the simulation time shown in Table 7.4 is for a 100/15 mesh whereas a 100/5 mesh will be used and so it will change the simulation time. The final simulation time accounting for both the mesh refinement and time step convergence study is about 36 hrs, which was deemed appropriate and practical.

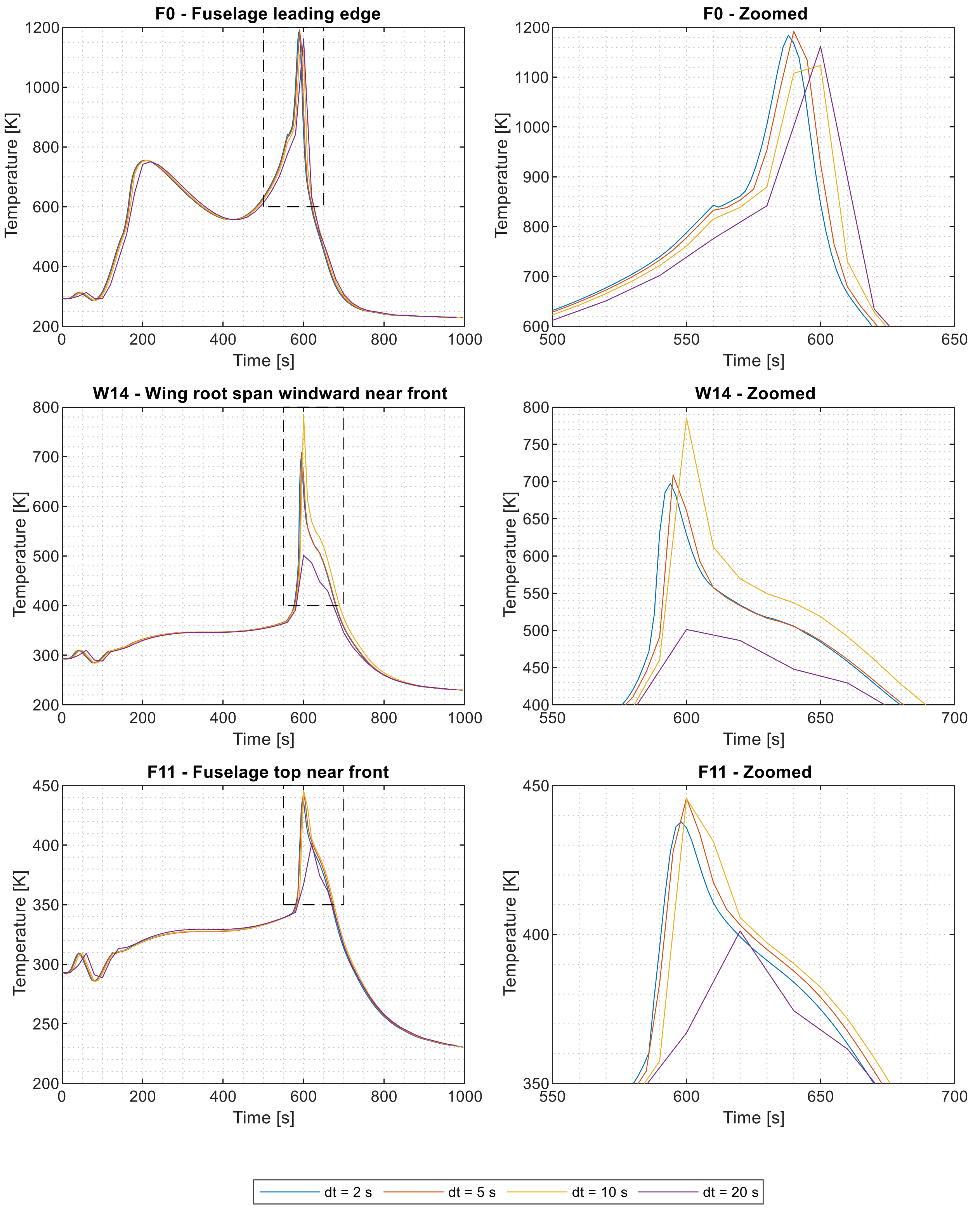

Figure 7.6. BMI CF time step convergence study results selection showing transient temperature and zoomed section of the transient temperature

Table 7.4. Simulation time for BMI CF time step convergence study

Time step $[\mathrm{s}]$	Simulation time $[\mathrm{hrs}]$
2	28.7
5	13.2
10	6.4
20	3.0

7.2. Material performance for different trajectories

The first vehicle models to be analysed are those that investigate the different materials specified in Section 2.4, which are simulated against the nine chosen trajectories, redisplayed in Figure 7.7. This section is aimed at answering the primary and sub research question 1. The material properties, redisplayed in Table 7.5, are input into a vehicle model and the material thickness, calculated from structural loading, is applied over the entire vehicle evenly. The mesh and time step setup used in this study is defined in Section 7.1. This section first compares the nine chosen trajectories for each material, explaining the effect on the vehicle and how it could be a suitable or unsuitable material choice. Secondly this section compares the performance of the four material choices with each other. One material is then chosen to continue the analysis of potential TPS for the remaining research sub-questions.

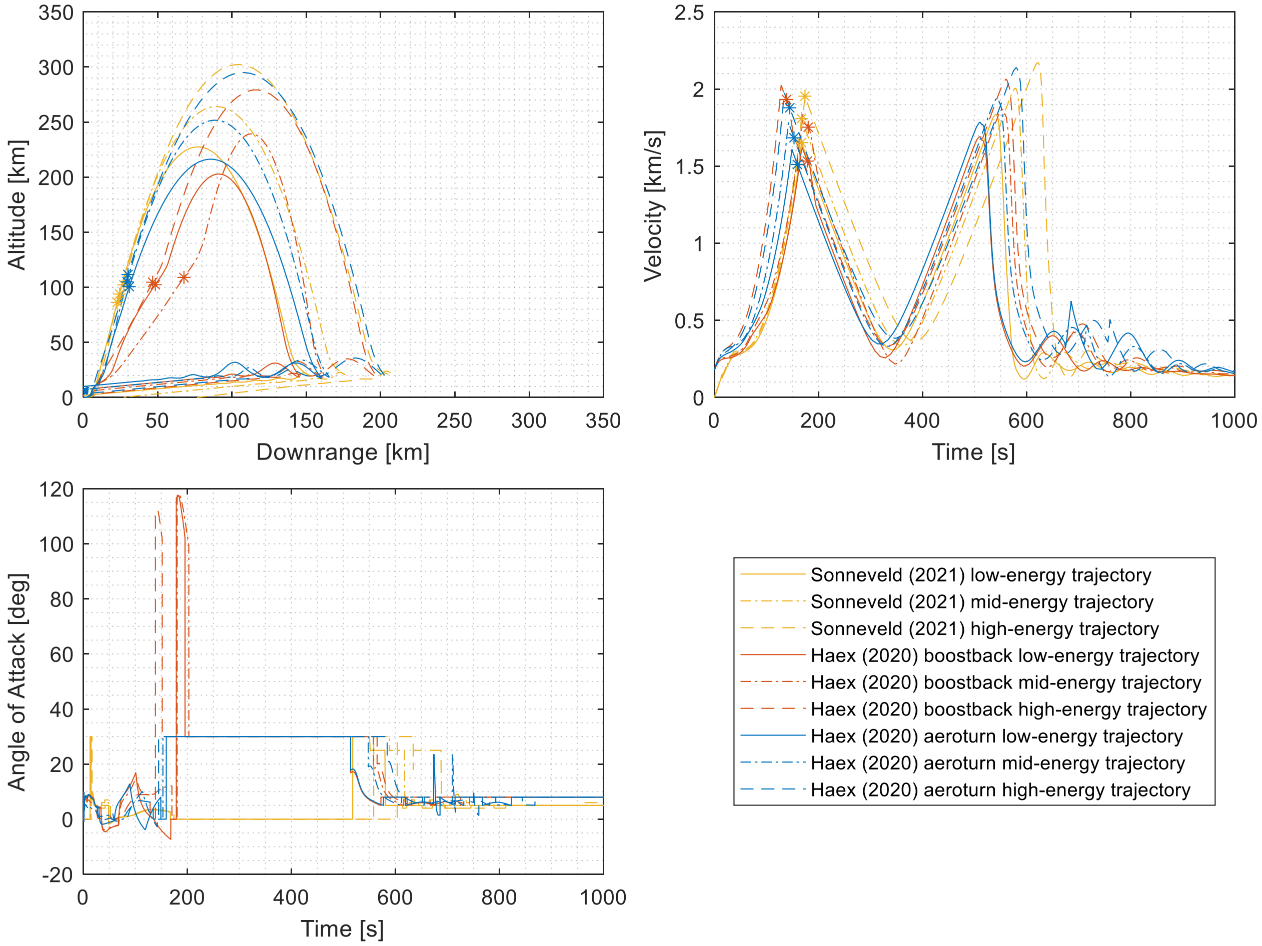

Figure 7.7. Mk-III chosen trajectories to analyse from this thesis from Haex (2020) and Sonneveld (2021). Astrix means staging with second stage. (Figure 2.3 repeated)

7.2.1. BMI CF

The BMI CF material analysis with a thickness of 2.38 mm was conducted for all nine trajectories, as shown in Figure 7.8. Three different points along the vehicle were chosen to be displayed in this figure, which are a representation of the different temperature profiles the entire vehicle experiences. More locations are plotted in Appendix C. This section will first discuss the general trends observed for all trajectories. After this, the specific application and use of BMI CF will be discussed.

Figure 7.8 shows that all nine trajectories have the same general trend in temperature, but each has different maximum temperature magnitudes and the peak temperatures are time offset. The first observation is that all trajectories have their temperature peak during re-entry. This is caused by the ascent into the atmosphere having a higher altitude for the same velocity, therefore there being less air for heat transfer. The ascent does cause heating as can be seen due to the smaller peaks during ascent at roughly 200 [s] flight time. Primarily for leading edges this ascent heating needs to be accounted for in design. This ascent heating brings into question the assumptions associated with the Haex (2020) boostback trajectories. During the boostback the angle of attack goes up to 120 degrees

Table 7.5. Material properties (Granta Design Limited, 2020). (Table 2.1 repeated)

Material	BMI CF		SiC CF		Titanium		Aluminium	
	In-plane	Out-of-plane	In-plane	Out-of-plane	In-plane	Out-of-plane	In-plane	Out-of-plane
Density $[\mathrm{kg/m^3}]$	1540		2600		4600		2920	
Max temperature $[\mathrm{K}]$	523		1373		1773		880	
Thermal conductivity $[\mathrm{W/mK}]$	2.425	0.725	20	7	7.6		117.5	
Specific heat capacity $[\mathrm{J/kgK}]$	945		630		560		935	
Yield Strength $[\mathrm{MPa}]$	507	32	363	225	1040		380	
Thermal expansion coefficient $[\mu\varepsilon/\mathrm{K}]$	11.85	23.85	5.2	2.8	9.1		22.4	
Minimum thickness $[\mathrm{m}]$	0.00238		0.003332		0.00115		0.00315	
Mass/unit area $[\mathrm{kg/m^2}]$	3.67		8.66		5.29		9.20	
Specific heat capacity per unit area $[\mathrm{J/m^2K}]$	3464		5458		2962		8600	

to provide thrust tangential to the gravity force. This thesis has made the assumption that the angle of attack is limited to 30 degrees due to the inability of the model to handle with higher angles of attack. The simulations show that there is heating occurring during the boostback. The primary issue with this is that the trailing-edge of the wing would then become the leading edge, which has a sharp edge. This means the aerodynamic heating of the trailing-edge becomes a lot larger because leading edge heating is related to the inverse square root of the leading edge radius. As has been said, the model in this thesis has not been set up to handle this but is a point of concern and requires future analysis if the boostback trajectory is to occur.

After the leading edge is heated from ascent it is cooled due to radiation and conduction to cooler parts of the vehicle. The non-leading edge sections of the vehicle (from hereon called flat sections) also have ascent heating but this heating is not nearly as influential to the material's thermal performance as that of the leading edges. The leading edges are also observed to be heated almost 1000 K more than the flatter portions of the vehicle. This is due to the angle between the flat portions of the vehicle and the flow which is lower than that of the leading edges. The equations in Section 5.2 already predicted that, due to the slowing of air in the leading edges, more kinetic energy is transferred to thermal energy therefore causing higher heating. The boundary layer slowing of air that causes the heating of the flat sections of the vehicle causes for a smaller amount of kinetic energy being transferred, hence causing a smaller amount of convective heat transfer.

An expected finding from analysing the nine trajectories is that the higher energy trajectories (with higher maximum altitudes and velocities) cause higher maximum temperatures of the material. Figure 7.8 shows that this temperature difference could be more than 300 K for the leading edge, and for the flat sections it could be more than 200 K. The leading edge data shows that this temperature difference is true for both the ascent and re-entry heating. This temperature difference was expected as more energy is required to be dissipated during re-entry to slow the vehicle down if the trajectory is a higher energy trajectory. During ascent the vehicle with high energy trajectories also require higher velocities, hence higher temperatures are expected. What is interesting is that the leading edge is cooled to almost the same temperature for all the trajectories between the ascent and re-entry heating. This is caused due to a combination of effects. Firstly, the high energy trajectories spending more time coasting between ascent and re-entry, therefore allowing more time for cooling. Secondly all trajectories have roughly the same horizontal velocity, meaning that the flow temperature in all these trajectories at the top of the flight path is nearly almost all the same. This means that all these trajectories have the flow cooling the vehicle to the same value. This can be seen by the fact that the

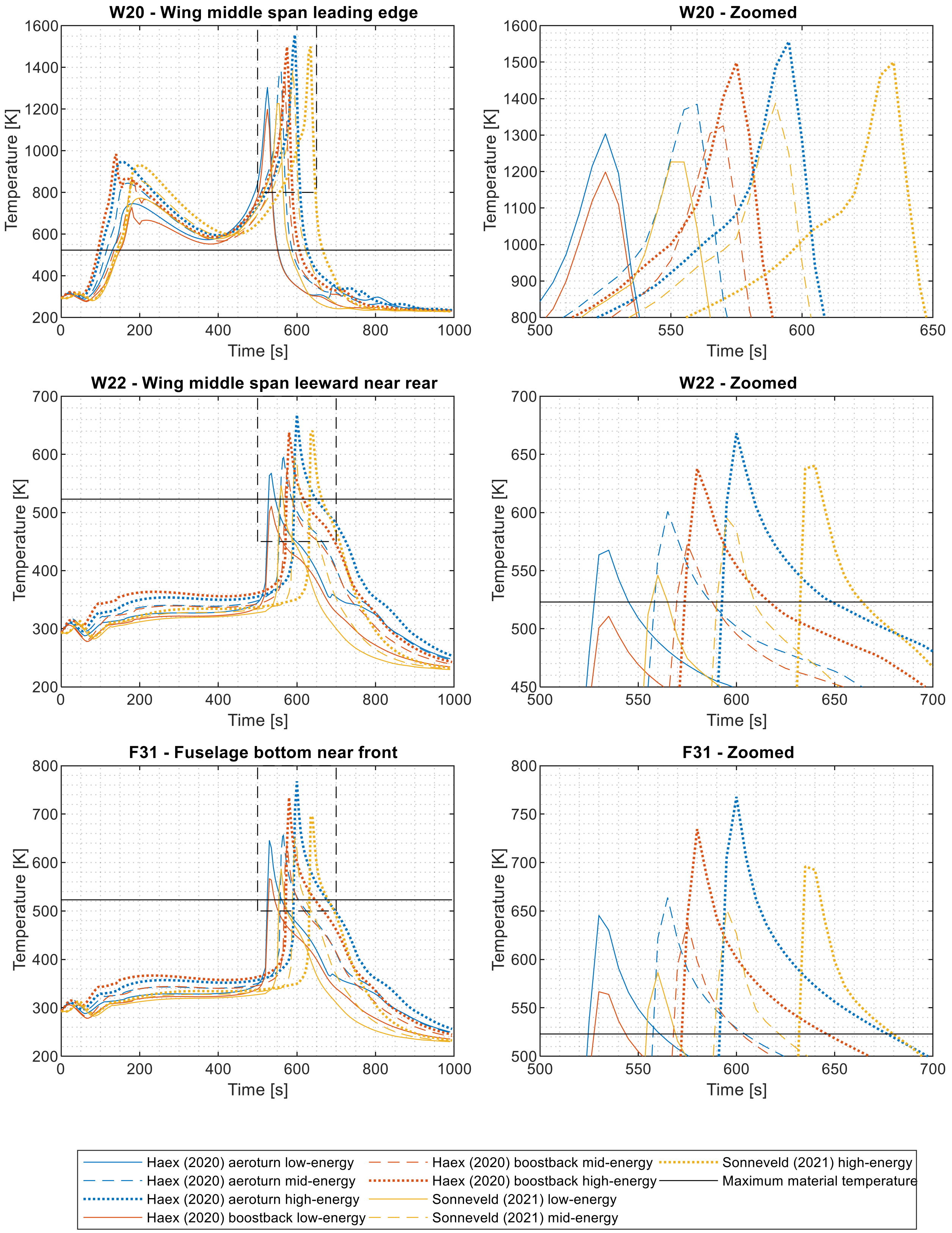

Figure 7.8. BMI CF temperature results along the nine chosen trajectories for three chosen locations on the vehicle's external surface.

boostback trajectories have a slightly lower temperature caused by their slightly slower horizontal velocity. The flat sections of the vehicle have lower flow temperatures and hence don't get heated or cooled as much and quickly by these effects.

Another effect observed in Figure 7.8 is that after re-entry the leading edges cool to below 250 [K] quickly after re-entry, whereas the flat section of the wing cools more slowly. Just as the leading edges experience higher conductive heating, it is expected that these portions of the vehicle experience higher conductive cooling as well. After re-entry the velocity quickly decreases to sonic velocities, which means that the air temperature becomes cold relative to the temperatures seen during supersonic flight. With the leading edges being high temperatures, this causes for rapid cooling. Also, at the leading edges the convective heat transfer coefficient is higher than that of the flatter portions of the vehicle, as displayed in Figure 7.9. This means that the convective cooling is larger just as the convective heating was.

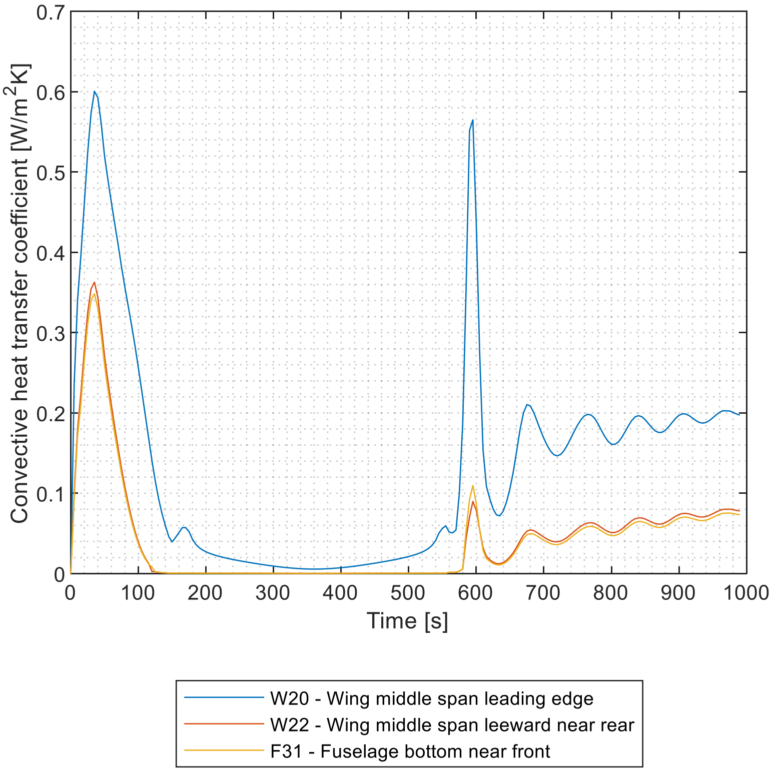

Figure 7.9. BMI CF coefficient of convective heat transfer results for three vehicle locations along the Sonneveld (2021) mid-energy trajectory.

Each of the three trajectory categories, *i.e.* Sonneveld (2021) trajectories, Haex (2020) aeroturn and Haex (2020) boostback trajectories, show trends and features unique to that category. The Sonneveld (2021) trajectories each have their maximum temperature peaks 30-40 [s] later compared to the Haex (2020) trajectories. This is explained by the fact that the Sonneveld (2021) trajectories start at 0 m/s velocity whereas the Haex (2020) trajectories start at Mach 0.2. The Haex (2020) trajectories do not include the initial runway acceleration of the vehicle whereas the Sonneveld (2021) trajectories do. This initial acceleration causes the maximum heating peaks to be later along the time scale. The second observation between the trajectories is that Haex (2020) boostback trajectories have a lower temperature peak compared to the aeroturn trajectories. The chosen boostback trajectories have a lower energy level compared to the chosen aeroturn trajectories, as shown in Figure 2.2. Due to the energy of the vehicle being different in these two trajectories, it is difficult to make an exact comparison. It is also observed that during ascent, boostback trajectories have a higher peak temperature compared to the same energy category aeroturn trajectory. During re-entry this is however not the case. This is likely due to the boostback having a lower re-entry velocity and a higher ascent velocity, due to it reducing its horizontal velocity after staging. Another observation in the boostback trajectories, caused by the burn after staging, is that there is a sharp decrease in temperature after the ascent. This can be explained by the sudden decrease in velocity, therefore causing a sudden decrease in flow temperature and causing a larger convective cooling heat transfer. The variation between the different trajectory categories means this thesis is able to capture a large design space for the Mk-III mission. It allows for a comparison of various thermal profiles based on a range of predicted and potential Mk-III trajectories.

Thus far the discussion in this section has been in regards to the general trends observed in the nine different trajectories for the BMI CF case. The BMI CF material, temperature shown in Figure 7.8, in its current state is not a suitable material choice for the Mk-III. The maximum material temperature is exceeded in all trajectories except for one, in the W22 location. This trajectory is only roughly 10 [K] off the maximum temperature, and so therefore still unsuitable given the accuracy of the model. Given that the BMI material maximum temperature is close to the maximum temperature of the vehicle flat sections it may be possible to provide additional TPS to decrease the peak temperature. This is however not reasonably possible for the leading edges as the peak temperature is more than three times the maximum material temperature. The reason BMI CF is still a suitable choice, beyond currently not being able to meet the temperature requirements, is due to its low mass. The BMI is in its current state the lowest weight option, meaning that there is a chance that even with a TPS system it remains the lowest mass option within the materials chosen in this thesis. This material is therefore going to be analysed within the next sections to evaluate its performance with a TPS.

7.2.2. SiC BF

The SiC CF material analysis with a thickness of 3.332 mm was conducted for all nine trajectories, as shown in Figure 7.10. Three different points along the vehicle were chosen to be displayed in this figure, which are a representation of the different temperature profiles the entire vehicle experiences. More locations are plotted in Appendix C. The general behaviour of the SiC CF for all nine trajectories is like that of BMI CF. A direct comparison of their difference will be made in Section 7.2.5.

The SiC CF material property maximum allowable temperature allows for the material to be appropriate for regions warmer than the BMI CF can handle. Figure 7.10 shows that the maximum material temperature is around the region where the re-entry peak temperature occurs. The high energy trajectories all exceed the SiC CF vehicle setup temperature, whereas the low and energy trajectories fall below the material threshold. Considering that the model has some errors, the SiC CF could be a suitable choice if trajectories are limited. Applying a TPS system to this material has potential to extend the trajectory operation range. Therefore, based on this data it is recommended to investigate a TPS system for SiC CF.

The SiC CF’s material temperature is far above the requirement for the flat sections of the vehicle. Because SiC CF is 2.5 times heavier than BMI CF it not be the preferred material choice for this portion of the vehicle. That is under the condition that a TPS system can be applied to BMI CF without an unjustifiable weight penalty. Considering this, the BMI CF-SiC CF material combination has potential to be possible as a material choice for the flat sections of the vehicle and leading edges respectively. Table 7.5 shows that the thermal expansion coefficient of SiC CF is about half that of BMI CF. Therefore, this material combination would require stress analysis to ensure suitable compatibility in the joint design.

7.2.3. Titanium

The titanium material analysis with a thickness of 1.15 mm was conducted for all nine trajectories, as shown in Figure 7.11. Three different points along the vehicle were chosen to be displayed in this figure, which are a representation of the different temperature profiles the entire vehicle experiences. More locations are plotted in Appendix C. The general behaviour of the titanium for all nine trajectories is like that of BMI CF. A direct comparison of their difference will be made in Section 7.2.5.

Figure 7.11 shows that the titanium maximum material temperature is above the temperatures seen at the leading edge and flat sections of the vehicle. This is with sufficient margin for errors caused by the model and shows that the titanium is a suitable choice for the entire vehicle. Comparing the material’s performance to that of BMI CF, Table 7.5 shows that the BMI CF would result in a 30% lighter structure (considering entire vehicle is made of one material). BMI CF requires analysis with TPS but if the weight increase of the TPS remains below the weight of titanium, it is the more suitable material for the flat portions of the vehicle. For the leading edges titanium weights almost 40% lighter compared to the SiC CF option displayed in Table 2.1. Considering that the SiC CF would require a TPS system to allow it to operate in all trajectories, titanium would be a more suitable choice. Therefore, SiC CF will not be investigated in the TPS study as it has a low likelihood of being more suitable than titanium.

The combination of BMI CF and titanium has been identified as a potential material combination that in terms of mass outperforms the other material choices thus far analysed. Table 7.5 shows that the

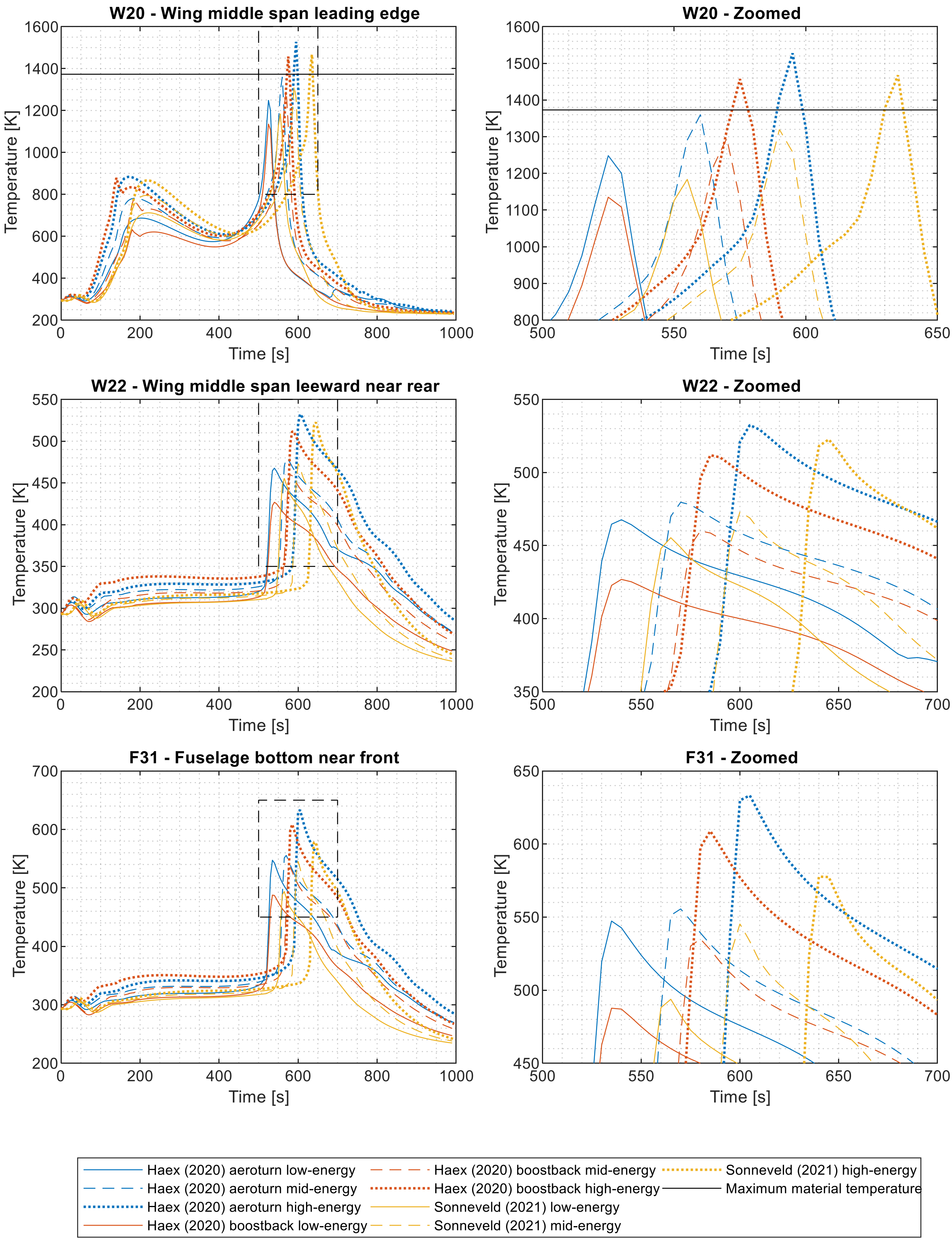

Figure 7.10. SiC CF temperature results along the nine chosen trajectories for three chosen locations on the vehicle's external surface.

thermal expansion coefficient of the two materials is within 25% of each other. Although not a perfect match this material combination has a high chance of producing low thermal stresses at the joint. A stress analysis would be required to confirm this but this stress analysis would also be required for a single material structure. The two materials are also compatible in terms of galvanic corrosion, which could cause long term problems with other material combinations (Yari, 2021).

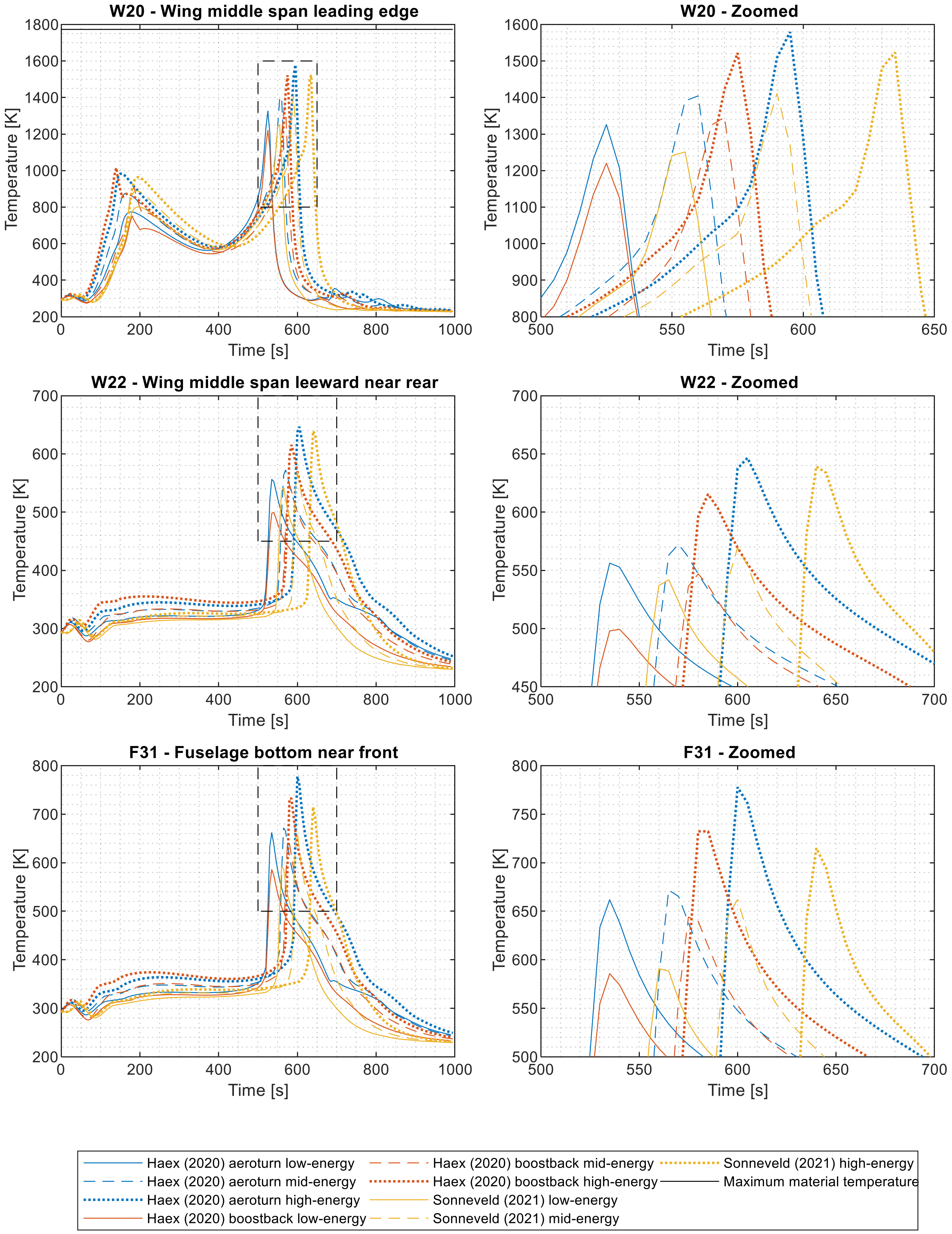

Figure 7.11. Titanium temperature results along the nine chosen trajectories for three chosen locations on the vehicle's external surface.

Identifying potential problems in design is part of this thesis' scope though analysing them would require a separate study and is outside this thesis scope. Due to the difference in composition of the titanium and BMI CF, a consideration with these materials would also be how to join them. Glue compatibility would be a challenge which would mean mechanical methods of joining these two materials would be needed. The material thickness of titanium could also be an issue. Although titanium has a higher yield strength, the thin thickness of the skin could lead to issues with manufacturing, operation and maintenance. Some examples of those issues could be buckling, resistance to impact damage and repairability.

7.2.4. Aluminium

The aluminium material analysis with a thickness of 3.15 mm was conducted for all nine trajectories, as shown in Figure 7.12. Three different points along the vehicle were chosen to be displayed in this figure, which are a representation of the different temperature profiles the entire vehicle experiences. More locations are plotted in Appendix C.

For all other material choices thus far analysed, the cooling of the leading edge during coasting has meant all nine trajectories cool to roughly the same temperature. For aluminium this is however not the case, as shown in Figure 7.12. There is roughly a 100 K difference between the high energy and low energy trajectories just before re-entry. Table 7.5 shows that aluminium has a much higher specific heat capacity per unit area compared to the other materials, which means that more energy is stored in the material. Hence a slower heating and cooling effect is observed in aluminium compared to the other materials. Section 7.2.5 will explain the differences between the material choices more. What is important is that the general behaviour explained in Section 7.2.1 is again followed by all the trajectories.

The maximum temperature of aluminium falls above that required for the flat sections but below that of the leading edges. For the leading edges aluminium is therefore not suitable, as an appropriate TPS system would be required to protect the aluminium from the heating. For the flat sections it is a suitable choice, with the exception that the weight is more than 70% higher than titanium. In terms of mass titanium would therefore be a more suitable choice. In terms of cost aluminium would be more suitable. Due to the re-usability aspect of the spaceplane, operational costs will likely dictate the cost of the spaceplane, meaning manufacturing costs are lower on the importance ladder (Haex, 2020).

7.2.5. Material Comparison

Having modelled and analysed all the materials separately, comparing the materials side-by-side for one trajectory also provides valuable information on the different material performances. Figure 7.13 shows the results of comparing (Haex, 2020) aeroturn high-energy trajectory. More trajectories were analysed in this manner and can be found in Appendix C. A first observation is that all four material choices, although different in magnitude, show the same trends along the trajectory. The leading edge is heated both during ascent and re-entry, whereas the flat sections are mainly heated during re-entry. The cooling during the coasting is observed on the leading edge for all four materials. Also, the rate of cooling after re-entry is seen to be similar for all four trajectories where the leading edge cools quickly, whereas the flat sections cool more slowly.

From Figure 7.13 it is obvious that similar temperature profiles are observed for BMI CF and titanium, whereas SiC CF and aluminium show slower changes in temperature. The effect means that aluminium reaches lower peak temperatures, but also cools slower, meaning the temperature of aluminium is highest at the final simulation time of 1000 [s]. SiC CF also shows this behaviour compared to the BMI CF and titanium, but the rate of temperature change is in between the two cases, hence resulting in an in between peak temperature. The different response rates can be attributed to the difference in specific heat capacity per unit surface area for all four materials. BMI CF and titanium have a similar specific heat capacity per unit area and also the lowest. Comparatively, aluminium's specific heat capacity per unit area is around 2.5 times larger, being the highest of the materials analysed. Therefore, aluminium can store more energy per unit surface area, meaning for the same thermal fluxes the temperature changes at a slower rate. Due to this lower rate of change the total amount of energy stored in the aluminium is likely higher than that of the other materials. This is because when heating occurs, due to the slower material temperature change, the temperature difference between flow and material remains larger, hence causing larger convective heat transfer. This is however not directly observed in the temperature profiles, due to the aluminium's higher specific heat capacity per unit area storing this additional energy within a smaller temperature change.

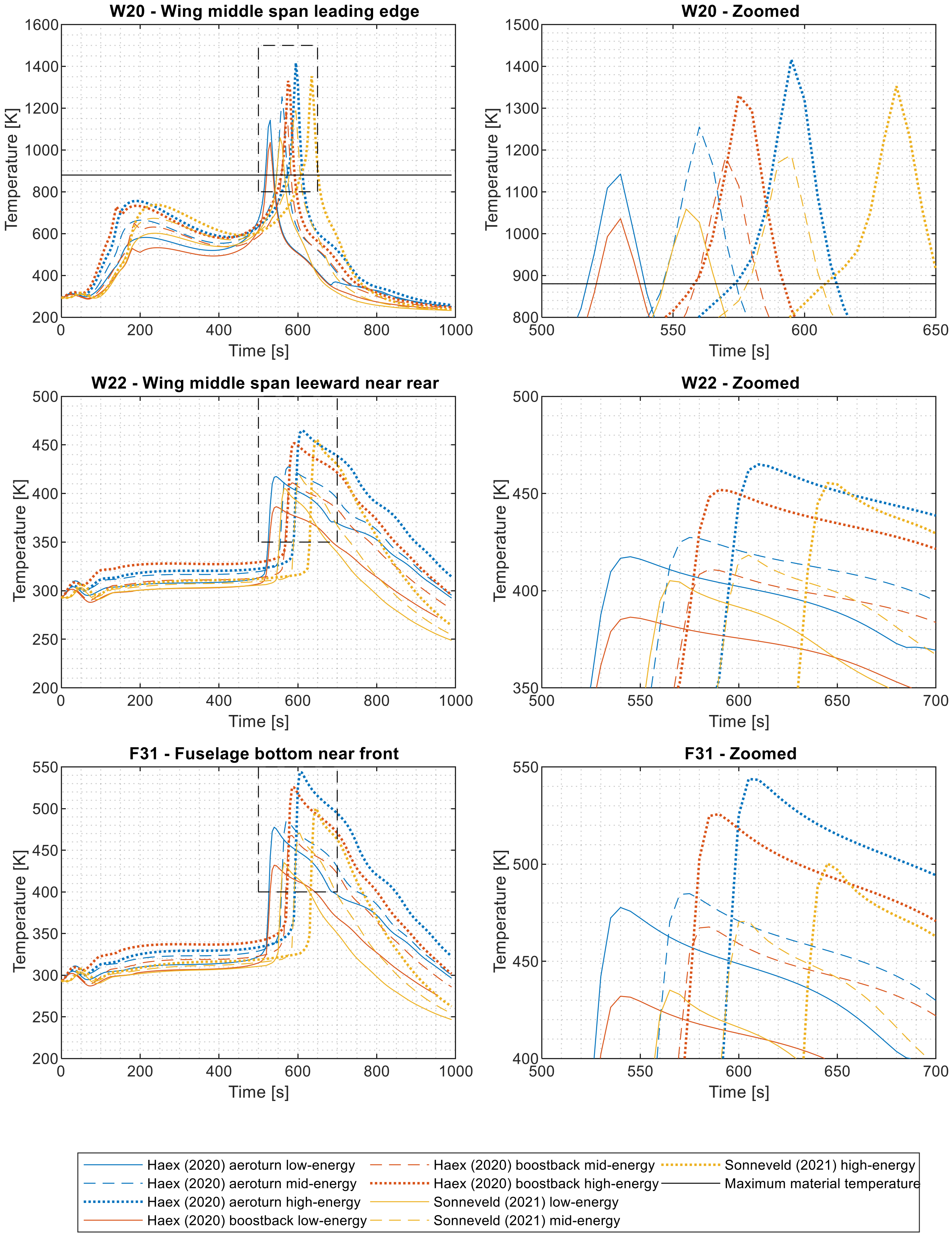

Figure 7.12. Aluminium temperature results along the nine chosen trajectories for three chosen locations on the vehicle's external surface.

There is not only a difference between the four materials in terms of external surface temperature at different locations along the vehicle, but there are also differences in the material temperature profiles in the surface's normal direction. As explained in Section 7.1.1, the vehicle's mesh is split up into five elemental layers in the normal direction to the vehicle's surface. This means that there are six nodes in the surface's normal direction, each with their own temperature. Figure 7.14 shows the temperature profile of these six nodes for the wing middle span leading edge location for the Sonneveld (2021)

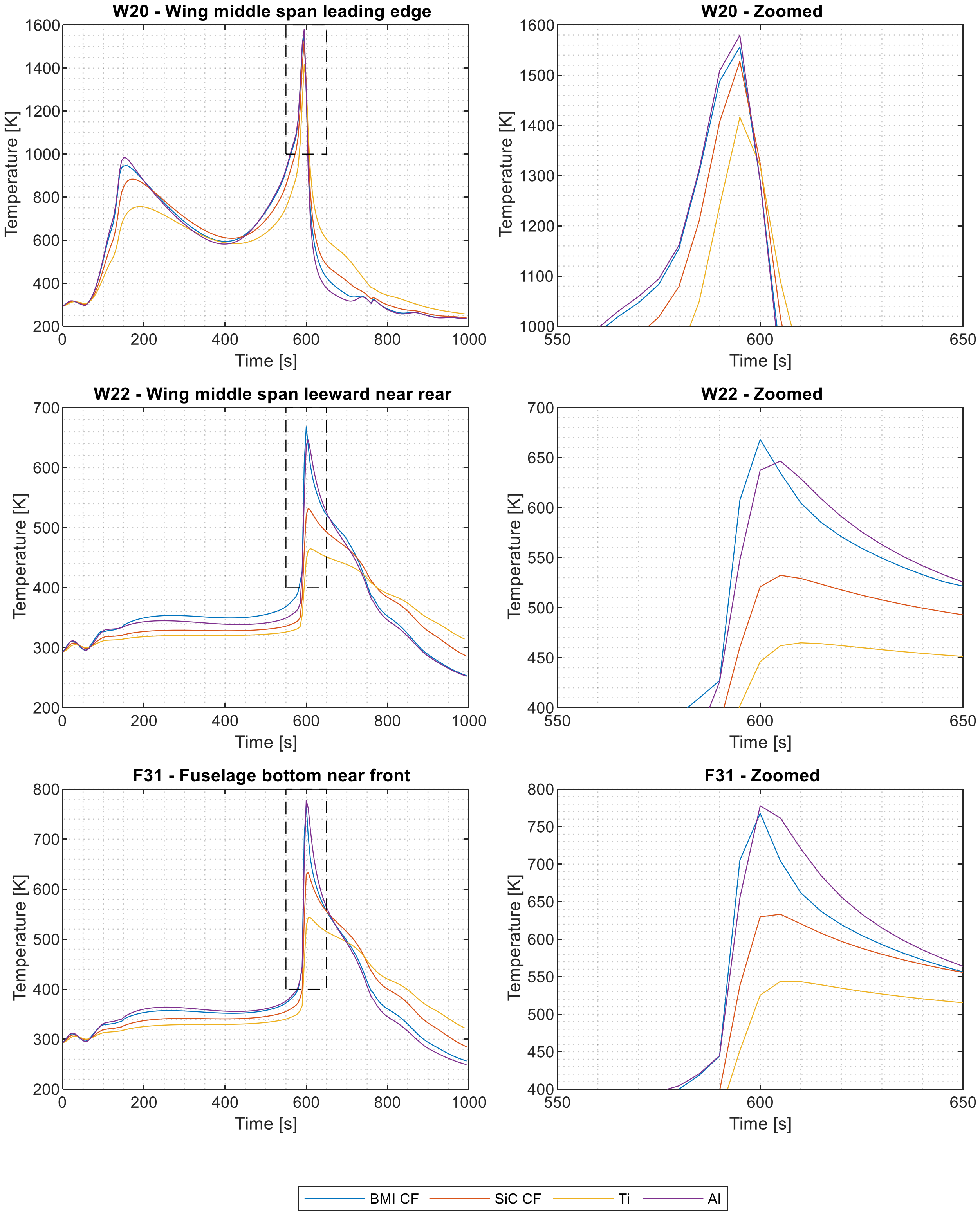

Figure 7.13. Temperature results of the four material choices for Haex (2020) aeroturn high-energy trajectory

aeroturn mid-energy trajectory. This figure shows that a nodal temperature gradient is primarily observed in BMI CF and slightly observed in SiC CF. The titanium and aluminium do not have an observable or significant temperature difference within their nodes that is outside the accuracy of the model. The difference in nodal temperature for the BMI CF materials is due to the low thermal conductivity, particularly the out-of-plane thermal conductivity. This thermal conductivity coefficient is more than an order of magnitude smaller than that of the other materials and means that energy within the material is transferred slower. The aluminium on the other hand has a very high thermal conductivity coefficient compared to the other materials and is observed to have a near uniform temperature. The SiC CF and titanium both have a similar thermal conductivity coefficient, but Figure 7.14 shows that the SiC CF has an internal to external skin temperature difference of a few 10’s of K

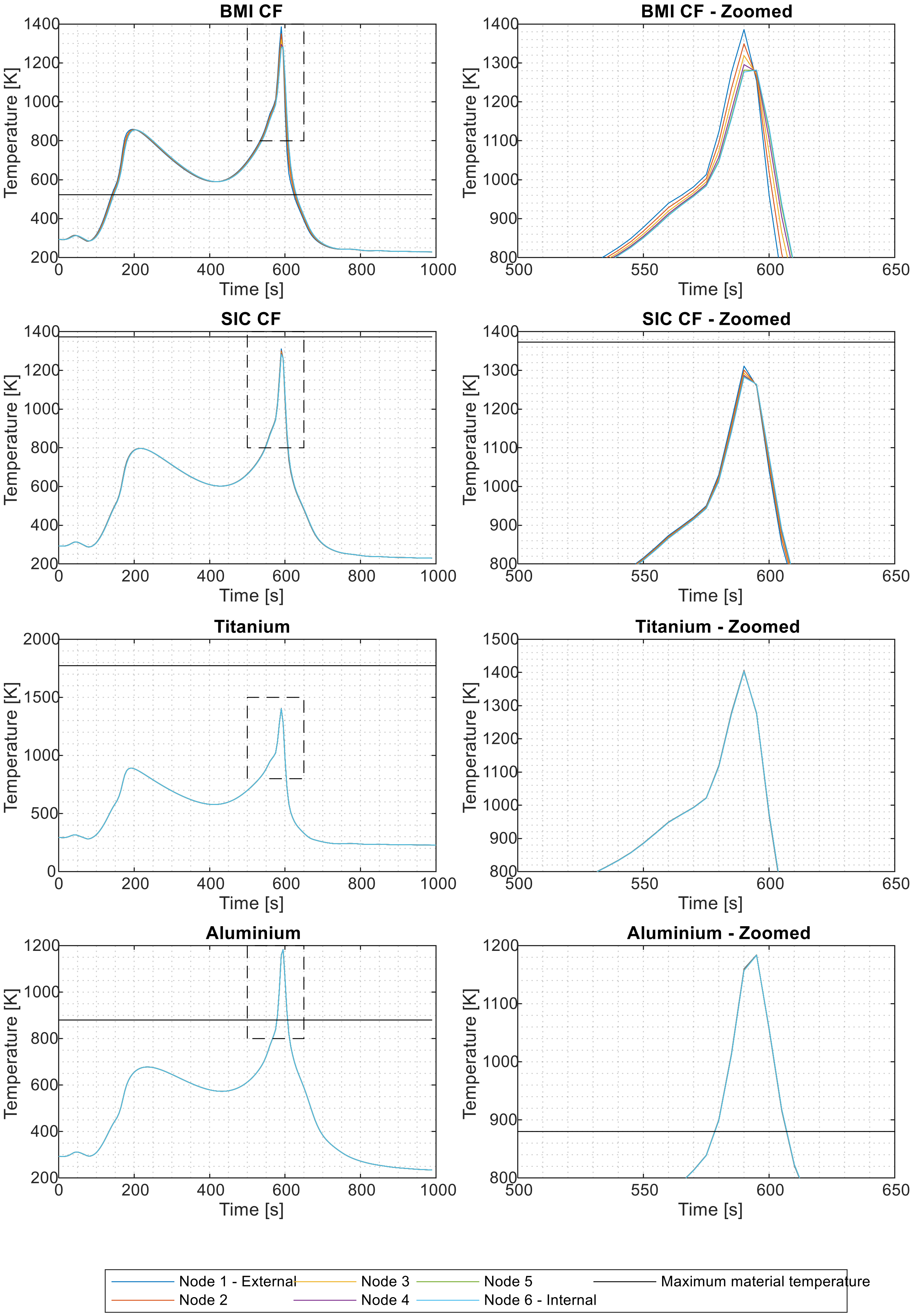

Figure 7.14. Vehicle node temperature results at the W20 wing middle span leading edge location in the normal direction to the skin for Sonneveld (2021) mid-energy trajectory.

whereas titanium's is smaller. The reason for this is due to the SiC CF being almost three times thicker than the titanium, meaning that the thermal conductivity coefficient multiplied by the node respective distance is lower for the SiC CF compared to the titanium. The almost double specific heat capacity per unit area for the SiC CF compared to the titanium would likely also have a contribution due to more heat being stored per degree temperature change.

7.3. Active thermal protection system

The idea behind the active cooling investigated within this thesis is the use of left-over pressurant from the ascent phase of the spaceplane. This pressurant is used to maintain the required pressure in both the oxidizer and fuel tanks but has no use after ascent. The pressurant in these tanks is therefore weight and to minimize re-entry loads can be dumped. This thesis however wants to investigate using this pressurant for a secondary purpose, dumping it during re-entry via the internal structure of the vehicle.

Section 5.3 explains the calculations behind finding the heat flux from cooling. The result is that the total amount of available pressurant for cooling purposes is 77.73 kg. It will be assumed that the change in temperature of the coolant within the cooling system is 50 K. Again, this assumes that a system can be designed to achieve this. For this thesis two different active cooling time spans were used. Cooling A actively cools for 100 $[s]$ from simulation time 550 to 650 $[s]$. Cooling B actively cools for 20 $[s]$ from simulation time 580 to 600 $[s]$. This results in a heat transfer rate of 40.5 and 202.6 kW for cooling A and B respectively. The surface area of the entire vehicle is 244 m^2 meaning that the heat flux during the active cooling A and B is 165.9 and 829.6 W/m^2.

Figure 7.16 shows the results of simulating active cooling systems A and B for the Sonneveld (2021) mid-energy trajectory. The result of this analysis is that the active cooling systems do not make a difference in temperature results of the Mk-III. It is therefore not a suitable cooling system to be implemented in the way it was specified in this thesis. The reason for its inefficiency is due to the very low heat flux it can create compared to the convective heat transfer flux shown in Figure 7.15. The convective heat transfer flux is in the order of 10^5 $[\mathrm{W/m^2}]$, meaning that the active cooling doesn't even mitigate 1 % of the convective heating.

Because this is an ineffective solution, other problems, such as the added mass, achieving the required cooling and pressure/temperature changes along the cooling system, will not be discussed.

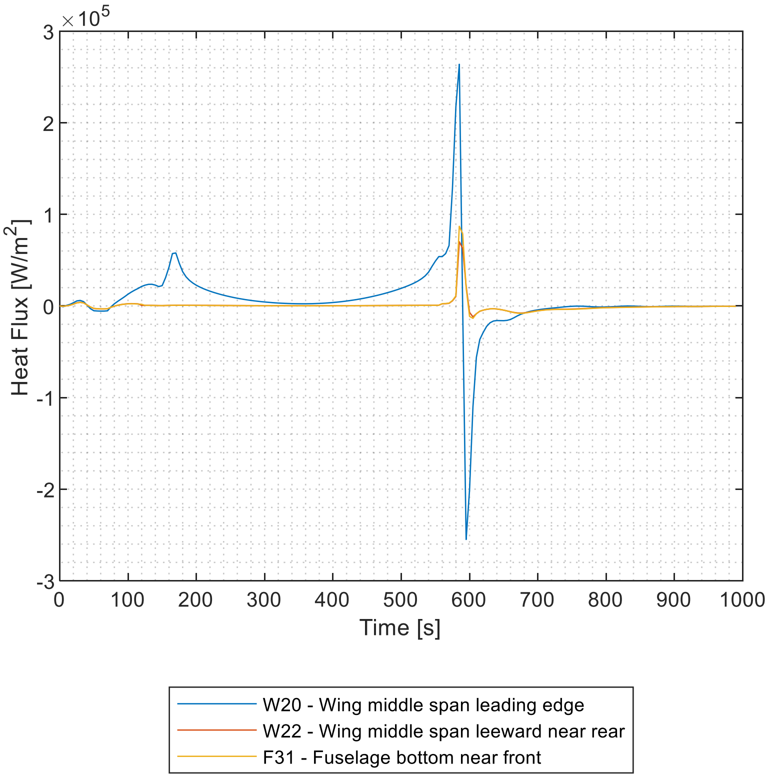

Figure 7.15. Convective heat flux for the Sonneveld (2021) mid-energy trajectory

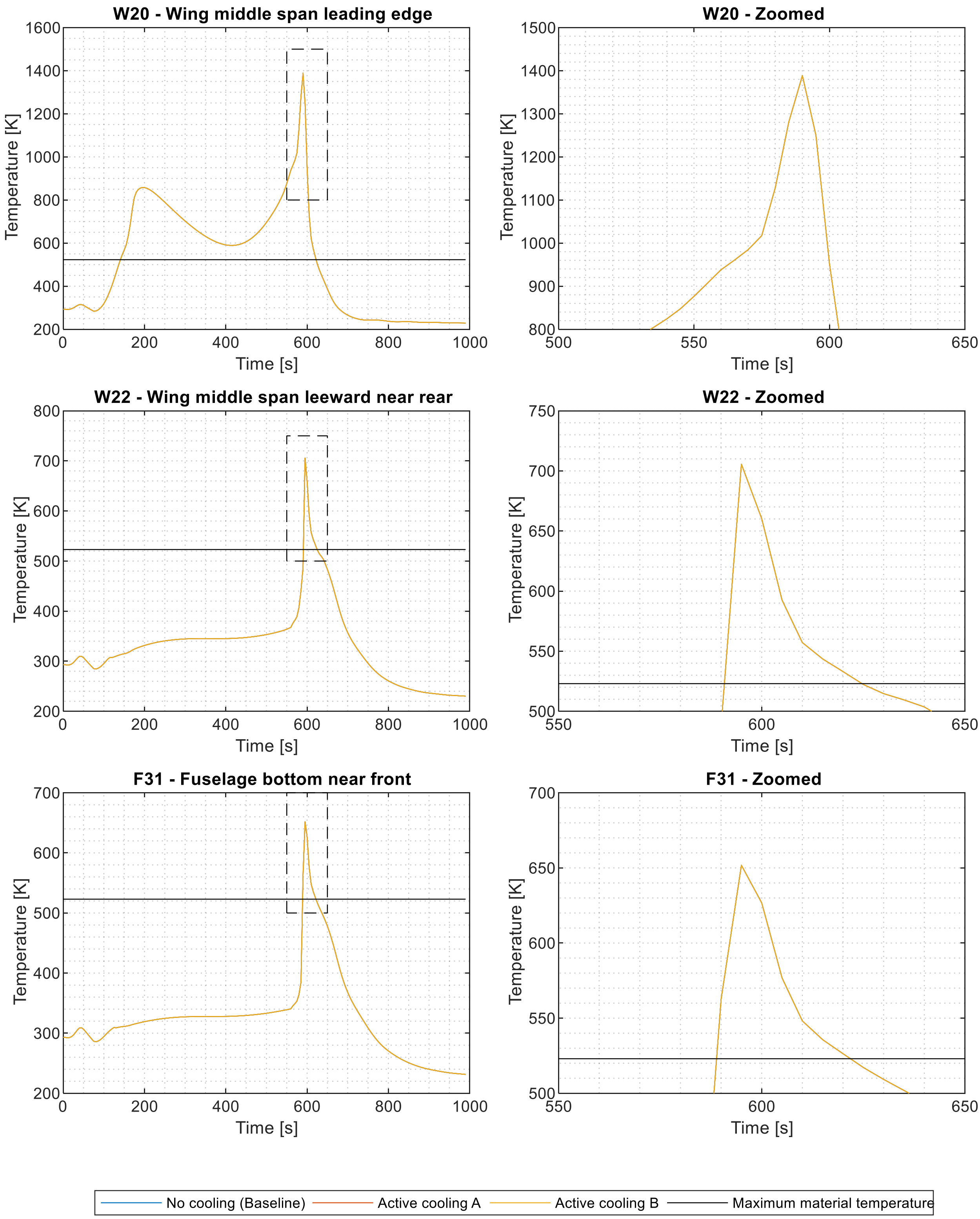

Figure 7.16. Temperature results for different active cooling solutions along the Sonneveld (2021) mid-energy trajectory.

7.4. Protective layers

7.4.1. Radiation

The external surface of the Mk-III is highly likely to be coated. The non-thermal reasons for this coating are due to the marketing and aesthetics of the vehicle or to control the surface roughness for aerodynamic purposes. Thermally the coating of the vehicle is key for the radiation properties. Thus far in the thesis an emissivity constant of 0.76 has been used to evaluate the radiative flux exiting the external surface of the vehicle. The surface coating can vary this constant, which is why this section has evaluated changing the constant to 0.68 and 0.84.

Figure 7.18 shows the results for analysing the Sonneveld (2021) mid-energy trajectory with emissivity constants 0.68, 0.76 and 0.84. This figure shows that all three simulation results follow almost exactly the same temperature, with differences in the order of a few 10 K almost solely at the leading edge. It should also be noted that this TPS study was focused on the flat sections of the wing. Therefore, if it only has a minor beneficial effect at the leading edge, it does not meet the needs of this study. The main reason for the small effect is due to the temperatures of the external skin still being low for radiation. It is clear from the results that the convective heat transfer dominates the heat flux as the temperature are too low for high radiative heat fluxes to be present. This is why the peak temperature and heating of the external skin appear almost identical for all three simulations. In saying this, Section 6.3.1 has shown that radiation cannot be omitted as it does still play a vital role in the cooling of the vehicle during coasting. This is seen in the cooling during coasting at the leading edge but also slightly

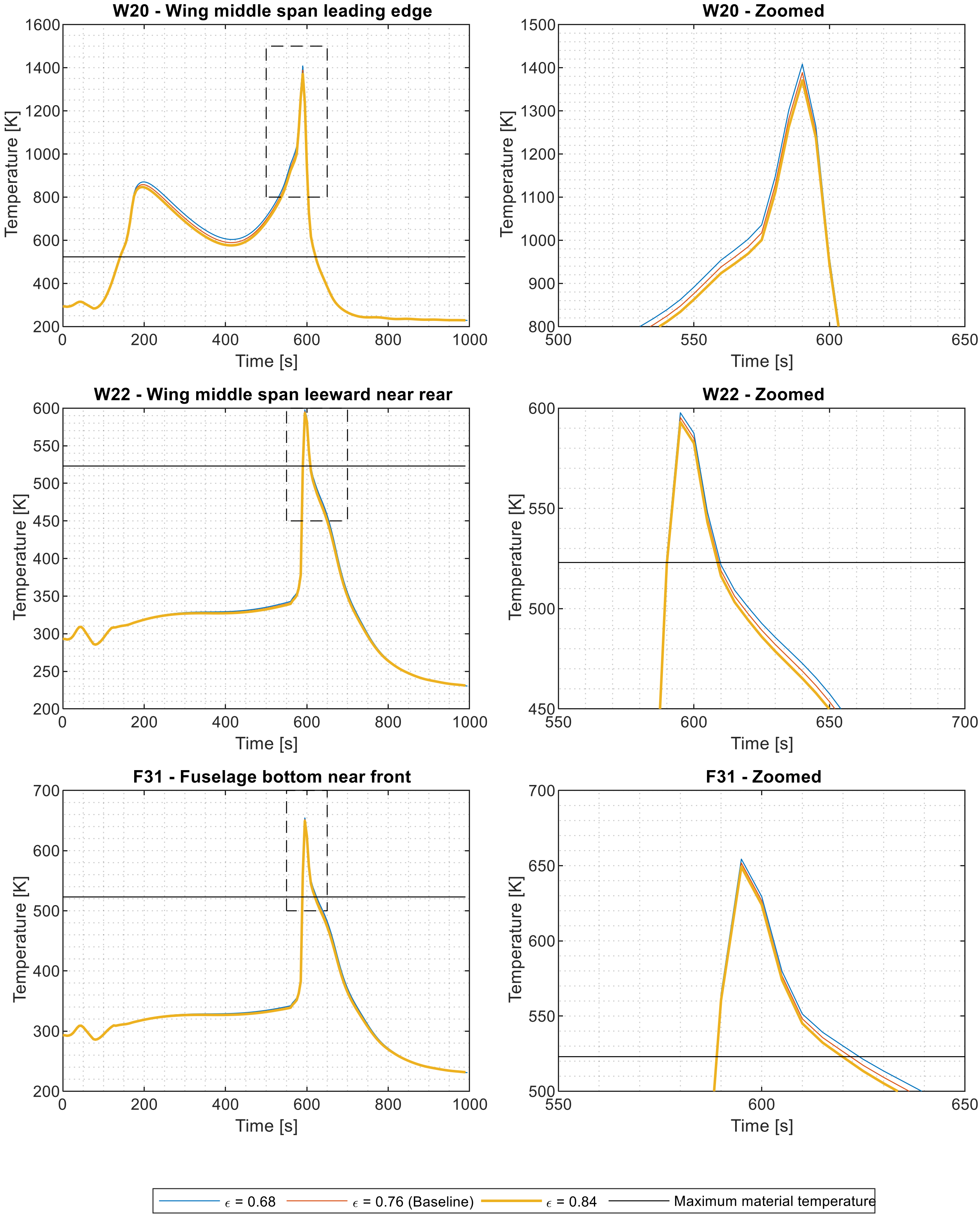

Figure 7.17. Temperature results for different emissivity constants along the Sonneveld (2021) mid-energy trajectory.

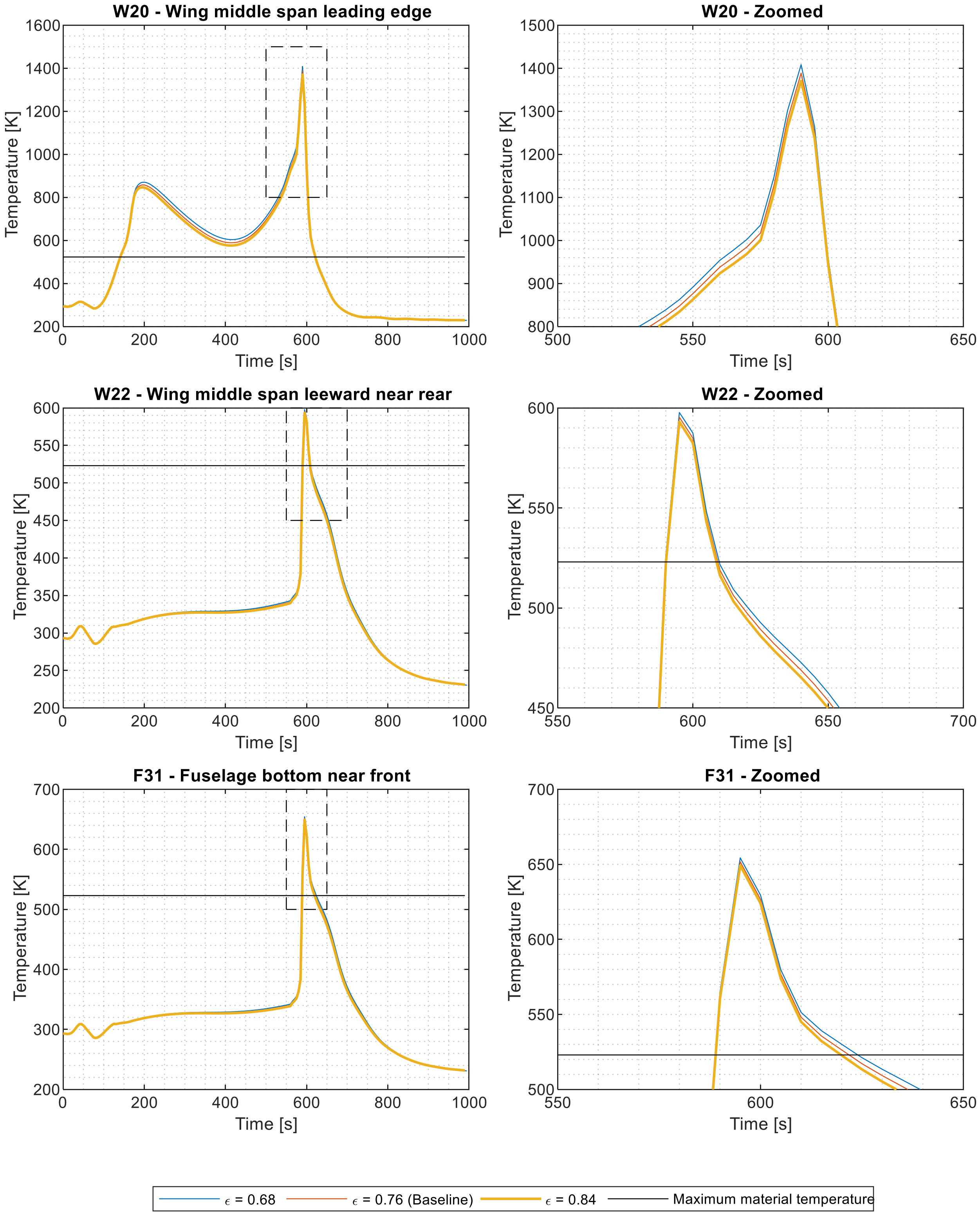

Figure 7.18. Temperature results for different emissivity constants along the Sonneveld (2021) mid-energy trajectory.

in the flat sections of the vehicles. If radiative cooling doesn't reduce the peak temperatures for it to be chosen as an effective TPS for the Mk-III, other requirements for the Mk-III coating should be prioritized. In saying that, the coating does still need to fulfil the temperature requirements set by this thermal analysis.

7.4.2. Insulation

Analysing the insulation TPS was done by adding a 1 mm thick layer of four different types of insulators on top of the structural BMI CF skin as shown in Figure 7.19. The goal of the insulator is to provide thermal protection for the flat sections of the vehicle if the material cannot withstand the thermal loads.

The method in how it does this, is to provide a low thermal conductivity layer on top of the material to provide a high temperature gradient between its hot and cold side. This section will describe the decisions made with this simulation and explain the results and implications thereof.

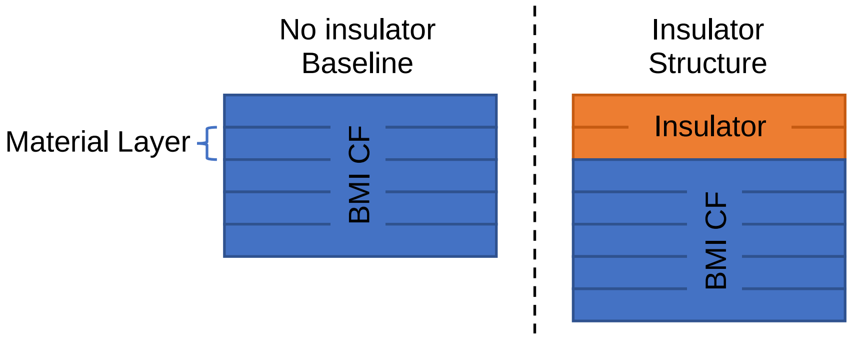

Figure 7.19. Insulator structural skin setup.

The four foams were selected from the GRANTA database (Granta Design Limited, 2020), chosen to provide an overview of the thermal insulator class. The material properties of the four foams are shown in Table 7.6. This material selection provides a wide range of material properties primarily including density and thermal conductivity. The materials available from GRANTA (Granta Design Limited, 2020) are not expected to be the insulation materials that will eventually be chosen for the Mk-III in case insulation is a suitable option. However, this database provides the best and most complete available dataset available for the purpose of this thesis. In the detailed design phase of the Mk-III, the manufacturers of various insulators can be contacted for better suited solutions that better meet the needs. For the purpose of this thesis, these insulators will provide an appropriate approximation of how an insulator could protect the structural components of the vehicle and answer the research question; whether an insulator could be a suitable TPS for the Mk-III.

Table 7.6. Material properties of the chosen insulators from GRANTA (Granta Design Limited, 2020).

Insulator Material	BMI CF Baseline		Alumina foam	Aluminium foam	Aluminum-SiC foam	Glass foam
Identifier	No insulator		A	B	C	D
Density $[\mathrm{kg/m^3}]$	1540		610	500	270	135
Mass/unit area $[\mathrm{kg/m^2}]$	3.67		4.28	4.17	3.94	3.80
Max temperature $[\mathrm{K}]$	523		2278	855.5	855.5	778
Thermal conductivity $[\mathrm{W/mK}]$	2.425	0.725	0.5835	10.5	4.75	0.0445
Insulator specific heat capacity $[\mathrm{J/kgK}]$	945		815	935	935	780
Structure specific heat capacity per unit area $[\mathrm{J/m^2K}]$	3464		3961	3931	3716	3569
Thermal expansion coefficient $[\mathrm{\mu\varepsilon/K}]$	11.85	23.85	8.75	19.5	21.5	8.6

A notable material property that can be compared between the insulators and BMI CF is the thermal conductivity. The BMI CF thermal conductivity, shown in Table 7.5, is around the same thermal conductivity as some of the insulators, even lower than some, as shown in Table 7.6. This means that the BMI CF itself also thermally insulates. This is observed during the previous chapters in terms of the temperature profile in the normal direction of the skin primarily shown in Section 7.2.5.

Figure 7.20 shows the temperature results of the external vehicle skin layer along the Sonneveld (2021) mid-energy trajectory for a few vehicle locations, which are representable of the entire vehicle temperature results. The first observation is that each case has a near identical temperature profile. The insulators have a small effect on the rate of heating, thereby resulting in slightly lower maximum

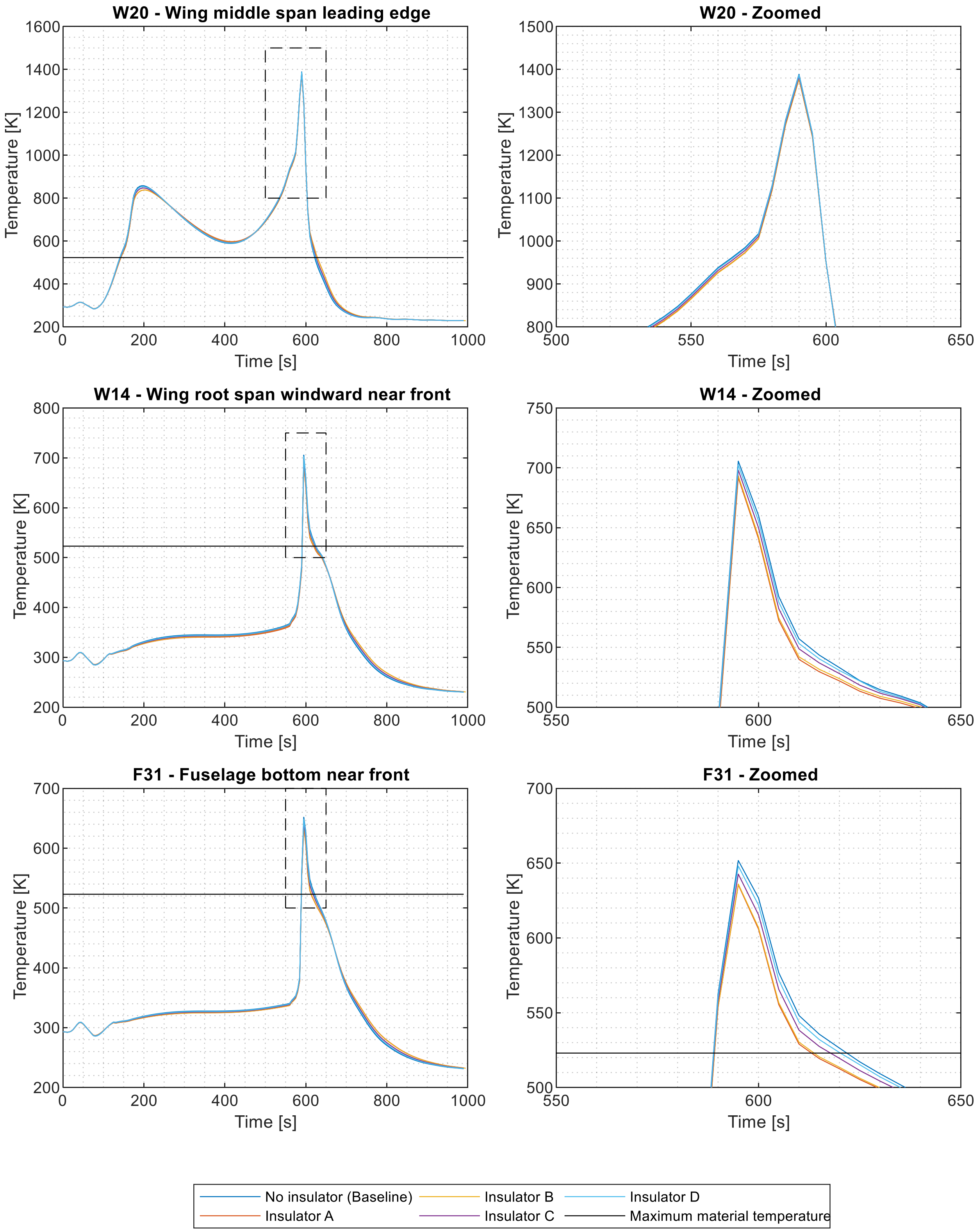

Figure 7.20. Temperature results of the external skin for different insulator at a selection of vehicle locations along the Sonneveld (2021) mid-energy trajectory.

temperatures in the order of a few 10’s of [K]. This is attributed to the higher specific heat capacity per unit area that an insulator creates. Thereby the vehicle skin can absorb more energy per unit area unit Kelvin resulting in lightly lower temperature increases and slightly slower temperature decreases. This is primarily seen in insulators A and B which have the highest heat capacity per unit area. The difference is not very large, as the difference in specific heat capacity per unit area between all cases in not very large. The primary concern of the external layer of the vehicle is however not how much it changes relative to the no insulator case, but whether it is below the maximum temperatures of the insulators. This is the case for all insulators tested, though insulator D does come close for certain wing locations and would warrant further investigation to be sure this is not an issue.

For the insulators, the key performance parameter is the temperature of the external most structural BMI CF layer. Figure 7.21 therefore shows the temperature of the external most BMI CF layer, which for the no insulator case is also the structure's external most skin layer. For the flat sections of the vehicle this figure shows that depending on the insulator chosen, the BMI CF skin maximum temperature decreases between 55-80 K for the 1 mm of insulator. The graphs show that just like the external skin temperature, higher specific heat capacity insulators result in lower maximum

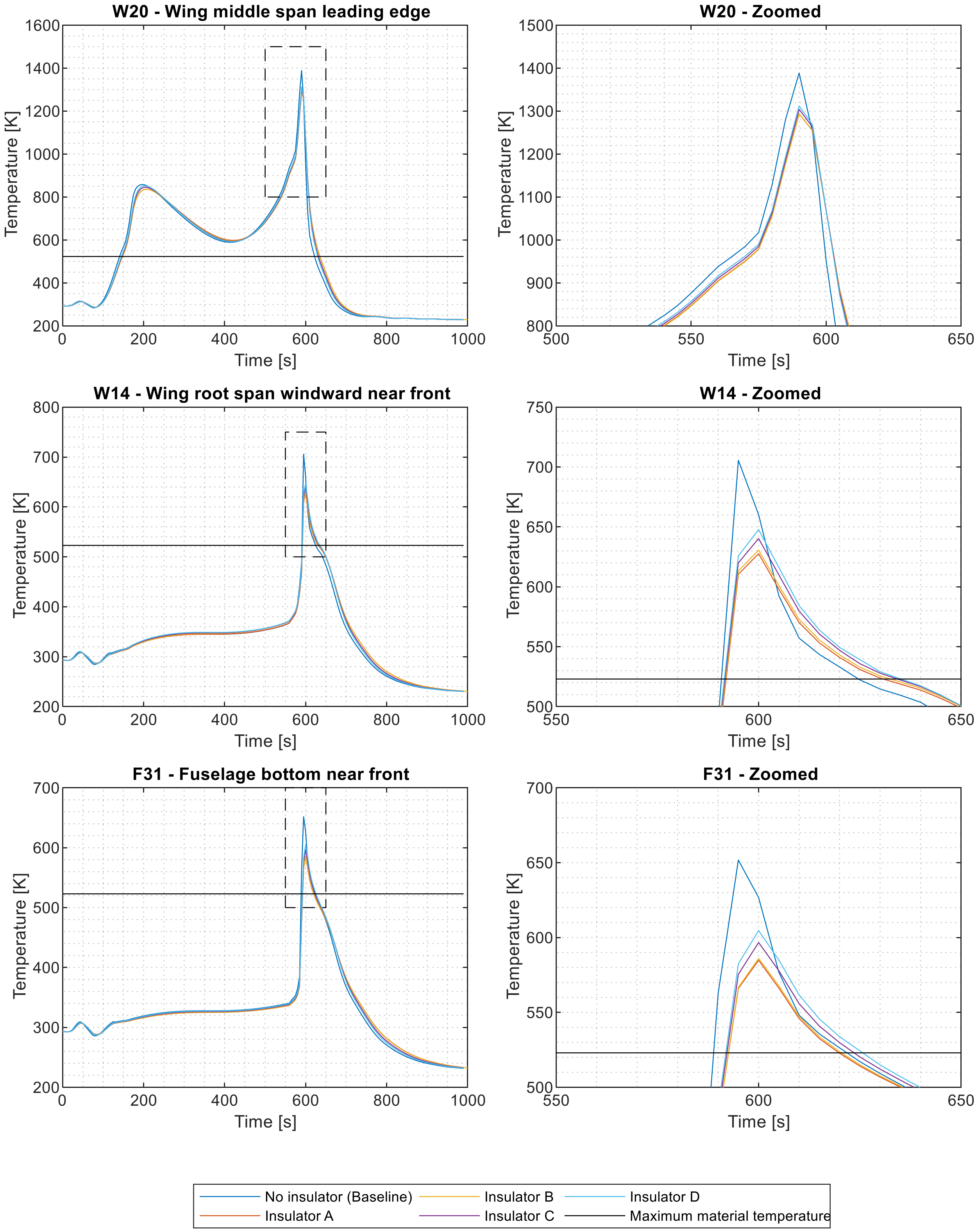

Figure 7.21. Temperature results of the outermost BMI material layer for different insulator at a selection of vehicle locations along the Sonneveld (2021) mid-energy trajectory.

temperatures. However, in terms of $[\mathrm{K}]$ per unit insulator mass, the lower density materials perform better. This means that even though these insulators would require to be thicker to produce the same performance, they would result in a smaller increase in mass. Therefore, these materials are more efficient.

None of the chosen insulators have been able to produce the required temperature decrease for the BMI CF to be below its maximum temperature. From rough calculations the thickness would have to increase about 3-4 times to produce sufficient insulation for the BMI CF. For insulators A and B this would mean that this material option and TPS combination would result in higher masses compared to the titanium material option. Insulators C and D would still remain from a mass perspective more beneficial, with insulator C only marginally so. This choice is however fully based on the structural assumptions discussed in Section 2.4 and therefore would require more detailed structural analysis.

Insulators have proven to be a sufficiently efficient enough solution to maintain the temperature of the structural BMI CF below its maximum temperature, while still being lighter than the titanium solution for the flat sections of the vehicle. However, there are still a number of questions and concerns that would ultimately decide which choice is more beneficial for the Mk-III. Firstly, the insulators chosen to be analysed here are likely not those that will be applied to the real Mk-III. For the conceptual stage of the Mk-III and the fact that each insulator roughly showed similar results, this analysis has provided sufficient proof that insulators could be a suitable TPS solution. The thickness required for the insulator is also not known. However, if the density of the insulator is sufficiently low then this will not likely cause major mass issues. This thickness should be investigated further in the future once more information about the insulator is known. This ties in with the absence of a reliable structural calculation, meaning that the mass trade-off is only an estimation and not a definitive statement. Therefore, any future insulation comparison with other material choices should include a structural analysis to provide fair and accurate trade-offs between the performance parameters. Lastly the insulators are required to be compatible with the structural material and be manufacturable. Any future investigated insulators should also have these considerations investigated as it is key to investigate potential implementable solutions now that the basic operational performance is proven.

7.5. Structural modifications

Structural changes to the vehicle can also provide thermal protection for the vehicle. Namely this section investigates changing the skin thickness to effectively create a heat sink. More material means that more energy can be absorbed per unit area per $[\mathrm{K}]$. Hence the temperature of the vehicle is expected to decrease. The heat sink effect is analysed in this section by increasing the number of layers for the BMI CF material from 5 layers to 6 and 7 layers thick while maintaining the layer thickness. Therefore, the material thickness is increased to 2.856 and 3.332 mm which is a thickness increase of 20 and 40% respectively. Table 7.7 shows the material properties of the heat sink vehicles per unit area of external skin.

Table 7.7.Material properties per unit area for the heat sink simulations from GRANTA (Granta Design Limited, 2020).

	Baseline	20% heat sink	40% heat sink
Minimum thickness $[\mathrm{m}]$	0.00238	0.002856	0.003332
Mass/unit area $[\mathrm{kg/m^2}]$	3.67	4.40	5.13
Specific heat capacity per unit area $[\mathrm{J/m^2K}]$	3464	4156	4849

Figure 7.22 shows the temperature results along the Sonneveld (2021) mid-energy trajectory for the external surface at a number of vehicle locations for the three vehicle skin thicknesses. The results show that the larger material thickness structures have a slower response to temperature changes. This means that adding material thickness results in lower peak temperatures. The external skin temperature decrease ranges from 30 to 70 K, which shows that it has a positive effect on the cooling of the external surface. While saying that, it comes at a significant mass penalty, making the mass trade-off between BMI CF and titanium negligible.

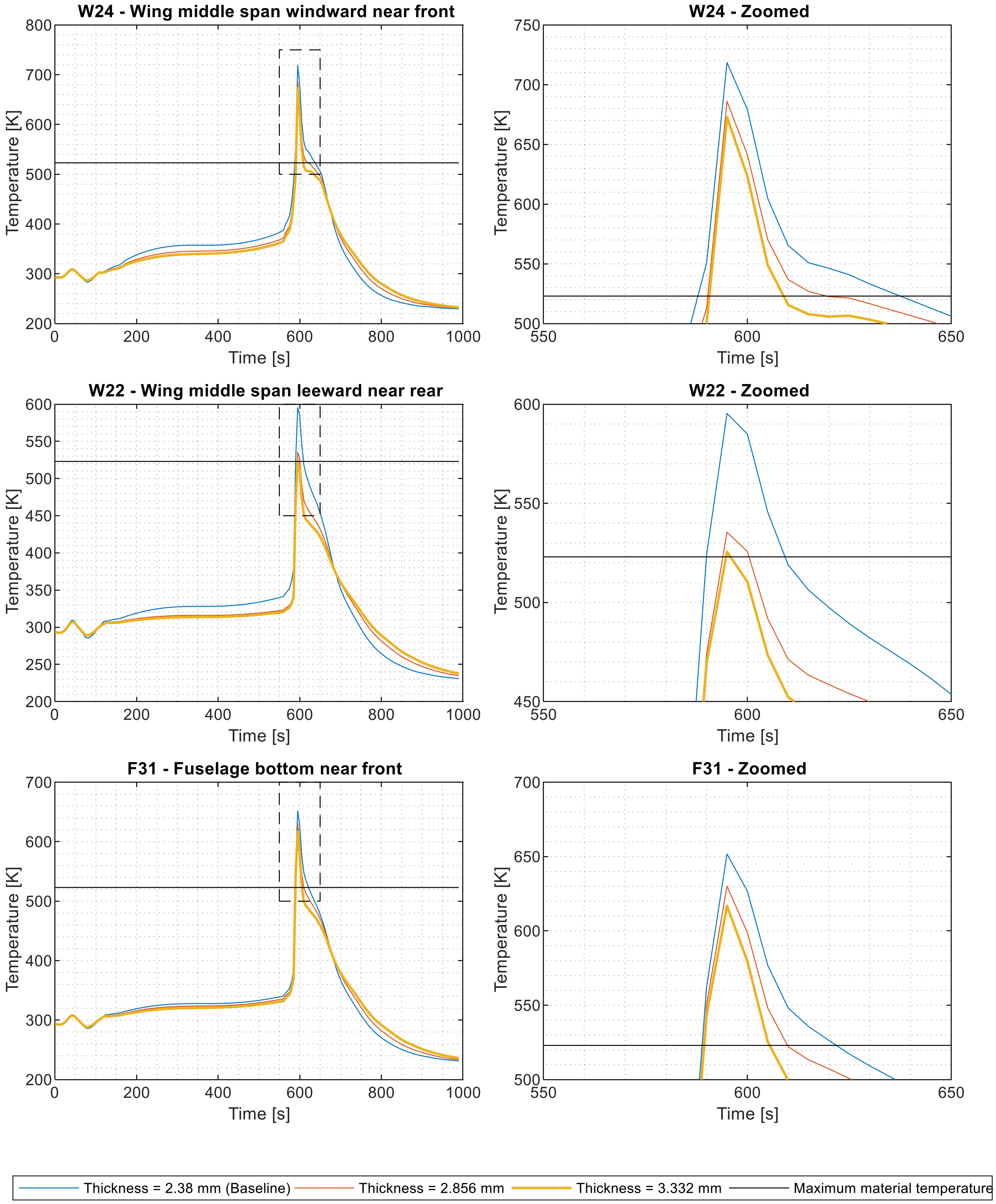

Figure 7.22. Temperature results for different material thickness for the material BMI CF for the Sonneveld (2021) mid-energy trajectory.

As well as the external skin temperature decreasing with added material, the internal temperature distribution within the vehicle skin also changes. Figure 7.23 and Figure 7.24 show the temperature results for the vehicle mesh nodes at the W22 and F31 locations respectively. These figures show two things. Firstly, the more internal layers have a lower maximum temperature compared to the more external layers. Secondly, internal layers react to temperatures with a small time delay, with the more internal layers having a larger delay. This is understandable given that the heat flux into and out of the vehicle is at the external surface, after which the heat propagates through conduction to the internal portions of the structure. Therefore, the external layers of the vehicle will experience temperature changes from the flow before the internal layers.

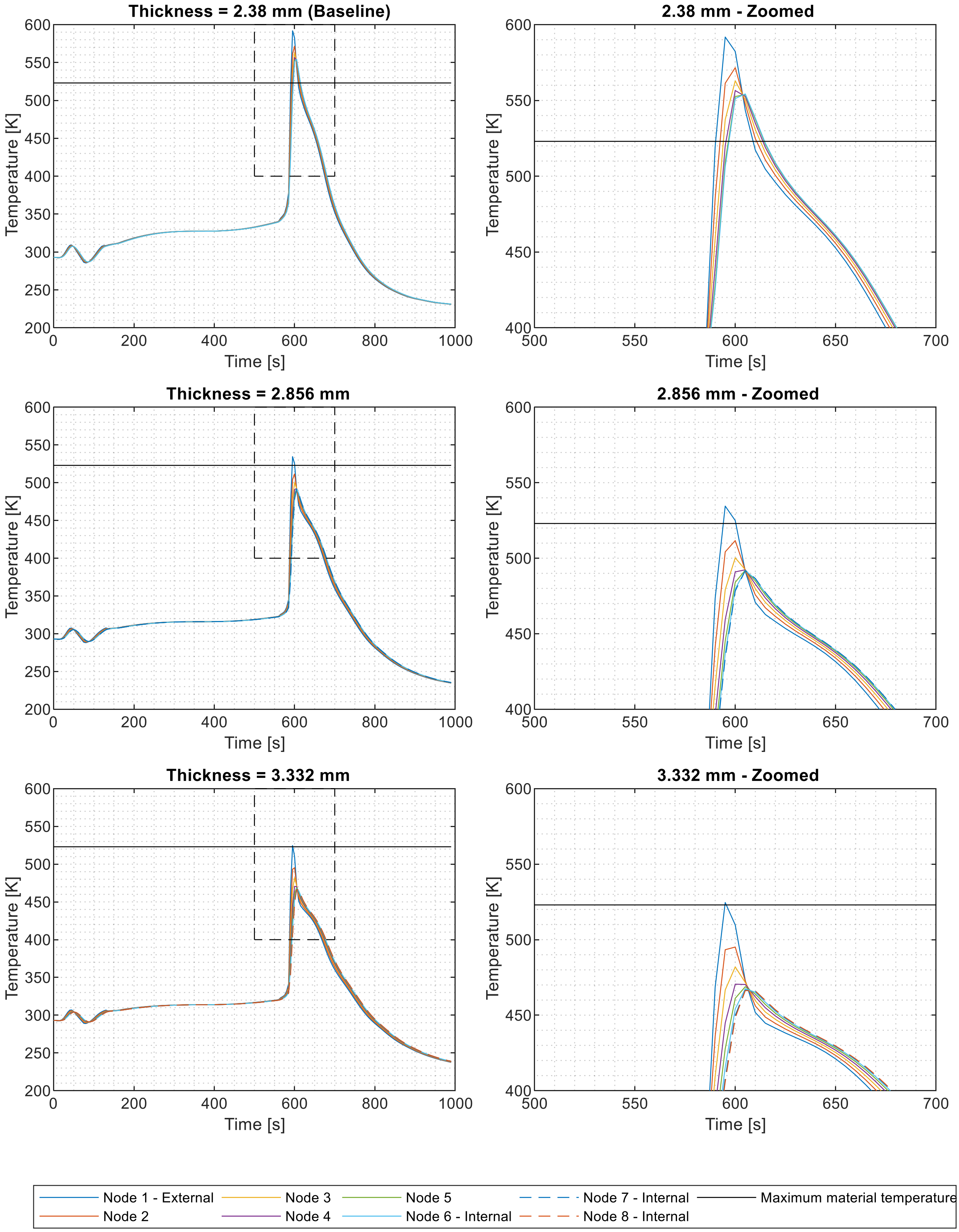
Thickness = 2.38 mm (Baseline)

2.38 mm - Zoomed

Thickness = 2.856 mm

2.856 mm - Zoomed

Thickness = 3.332 mm

3.332 mm - Zoomed

Figure 7.23. Vehicle node temperature results at the W22 wing middle span leeward near rear location in the normal direction to the skin for different BMI CF material thicknesses along the Sonneveld (2021) mid-energy trajectory.

A key finding in Figure 7.22 is that the W22 location has a large external surface temperature jump compared to the other locations shown in the figure. Figure 7.23 and Figure 7.24 show that although the temperature distribution of the external surface layers does not change by the same amount, the internal layers do. For the W22 location the maximum internal layer temperature decreases from 555 to 465 K and for the F31 location it decreases from 600 to 530, both of which is around the same difference. This means that the larger difference in external temperature change for material thickness

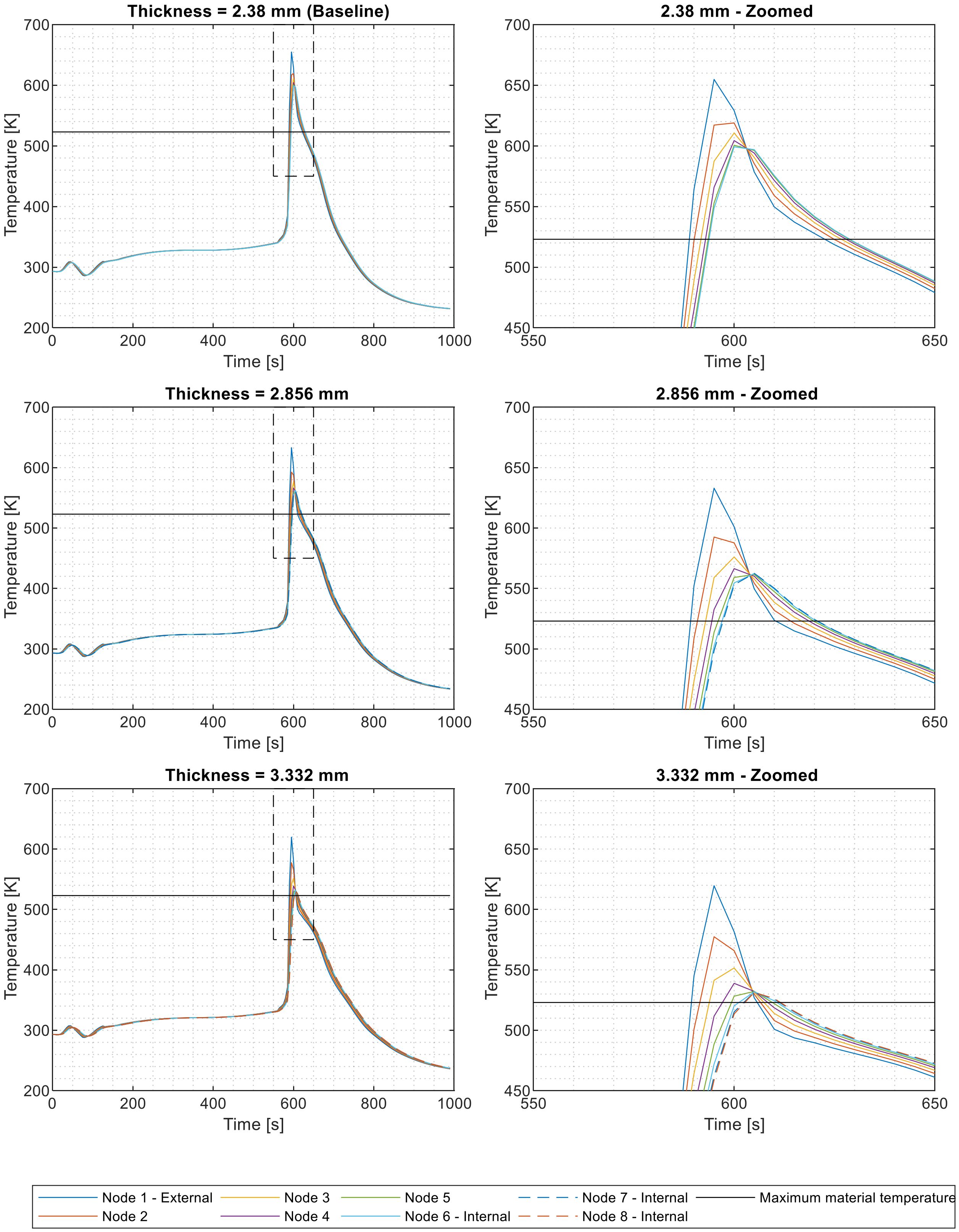

Figure 7.24. Vehicle node temperature results at the F31 fuselage bottom near front location in the normal direction to the skin for different BMI CF material thicknesses along the Sonneveld (2021) mid-energy trajectory.

between these two locations is primarily in the external layers of the surface. The core reason behind this phenomenon was not uncovered and further investigation is required. However, this phenomenon is solely confined to the lower temperature sections of the vehicle. This means it is not a design driving area of the vehicle and does not influence the decisions and findings for this thesis' research questions.

Another observation to both Figure 7.21 and Figure 7.22 is that the difference between internal and external surface node location becomes larger for thicker skins. This effect can be attributed to the increased thickness of the material, while the thermal conductivity coefficient remains constant. This means the temperature gradient remains roughly the same, but the thickness means the energy has to travel a further distance, hence causing a larger temperature difference.

This study into the use of the skin material as its own heat sink has shown that there is potential for the absorption of energy within a larger volume to decrease the temperature of the skin. However, this method comes at a large mass penalty bringing into question why titanium shouldn't be used over the BMI CF. If the mass of these two choices is similar, then thermodynamically the titanium has an assurance that it won't reach its maximum operating temperature. Titanium also won't cause other issues such as joining of two different materials. To answer if there is a noticeable mass difference between the two solutions, a better structural analysis is required which would require a future analysis.

8. Sensitivity

Having created a model to use for simulating the aerothermal behaviour during a trajectory of the Mk-III and using this to analyse the research questions has been the key goal of this thesis. However, creating a new model requires great understanding of the limitations and sensitivity of this model. The model description in Chapter 5 describes a large number of the limitations originating from the numerical methods used. Chapter 6 attempts to validate the model and thereby quantify these limitations by comparing the model results with known flight and other simulation data. Both these sections don't fully analyse the implication of model sensitivities, which is the effect on the final result due to changes in the input. If there are parameters to which the model is sensitive to, it means that to get accurate results we require accurate predictions of these parameters. This section will describe and analyse the sensitivities of the model used in this thesis.

8.1. Sensitivity in previous chapters

The sensitivity study has already been partially conducted within Chapter 7. This chapter will link the results in Chapter 7 to the sensitivity study and explain the effect of these sensitivities.

The research questions attempt to address the aerothermodynamic concerns currently of importance to the Mk-III spaceplane. Because of the design stage of the Mk-III these questions, primarily the main research question, accepts the broad range of potential uncertainties in the mission. These uncertainties in the design are uncertainties that carry on as input to the model and therefore become sensitivities. Therefore, for a number of model sensitivities, data from the research questions in Chapter 1 can be used.

8.1.1. Trajectory

The 'various trajectories' stated in the primary research question and chosen in Section 2.2 are a sensitivity parameter analysed in Section 7.2. One of the largest uncertainties due to the conceptual stage of the vehicle is the expected trajectory the Mk-III will fly. The chosen trajectories from the larger available simulated trajectories cover a range which includes maximum altitudes between 200 to 300 km and maximum velocities between 1.7 to 2.2 km/s. This signifies a reasonable amount of uncertainty in the amount of energy the vehicles will have upon re-entry. The third element which defines the trajectory, angle of attack, has a smaller effect on the amount of energy but does influence where the stagnation point is. The nine chosen trajectories also have different angles of attack ranging primarily from 0 to 10 degrees.

Having identified that the chosen trajectories hold three key sensitivity parameters, the figures in Section 7.2 show the sensitivity of these parameters. Firstly, the altitude and velocity are highly linked to each other. Primarily the vertical velocity and the altitude due to the transformation of potential energy from the altitude to kinetic energy from the velocity and vice versa. The horizontal velocity remains relatively constant during the ascent, coasting and re-entry, except for the boostback trajectories but is still of similar magnitude for all trajectories. What the figures in Section 7.2 primarily show is that the maximum temperature at all locations follow the same trend as the maximum altitude and velocity of those trajectories. A higher maximum altitude and velocity results in a higher maximum temperature. This range in maximum temperature can be up to a few hundred $[\mathrm{K}]$ at the stagnation point but is highly dependent on the location of the vehicle. Temperatures of cooler sections of the vehicle don't vary as much, but still vary by more than a 100 $[\mathrm{K}]$ when changing the trajectory. Therefore, the trajectory altitude and velocity are sensitive parameters of the model.

The angle of attack is a harder parameter to model the sensitivity of within the chosen trajectories, due to the large effects from the altitude and velocity, as well as the more random behaviour of the angle of attack. The angle of attack parameter has a large influence on the altitude and velocity through the trajectory simulations. It affects the aerodynamic properties, which have an influence on the rate of ascent and descent, the amount of energy lost by drag and therefore the altitude and velocity at which maximum heating occurs. Hence, the aerothermal behaviour of the Mk-III is affected by the angle of attack indirectly through the trajectory simulations, which are accounted for by the altitude and velocity trajectory data. The second effect the angle of attack has, is the effect on the location of the stagnation point and local coefficient of pressure. This means that if the angle of attack changes, the aerodynamic heating will change slightly for a local vehicle location, but looking at the vehicle on a whole will only cause that heating to shift to a different location. The angle of attack between the trajectories varies through a range of roughly 0 to 10 degrees, meaning location changes are only small. Changing the stagnation point location won't have an effect on the material choice not already covered by the altitude and velocity. Therefore, it does not influence the answering of the research questions and goals of this thesis.

The trajectory has been identified as holding some key sensitivity parameters for this model. It is uncertain that the Mk-III at any stage in its design process may decrease this uncertainty, due to the simple fact that it will be designed to hold a variety of payloads that may need to go into different orbits. Therefore, these parameters are key to understanding the sensitivities of the model, but will result in the most extreme trajectory being chosen for future aerothermodynamic design.

8.1.2. Material

Sub-research-questions 1 and 2.4 concern themselves with changing materials, material properties and material thicknesses. Each of these parameters themselves is a sensitivity parameter that has been evaluated in Section 7.2.5.

The material properties can vary widely depending on the chosen material. Key properties that are important for thermal purposes are the density, specific heat capacity and thermal conductivity. The chosen materials shown in Table 2.1 and Table 7.5 show that these properties vary widely between the four materials selected for this thesis, meaning that this thesis is able to display the variation these properties hold. Figure 7.13 and Figure 7.14 show the results of comparing these different materials and Section 7.2.5 has described what material properties are affecting the different phenomenon. It is shown that the specific heat capacity in conjunction with the density and material thickness has an observable impact on the temperature of the vehicle skin. This sensitivity study shows that the material properties should be accurately modelled to ensure the simulations are representable of the true vehicle.

The material thickness of the vehicle skins has been calculated by a simple structural analysis described in Section 2.4. These thicknesses were varied to act as a heat sink for answering research question 2.4 in Section 7.5. The analysis shows that there is an observable effect of adding material thickness in the order of a few 10's of $[\mathrm{K}]$ per 20% thickness increase. Although material thickness variations are always present in any manufacturing process, it is unlikely that these are going to be equivalent to larger variations than 20% of the material's thickness. This is particularly true given the application and the cost of excessive mass while ensuring structural requirements are met. Therefore, this parameter is going to affect the maximum temperature of the vehicle, but not to an extend that it is likely to cause a structural material change. If there was a material change required due to the material thickness sensitivity, then this points to problems in the analysis and design such as improper safety factors.

8.1.3. Shape

The last sensitivity parameters that have already been covered in this thesis are the parameters that are associated with shape. For thermodynamics and the Mk-III shape this primarily refers to leading edge radii and sweep angles of the wing. These two parameters have not been part of a research question but have in part been covered in Chapter 5 by the equations. The other shape parameters of the vehicle are not covered in this discussion as they do not influence the thermodynamics in a way that influences the TPS. Parameters such as surface angles change the local conditions, but not the overall conditions of the vehicle.

The leading edge radius is linked to the thermodynamics of the leading edge by Eq. 5.21. This equation shows that the heat flux of the vehicle is inversely proportional to the square root of the leading edge radius. This means if the leading edge radius is increased, the heating rate of the leading edge is decreased. Therefore, the leading edge can be expected to have a lower temperature. It cannot be assumed that the relationship between the leading edge radius and the maximum temperature will also be square root inversely proportional but it can be used as a rough approximation. The reason for this approximation not being 100% accurate for the temperature, is because if the heating rate is lower, than the temperature difference between the flow and structure becomes larger, therefore slightly increasing the heating rate again. This would therefore counteract some of the lower heat flux by the convection coefficient.

The impact of the leading edge wing sweep is not as large and direct as that of the radii, but does impact the recovery enthalpy in Eq. 5.15. This equation shows that the wing sweep can have an impact on the amount of kinetic energy from the flow being converted to thermal energy in the boundary layer. This directly influences the amount of energy being transferred, as the recovery enthalpy is used for the difference in flow enthalpy and wall enthalpy in the heat flux calculation. Again, though this sensitivity parameter can be traced without doing a simulation and is likely not going to a deciding factor in the TPS choice given the importance of aerodynamic performance for the entire mission.

8.2. Laminar - Turbulent

As has already been identified during the model validation in Section 6.3.1, the simulation results are highly dependent on whether the flow is laminar or turbulent. This section will repeat the same analysis but for the Mk-III given that the trajectory is different to that of the X-15.

The results of simulating a fully turbulent or laminar case are compared to the implemented turbulent-laminar transition model in Figure 8.1. The first notable trend is that during the first ~50 [s] of flight and last ~400 [s] of the flight time analysed, the temperature trends follow the fully turbulent model. In between these two times, which consists of the later portion of the ascent, coasting and initial re-entry, the temperature trends follow the laminar temperature results. Figure 8.2 shows that the reason for this is due to the transitioning model used and that all three locations all transition at roughly the same flight time between laminar and turbulent. As discussed in Section 6.3.1, the trajectory from the Mk-III was expected to be similar to flight test 1 of the X-15 in the sense that both would have a parabolic flight path. Both these flight paths result in a sharp decrease of the local Reynolds number at all vehicle locations and hence a clear transitioning point for the laminar-turbulent transition.

As has been discussed, the transition between laminar to turbulent occurs during the re-entry of the Mk-III just before the 600 [s] mark for the Sonneveld (2021) mid-energy trajectory analysed for this sensitivity study. What Figure 8.1 shows is that this results in the maximum skin temperature of the vehicle being in between the maximum skin temperature observed in the fully laminar and fully turbulent cases. This is caused by the material starting off at a lower temperature due to the laminar flow during the coasting, but transitioning to turbulent flow during the high heat flux portion of the flight. The limits of the fully laminar and turbulent case therefore provide important limits for what the vehicle could potentially experience. The simulated transitioning model could vary from the current estimate due to a variety of factors that could influence when the laminar-turbulent transition occurs. However due to the sudden increase of Reynolds number during re-entry it is unlikely that the time at which transition occurs will vary hugely.

Figure 8.2 shows the Reynolds number along the trajectory at a selection of vehicle locations. These Reynolds numbers can, in the figure, be visually compared to the transition Reynolds number. If the Reynolds number is above the transition Reynolds number, then the flow is turbulent, else it is laminar. Figure 8.2 shows that for certain vehicle locations the fully turbulent temperature profile experiences multiple peak temperatures during the coasting portion of the flight. For this particular application this is actually not an important feature, because the Reynolds number during this portion of the flight is well below the transition Reynolds number, meaning that it is unlikely to transition to turbulent flow. It is however a very interesting feature, likely caused by a combination of the periods of flight where maximum velocity occurs, changes of the angle of attack during flight and the changing atmospheric properties.

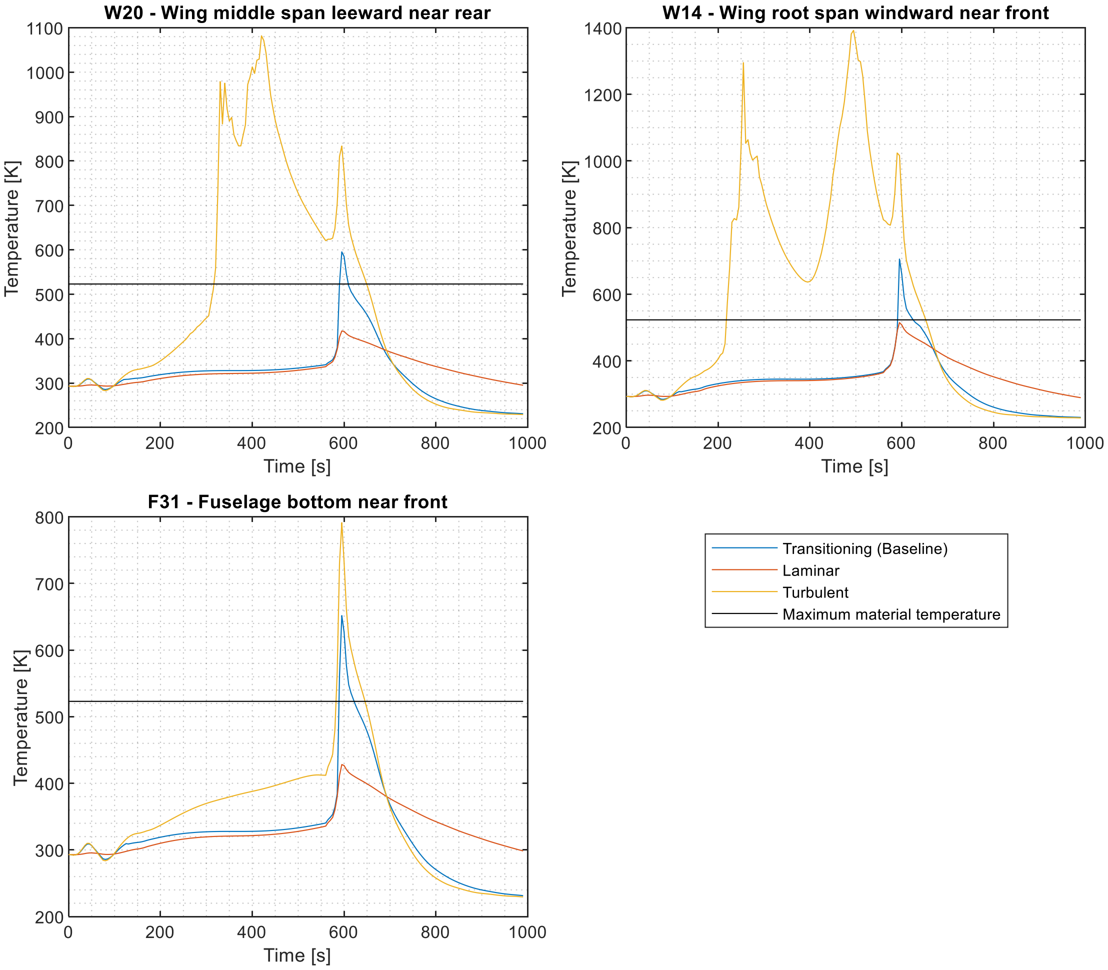

Figure 8.1. Temperature history of a turbulent, laminar and transitioning model simulation for the Sonneveld (2021) mid-energy trajectory.

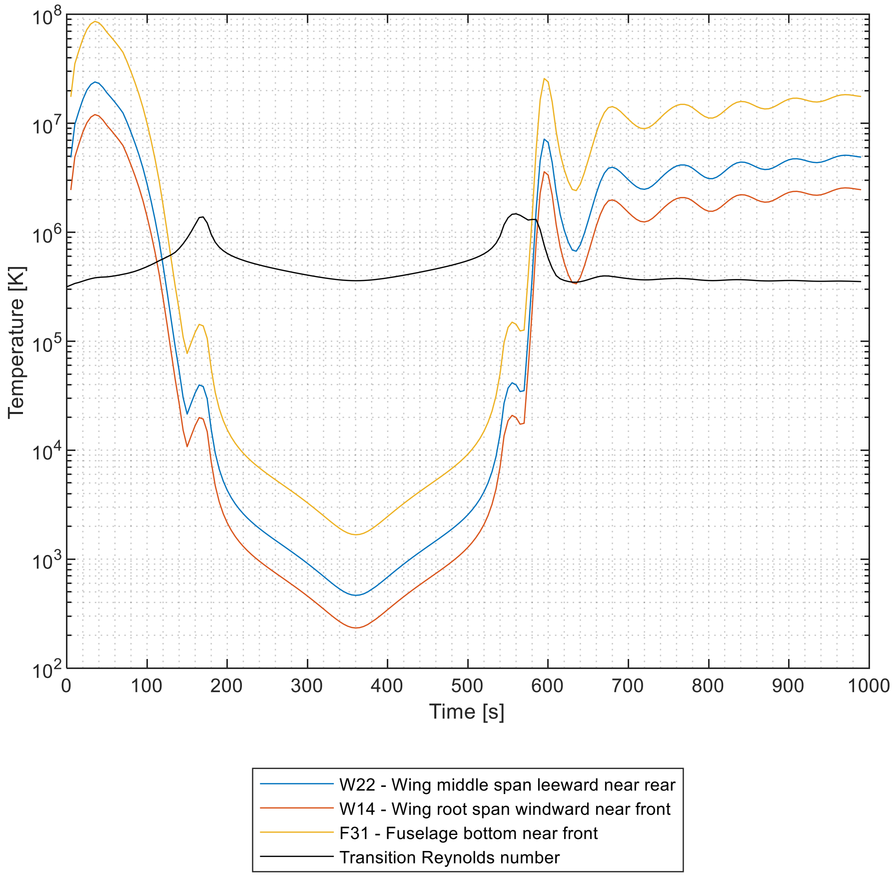

Figure 8.2. Sonneveld (2021) mid-energy trajectory Reynolds number at different vehicle locations and the transition Reynolds number.

9. Conclusions and Recommendations

An aerothermodynamic model has been used to analyse the Dawn Aerospace Mk-III spaceplane concept. This spaceplane is part of a horizontal take-off and landing launcher concept, aimed at launching small satellites by means of a first stage spaceplane and second stage rocket integrated into the existing aerospace. Operating the Mk-III spaceplane (Mk-III) as an aeroplane means this concept has a unique mission resulting in a unique aerothermodynamic analysis. The aerothermodynamic model explained in this thesis, in Chapter 4 and 5, is used to answer the research questions in Chapter 7. From these results a number of conclusions can be drawn that are useful for the Mk-III design and will be explained in Section 9.1. This thesis is only the initial aerothermodynamic analysis for the Mk-III concept aimed at exploring the design space. Therefore, recommendations for future research and development is given in Section 9.2.

9.1. Conclusion

The conclusions of the research questions analysed in Chapter 7 are explained here. The research questions are answered by using the results from Chapter 7 while incorporating uncertainties discussed in the sensitivity study and taking into consideration the limitations of the model itself. The sub-research-questions stated in Chapter 1 are designed to answer aspects of the primary research questions. Therefore, first the two sub-research-questions will be discussed and used to conclude the primary research question.

9.1.1. Sub-research-question 1

What material choices would be suitable to implement on the Mk-III spaceplane for the range of different design trajectories.

Four materials were analysed in Section 7.2; BMI CF, SiC CF, titanium and aluminium. Comparing these four materials for a single trajectory showed that the specific heat capacity per unit surface area of each material may cause variations of the maximum temperatures ranging to more than 200 K. The specific heat capacity per unit surface area of a material is dependent on both the specific heat capacity of the material and the material thickness. The higher this value, the lower the maximum material temperature and the slower the heating and cooling of the material. The BMI CF and titanium having a similar low specific heat capacity per unit surface area means that they exhibit the highest temperatures and fastest response to heat flux. The aluminium on the other hand acts as an effective heat sink, caused by the high specific heat capacity per unit surface area, therefore having lower maximum temperatures along the trajectory.

The trajectories chosen can have a considerable influence on the temperature profile of a material. The highest and lowest trajectory analysed can produce maximum temperature differences of around 400 K. Therefore, if a material is on the edge of thermal capability, then trajectory limitations can play a role in the design of the vehicle. At this stage of the vehicle design it is uncertain which design criteria will be leading, given that increased trajectory capability can bring in a significant amount of revenue and market share. On the other hand, thermally requiring to always achieve a high trajectory may come at a mass penalty, due to different material choices or larger TPS. Therefore, it could also be that different sub-vehicles with different TPS designs can be manufactured to minimize operational costs for specific trajectories. Therefore, this is definitely a design consideration but not suitable for a trade-off at this stage in the design.

Titanium is the only material analysed that, without a thermal protection system (TPS), can withstand the temperatures experienced by the vehicle at every location of the vehicle for every trajectory analysed. According to the structural thickness calculations it is also the second lightest option. Therefore, investigating this problem from solely a thermal and mass point of view, titanium is a reasonable choice for the vehicle's hot regions. The only material lighter than titanium is the BMI CF, which, without a TPS, could not withstand the temperatures of the non-leading edge sections of the vehicle for any trajectory. According to the structural calculation used in Section 2.4 the mass saving could be upward of 30% if BMI CF was used for the entire vehicle. However, without a TPS this material choice would not meet the thermal requirements. This is why the BMI CF is recommended as the analysed material for sub-research-question 2.

Any material selection for a vehicle that attempts to be at the forefront of engineering will pose design problems. Combining a composite with a metal would be expected to pose more engineering problems than a single material choice. The primary issue with these materials would be in joining the two types of materials together. A composite and metal are rarely compatible for a glue joint so this would need to be specifically designed for. Also manufacturing two material classes would mean two different types of manufacturing methods, which could add up to higher manufacturing costs. The BMI CF and titanium material combination are however not completely incompatible. In terms of their thermodynamic behaviour, Section 7.2.5 shows that both have a similar thermal profile along the trajectory. This helps, given that the thermal expansion ratio of both materials is also within 25% of one another. Lastly, due to the inertness of titanium, galvanic corrosion between the materials is not an issue that requires consideration (Yari, 2021).

The two other materials, SiC CF and aluminium, both, in terms of mass, cannot outperform titanium or BMI CF. Therefore, these two materials are not recommended for further study unless more comprehensive structural calculation inform the design being lighter.

9.1.2. Sub-research-question 2

How can a thermal protection system extend the trajectory operating range of a structural material choice from sub-question 1?

Four different types of TPS were modelled for the BMI CF material analysed in Section 7.2.1; active cooling, radiative coating, insulation and heat sink. These options were analysed for a TPS on the non-leading edge sections of the vehicle. The active cooling comes in the form of the nitrogen, used as pressurant for the fuel and oxidizer tanks cooling the inside of the vehicle skin for a small period of time during re-entry. The coating TPS would influence the emissivity coefficient for radiative cooling. The insulation would add an insulator on the external surface of the vehicle, providing heat flow resistance between the flow and the structural material. The heat sink TPS was investigated in this thesis by means of thicker structural material, thereby increasing the specific heat capacity per unit surface area of the structure.

For the active and radiative cooling TPS, the conclusion is that they are ineffective for the Mk-III mission. The active cooling can only provide a heat flux up to 1% compared to the heat flux convection produces. The radiative cooling does influence the temperature profile along the trajectory, but does not influence the material temperature sufficiently to protect the structure and therefore thermally does not need to be designed for. This is caused by the radiative cooling being related to the temperature to the power of four and the temperature not being large enough for it to be effective compared to the convective heat flux.

The heat sink TPS does have an impact on the maximum temperature experienced by the material, but is not recommended for future studies. If suitably designed, a heat sink could be TPS that thermally meets the requirements. However, none of the solutions investigated in this thesis were able to achieve this, though did demonstrate the capability. The issue with this type of TPS is mass. The heat sink was tested up to a point where the mass of the BMI CF structure would be the same as that of the titanium structure. Having to go beyond this to meet the thermal requirements, means that titanium would be the better option from a mass perspective.

Adding an insulator to the external surface of the BMI CF structure was the only TPS that is predicted to be able to thermally meet the Mk-III requirements, as well as remain the lowest mass option for the non-leading edge sections of the vehicle. Section 7.4.2 shows that the 1 mm insulation layers tested were able to lower the maximum temperature experienced by the BMI CF structure by 50 to 70 K. Increasing this insulation layer by 4 to 5 times has potential of meeting the thermal requirements for BMI CF. For the low-density insulators this would still mean the structure would remain below the mass of the titanium structure. It is recommended that in future analysis this option in investigated further. Thicker insulators were purposefully not investigated in this thesis because of the uncertainty around the mass calculation of each material and TPS structure. Therefore, the capability was demonstrated and future research can use this to do a more detailed analysis.

9.1.3. Primary research question

What thermal protection systems have potential to be implemented on the Dawn Aerospace Mk-III spaceplane for a range of different design trajectories.

From the two sub-research-questions there are two recommended TPS that are suitable for the Mk-III.

Firstly, a fully titanium spaceplane will be able to fully meet all the thermal and mission requirements for the Mk-III. Thermally, the maximum temperature of titanium will not be reached by any vehicle element, even accounting for the uncertainty of the model. Therefore, this is the safe choice for the vehicle.

The alternative recommendation is a combination of titanium and BMI CF, where the BMI CF has an insulation layer. BMI CF could be applicable to the non-leading edge sections of the vehicle if a suitable TPS can be designed by means of an insulation layer. The insulator TPS was investigated in sub-research-question 2 and was deemed the only suitable TPS that both meets the thermal performance requirements and could be of lower mass than the titanium solution. For the leading edge titanium would still be required, as BMI CF cannot be protected against the high temperatures in this region. This material combination choice can be performance wise more beneficial, though would be expected to engineering wise be more complicated due to the two materials being of different class. This could pose engineering problems in the form of manufacturing methods, costs and joining.

All other material choices investigated either did not meet the thermal requirements or were heavier than these two solutions.

9.2. Recommendations

A number of new research topics have been identified during the design and use of the model created in this thesis. The new topics identified are structural analysis, CFD analysis, integration of structural analysis, variable time step and a different integration method. Although the aerothermodynamic analysis in this thesis is complete, it is recommended that the structural and CFD analysis are completed before any future aerothermodynamic analysis is done. These analyses will allow for a better mass trade-off between the different TPS solutions and allow for more accurate results to be analysed to ensure model error is not influencing the design decisions.

9.2.1. Structural analysis

One of the largest uncertainties introduced in this thesis is the required skin thickness. Section 2.4 introduces and explains the simple structural model, used to estimate the material skin thickness required for each material to meet the vehicle's structural loads. This analysis is by no means an inclusive structural analysis and only aims to provide an even structural strength for each vehicle. Therefore, there is significant improvement in this field.

The aims of a structural analysis from an aerothermodynamic point of view would be to get a better approximation of the material thicknesses for the two potential TPS and get an estimate of their masses. This would mean the aerothermodynamic analysis from this thesis can be re-done, based on the updated structure and a real trade-off can be made between their thermal performance and performance from a mission point of view.

This thesis has identified the structural analysis as a required improvement for a future aerothermodynamic analysis. Without it, a proper trade-off, a decision cannot be made between materials that performance wise appear close to each other. Material thickness has also been seen to have an impact on the temperature of the vehicle, meaning that a more accurate prediction of this could influence the material choice from a thermal point of view.

9.2.2. CFD

At the start of the thesis the aim was to design a secondary model which replaces the engineering methods for predicting flow-based heat flux with a CFD model. This was not completed due to issues with the program itself, particularly within the coupling between the structural and flow simulators. The errors were unrelated to the accuracy of the flow and structural simulations but rather due to the communication between the two programs. The issue has been passed on the program provider's help desk but no solution has yet been found and it is currently still actively being investigated. For the thesis the CFD was deemed unnecessary for answering the research questions so is a recommendation for future work.

The accuracy of implementing a CFD model is expected to be high due to being able to account for the more complex flow around the spaceplane. This accuracy comes at the expense of time. This simulation would therefore complement the existing simulation from this thesis. Joining the two would allow the accuracy of CFD and the larger amount of data from engineering methods to be used together to create a large but accurate analysis without the extreme time cost.

It is recommended that this analysis is also developed prior to future aerothermodynamic analysis. The current analysis is sufficient for the current stage of the Mk-III design process. However, future design stages will require higher accuracy and assurance in the aerothermodynamic analysis.

9.2.3. Integrate structural analysis

Unlike the detailed structural analysis, this research package would look into integrating the structural analysis into the existing model. ANSYS mechanical is capable of doing a structural analysis, as well as a thermal analysis. Changing the input file settings and importing forces from the aerodynamic pressure calculations can be a crude but quick structural analysis.

The pressure predictions in the engineering methods are suitable for high supersonic flights, which is where most thermodynamic heating occurs. For a structural analysis, the question then arises whether this would be useful. Maximum loading can occur both during re-entry or during take-off/landing which means that this structural analysis would only remain a prediction, rather than provide conclusive results from which design decisions can be made. This type of structural analysis also doesn't capture potential more complex loading on the wing. Nonetheless, it is recommended that this is implemented due to the expected ease of implementation.

This type of structural analysis could also be implemented together with the CFD improvement, which could result in more accurate loading conditions, also for lower speed sections of the trajectory.

9.2.4. Variable time step

A conscious decision was made that a constant time step would be used in this thesis. However, the results show that heat flux changes happen slowly, except during re-entry. A constant time step for the entire trajectory is not an effective method of integrating over the trajectory. It is therefore recommended that a variable time-step method is introduced, which calculates the heat flux change and adapts the time-step based on the result. This should decrease simulation time meaning that more accurate meshes could be used without excessive simulation time.

9.2.5. Integration method

Currently the integration of temperature along the trajectory due to the heat flux is done based on Euler's method. This method is a simple method to implement but there are other integration methods that are more efficient in terms of the simulation time. It is recommended that future analysis investigate the use of higher order integration methods in order to decrease simulation time or produce higher accurate results for the same simulation time.

References

Adrian, D. (2007). *Course Material for 10.37 Chemical and Biological Reaction Engineering.* Retrieved from Massachusette Institute of Technology: https://ocw.mit.edu/courses/chemical-engineering/10-37-chemical-and-biological-reaction-engineering-spring-2007/lecture-notes/biot_numbers.pdf

Anderson, J. D. (2006). *Hypersonic and high-temperature gas dynamics.* American Institute of Aeronautics and Astronautics.

ANSYS Inc. (2006). *Modelling Turbulent Flows. Introductory FLUENT Training.* Retrieved from http://www.southampton.ac.uk/~nwb/lectures/GoodPracticeCFD/Articles/Turbulence_Notes_Fluent-v6.3.06.pdf

Baldwin, B., & Lomax, H. (1978). Thin-layer approximation and algebraic model for separated turbulentflows. *16th aerospace sciences meeting*, (p. 257).

Banas, R. P. (1965). *Comparison of Measured and Calculated Turbulent Heat Transfer in a Uniform and Nonuniform Flow Field on the X-15 Upper Vertical Fin at Mach Numbers of 4.2 and 5.3.*

Banner, R. D., Kuhl, A. E., & Quinn, R. D. (1962). *Preliminary results of aerodynamic heating studies on the X-15 airplane.* National Aeronautics and Space Administration.

Baranowski, L. (1971). Influence of Cross-Flow on Windward Centerline Heating. *McDonnell Douglas Astronautics Co., Rept*, E0535.

Barth, T. (2008). Aero-and thermodynamic analysis of SHEFEX I. *Engineering Applications of Computational Fluid Mechanics*, 76-84.

Barth, T., & Longo, J. M. (2010). Advanced aerothermodynamic analysis of SHEFEX I. *Aerospace Science and Technology*, 587-593.

Boehrk, H. (2014). Transpiration cooling at hypersonic flight-AKTiV on SHEFEX II. *11th AIAA/ASME Joint Thermophysics and Heat Transfer Conference*, (p. 2676).

Conner, M. (2017). *Orbital Sciences Corporation X-34.* Retrieved from https://www.nasa.gov/centers/armstrong/history/experimenatl_aircraft/X-34.html

Connor, N. (2021). *What is Fourier's Law of Thermal Conduction*. Retrieved from Thermal Engineering: https://www.thermal-engineering.org/what-is-fouriers-law-of-thermal-conduction-definition/

Culham, J. R. (2016). *Engineering Courses Online ECE309 Radiation Heat Transfer Lecture Notes.* Retrieved from http://www.mhtlab.uwaterloo.ca/courses/ece309/lectures/notes/S16_chap7_web.pdf

Dawn Aerospace. (2021a). *Dawn Aerospace Wiki.*

Dawn Aerospace. (2021b). *Dawnaerospace.com.* Retrieved from https://www.dawnaerospace.com/

Delft, T. (n.d.). *High Speed Wind Tunnels.* Retrieved from https://www.tudelft.nl/lr/organisatie/afdelingen/aerodynamics-wind-energy-flight-performance-and-propulsion/facilities

Duarte, G., Silva, M., & Castro, B. (2009). Aerodynamic Heating of Missile/Rocket-Conceptual Design Phase. *Proceeding of COBEM 2009, 20th International Congress of Mechanical Engineering.*

Engle, C., & Praharaj, S. (1983). MINIVER upgrade for the AVID system, vol. I: LANMIN User's Manual. *NASA CR-172212*.

Evelyne, R. (2017). Thermal Protection System Analysis and Sizing for Spaceplane Configurations: Preliminary design of the TPS and optimization of the insulation layer.

Gibbs, Y. (2014). *NASA Armstrong Fact Sheet: X-15 Hypersonic Research Program*. Retrieved from NASA: https://www.nasa.gov/centers/armstrong/news/FactSheets/FS-052-DFRC.html

Gibbs, Y. (2014). *NASA Armstrong Fact Sheet: X-34 Advanced Technology Demonstrator*. Retrieved from NASA: https://www.nasa.gov/centers/armstrong/news/FactSheets/FS-060-DFRC.html

Gigahertz-Optik. (n.d.). *Reflection, Transmission and Absorption.* Retrieved from https://www.gigahertz-optik.de/en-us/basics-light-measurement/light-color/reflec-trans-abs#:~:text=Reflection%20is%20the%20process%20by,electromagnetic%20radiation%20through%20a%20medium.

Gnoffo, P. (1989). Upwind-biased, point-implicit relaxation strategies for viscous, hypersonic flows. *9th Computational Fluid Dynamics Conference*, (p. 1972).

Gnoffo, P. A. (1989). *Conservation equations and physical models for hypersonic air flows in thermal and chemical nonequilibrium.* National Aeronautics and Space Administration, Office of Management, Scientific and Technical Information Division.

Gnoffo, P. A. (1990). An upwind-biased, point-implicit relaxation algorithm for viscous, compressible perfect-gas flows.

Gong, L., Quinn, R. D., & Ko, W. L. (1982). Reentry heating analysis of space shuttle with comparison of flight data.

Granta Design Limited. (2020). GRANTA EduPack. Ansys Inc.

Gupta, R., Lee, K., Zoby, E., Moss, J., & Thompson, R. (1990). "Hypersonic viscous shock-layer solutions over long slender bodies. I-High Reynolds number flows. *Journal of Spacecraft and Rockets*, 175-184.

Haex, T. (2020). *Dawn Aerospace Mk-III: An exploration of cost driven mission scenarios of a winged Two Stage to Orbit semi-Reusable Launch Vehicle integrated in the common airspace.* Delft University of Technology.

Hamilton, H. H., Greene, F. A., & DeJarnette, F. R. (1994). Approximate method for calculating heating rates on three-dimensional vehicles. *Journal of Spacecraft and Rockets*, 345-354.

Hansen, F. C. (1958). *Approximations for the thermodynamic and transport properties of high-temperature air.* National Advisory Committee for Aeronautics.

Harten, A. (1997). High resolution schemes for hyperbolic conservation laws. *Journal of computational physics*, 260-278.

Hassain, M., & Qureshi, M. N. (2013). Prediction of transient skin temperature of high speed vehciel through CFD. *6th International Conference on Recent Advances in Space Technology (RAST)* (pp. 723-728). IEEE.

Husain, M., Jamshed, S., & Qureshi, N. (2012). Transient aero-thermal analysis of high speed vehicles using CFD. *Proceedings of 2012 9th International Bhurban Conference on Applied Sciences & Technology (IBCAST)* (pp. 171-175). IEEE.

Kemp, N. H., & Riddell, F. (1957). Heat transfer to satellite vehicles re-entering the atmosphere. *Journal of Jet Propulsion*, 132-137.

Kleb, W. L., Wood, W. A., Gnoffo, P. A., & Alter, S. J. (1999). Computational aeroheating predictions for X-34. *Journal of spacecraft and rockets*, 179-188.

Ko, W. L., Quinn, R. D., & Gong, L. (1986). Finite-element reentry heat-transfer analysis of space shuttle orbiter.

Ko, W. L., Quinn, R. D., & Gong, L. (1988). Effect of internal convection and internal radiation on the structural temperatures of space shuttle orbiter.

Ko, W. L., Quinn, R. D., Gong, L., Schuster, L. S., & Gonzales, D. (1982). Reentry heat transfer analysis of the space shuttle orbiter. *NASA CP-2216*, 295-325.

Kurganov, V. A. (n.d.). *Adiabatic wall temperature*. Retrieved from Thermopedia: https://www.thermopedia.com/content/291/

Moeckel, W. E. (1957). *Oblique-shock relations at hypersonic speeds for air in chemical equilibrium.* National Advisory Committee for Aeronautics.

Mooij, E. (2019). *AE4870B - Re-entry Systems: Gliding Entry.*

Moran, M. J., Shapiro, H. N., Boettner, D. D., & Bailey, M. B. (2010). *Fundamentals of engineering thermodynamics.* John Wiley & Sons.

NASA. (1976). *US standard atmosphere.* National Oceanic and Atmospheric Administration.

NASA. (2017). *Space Shuttle.* Retrieved from https://www.nasa.gov/audience/forstudents/5-8/features/nasa-knows/what-is-the-space-shuttle-58.html

NASA. (2017). *X-15 No.1 Rocket-Powered Aircraft.* Retrieved from https://www.nasa.gov/centers/dryden/multimedia/imagegallery/X-15/E-5251.html

National Institute of Standards and Technology (NIST), U. D. (2021). *Isobaric Properties for Nitrogen*. Retrieved from NIST Chemistry WebBook, SRD69: https://webbook.nist.gov/cgi/fluid.cgi?P=1.7&TLow=100&THigh=2000&TInc=10&Applet=on&Digits=5&ID=C7727379&Action=Load&Type=IsoBar&TUnit=K&PUnit=bar&DUnit=kg%2Fm3&HUnit=kJ%2Fkg&WUnit=m%2Fs&VisUnit=Pa*s&STUnit=N%2Fm&RefState=DEF

Pezzella, G., Marini, M., Roncioni, P., Kauffmann, J., & Tomatis, C. (2009). Preliminary design of vertical takeoff hopper concept of future launchers preparatory program. *Journal of Spacecraft and Rockets*, 788-799.

Pezzella, G., Martini, M., De Matteis, P., Kauffmann, J., Dapra, A., & Tomatis, C. (2010). Aerothermodynamic analyses of four reusable launchers in the framework of ESA future launchers preparatory programme. *Aerotecnica Missili & Spazio (J Aerosp Sci Technol Syst)*.

Pezzella, G., Martini, M., Roncioni, P., Kauffmann, J., & Tomatis, C. (2008). Aerodynamic and Aerothermodynamic evaluation of the VTO Hopper concept in the frame of ESA Future Launchers Preparatory Program. *15th AIAA international space planes and hypersonic systems and technologies conference*, (p. 2639).

Prabhu, D. K. (2004). System design constraints-trajectory aerothermal environments. *RTO AVT/VKI lecture series in critical technologies for hypersonic vehicle development*, 14.

Quinn, R. D. (2000). *A method for calculating transient surface temperatures and surface heating rates for high-speed aircraft.* NASA Dryden Flight Research Center.

Quinn, R. D., & Gong, L. (1990). Real-time aerodynamic heating and surface temperature calculations for hypersonic flight simulation.

Reed, R. D., & Watts, J. D. (1961). Skin and structural temperatures measured on the X-15 airplane during a flight to a Mach number of 3.3.

Riley, C. J., & Kleb, W. I. (1998). *Aeroheating Predictions for X-34 Using an Inviscid-Boundary Layer Method.* NASA.

Roe, P. L. (1981). Approximate Riemann solvers, parameter vectors, and difference schemes. *Journal of computational physics*, 357-372.

Schlichting, H., & Gersten, K. (2016). *Boundary-layer theory.* Springer.

Schmitz, K. S. (2017). *Physical Chemistry: Concepts and Theory.* Elsevier Inc.

Schwarz, W. (2019). *Thermal FSI of a Sounding Rocket Through the Atmosphere.* Retrieved from https://www.ansys.com/resource-library/webinar/thermal-fsi-rocket-sound

Simsek, B., Kuran, B., Ak, M. A., & Uslu, S. (2016). Aerodynamic Heating Prediction Tool for a Supersonic Vehicle for Conceptual Design Phase. *46th AIAA Thermophysics Conference*, (p. 4428).

Sommers, A. (2012). How to Calculate the Free Convection Coefficient for Vertical or Horizontal Isothermal Planes.

Sonneveld, V. (2021). *Aerodynamic Design and Analysis of a Two Stage to Orbit Winged semi-Reusable Launching Vehicle.* Delft: Technical University Delft.

Spruijt, M. R., & Zandbergen, B. T. (1996). Spaceplane Aeroheating: Some Simple Estimation Methods.

Stillwell, W. H. (1965). *X-15 Research Results: With a Selected Bibliography.* Scientific and Technical Information Division, National Aeronautics and Space Administration.

Van Kesteren, M. (2013). Air Launch versus Ground Launch: a Multidisciplinary Design Optimization Study of Expendable Launch Vehicles on Cost and Performance.

Weihs, H. (n.d.). *SHEFEX – Sharp Edge Flight Experiment.* Retrieved from DLR: https://www.dlr.de/bt/en/desktopdefault.aspx/tabid-4519/7395_read-10112/#/gallery/33955

Wurster, K. E., Riley, C. J., & Zoby, V. E. (1999). Engineering aerothermal analysis for X-34 thermal protection system design. *Journal of Spacecraft and Rockets*, 216-228.

Yari, M. (2021). *Galvanic Corrosion of Metals Connected to Carbon Fiber Reinforced Polymers*. Retrieved from CorrosionPedia: https://www.corrosionpedia.com/galvanic-corrosion-of-metals-connected-to-carbon-fiber-reinforced-polymers/2/1556

Yee, H. C. (1985). On symmetric and upwind TVD scheme.

Young, J., & Crippen, R. (2011). *Wings in orbit: Scientific and Engineering Legacies of the Space Shuttle, 1971-2010.* Government Printing Office.

Zandbergen, B. (2020). TU Delft AE4-S01 Thermal Rocket Propulsion Reader.

Zoby, E. V., & Simmonds, A. (1985). Engineering flowfield method with angle-of-attack applications. *Journal of spacecraft and rockets*, 398-404.

Appendix A. Engineering Methods Air and Atmospheric Model

A.1. Air Model

A.1.1. Air composition and dissociation

The method that will be described here, models high temperature air by assuming dissociation and ionization occurs (Hansen, 1958). Dissociation of air and ionization of air occurs at high temperatures where the oxygen and nitrogen in the air first dissociate into their elemental states and then ionize at even higher temperatures. In the method followed the components of air are $\mathrm{N_2}$, $\mathrm{O_2}$, O, N, $\mathrm{O^+}$, $\mathrm{N^+}$ and $\mathrm{e^-}$.

It should be noted that there are other components to the air (particularly NO) which have been neglected, due to their effect falling within the error of the method. The aim of this method is to make a good approximation of the thermodynamic properties at high temperatures, leading to errors of only a few percent (Hansen, 1958). However, this means that at low temperatures the method becomes higher in error. Low speed and temperature errors are acceptable for this application as the heat transfer increases with temperature. Therefore, an error at lower temperatures has far less effect than the same (percentage) error at high temperatures.

A.1.2. Partition functions

The partition function represents the sum of all possible energies for that system (Schmitz, 2017). Hansen (1958) gives an approximation of the partition function for each of the components within the air. Equations A.1 to A.7 presents these equations in their final approximation form. A note to be made is that the units for pressure in these equations are units of atmosphere.

$$\ln\big(Q(N_2)\big) = \frac{7}{2}\ln(T) - 0.42 - \ln\left(1 - \mathrm{e}^{-\frac{3390}{T}}\right) - \ln(p) \tag{A.1}$$

$$\ln\big(Q(O_2)\big) = \frac{7}{2}\ln(T) + 0.11 - \ln\left(1 - \mathrm{e}^{-\frac{2270}{T}}\right) + \ln\left(3 + 2\mathrm{e}^{-\frac{11390}{T}} + \mathrm{e}^{-\frac{18990}{T}}\right) - \ln(p) \tag{A.2}$$

$$\ln\big(Q(O)\big) = \frac{5}{2}\ln(T) + 0.50 + \ln\left(5 + 3\mathrm{e}^{-\frac{228}{T}} + \mathrm{e}^{-\frac{326}{T}} + 5\mathrm{e}^{-\frac{22800}{T}} + \mathrm{e}^{-\frac{48600}{T}}\right) - \ln(p) \tag{A.3}$$

$$\ln\big(Q(N)\big) = \frac{5}{2}\ln(T) + 0.30 + \ln\left(4 + 10\mathrm{e}^{-\frac{27700}{T}} + 6\mathrm{e}^{-\frac{41500}{T}}\right) - \ln(p) \tag{A.4}$$

$$\ln\big(Q(O^+)\big) = \frac{5}{2}\ln(T) + 0.50 + \ln\left(4 + 10\mathrm{e}^{-\frac{38600}{T}} + 6\mathrm{e}^{-\frac{58200}{T}}\right) - \ln(p) \tag{A.5}$$

$$\begin{aligned}\ln\big(Q(N^+)\big) = {} & \frac{5}{2}\ln(T) + 0.30 \\ & + \ln\left(1 + 3\mathrm{e}^{-\frac{70.6}{T}} + 5\mathrm{e}^{-\frac{188.9}{T}} + 5\mathrm{e}^{-\frac{22000}{T}} + \mathrm{e}^{-\frac{47000}{T}} + 5\mathrm{e}^{-\frac{67900}{T}}\right) - \ln(p)\end{aligned} \tag{A.6}$$

$$\ln\big(Q(e^-)\big) = \frac{5}{2}\ln(T) - 14.24 - \ln(p) \tag{A.7}$$

Where

Q are the partition functions

To estimate the enthalpy both the partition functions for standard states of unit concentration (subscript c) and unit pressure (subscript p) are calculated according to Eq. A.8 and A.9 for each of the elements.

$$Q_c = \frac{p}{RT} Q \tag{A.8}$$

$$Q_p = pQ \tag{A.9}$$

A.1.3. Enthalpy and specific heat for air components

To calculate the enthalpy and specific heat of air, first the enthalpy and specific heat of the components of the air must be calculated. For all components of air, the translational and electronic excitations contribute to the internal energy, enthalpy and specific heat at constant volume and pressure. Equations A.10 to A.13 show the approximate equations for these quantities, where Table A.1 (Hansen, 1958) provides the input variables for all unknowns of each species. For the diatomic molecules ($\mathrm{N_2}$ and $\mathrm{O_2}$) the rotational and vibrational energy must be accounted for. For this the Eq. A.14 and A.15 must be added to Eq. A.10 and A.12 respectively.

$$\left(\frac{E - E_0}{RT}\right)_{t+e} = \frac{3}{2} + \frac{\sum \frac{\epsilon_n}{kT} g_n \mathrm{e}^{-\frac{\epsilon_n}{kT}}}{\sum g_n \mathrm{e}^{-\frac{\epsilon_n}{kT}}} \tag{A.10}$$

$$\left(\frac{H - E_0}{RT}\right)_{t+e} = \left(\frac{E - E_0}{RT}\right)_{t+e} + 1 \tag{A.11}$$

$$\left(\frac{C_v}{R}\right)_{t+e} = \frac{3}{2} + \frac{\sum \left(\frac{\epsilon_n}{kT}\right)^2 g_n \mathrm{e}^{-\frac{\epsilon_n}{kT}}}{\sum g_n \mathrm{e}^{-\frac{\epsilon_n}{kT}}} - \left(\frac{\sum \frac{\epsilon_n}{kT} g_n \mathrm{e}^{-\frac{\epsilon_n}{kT}}}{\sum g_n \mathrm{e}^{-\frac{\epsilon_n}{kT}}}\right)^2 \tag{A.12}$$

$$\left(\frac{C_p}{R}\right)_{t+e} = \left(\frac{C_v}{R}\right)_{t+e} + 1 \tag{A.13}$$

$$\left(\frac{E}{RT}\right)_{r+v} = 1 + \frac{hv}{kT}\left(\mathrm{e}^{\frac{hv}{kT}} - 1\right)^{-1} \tag{A.14}$$

$$\left(\frac{C}{R}\right)_{r+v} = 1 + \left(\frac{hv}{2kT}\right)^2 \left(\sinh\left(\frac{hv}{2kT}\right)\right)^2 \tag{A.15}$$

Where

E is the internal energy per mole $[\mathrm{J/mol}]$
$\frac{\epsilon_n}{k}$ is the electronic energy $[\mathrm{K}]$
g_n is the electronic degeneracy
H is the enthalpy per mole $[\mathrm{J/mol}]$
C_v is the specific heat at constant volume per mol $[\mathrm{J/molK}]$
C_p is the specific heat at constant pressure per mol $[\mathrm{J/molK}]$
$\frac{hv}{k}$ is the vibrational constant

A.1.4. Equilibrium constants

The dissociation of air is a chemical reaction that has an equilibrium quantity of reactants and products based on the state. In an equilibrium state there is a balance between the amount of products and reactants which is dependent on the state of the air (*e.g.* temperature and pressure) (Hansen, 1958), as shown in Eq. A.16. The 'a' in Eq. A.16 represents the reactants and the 'b' represents the products.

Table A.1. Partition Function Constant for the Major Components of Air (Hansen, 1958)

Particle	Molecular weight M [g/mol]	Vibrational constant $\frac{hv}{k}$ [K]	Electronic degeneracy g_n	Electronic energy $\frac{\epsilon_n}{k}$ [K]
N_2	28	3390	1	0
O_2	32	2270	3	0
			2	11390
			1	18990
O	16		5	0
			3	228
			1	326
			5	22800
			1	48600
N	14		4	0
			10	27700
			6	41500
O^+	16		4	0
			10	38600
			6	58200
N^+	14		1	0
			3	70.6
			5	188.9
			5	22000
			1	47000
			5	67900
e^-	1/1820		2	0

$$\sum a_i A_i \rightleftharpoons \sum b_i B_i \qquad \textit{A.16}$$

Where

a is the stoichiometric reaction coefficients of the reactants
A is the reaction components in the chemical reaction
b is the stoichiometric reaction coefficients of the products
B is the product components in chemical reaction

To determine the amount of products and reactants the equilibrium constant is used. There are four chemical reactions that are considered within this model of air. These are

$$O_2 \rightleftharpoons 2O \qquad \textit{A.17}$$

$$N_2 \rightleftharpoons 2N \qquad \textit{A.18}$$

$$O \rightleftharpoons O^+ + e^- \qquad \textit{A.19}$$

$$N \rightleftharpoons N^+ + e^- \qquad \textit{A.20}$$

The equilibrium constants for each of these reactions are approximated by Eq. A.21 to A.24.

$$\ln\left(K_p(O_2 \to 2O)\right) = -\frac{59000}{T} + 2\ln\left(Q_p(O)\right) - \ln\left(Q_p(O_2)\right) \qquad \textit{A.21}$$

$$\ln\left(K_p(N_2 \to 2N)\right) = -\frac{113200}{T} + 2\ln\left(Q_p(N)\right) - \ln\left(Q_p(N_2)\right) \qquad \textit{A.22}$$

$$\ln\left(K_p(O \to O^+ + e^-)\right) = -\frac{158000}{T} + \ln\left(Q_p(O^+)\right) + \ln\left(Q_p(e^-)\right) - \ln\left(Q_p(O)\right) \qquad \textit{A.23}$$

$$\ln\left(K_p(N \to N^+ + e^-)\right) = -\frac{168800}{T} + \ln\left(Q_p(N^+)\right) + \ln\left(Q_p(e^-)\right) - \ln\left(Q_p(N)\right) \qquad \textit{A.24}$$

Where

K_p is the chemical equilibrium constant for pressure units

For the calculation of thermal conductivity the logarithmic derivatives of the equilibrium constants are required. Using the initial chemical equation and Eq. A.25 to A.28 the derivatives are defined for each of the reactions.

$$K_c = K_p (RT)^{\sum a_i \sum b_i} \tag{A.25}$$

$$T\frac{d\ln(K_c)}{dT} = \frac{\Delta E_0}{RT} + \sum b_i \left(\frac{E - E_0}{RT}\right)_{B_i} - \sum a_i \left(\frac{E - E_0}{RT}\right)_{A_i} \tag{A.26}$$

$$T\frac{d\ln\left(K_p\right)}{dT} = T\frac{d\ln(K_c)}{dT} + \sum b_i - \sum a_i \tag{A.27}$$

$$\Delta E_0 = \sum b_i E_0(B_i) - \sum a_i E_0(A_i) \tag{A.28}$$

Where

K_c is the chemical equilibrium constant for concentration units

A.1.5. Mole fraction

Now that the equilibrium constants are known for each of the reactions, it is time to consider when they will occur. For the air component in this approximate model, the different dissociation reactions can be split up or joined together to form various stages of reactions. First oxygen dissociation occurs essentially completely before the dissociation of nitrogen starts. This means these two processes can be separated and are assumed independent for this approximation method. Also, an approximation is that the nitrogen and oxygen ionization occurs at roughly the same temperature and with the same energy change. This means that these reactions can be lumped into a single species, where a population weighted average property is used (Hansen, 1958).

Having split up and lumped together these reactions allows for them to be considered separate and occurring after one another. Starting with the dissociation of oxygen, the fraction of dissociation is defined by Eq. A.30. The dissociation of nitrogen occurs next once the fraction of dissociation of oxygen has reached the limit of 0.2. Equation A.32 defines the fraction of dissociation for nitrogen. Once the dissociation fraction has reached the limit of 0.8, the nitrogen dissociation is complete and the ionization will start. The ionization of both oxygen and nitrogen are approximated to be a single species represented by the population weighted average of oxygen and nitrogen. Equation A.33 shows the definition of the equilibrium constant for the ionization reaction. This can be used in the equation for defining the fraction of dissociation for the ionization as per Eq. A.34.

$$K_{p1} = \frac{4\epsilon_1^2 p}{(1+\epsilon_1)(0.2-\epsilon_1)} \tag{A.29}$$

$$\epsilon_1 = \frac{-0.8 + \sqrt{0.64 + 0.8\left(1 + \frac{4p}{K_{p1}}\right)}}{2\left(1 + \frac{4p}{K_{p1}}\right)} \tag{A.30}$$

$$K_{p2} = \frac{4\epsilon_2^2 p}{(1.2+\epsilon_2)(0.8-\epsilon_2)} \tag{A.31}$$

$$\epsilon_2 = \frac{-0.4 + \sqrt{0.16 + 3.84\left(1 + \frac{4p}{K_{p2}}\right)}}{2\left(1 + \frac{4p}{K_{p2}}\right)} \tag{A.32}$$

$$K_{p3} = 0.2K_p(O \rightarrow O^+ + e^-) + 0.8K_p(N \rightarrow N^+ + e^-) \qquad A.33$$

$$\epsilon_3 = \left(1 + \frac{p}{K_{p3}}\right)^{-\frac{1}{2}} \qquad A.34$$

Where

$\epsilon_{1,2,3}$ are the fraction of molecules dissociated/atoms ionized

Carrying on with the equilibrium reactions, the mole fractions of each of the air species can be defined using these dissociation fractions as per Eq. A.35 to A.39. The definition of compressibility is Eq. A.40.

$$x(O_2) = \frac{0.2 - \epsilon_1}{Z} \qquad A.35$$

$$x(N_2) = \frac{0.8 - \epsilon_2}{Z} \qquad A.36$$

$$x(O) = \frac{2\epsilon_1 - 0.4\epsilon_3}{Z} \qquad A.37$$

$$x(N) = \frac{2\epsilon_2 - 1.6\epsilon_3}{Z} \qquad A.38$$

$$x(N^+ + O^+) = x(e^-) = \frac{2\epsilon_3}{Z} \qquad A.39$$

$$Z = 1 + \epsilon_1 + \epsilon_2 + 2\epsilon_3 \qquad A.40$$

Where

x is the mole fraction

It is important to realise that these three reactions occur over a range of temperatures from 0 [K] up to roughly 15000 K. However, as Figure 3.5 (Hansen, 1958) shows that it is unlikely we will reach extremely high temperatures (note that this is only an approximation). It shows its likely the Mk-III would reach temperatures between 1500 and 2000 K given our re-entry velocity of roughly 2000 m/s. Within this temperature range it is expected that only oxygen dissociation will occur as shown visually in Figure A.1 (Anderson, 2006). This figure does not show the effect of pressure where lower pressures will cause dissociation and ionization to occur earlier, but the effects of pressure. Due to the fact that these calculations will only be done once to design lookup tables, this added complexity with adding other dissociations and ionizations is not a concern.

A.1.6. Enthalpy and specific heat for air

Up to this point the properties and concentrations of the components of air have been calculated. Now that those are known, the properties of the air itself can be calculated, starting with the internal energy and enthalpy. The dimensionless internal energy is calculated by Eq. A.41 where the sum of all internal energies of the air components are added. This can be used in Eq. A.42 to calculate the enthalpy of the air. It should be noted that these equations are in the form of enthalpy and internal energy per mole, where the molar mass to transfer it to an enthalpy and internal energy per kg is the molar mass of the undissociated air (29 [g/mol]). The compressibility factor accounts for any difference in molar mass due to dissociation effects.

$$\frac{ZE}{RT} = Z\sum_i x_i \frac{E_i}{RT} \qquad A.41$$

$$\frac{ZH}{RT} = \frac{ZE}{RT} + Z \qquad A.42$$

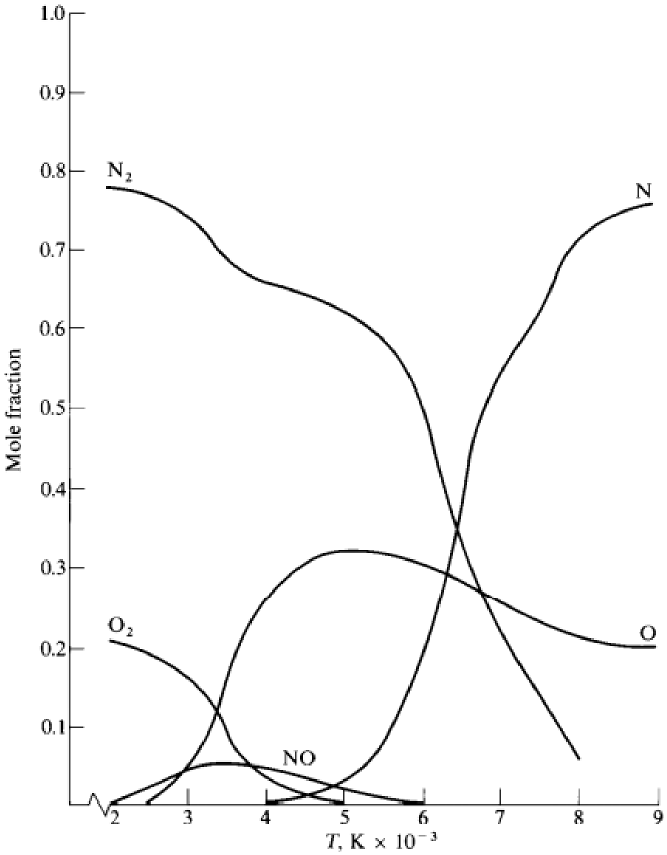

Figure A.1. Composition of equilibrium air against temperature at 1 atmosphere pressure (Anderson, 2006)

The specific heat at constant pressure can be calculated according to Eq. A.43. Hamilton, Greene, & DeJarnette (1994) states that the equation for the specific heat at constant pressure (and the specific heat at constant volume) are not very accurate and only fall within a 10 % error margin. Because the gas is reacting, causing a change in chemical composition, the ideal gas relation of specific heat ratio and the specific heat values cannot be made using the gas constant. Instead, Eq. A.44 is used to calculate the specific heat ratio where central differencing theory can be used to calculate the derivatives and Figure A.2 can be used to find the dimensionless speed of sound.

$$\frac{ZC_p}{R} = \frac{1}{R}\left(\frac{\partial ZH}{\partial T}\right)_p = Z\sum_i x_i\left(\frac{C_i}{R}+1\right) + T\sum_i\left(\frac{E_i}{RT}\right)\left(\frac{\partial Zx_i}{\partial T}\right)_p \qquad A.43$$

$$\frac{a^2\rho}{p} = \gamma\frac{1+\left(\frac{T}{Z}\right)\left(\frac{\partial Z}{\partial T}\right)_\rho}{1+\left(\frac{T}{Z}\right)\left(\frac{\partial Z}{\partial T}\right)_p} \qquad A.44$$

Where

a is the speed of sound $[\mathrm{m/s}]$

A.1.7. Viscosity

The transport property viscosity can be calculated by the summation formula for a mixture of hard spherical molecules, as shown in Eq. A.45. The ratio of mean free paths required in this equation is given by Eq. A.46. The collision cross section (S) is formulated in Hansen (1958), however there is also a tabulated form. The collision cross sections vary with temperatures but can be approximated using the tabulated form due to the low level of variations. Table A.2 (Hansen, 1958) shows these collision cross sections for the different reactions at various temperatures. The reference viscosity in Eq. A.45 is defined as per Eq. A.47 where the reference viscosity in the equation is in units $[\mathrm{g/cms}]$.

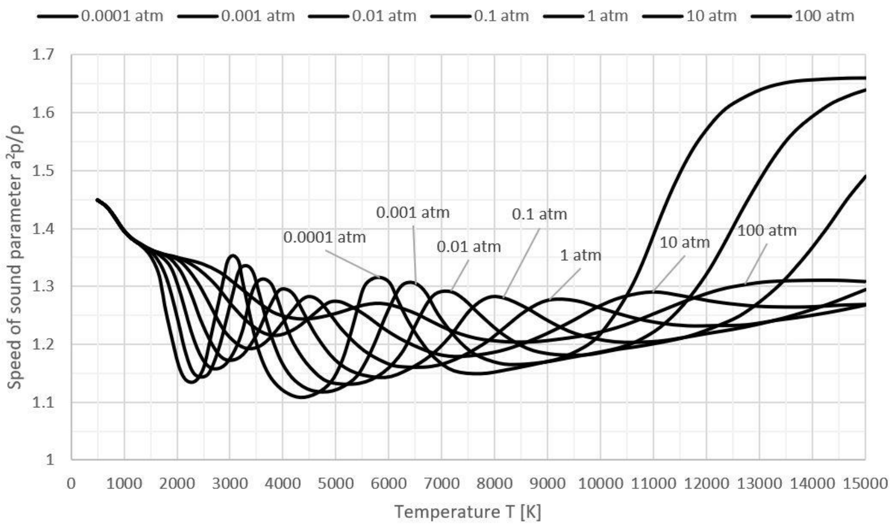

Figure A.2. Dimensionless speed of sound (Hamilton et al., 1994).

Table A.2. Collision Cross Section (Hansen, 1958). Blank spaces are left in areas where data is not needed as either there are only products or reactants

T [K]	S_0 $[10^{-16}\mathrm{cm}^2]$	$\frac{S(N_2-N)}{S_0}$	$\frac{S(N-N)}{S_0}$	$\frac{S(N_2-e)}{S_0}$	$\frac{S(e-e)}{S_0}$	$\frac{S'(N_2-N)}{S_0}$	$\frac{S'(N-N)}{S_0}$
500	38.4	0.946	0.894			0.877	0.761
1000	34.9	0.920	0.838			0.843	0.703
1500	33.7	0.889	0.785			0.817	0.652
2000	33.2	0.886	0.742			0.794	0.611
2500	32.8	0.846	0.705			0.775	0.578
3000	32.6	0.830	0.676			0.759	0.551
3500	32.4	0.815	0.650			0.745	0.527
4000	32.3	0.803	0.628			0.733	0.507
4500	32.2	0.792	0.608			0.722	0.489
5000	32.1	0.782	0.591			0.712	0.473
5500	32.0	0.773	0.575	0.397	89.9	0.703	0.458
6000	32.0	0.764	0.561	0.380	75.6	0.695	0.445
6500	31.9	0.757	0.548	0.366	64.5	0.688	0.433
7000	31.9	0.750	0.536	0.353	55.7	0.681	0.422
7500	31.9	0.743	0.524	0.342	48.6	0.674	0.412
8000	31.8	0.737	0.514	0.331	42.8	0.668	0.402
8500	31.8	0.731	0.504	0.321	37.9	0.662	0.393
9000	31.8	0.725	0.495	0.313	33.8	0.657	0.385
9500	31.8	0.720	0.486	0.304	30.4	0.652	0.377
10000	31.8	0.715	0.478	0..297	27.4	0.647	0.370
10500	31.8	0.710	0.470	0.290	24.9	0.642	0.363
11000	31.8	0.706	0.463	0.283	22.7	0.637	0.356
11500	31.7	0.701	0.456	0.281	20.8	0.633	0.350
12000	31.7	0.697	0.448	0.270	19.09	0.629	0.342
12500	31.7	0.693	0.443	0.266	17.60	0.625	0.338
13000	31.7	0.689	0.437	0.261	16.27	0.612	0.332
13500	31.7		0.431	0.256	15.10		0.327
14000	31.7		0.426	0.252	14.04		0.322
14500	31.6		0.420	0.247	13.09		0.316
15000	31.6		0.415	0.243	12.24		0.312
$S(N_2-N)=S(O_2-O)=S(N_2-O)$							
$S(N-N)=S(O-O)=S(N-O)=S(N-N^+)=S(O-O^+)$							
$S(N-e)=S(O-e)$							
$S'(N_2-N)=S'(O_2-O)=S'(N_2-O)$							
$S'(N-N)=S'(O-O)=S'(N-O)=S'(N-N^+)=S'(O-O^+)$							

$$\frac{\mu}{\mu_0} = \sum_i \sqrt{\frac{M_i}{M_0}} x_i \frac{\lambda_i}{\lambda_0} \qquad \text{A.45}$$

$$\frac{\lambda_0}{\lambda_i} = \sum_i x_j \frac{S_{ij}}{S_0} \left(\frac{1 + \frac{M_i}{M_j}}{2} \right)^{\frac{1}{2}} \qquad \text{A.46}$$

$$\mu_0 = 1.462 \cdot 10^{-5} \frac{\sqrt{T}}{1 + \frac{112}{T}} \qquad \text{A.47}$$

Where

λ is the mean free path of molecule
S_{ij} is the collision cross section of particle i with particle j

A.1.8. Prandtl number

The last parameter required is the Prandtl number. To calculate the Prandtl number, the thermal conductivity needs to be calculated which requires two separate calculations. First the thermal conductivity due to the molecular collisions needs to be calculated, which occurs in dissociated and undissociated gasses. This calculation is given by Eq. A.48 where the additional inputs not determined by previous sections can be found in Eq. A.49 and A.50. The second component of thermal conductivity is the thermal conductivity caused by diffusion to maintain chemical equilibrium. Equation A.51 shows the equation that approximates this quantity. In this case the reference thermal conductivity is defined in Eq. A.52. The summation in the denominator can be simplified by assuming negligible difference between the oxygen and nitrogen atoms mass. These simplifications for oxygen dissociation reaction, nitrogen dissociation reaction and ionization reaction are shown in Eq. A.53, A.54 and A.55 respectively.

$$\frac{k_n}{k_0} = \sum_i \left(\sqrt{\frac{M_i}{M_0}} x_i \frac{\lambda_i}{\lambda_0} \right) \frac{M_0}{M_i} \left[\frac{4}{19} \left(\frac{C}{R} \right)_i + \frac{9}{19} \right] \qquad \text{A.48}$$

$$C_i = \frac{3}{2} R \qquad \text{A.49}$$

$$k_0 = \frac{19}{4} \frac{R}{M_0} \mu_0 \qquad \text{A.50}$$

$$\frac{k_r}{k_0} = \frac{\frac{12\sqrt{2}}{95} \left(T \frac{d \ln(K_p)}{dT} \right)^2}{\sum_i \sum_j \left[\frac{M_i M_j}{M_0 (M_i + M_j)} \right]^{\frac{1}{2}} \frac{S'_{ij}}{S_0} \frac{a_i}{x_i} (a_i x_j - a_j x_i)} \qquad \text{A.51}$$

$$k_0 = \frac{95\sqrt{\pi}}{64} \frac{R}{N_0 S_0} \sqrt{\frac{RT}{M_0}} \qquad \text{A.52}$$

$$\sum_i \sum_i = \frac{S'(N_2 - N)}{\sqrt{3} S_0} \left[\frac{[x(O) + 2x(O_2)]^2}{x(O) x(O_2)} + \frac{4x(N_2)}{x(O)} \right] + \frac{x(N_2)}{\sqrt{2} x(O_2)} \qquad \text{A.53}$$

$$\sum_i \sum_i = \frac{S'(N_2 - N)}{\sqrt{3} S_0} \left[\frac{[x(N) + 2x(N_2)]^2}{x(N) x(N_2)} + \frac{x(O)}{x(N_2)} \right] + \frac{S'(N - N)}{S_0} \frac{2x(O)}{x(N)} \qquad \text{A.54}$$

$$\sum_{i}\sum_{i} = \left[\frac{1}{2}\frac{S'(N-N)}{S_0} + \frac{1}{230}\frac{S'(N-e^-)}{S_0}\right]\frac{[x(N)+x(N^+)]^2}{x(N)x(N^+)} \tag{A.55}$$

Now that the thermal conductivity, specific heat at constant pressure and viscosity are known the Prandtl number can be calculated according to Eq. A.56.

$$\mathrm{Pr} = \frac{4}{19}\left(\frac{ZC_p}{R}\right)\frac{\frac{\mu}{\mu_0}}{\frac{k}{k_0}} \tag{A.56}$$

A.2. US76 Atmospheric Model

The United States Standard Atmosphere is a standard atmospheric model that was created in 1958 and last updated in 1976. The atmospheric model, valid up to 1000 [km] at a latitude of 45° North, assumes linear temperature rates for the lower atmosphere (below 86 [km]) and includes variations in composition at higher altitudes. The full model of the US76 standard atmosphere is given in NASA (1976) however its equations are summarized in Van Kesteren (2013).

The US76 uses two different types of altitude; the geometric altitude (Z) and the geopotential altitude (H) (Van Kesteren, 2013). The geometric altitude is the height above ground whereas the geopotential altitude is a redefinition of geometric altitude, assuming that the gravitational acceleration is constant with changing altitude. For the lower atmosphere (below geometric altitude 86 [km]) the atmosphere is divided up into eight layers. Equation A.57 provides the equation for the molecular temperature of the atmosphere up to 86 [km] geometric altitude using the input values of Table A.3. Note that a geometric altitude of 86 [km] corresponds to a geopotential altitude of 84.85 [km].

$$T_M = T_{M,b} + L_{M,b}(H - H_b) \tag{A.57}$$

Where

H is the geopotential altitude [km]

Table A.3. US Standard Atmosphere 1976 reference height, temperature gradient and reference pressure for geometric altitude up to 86 [km].

Layer (b)	H_b [km]	$L_{M,b}$ [K/km]	p_b [Pa]
0	0	-6.5	101325
1	11	0	22632
2	20	1.0	5475
3	32	2.8	868
4	47	0	111
5	51	-2.8	79
6	71	-2.0	4
7	84.85	-6.5	4

Between 86 and 91 [km] altitude there exists an isothermal layer at 180.87 [K]. At the next layer (between 91 and 110 [km] altitude) the temperature can be described by Eq. A.58. In this equation T_8 is 263.19 [K] and Z_9 is 91 [km].

$$T = T_8 - 76.2\sqrt{1 - \left(\frac{Z - Z_8}{-19.94}\right)^2} \tag{A.58}$$

Where

Z is the geometric altitude [km]

The 9th layer of the US76 standard atmosphere is defined over an altitude of 110 to 120 [km] and described by Eq. A.59 where T_9 is 240 [K] and Z_9 is 110 [km].

$$T = T_9 + 12(Z - Z_9) \tag{A.59}$$

The last layer ranges up to an altitude of 1000 km and is defined according to Eq. A.60 to A.62. Within these equations T_∞ is the exoatmospheric reference temperature of 1000 $[\mathrm{K}]$, Z_{10} is 120 $[\mathrm{km}]$, T_{10} is 360 $[\mathrm{K}]$ and r_0 is 6356.76 $[\mathrm{km}]$.

$$T = T_\infty - (T_\infty - T_{10})\mathrm{e}^{-\gamma\xi} \tag{A.60}$$

$$\gamma = \frac{12}{T_\infty - T_{10}} \tag{A.61}$$

$$\xi = \frac{(Z - Z_{10})(r_0 + Z_{10})}{r_0 + Z} \tag{A.62}$$

Where

r_0 is the effective Earth radius $[\mathrm{km}]$

The equations within this section have thus far only covered the temperature distribution of the US76 Standard Atmospheric model but have not covered pressure and other atmospheric properties. For altitudes below 86 $[\mathrm{km}]$ the pressure can be calculated for the linear and isothermal temperature layers according to Eq. A.63 and A.64 respectively. The inputs for these equations can be found in Table A.3. It should be noted that below 80 $[\mathrm{km}]$ the molar mass of air does not change and that between 80 and 86 $[\mathrm{km}]$ altitude the change in molar mass is only 0.04 %. This change is considered negligible.

$$p = p_b \left(\frac{T_{M,b}}{T_{M,b} + L_{M,b}(H - H_b)} \right)^{\frac{g_0 M}{R L_{M,b}}} \tag{A.63}$$

$$p = p_b \left(\frac{-g_0 M (H - H_b)}{R_A T_{M,b}} \right) \tag{A.64}$$

Where

M is the mean molecular weight $[\mathrm{kg/mol}]$

For altitudes above 86 $[\mathrm{km}]$ the pressure can be found by solving Eq. A.65 using the $\sum n_i$ tabulated results for each gas species from NASA (1976).

$$p = \sum p_i = \sum n_i k T \tag{A.65}$$

Where

$\sum n_i$ are the number densities of the atmospheric gas components
k is the Boltzmann constant ($1.38065 \cdot 10^{-23}$ $[\mathrm{m^2 kg/s^2 K}]$)

Lastly using the assumption that the atmosphere is a perfect gas the density of the atmosphere can be found using the ideal gas law as shown in Eq. A.66.

$$\rho = \frac{pM}{RT} \tag{A.66}$$

Appendix B. Reference Vehicles

The Mk-III is not the first spaceplane ever to be built. There have been many predecessors that have a variety of different missions. Some have never flown while others have had many flights. This chapter will discuss some of these spaceplanes or space vehicles, including their missions and how the thermal analysis was conducted. These vehicles will be compared to the Mk-III as it will show that the Mk-III has unique aspects with respect to each. It should be noted that the reference vehicles discussed in this chapter are only a selection of many vehicles that have been created or designed. The selection is based on their flight heritage, similarity to the Mk-III in both mission and trajectory as well as the literature about their thermal analysis.

B.1. X-15

The X-15, Figure B.1 (NASA, 2017), designed by NASA in collaboration with the Air Force, the Navy and North American Aviation Inc, was designed to research piloted hypersonic and space flight (Gibbs, 2014). The goal of the X-15 program was to explore the aerodynamic heating rates, stability and control, physiological phenomena and other effects associated with hypersonic flight. Unofficially, the X-15 set speed and altitude records of 2020.6 ms^{-1} and 107.96 km respectively. One of the primary goals of the X-15 flight program was to measure and analyse the aerodynamic heating within the design flight envelope with maximum velocity 1788.2 ms^{-1} and altitude 107.83 km (Stillwell, 1965) as shown in Figure B.2 (Stillwell, 1965). This meant that the X-15 flew twice the speed and three times the altitude of any other aircraft in existence at that time.

Figure B.1. X-15 (NASA, 2017)

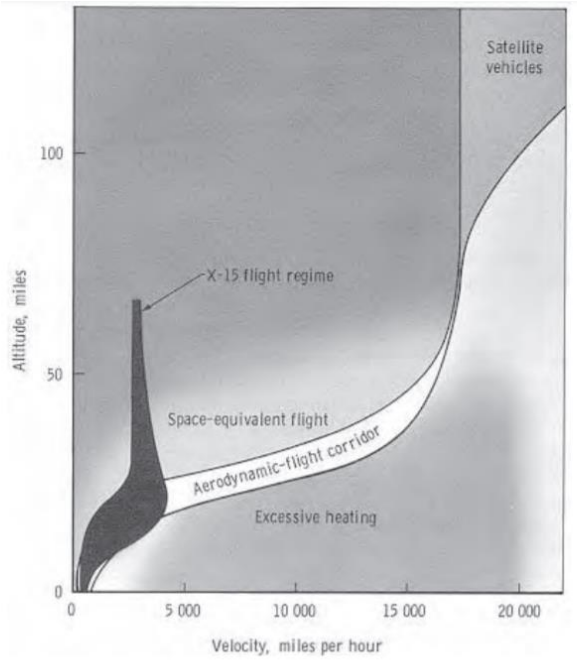

Figure B.2. X-15 explorable aerodynamic-flight corridor compared to the flight corridor of a lifting-body re-entry spacecraft from orbit (Stillwell, 1965)

The X-15 was air launched from a B-52 aircraft after which the engine would burn for 80 to 120 $[\mathrm{s}]$ depending the particular mission that day (Gibbs, 2014). After burn the flight would last 8 to 12 $[\mathrm{min}]$ which included a glided flight and landing. The trajectory profile for the design speed and altitude flight is shown in Figure B.3 (Stillwell, 1965).

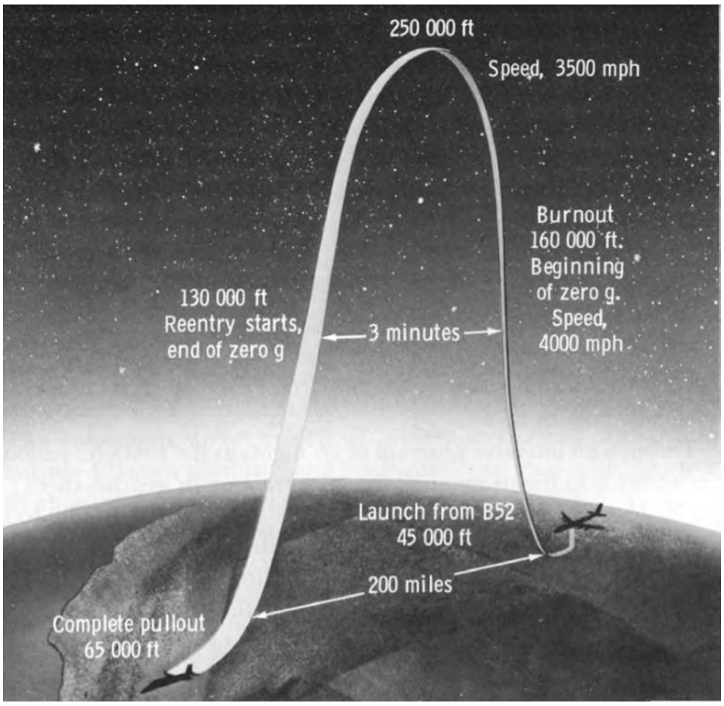

Figure B.3. X-15 Flight profile of design speed and altitude flight (Stillwell, 1965)

The X-15s produced were equipped with numerous thermocouples to measure the internal temperatures of the X-15 structure. For a few of these flights where high skin-heating rates and low skin temperatures were present, the measured data could be reduced to heat-transfer data (Banner, Kuhl, & Quinn, 1962). The analysis of the X-15 showed that both the turbulent heat-transfer calculated by Eckert's reference-temperature method and the Theory of Van Driest overestimated the measured value by as much as 60% (Banner, Kuhl, & Quinn, 1962). A problem that engineers faced with both these methods was the difficulty in extrapolating turbulent heat-transfer data available (Banner, Kuhl, & Quinn, 1962). An assumption made in the entire X-15 analysis is the fluid has attached shock flow conditions (Banner, Kuhl, & Quinn, 1962). Alongside this assumption neglecting the effect of heating rate and using the turbulent Eckert's reference-temperature method showed the best correlation between measured and calculated values. Neglecting the heating rate was accomplished by the substitution of the boundary-layer recovery temperature for the skin temperature in the reference temperature equation (Banner, Kuhl, & Quinn, 1962; Banas, 1965).

B.2. Space Shuttle

The Space Shuttle, Figure B.4 (NASA, 2017), first flown in 1981, was designed by NASA as the first reusable spacecraft (Young & Crippen, 2011). Being able to both carry heavy cargo as well as provide astronaut space habitability allowed flexibility in the Space Shuttle's missions. It was capable of both launching satellites or space station modules (including the International Space Station) as well as have the capability of repair and assembly within the space environment.

The Space Shuttle was constructed out of three major components, the two solid rocket boosters, the external tank and the Orbiter vehicle (Young & Crippen, 2011). For launch the Space Shuttle would operate as a rocket in vertical take-off, as seen in Figure B.6 (Young & Crippen, 2011). It would discard the two boosters which were recovered for re-usability. The external tank would take the Orbiter vehicle up to a safe orbit after which it would be released and burn up in the atmosphere upon re-entry. The Orbiter was the main component of the Space Shuttle, carrying the cargo and crew. The Orbiter had the capability of a total mission duration of 12 to 16 days. After this the Orbiter vehicle would fire its thrusters to a re-entry trajectory leading to an hour long re-entry. The Orbiter vehicle would eventually land horizontally on a runway after having performed a gliding re-entry.

The Space Shuttle Orbiter operated in an altitude range of 185 to about 590 km where the orbital velocity is about 7822 ms^{-1} (Young & Crippen, 2011). During the descent phase of roughly 1 [hrs] and 5 [min] the Orbiter vehicle had to decelerate from this condition to a roughly 96 ms^{-1} for the horizontal landing. The energy lost due to primarily friction between the atmosphere and caused vehicle temperatures ranging between 927°C and 1600°C.

Figure B.4. Space Shuttle (NASA, 2017)

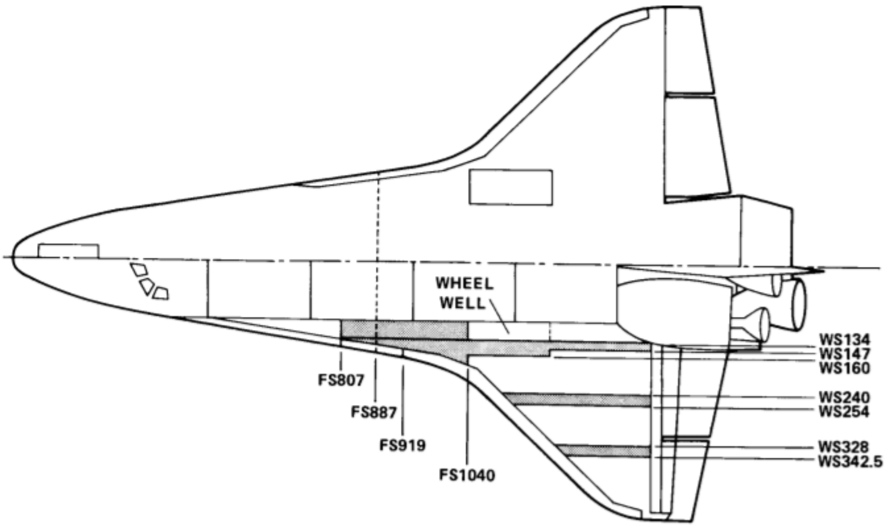

Figure B.5. Space Shuttle Wing and Fuselage Thermal Analysis Locations Analysed (Ko, Quinn, & Gong, 1986)

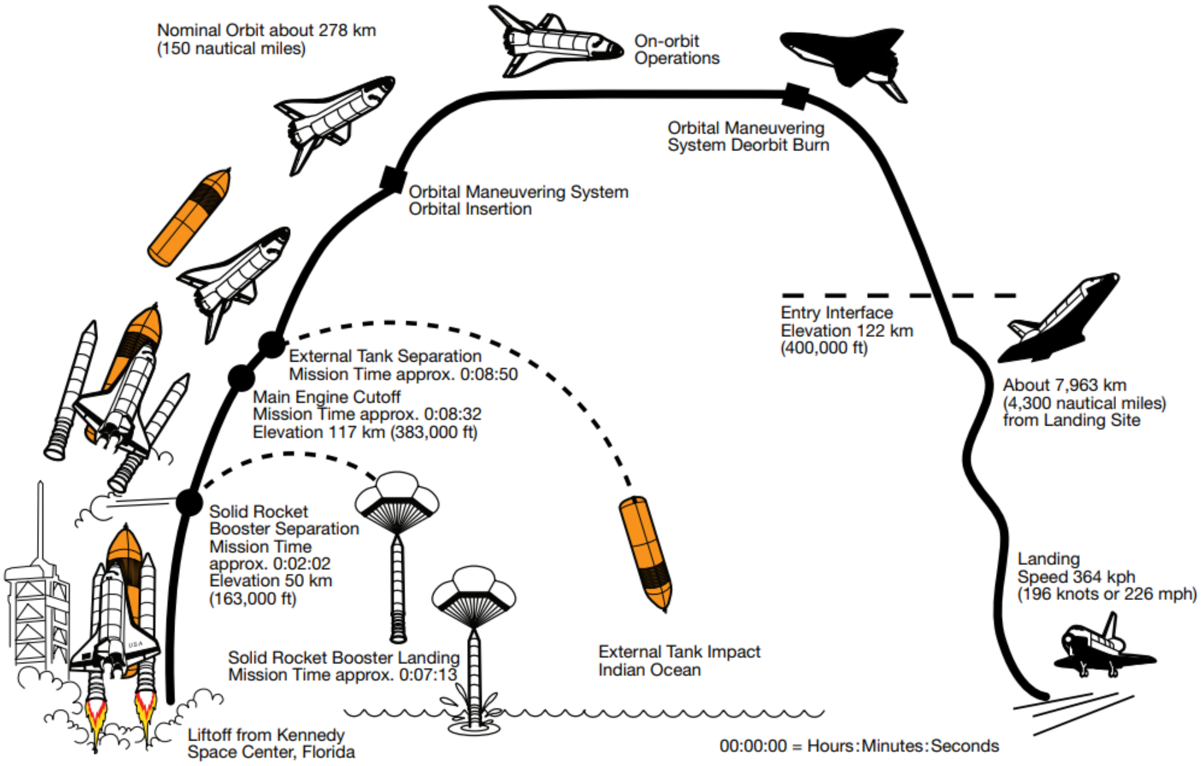

Figure B.6. Space Shuttle Flight Operations Sequence (Young & Crippen, 2011)

The Space Shuttle Orbiter had extensive thermal analysis carried out on it both before and after taking flight. The analysis computed the re-entry external heating rates and surface temperatures using the theoretical thin skin NASA program (Ko et al., 1982). Multiple three-dimensional wing segments and one two-dimensional fuselage section were selected for the thermal analysis as shown in Figure B.5 (Ko et al., 1986). This program evaluates the one-dimensional thin skin heating equations using the Eckert's reference enthalpy method and van Driest theories for laminar and turbulent heat transfer quantities respectively on the wing segments (Gong et al., 1982; Ko et al., 1982). On the fuselage cross section the wing methods were used alongside the turbulent swept-cylinder theory of Beckwith and Gallagher and the laminar swept-cylinder theory of Fay and Riddell. Because of the complex shape of the fuselage section which method was used to predict the heating varied. The local inviscid flow conditions were computed by the use of the Prandtl-Meyer expansion theory using the oblique shock theory for the wing and using initial flow conditions equal to the free-stream conditions for the fuselage. A prediction on the amount of thermal heating experienced when flow was separated from the vehicle was also made based on a fraction of the heating as a laminar attached flow would give. The input to these thermal analyses were the nominal trajectories for the STS-1 or STS-5 (Ko et al., 1988) nominal trajectory.

The thermal modelling within the structure was conducted using the electrical resistance capacity analogy (finite element thermal analysis) (Gong et al., 1982; Ko et al., 1982). Initially only aerodynamic heating, external radiation and internal radiation were included in analysis. However, due to the difference between measured and computed internal temperature results, especially after touchdown, and the discovery of the wing structure being exposed to the atmosphere meant that internal convection was later included in the analysis (Ko et al., 1988). This analysis showed that excluding the internal radiation and convection effects could cause the internal temperatures to be overestimated by up to 90%. Other important effects included in the Space Shuttle thermal analysis are that the effect of the gap between the TPS tiles were accounted for by reducing the thickness of the structure within the model.

B.3. X-34

The X-34, Figure B.7 (Conner, 2017), was a cooperative project with NASA and Orbital Sciences Corporation aimed at designing a reusable flight demonstration test bed and demonstrate the use of a streamlined management approach alongside a rapid schedule and limited testing (Gibbs, 2014; Kleb, Wood, Gnoffo, & Alter, 1999). NASA wanted to reduce the cost of launching payloads into orbit by 10 fold with the use of the X-34 and to demonstrate the ease of access to space with greater reliability. The X-34 was expected to fly up to Mach 8 and reach an altitude of approximately 80 km. The X-34 flew three captive carry flights but the program was discontinued before more flights could be conducted, including any powered flights.

Even though no real flight data has been able to be gathered from the X-34 in regards to the thermal behaviour of the spaceplane, the development phase did include thermal analysis for the projected missions. The analysis was carried out in two parts. The first was an analysis into the peak temperatures experienced at various locations to determine the type of TPS requirements over the surfaces of the X-34. The peak heating condition on the trajectory was identified and analysed using CFD (Kleb, Wood, Gnoffo, & Alter, 1999). The CFD program utilizes and upward-biased point-implicit relaxation algorithm (Gnoffo P. , 1989; Gnoffo P. A., 1990) that finds a numerical solution to simplified Reynolds-averaged Navier-Stokes equations for three-dimensional viscous hypersonic flow in thermo-chemical non-equilibrium. The Navier-Stokes equations are simplified by the thin-layer assumption (Kleb et al., 1999). The Roe's flux-difference splitting (Roe, 1981) and Harten's entropy fix (Harten, 1997) with second-order corrections that are based on Yee's symmetric total-variation-diminishing scheme (Yee, 1985) are used to calculate the upwind-biased inviscid flux. The Balwin-Lomax algebraic turbulence model (Baldwin & Lomax, 1978) is used with damping term according to (Gupta, Lee, Zoby, Moss, & Thompson, 1990) where the air is assumed to behave as a perfect gas. A radiation-equilibrium boundary condition is assumed using the Stefan-Boltzmann relation (Kleb et al., 1999).

The second analysis conducted is the transient thermal analysis to determine the thickness of the TPS (Wurster, Riley, & Zoby, 1999). Rather than the more complex Navier-Stokes equations, this analysis calculated the flow field using an inviscid flow CFD analysis. This flow field then used an inviscid/boundary layer methodology to compute both the laminar and turbulent surface heating rates (Hamilton et al., 1994). An approximate heating method (Zoby & Simmonds, 1985) and axisymmetric analogy concept for three-dimensional boundary layers are used in this process. Due to the nature of the inviscid CFD analysis this method could be conducted at more points along the trajectory. To interpolate further between these data points a program called MINIVER (Wurster et al.,1999; Engle & Praharaj, 1983) was used. This used approximate heating methods in conjunction with simplified flowfield and vehicle shapes. Post-shock and local flow properties are based on either normal-shock or sharp-cone entropy method and the angle of attack is accounted for either by an equivalent tangent-cone or an approximate cross-flow option (Baranowski, 1971). The program also allowed three-dimensional effects to be calculated by the use of Mangler transformation (Schlichting & Gersten, 2016) for flat-plate or sharp-cone conditions.

Figure B.7. X-34 (Conner, 2017)

B.4. Hopper

The Hopper is a reusable launch vehicle developed by ESA as part of the Future Launchers Preparatory Programme. Two Hopper concepts, a horizontal take off (as shown in Figure B.8) and vertical take off (as shown in Figure B.9), were part of the analysed frameworks for this program (Pezzella et al., 2010). The mission specified is to bring 8000 kg of payload into Geostationary Transfer Orbit. Both the horizontal take off and vertical take off Hopper concepts have a similar trajectory where staging with the second stage and payload occurs at an altitude of roughly 130 km and re-entry speeds are similarly around Mach 15 at 120 km altitude (Pezzella et al., 2010). From their thermal analysis both the horizontal take off and vertical take off Hopper experience peak heating at an altitude and Mach number of roughly 50 km and 14 respectively (Pezzella et al., 2010).

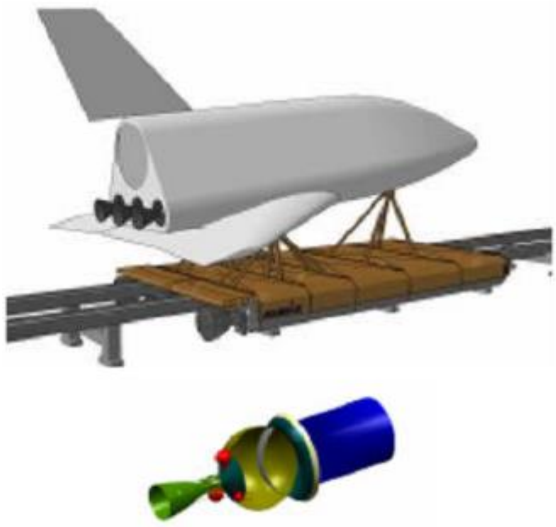

Figure B.8. Horizontal take-off Hopper (Pezzella et al., 2010)

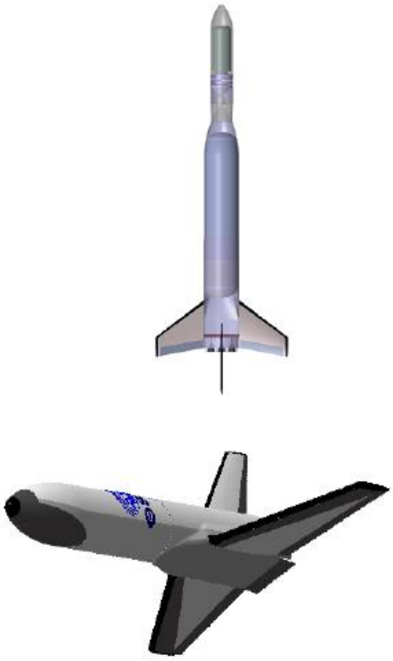

Figure B.9. Vertical take-off Hopper (Pezzella et al., 2010)

The vertical take off Hopper has had preliminary thermal analyses carried out on it. Because of the preliminary nature of this analysis primarily engineering methods with a small CFD analysis was conducted to provide initial thermal predictions. 3D Panel Methods using simplified methods such as the local surface inclination methods and approximate boundary-layer methods were used (Pezzella et al., 2008). Whether the vehicle component was modelled as either a flat plate or leading edge determined the appropriate boundary layer method. The thermal analysis consisted of a one-dimensional boundary layer method along the inviscid surface streamlines generated by the aerodynamic analysis. The thermal analysis was split into a few sections. First the heat transfer density profiles at stagnation points of the fuselage and three selected wing sections were analysed using the Detra-Kemp-Riddell method (Prabhu, 2004; Kemp & Riddell, 1957; Pezzella et al., 2008) for the fuselage and a modified equation for the wing stagnation points. These were conducted along the entire re-entry trajectory but assumes that the entire flow is in the continuum regime. This data was used to select a number of trajectory points that would with less data points predict the same heating of the entire trajectory. The heat flux for these points were modelled based on a laminar flow condition where air was modelled as a perfect gas using a cold wall boundary (of 300 K) assumption. Also data points were chosen for CFD analysis which solved the flow-field including chemical and vibrational non-equilibrium in the continuum regime. It did so with a finite volume approach using a flux difference splitting upwards scheme with second order ENO-like (Essentially Non-Oscillatory) reconstruction of cell interface values. Viscous fluxes were calculated using central differencing and time integration performed by using Euler Forward scheme coupled to a point implicit treatment of species and vibrational energies source terms. It is important to understand that the analysis of the vertical take off Hopper is preliminary. Pezzella, Marini, Roncioni, Kauffmann, & Tomatis (2009) states the analysis is missing accurate CFD analysis, laminar to turbulent transition, shock-shock interaction and real gas effects. For the preliminary analysis it was determined these methods were sufficient but real questions remained for further detailed design.

B.5. Shefex

SHEFEX (SHarp Edge Flight Experiment) is a program developed by DLR of which thus far two have been flight tested (Weihs). They are launched on an adapted sounding rocket to allow high speed measurement of the TPS onboard. The SHEFEX I, as shown in Figure B.10 (Weihs), was designed to demonstrate the potential of a facetted TPS with cooled and uncooled leading edges. SHEFEX II, as shown in Figure B.11 (Weihs), also used the facetted skin to evaluate a multitude of different TPS. The SHEFEX system has increased its performance in both speed and time. The SHEFEX I was able to perform Mach 6 flight for 20 sec, SHEFEX II able to reach Mach 10-11 for 45 sec and SHEFEX III is aimed at reaching Mach 20 for 15 min.

Figure B.10. SHEFEX I (Weihs)

Figure B.11. SHEFEX II (Weihs)

The thermal analysis on the SHEFEX I was conducted using a loosely coupled transient flow and structural analysis (Barth & Longo, 2010). For the CFD model the two equation k-ω model using a second order upwind scheme (Barth & Longo, 2010). For time discretization a three stage Runge-Kutta method was used. The structural analysis was conducted using the Finite Element Theory. The two simulations were coupled using a coupling environment where the out heat transfer flux at the wall from the flow analysis was used as input to the structural analysis and where the wall temperature output from the structural analysis was used as input to the flow analysis. Figure B.12 (Barth & Longo, 2010) shows the setup of this coupled environment. This iterative process was carried out for each time step until convergence was reached. The relation between the flow analysis time step and the structural analysis time step was computed using Eq. B.1 and B.2 (Barth & Longo, 2010).

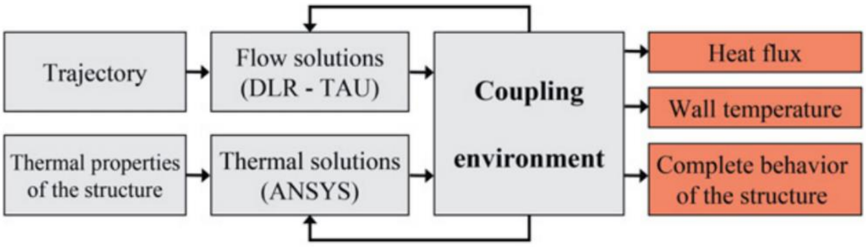

Figure B.12. SHEFEX I loosely coupled schematic (Barth & Longo, 2010)

$$\frac{t_{\text{fluid}}}{t_{\text{structure}}} = \frac{\alpha}{RV} \tag{B.1}$$

$$\alpha = \frac{k}{\rho c_p} \tag{B.2}$$

Where

α is the thermal diffusivity $[\mathrm{m}^2/s]$

After the successful demonstration of faceted surfaces of the SHEFEX I, the SHEFEX II focused on the testing and implementation of TPS and control systems. One particular test on the SHEFEX II was regarding a porous film cooled TPS (Boehrk, 2014). For this evaluation a semi-analytical tool which is based on evaluating the transient heat balance at the surface was used. This tool evaluated the thermal behaviour of a porous material where coolant flowed into the boundary layer of the flow.

B.6. Summary of reference vehicle analyses and comparison to Mk-III

The X-15 explored new boundaries for flight meaning at the time the thermal equations governing this area was unknown. Extrapolation of methods available caused for significant overestimation of the thermal loads on the X-15. Comparing the X-15 with the Mk-III shows that the trajectory shape (apogee and speed) are comparable to the Mk-III however the X-15 has sharp leading edges. The X-15 was designed using extrapolation of supersonic design ideas meaning that it is unlikely the Mk-III will have some of the sharp features the X-15 has.

The Space Shuttle uses engineering methods to analyse the flow field using that as input into the structural analysis. In doing so it is assuming wall temperatures. Both laminar and turbulent simulations are carried out with transition between laminar and turbulent flow being accounted for. The thermal analysis also accounts for convection within the wing and the heat transfer between the top and bottom wing skins to account for their linked behaviour. The Space Shuttle's mission is significantly higher thermally loaded than the Mk-III will be expected to due to it returning from orbit. However shape wise the Space Shuttle fits the Mk-III very well.

The X-34 has never flown sufficiently to test the TPS meaning that it never received flight data to validate the thermal analysis. The thermal analysis that was carried out uses mainly engineering methods but also CFD. The analysis was confined to a flow analysis due to the assumption that the TPS was sufficiently insulative to not require an FEA analysis. The X-34's mission is however relatively in line with the Mk-III mission and trajectory.

The Vertical Take Off Hopper had a thermal analysis carried out on it using engineering methods with a small amount of CFD. This analysis assumed a cold wall boundary condition and did not include an FEA analysis. Also only the laminar flow conditions were analysed. This preliminary thermal analysis was deemed sufficient however it was missing the laminar-to-turbulent transition, accurate CFD, shock-shock interactions and real gas effects. Although the mission of the Hopper is similar to the Mk-III its speed and altitude are significantly faster and higher than that expected of the Mk-III.

The SHEFEX is unlike other vehicles as it is not a spaceplane but rather a test platform for TPS. The analysis on the SHEFEX I was done by a loosely coupled CFD and FEA analysis where the heat flux and wall temperatures were exchanged between the two to converge to a solution. The SHEFEX has sharp edges and faceted surfaces meaning that its shape is not representative of a potential shape of the Mk-III. However the SHEFEX I's test time does fit within the Mk-III expected trajectory.

What is shown with the reference vehicles is that the methods used for the thermal analysis become increasingly more advanced but also become increasingly more orientated towards CFD and numerical calculations. This is an overall trend seen in the industry due to the ever increasing computational power. Engineering methods definitely are still of use but are increasingly less implemented or implemented in increasingly less situations as CFD replaces them.

This section has demonstrated that there is no one single reference vehicle applicable to the Mk-III. Instead depending on the particular part of the vehicle, trajectory or mission of the Mk-III a different reference vehicle should be used. Therefore, the validation of any analysis in this thesis multiple of these vehicles should be referenced.

Appendix C. Result figures

This appendix shows the results of all locations specified in for all the materials and TPS solutions analysed in Chapter 1.

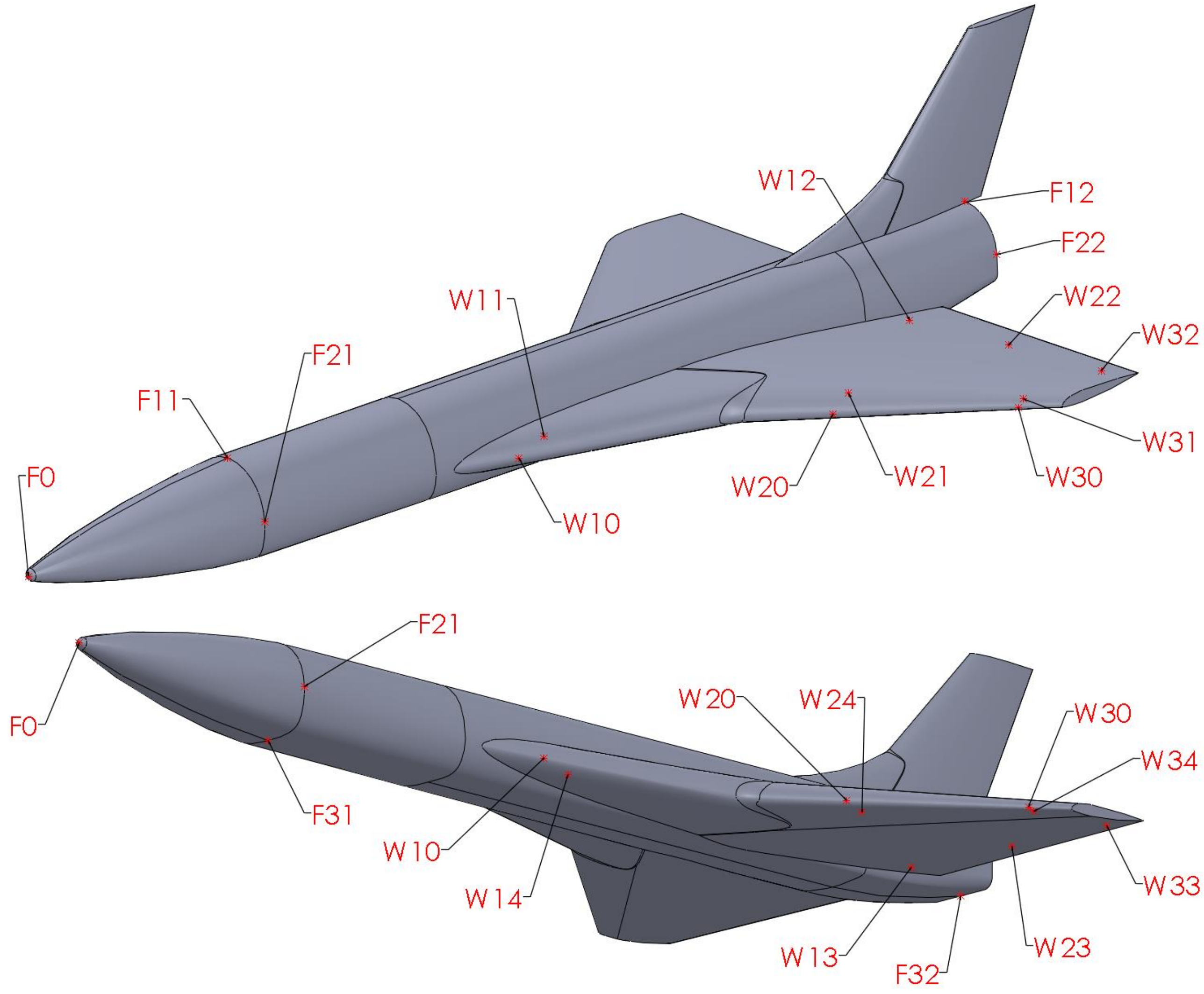

Figure C.1. Mk-III vehicle locations that are plotted and analysed. (Same as Figure 7.1)

C.1. BMI CF

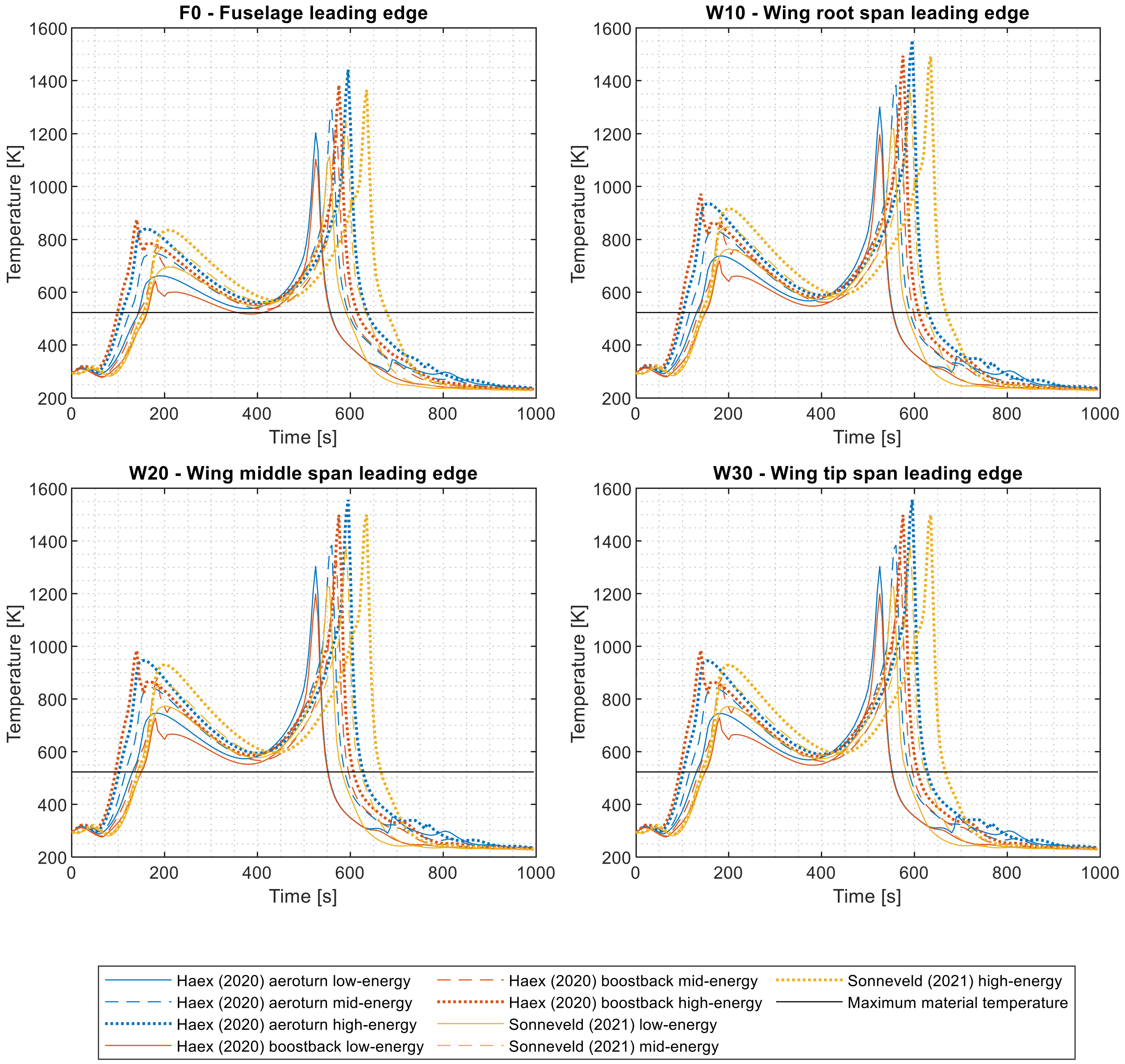

Figure C.2. BMI CF temperature results for leading edge locations along the external surface of the vehicle.

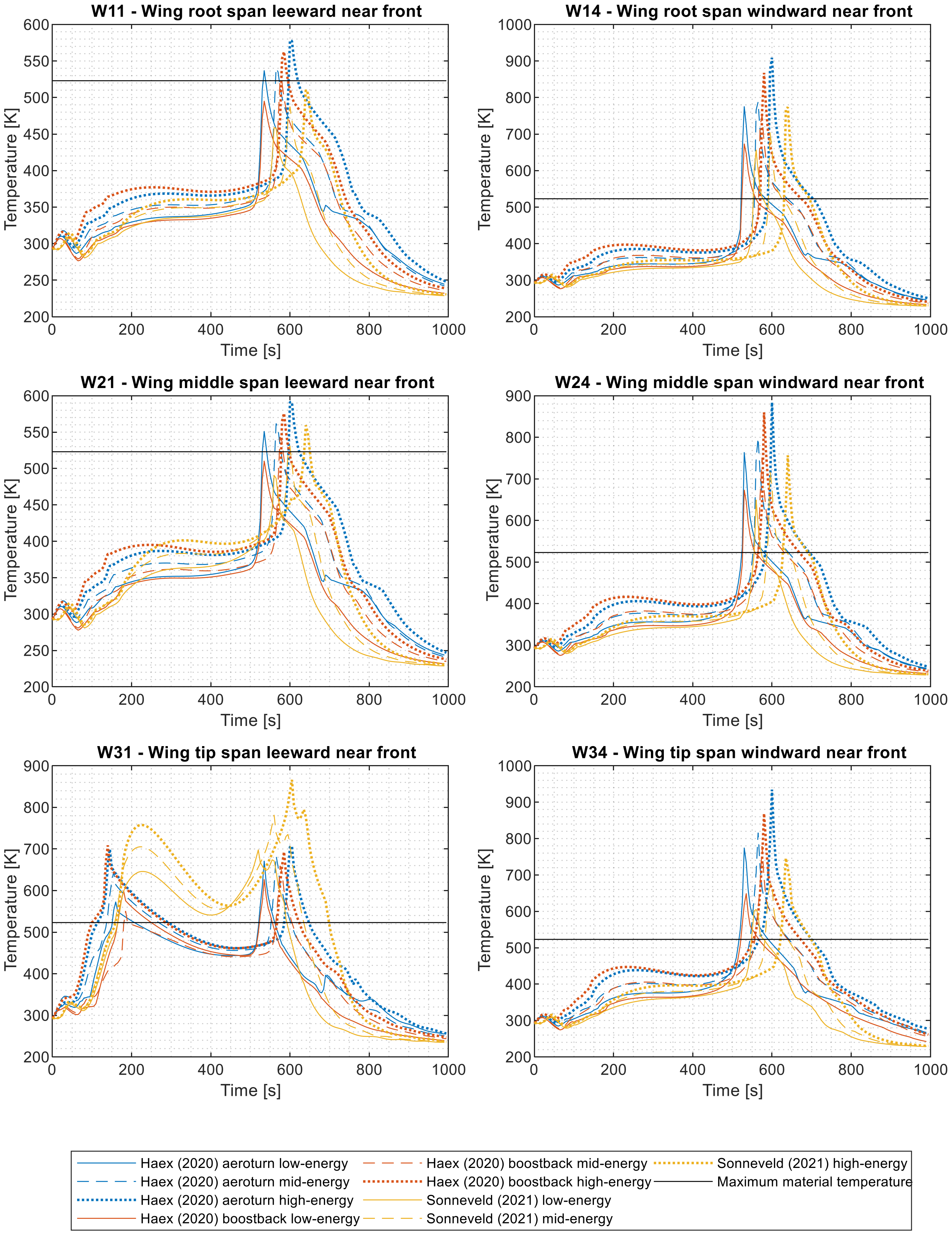

Figure C.3. BMI CF temperature results for front wing locations along the external surface of the vehicle.

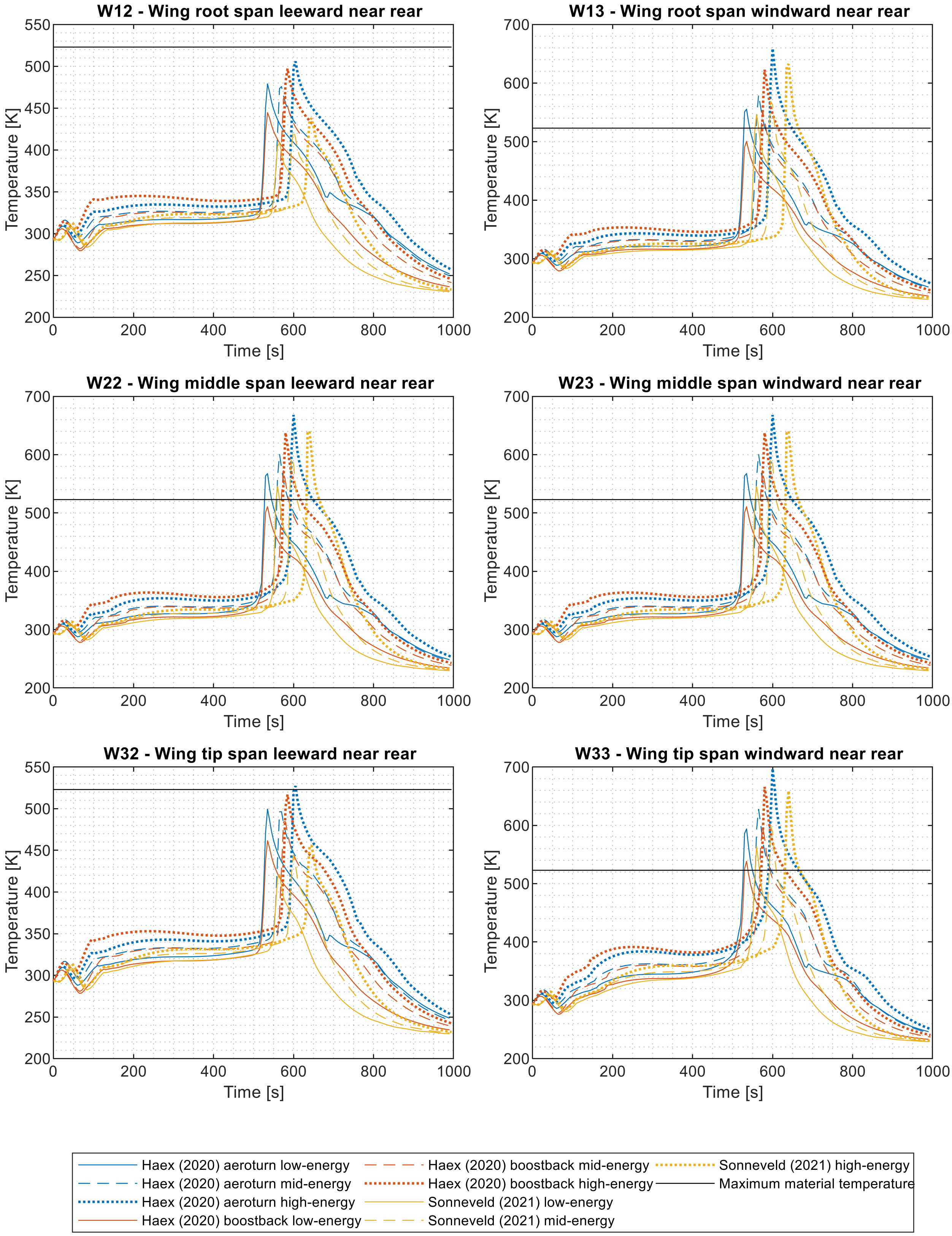

W12 - Wing root span leeward near rear

W13 - Wing root span windward near rear

W22 - Wing middle span leeward near rear

W23 - Wing middle span windward near rear

W32 - Wing tip span leeward near rear

W33 - Wing tip span windward near rear

Figure C.4. BMI CF temperature results for rear wing locations along the external surface of the vehicle.

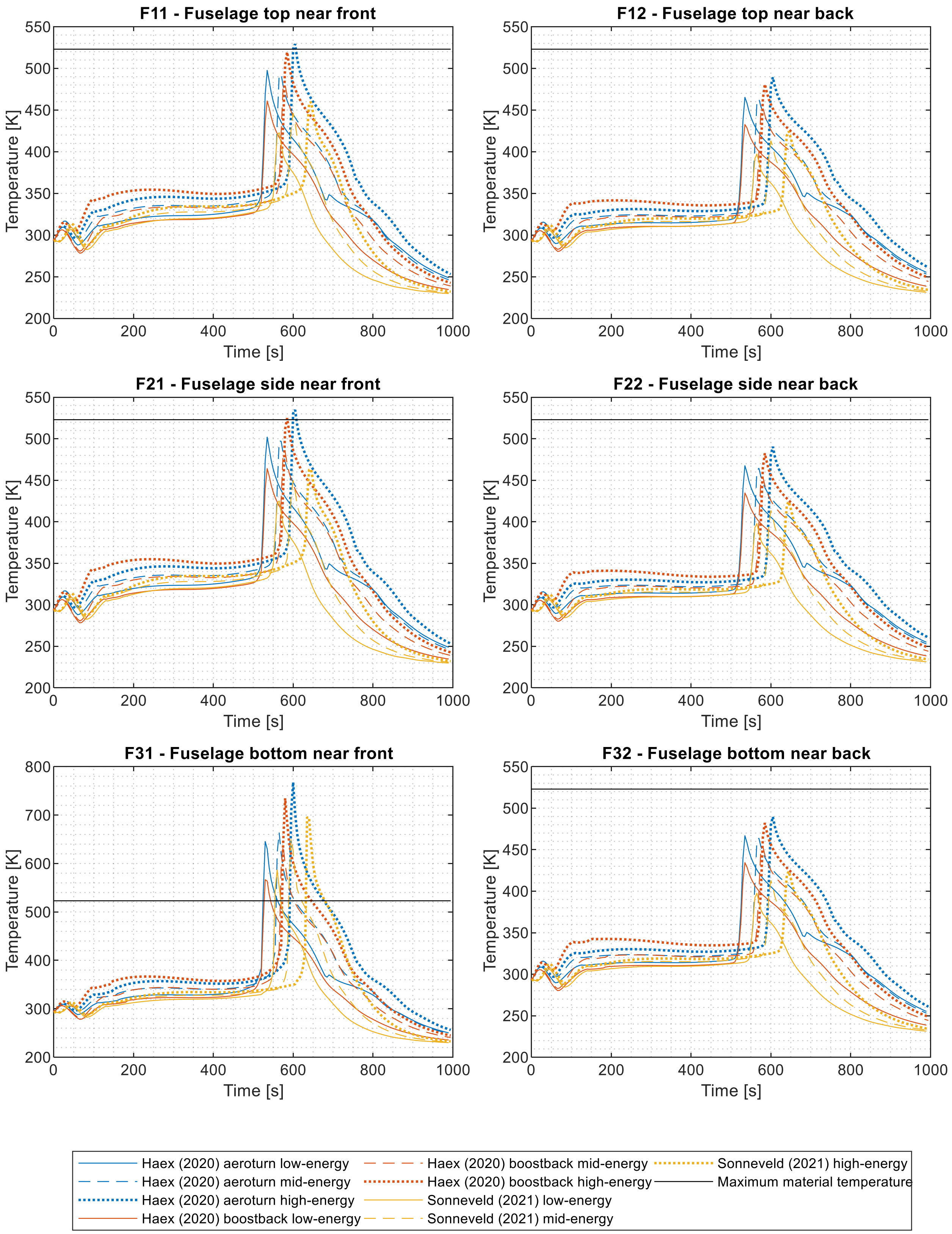

Figure C.5. BMI CF temperature results for fuselage locations along the external surface of the vehicle.

C.2. SiC CF

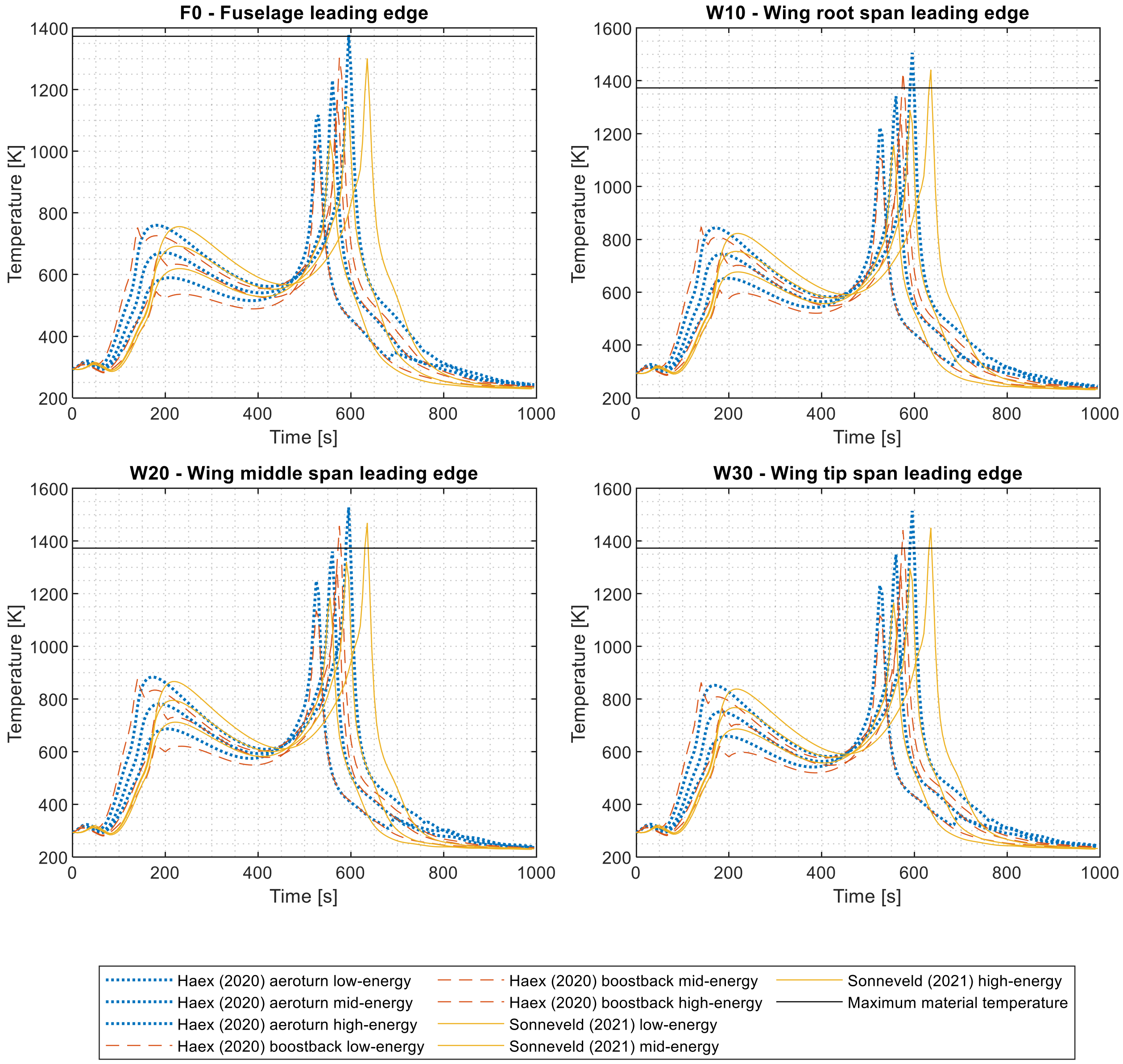

Figure C.6. SiC CF temperature results for leading edge locations along the external surface of the vehicle.

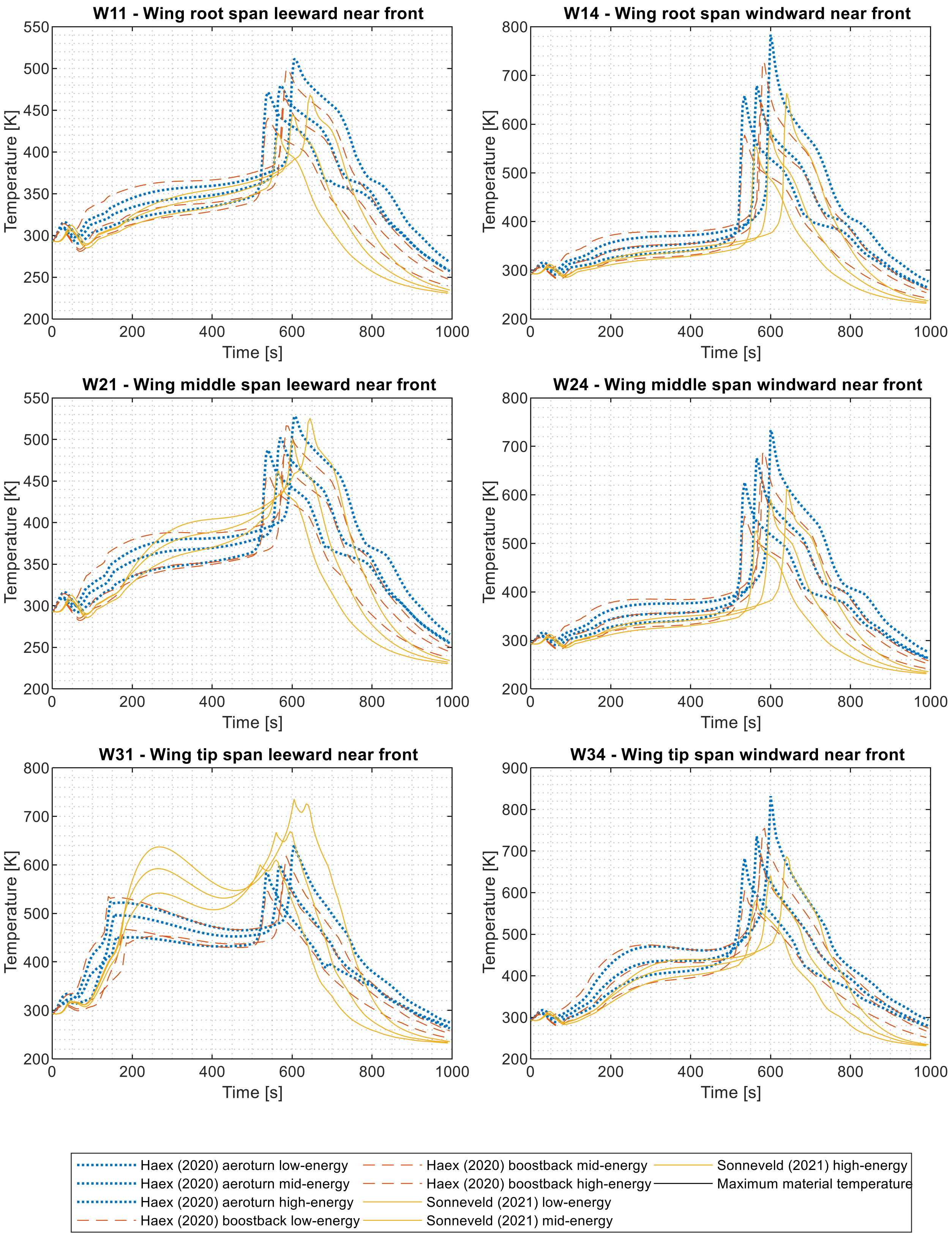

Figure C.7. SiC CF temperature results for front wing locations along the external surface of the vehicle.

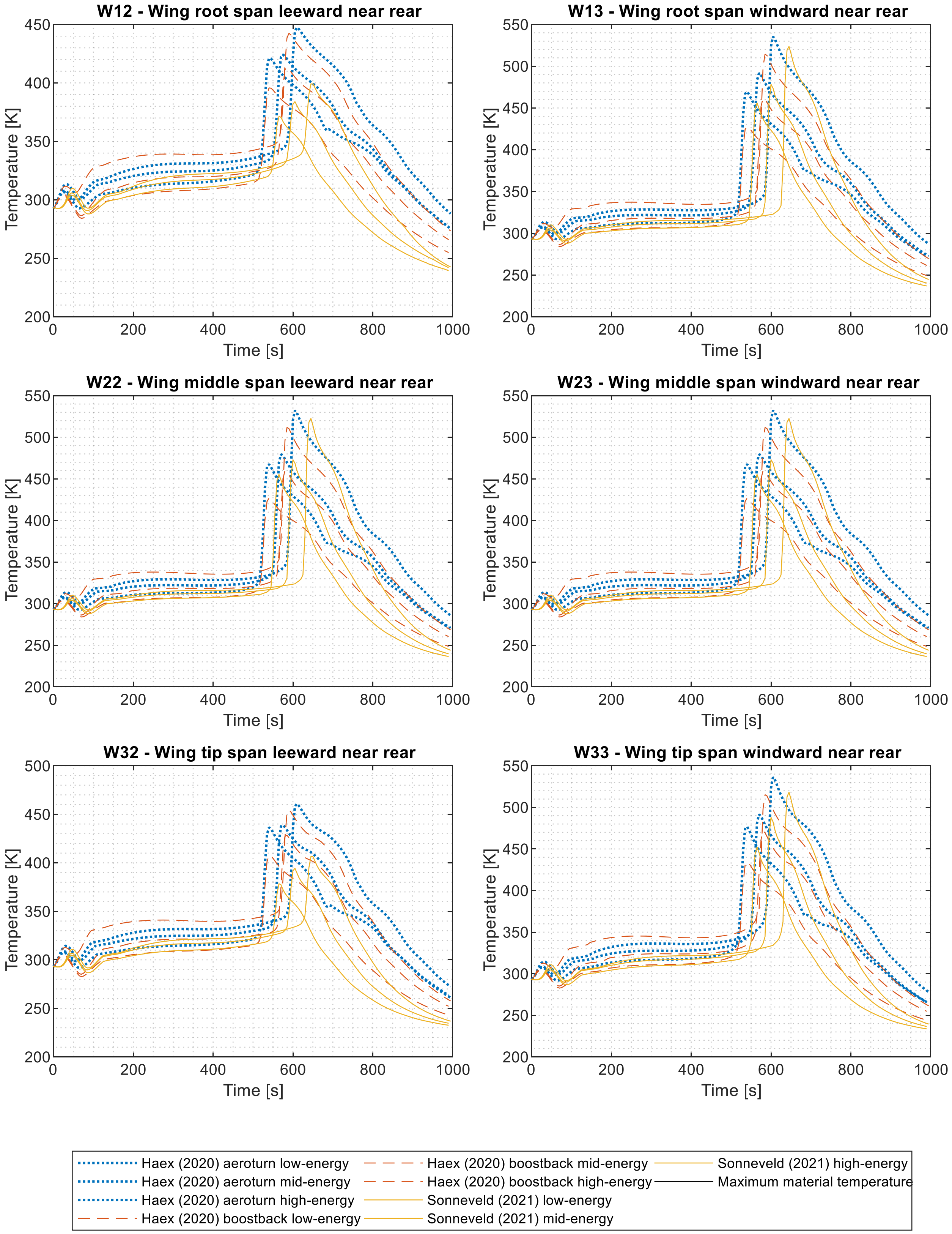

Figure C.8. SiC CF temperature results for rear wing locations along the external surface of the vehicle.

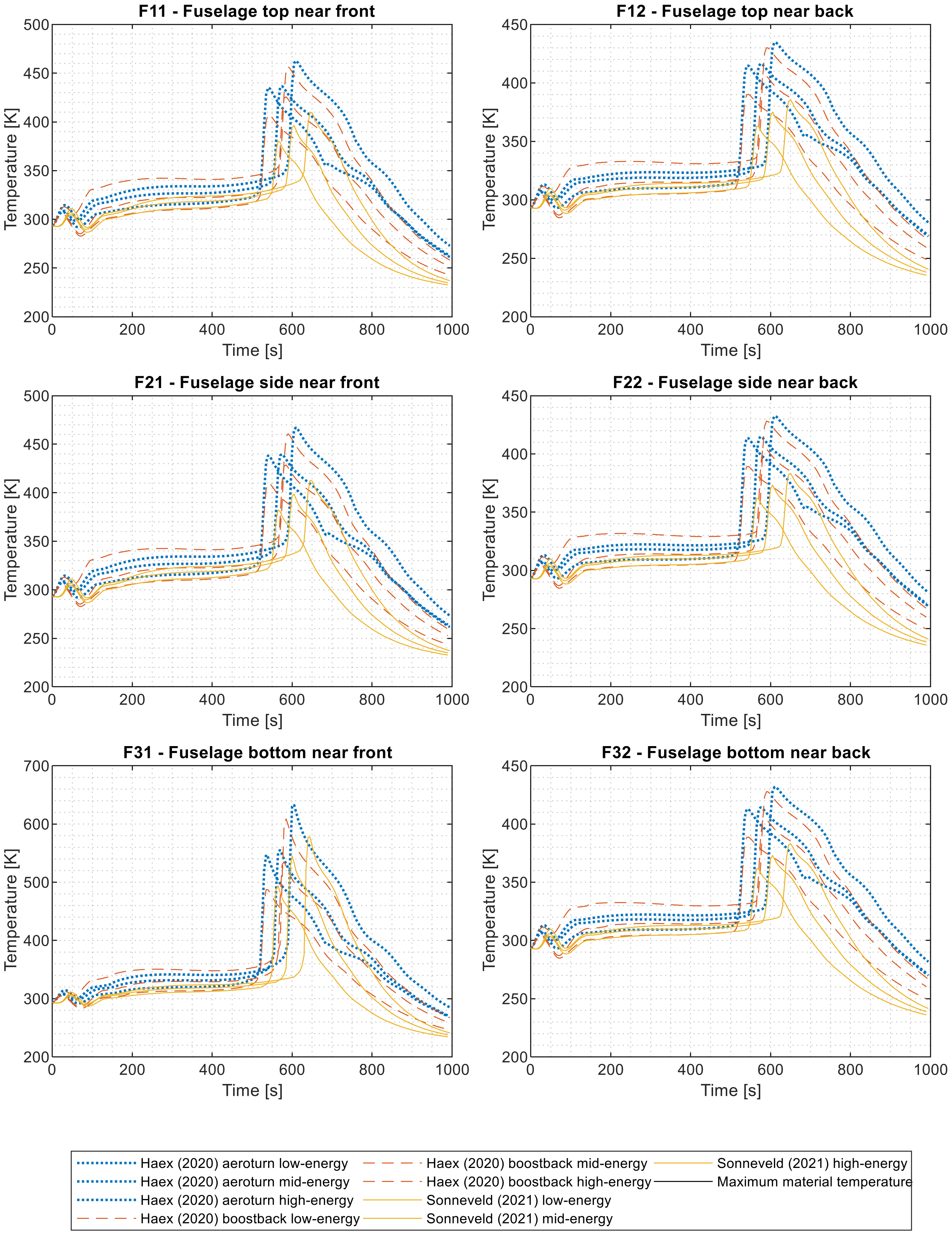

Figure C.9. SiC CF temperature results for fuselage locations along the external surface of the vehicle.

C.3. Titanium

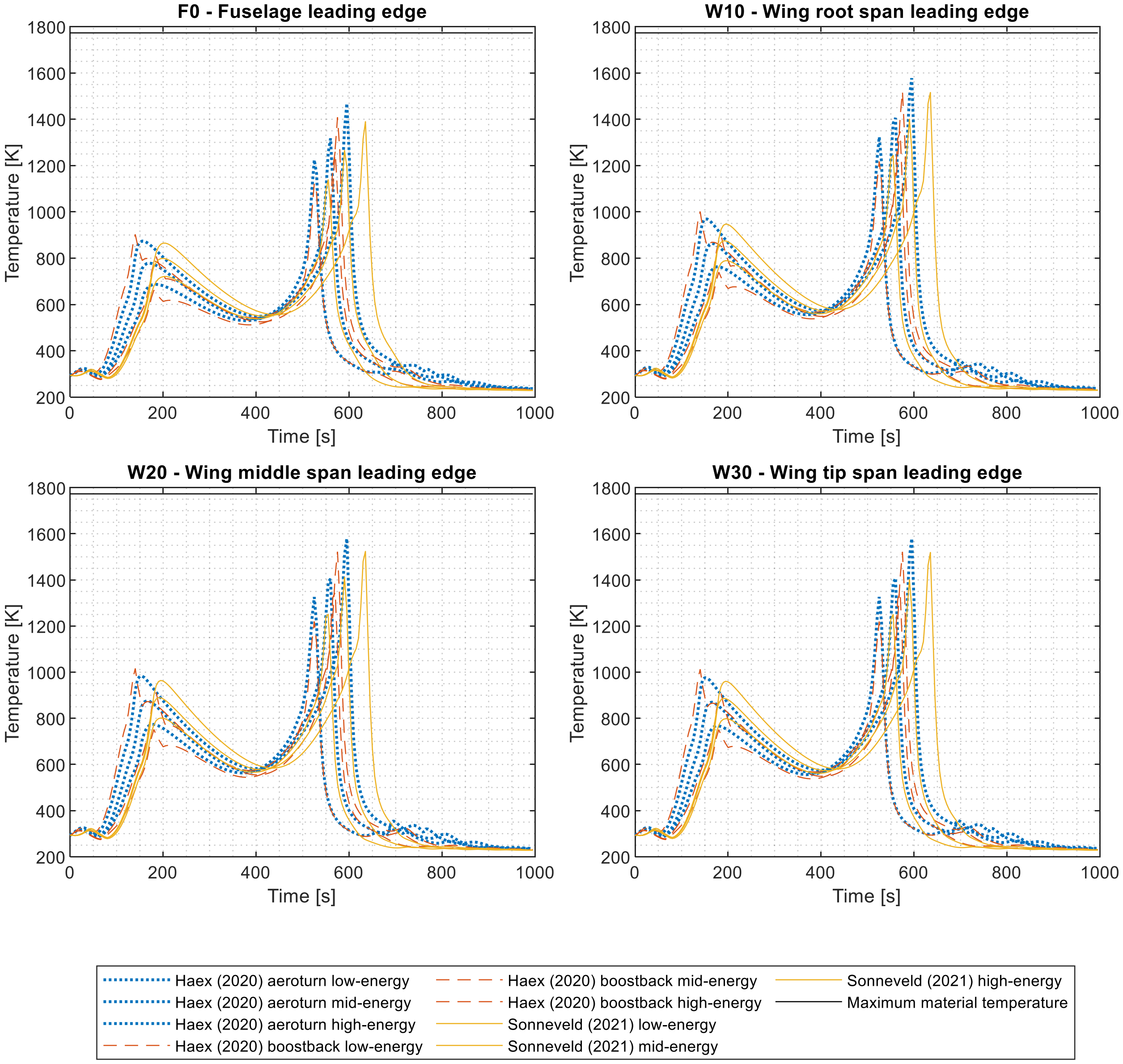

Figure C.10. Titanium temperature results for leading edge locations along the external surface of the vehicle.

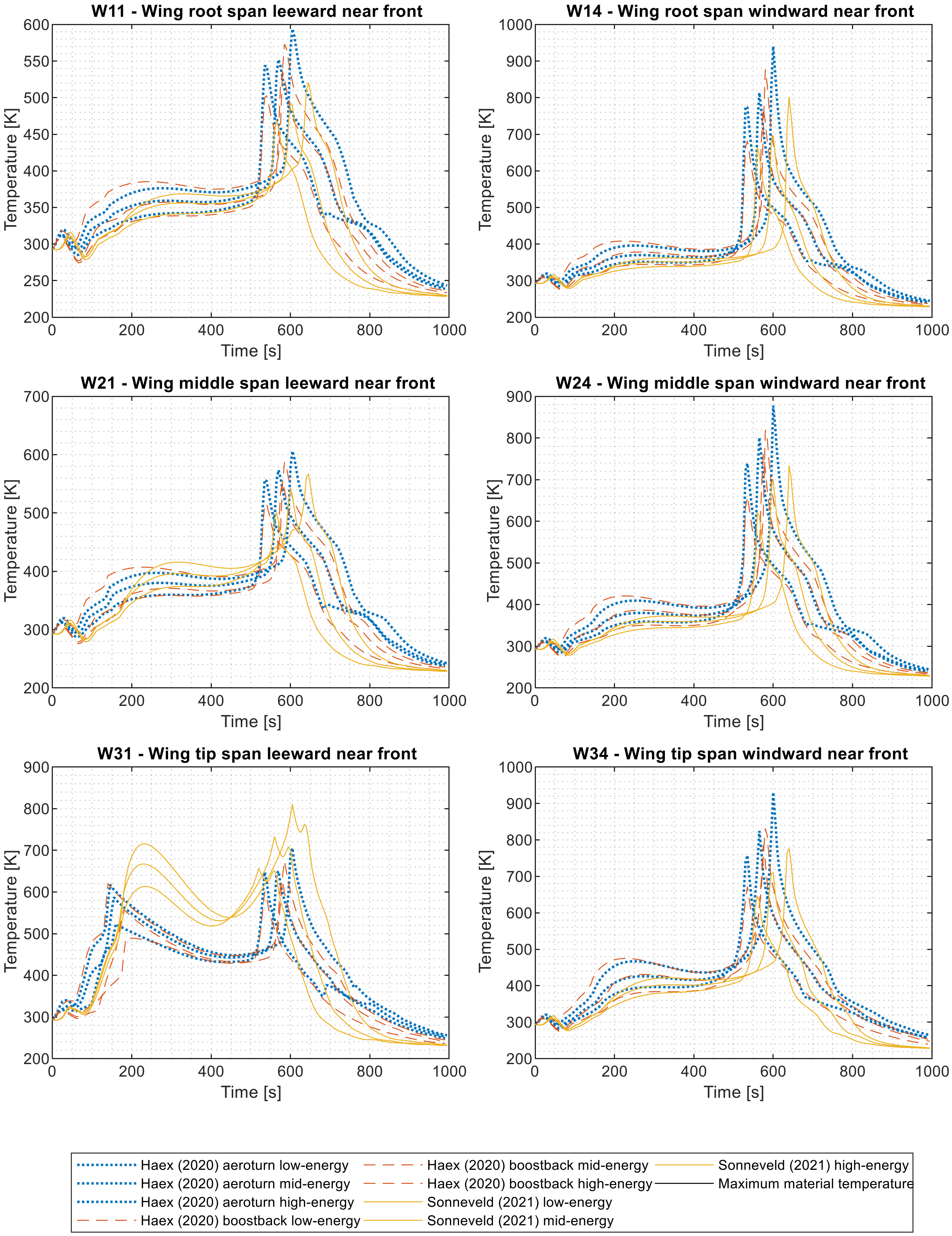

Figure C.11. Titanium temperature results for front wing locations along the external surface of the vehicle.

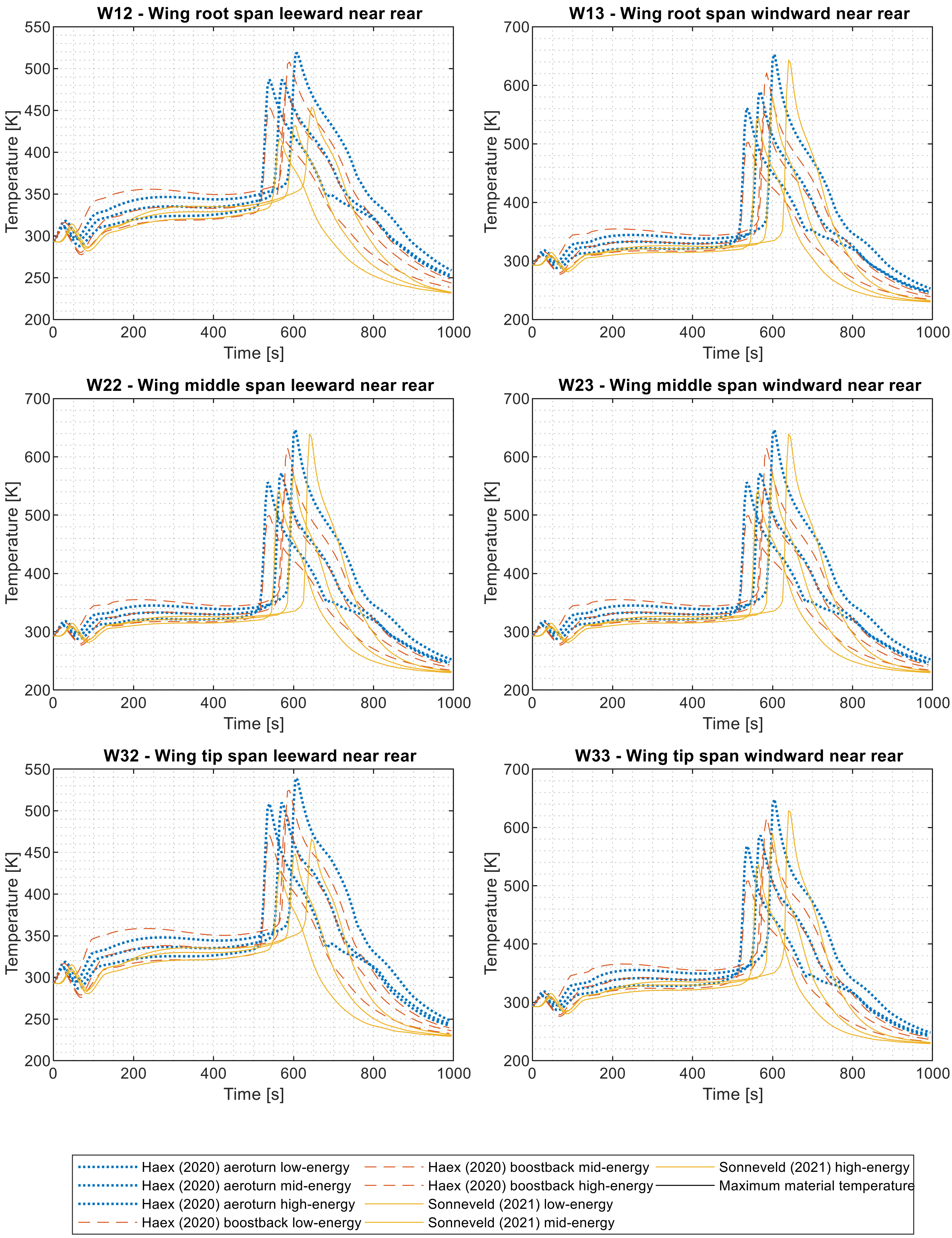

Figure C.12. Titanium temperature results for rear wing locations along the external surface of the vehicle.

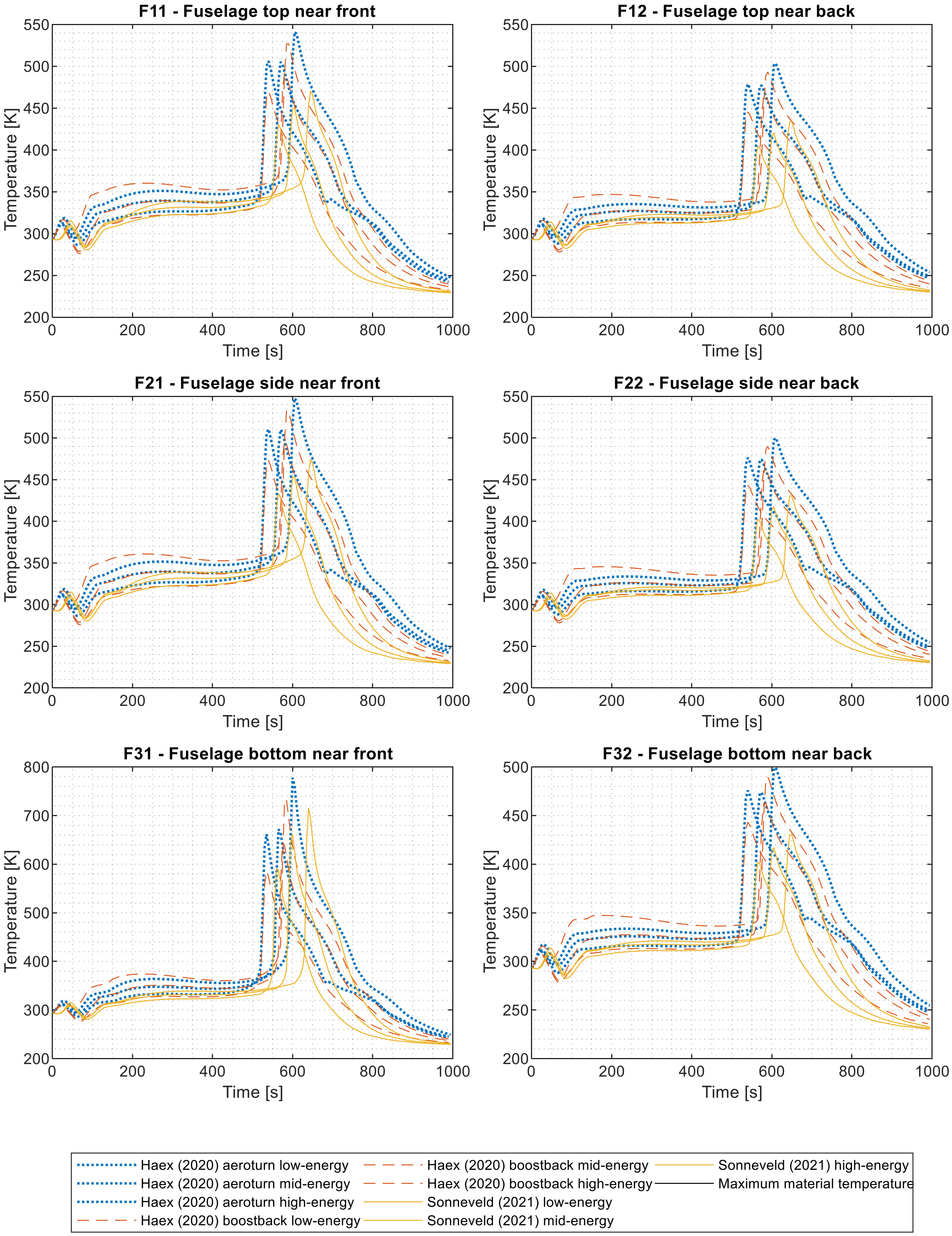

Figure C.13. Titanium temperature results for fuselage locations along the external surface of the vehicle.

C.4. Aluminium

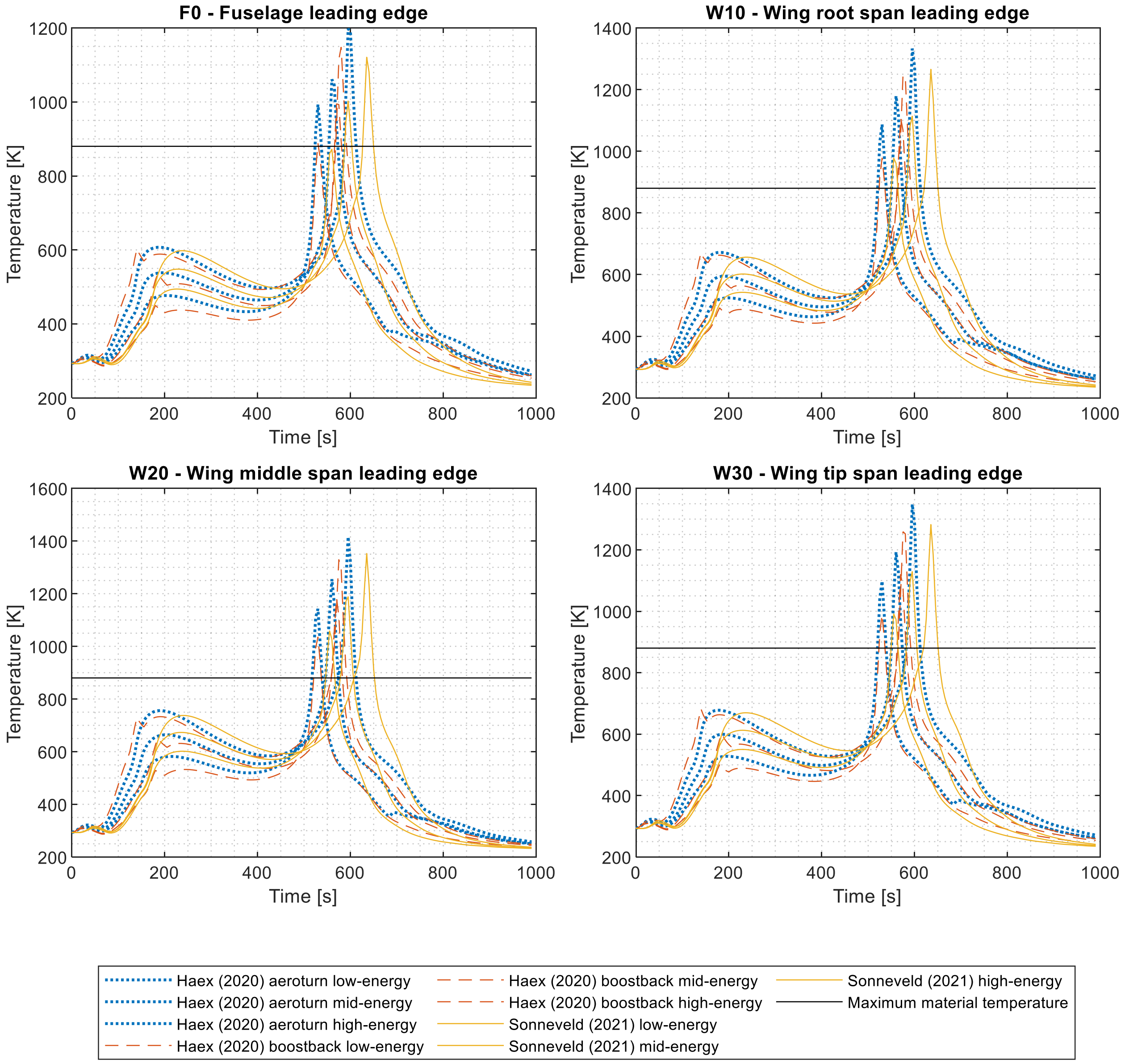

Figure C.14. Aluminium temperature results for leading edge locations along the external surface of the vehicle.

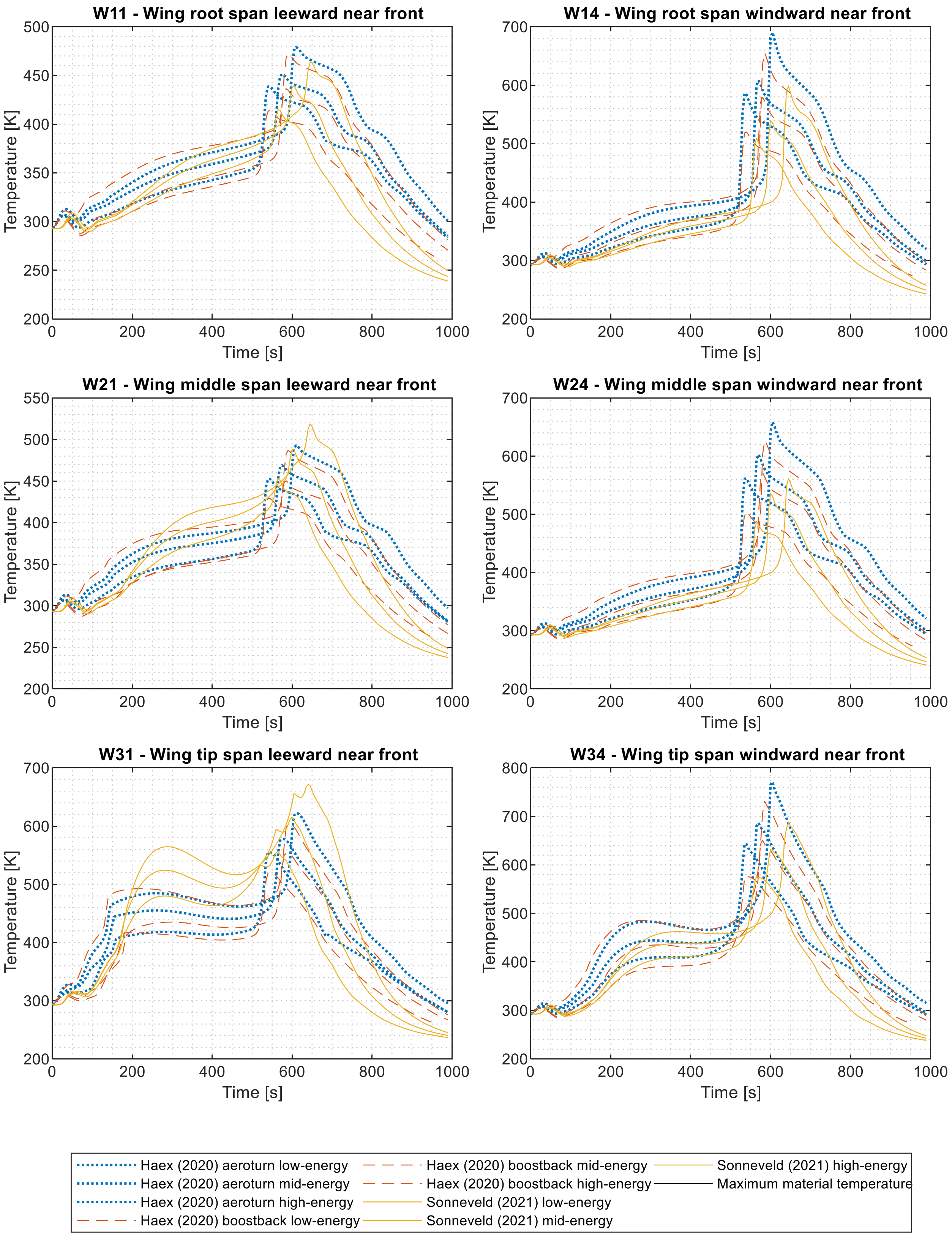

Figure C.15. Aluminium temperature results for front wing locations along the external surface of the vehicle.

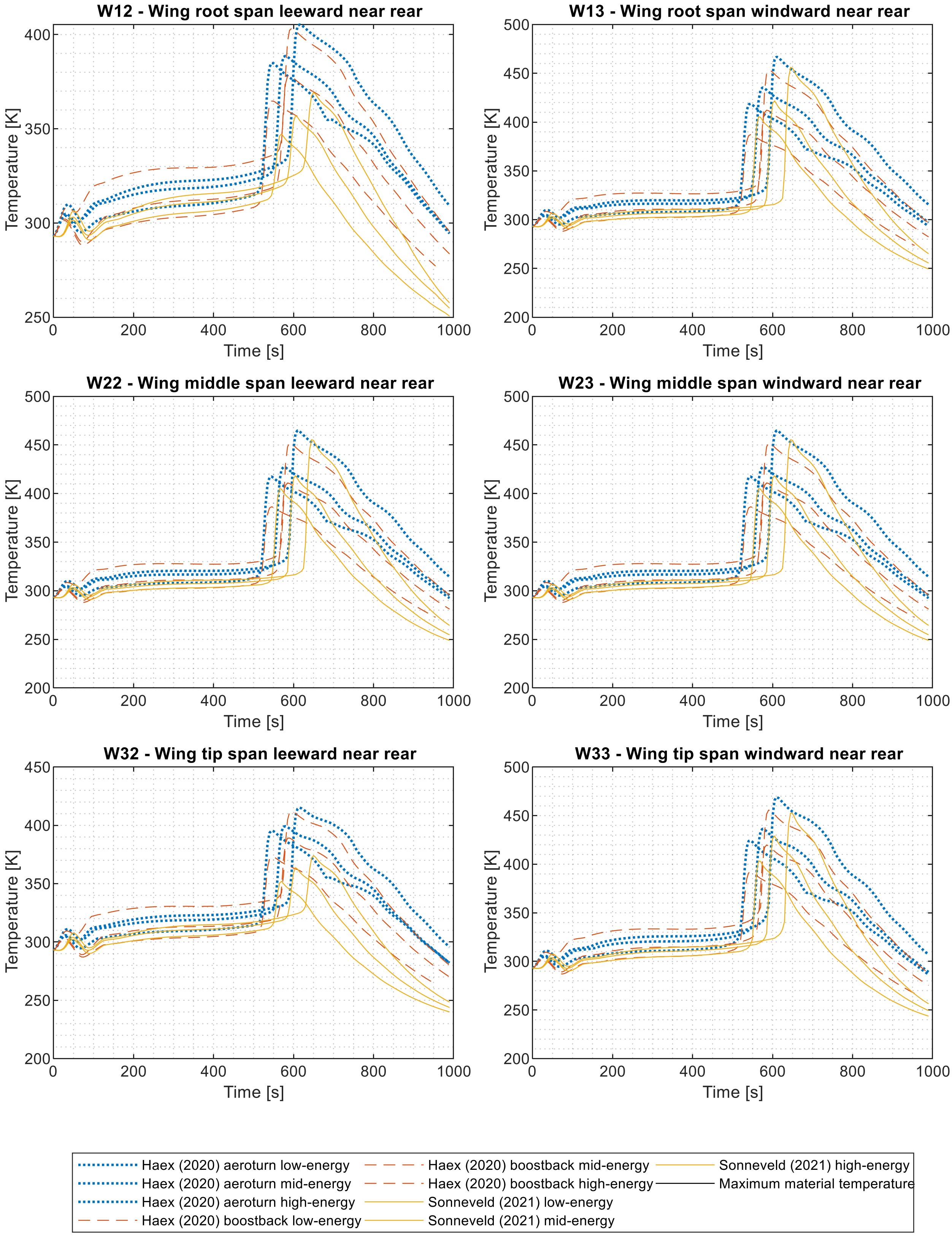

Figure C.16. Aluminium temperature results for rear wing locations along the external surface of the vehicle.

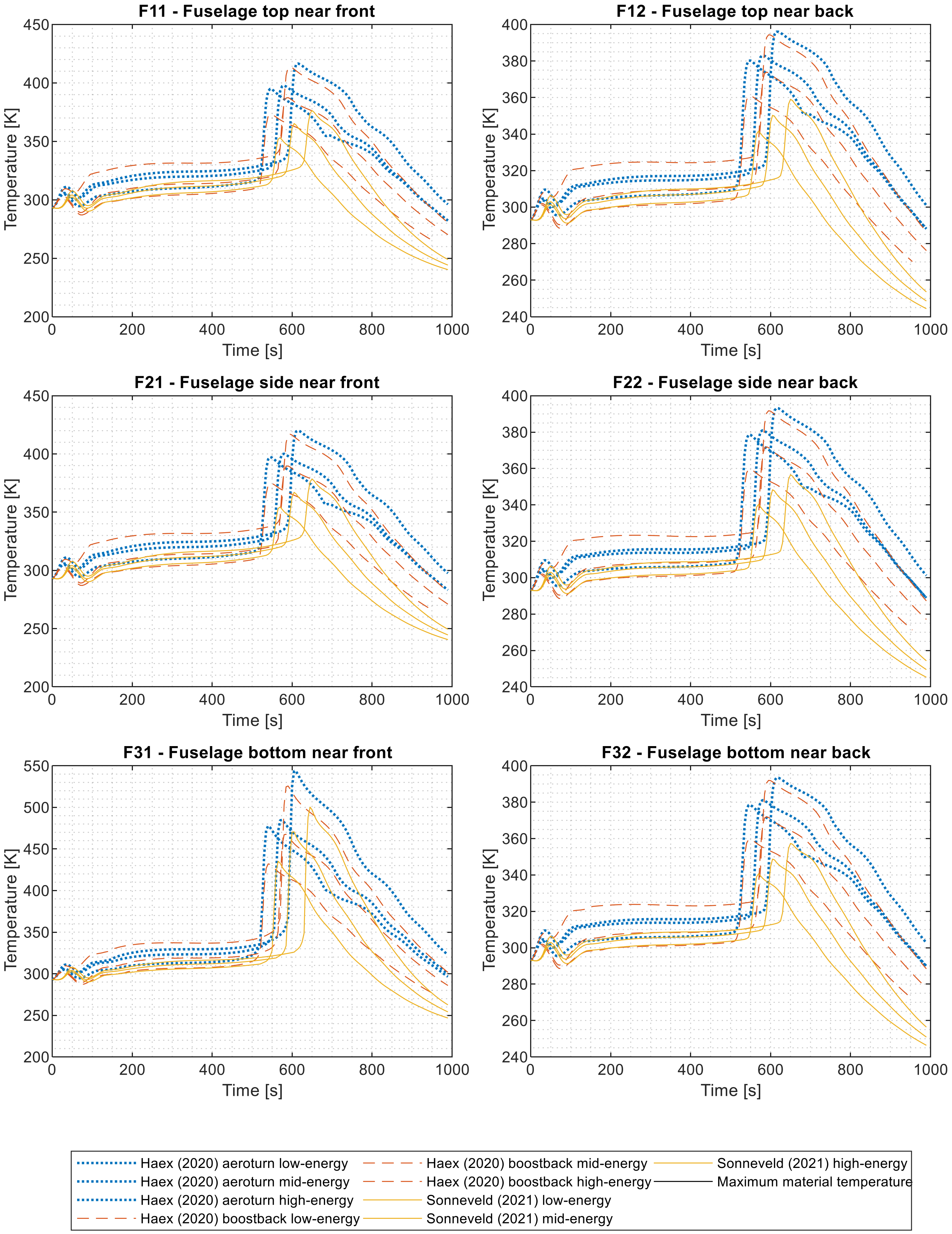

Figure C.17. Aluminium temperature results for fuselage locations along the external surface of the vehicle.

C.5. Material Comparison

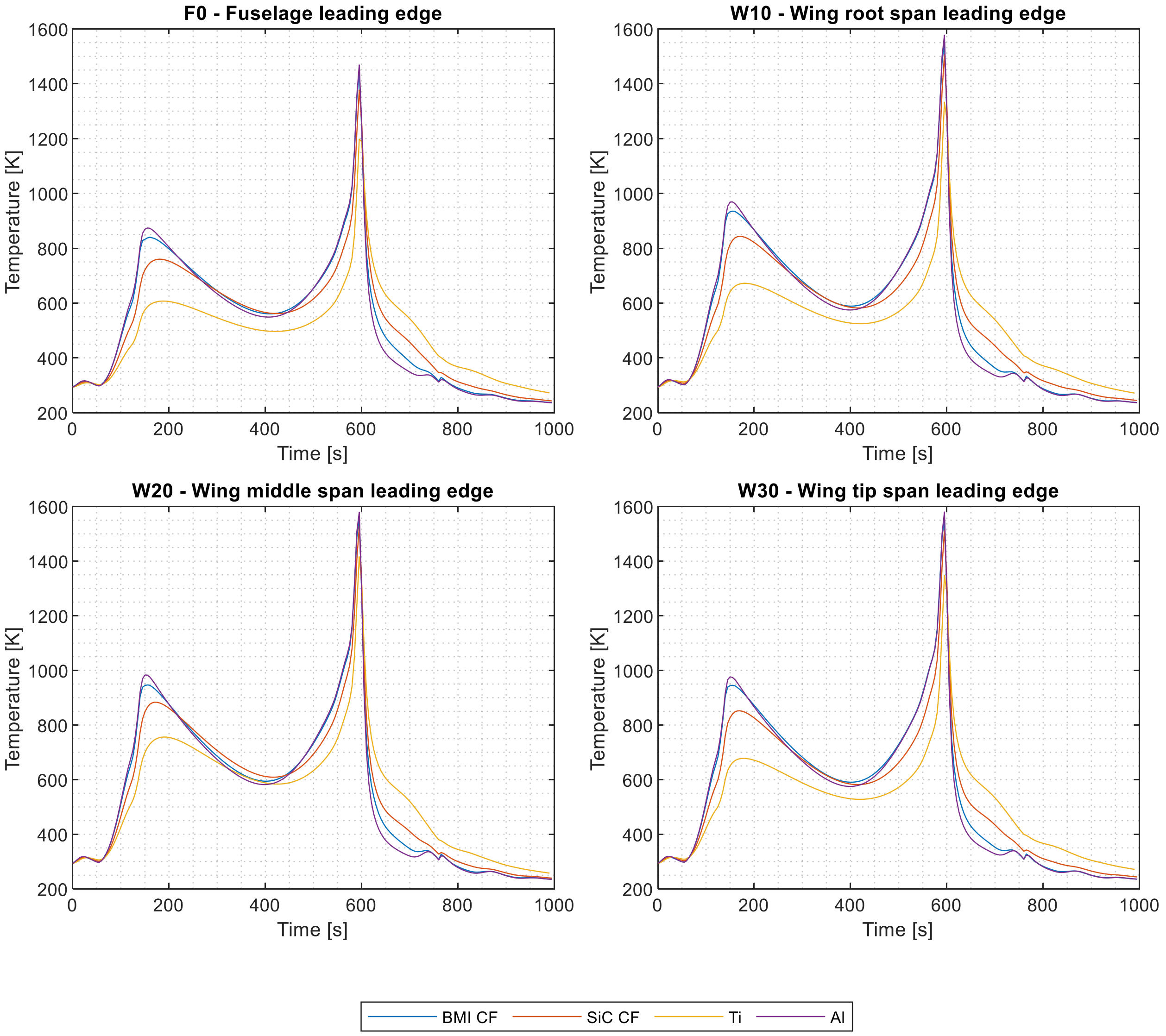

Figure C.18. BMI CF, SiC CF, titanium and aluminium temperature results for leading edge locations along the external surface of the vehicle for the Haex (2020) aeroturn high-energy trajectory.

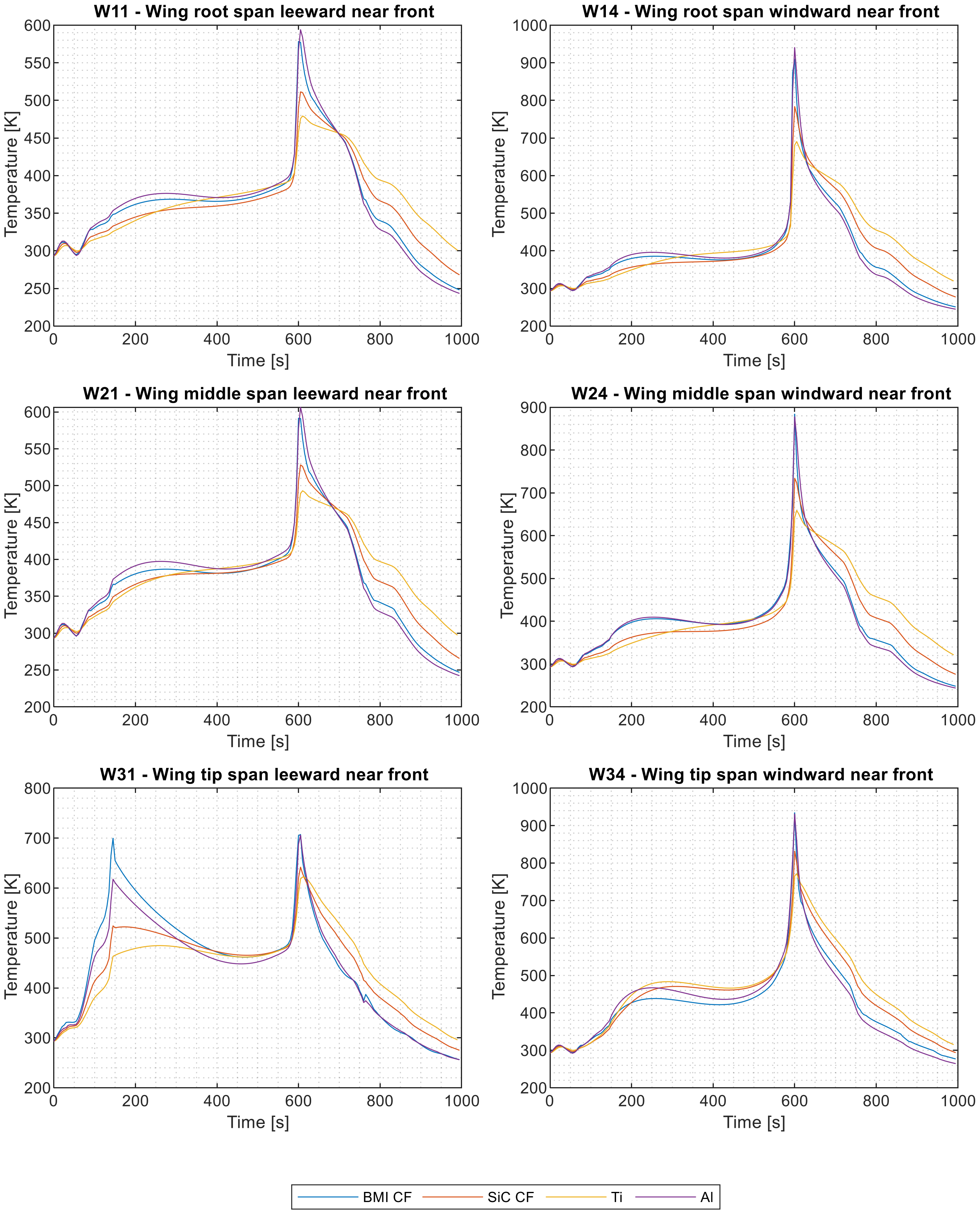
W11 - Wing root span leeward near front

W14 - Wing root span windward near front

W21 - Wing middle span leeward near front

W24 - Wing middle span windward near front

W31 - Wing tip span leeward near front

W34 - Wing tip span windward near front

Figure C.19. BMI CF, SiC CF, titanium and aluminium temperature results for wing front locations along the external surface of the vehicle for the Haex (2020) aeroturn high-energy trajectory.

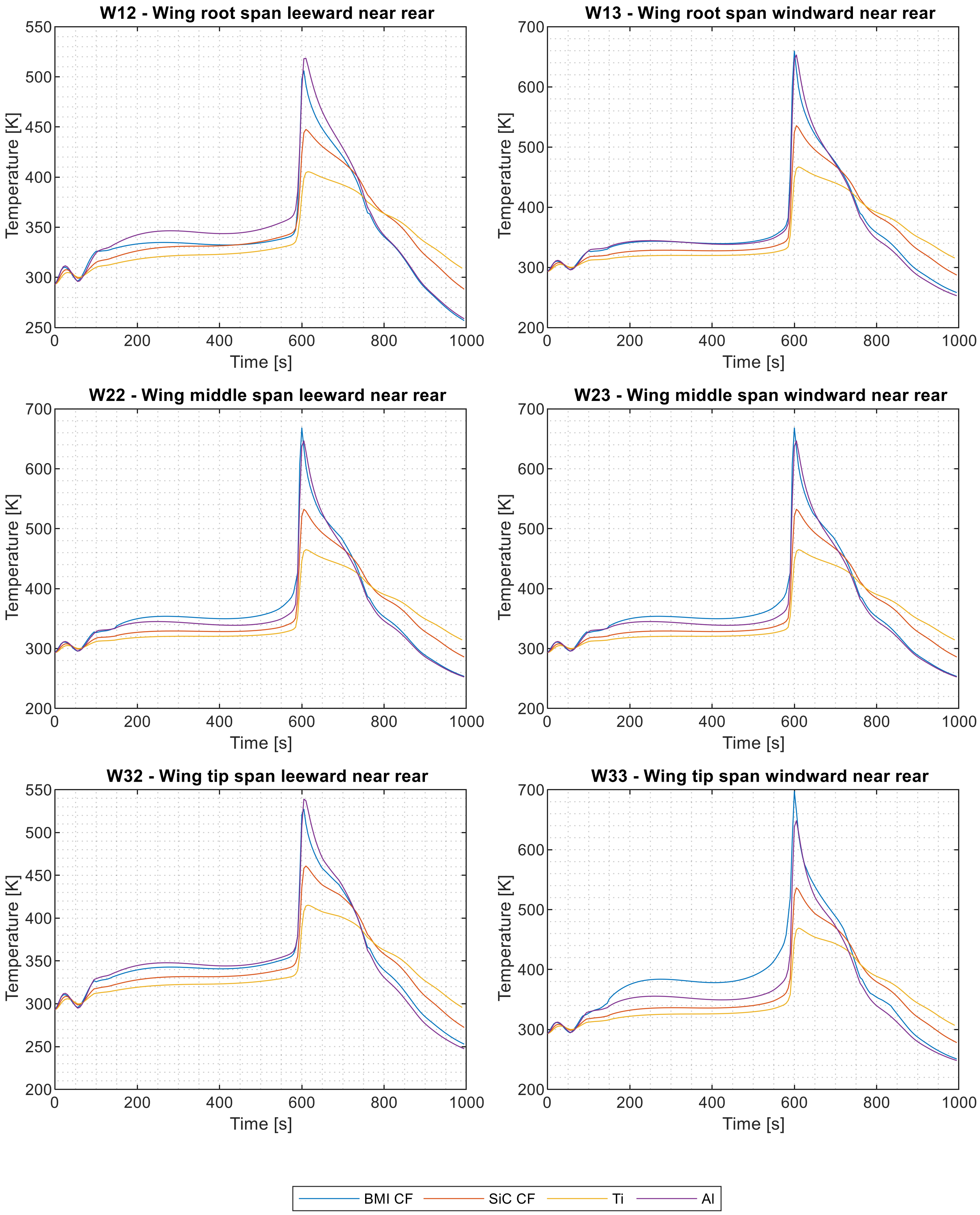

Figure C.20. BMI CF, SiC CF, titanium and aluminium temperature results wing rear locations along the external surface of the vehicle for the Haex (2020) aeroturn high-energy trajectory.

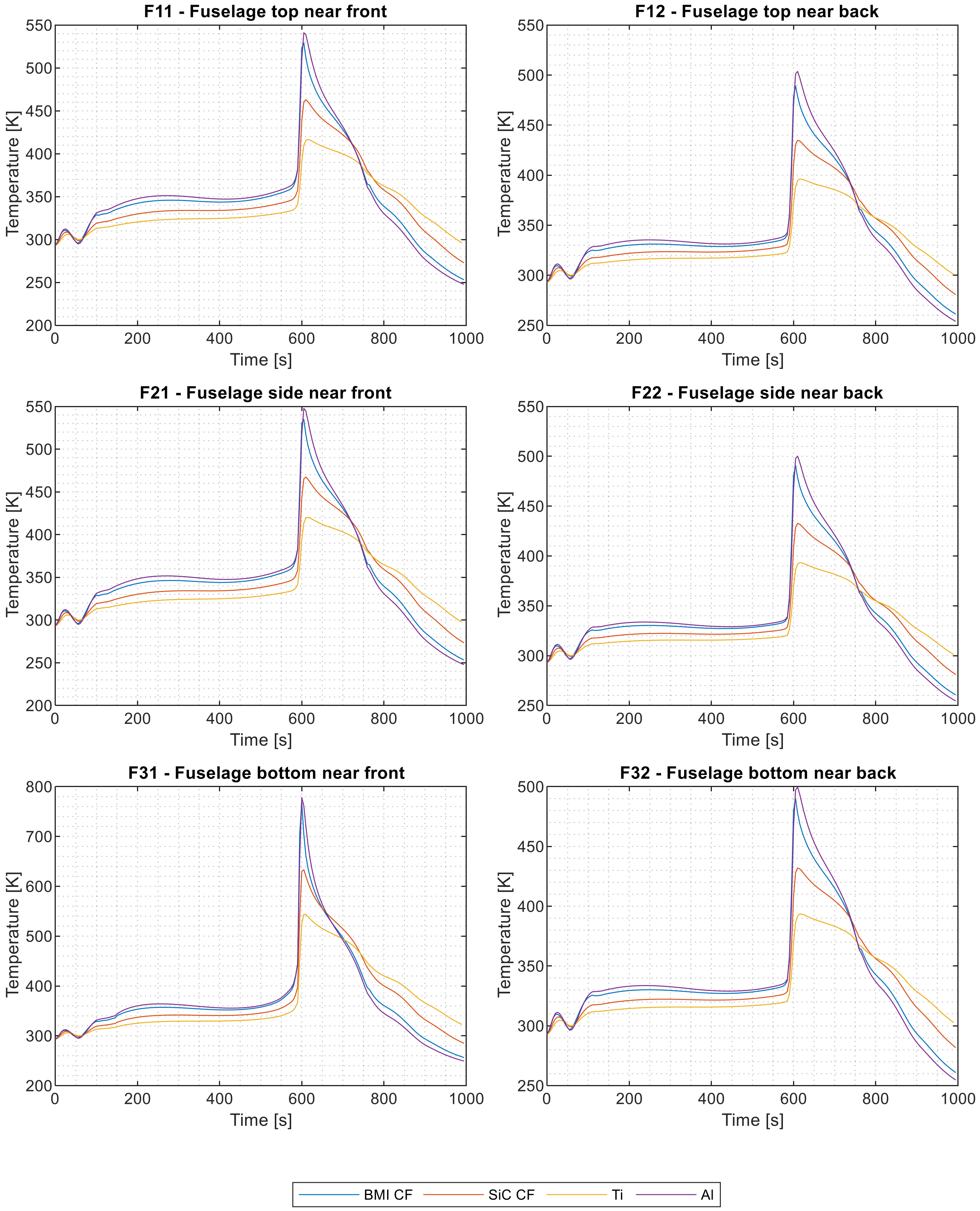
F11 - Fuselage top near front

F12 - Fuselage top near back

F21 - Fuselage side near front

F22 - Fuselage side near back

F31 - Fuselage bottom near front

F32 - Fuselage bottom near back

Figure C.21. BMI CF, SiC CF, titanium and aluminium temperature results for fuselage locations along the external surface of the vehicle for the Haex (2020) aeroturn high-energy trajectory.

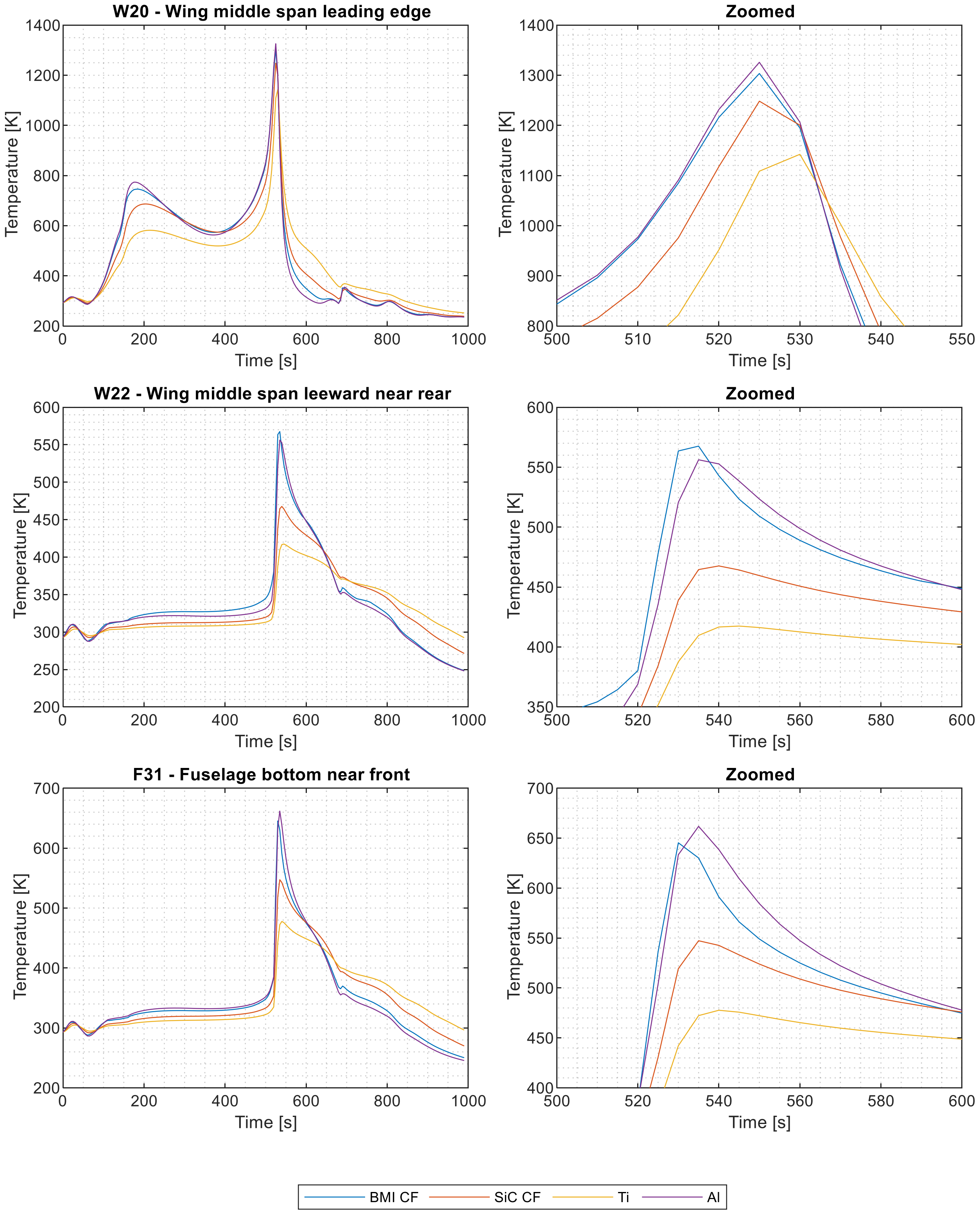

Figure C.22. BMI CF, SiC CF, titanium and aluminium temperature results for selected locations along the external surface of the vehicle for the Haex (2020) aeroturn low-energy trajectory.

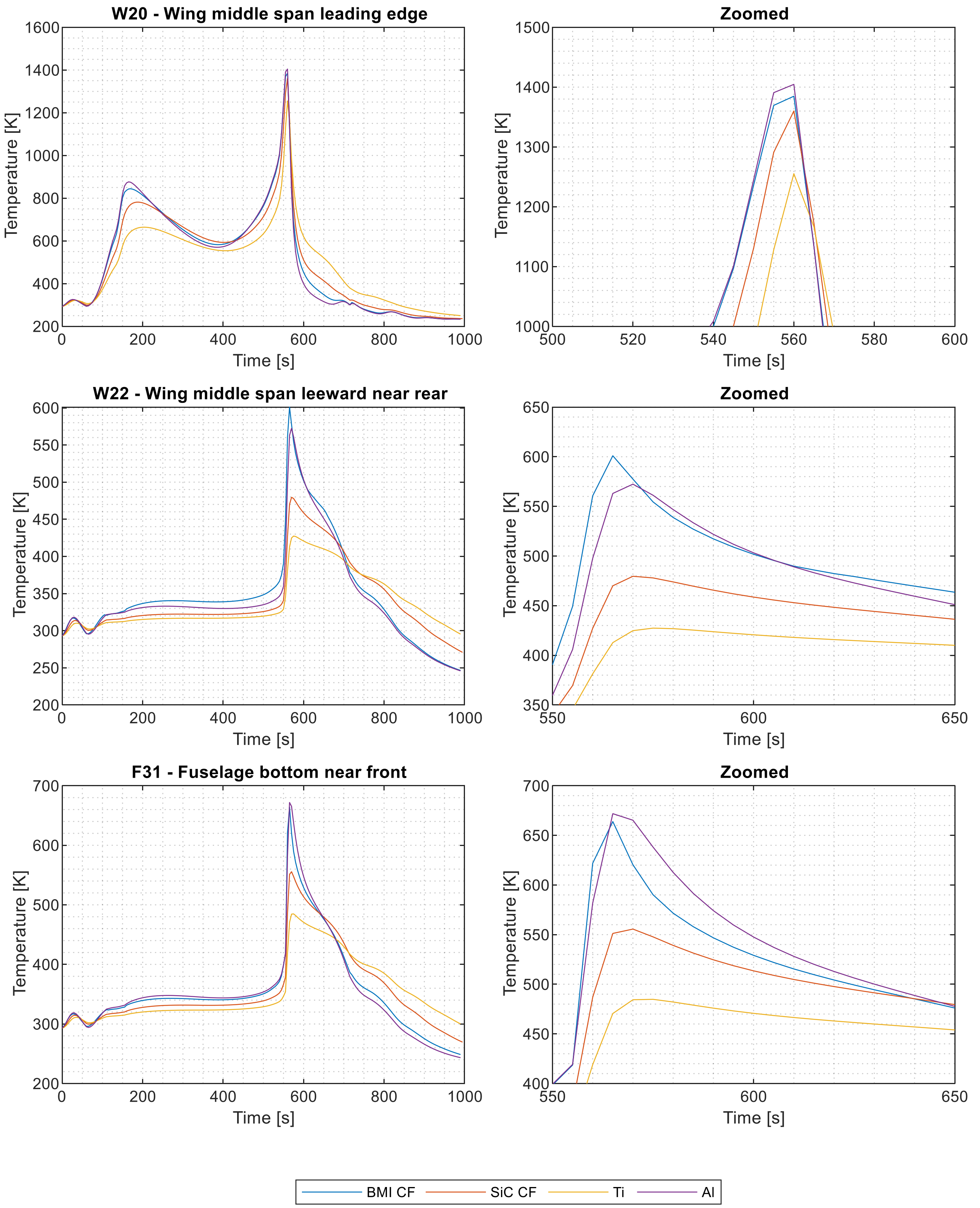

Figure C.23. BMI CF, SiC CF, titanium and aluminium temperature results for selected locations along the external surface of the vehicle for the Haex (2020) aeroturn mid-energy trajectory.

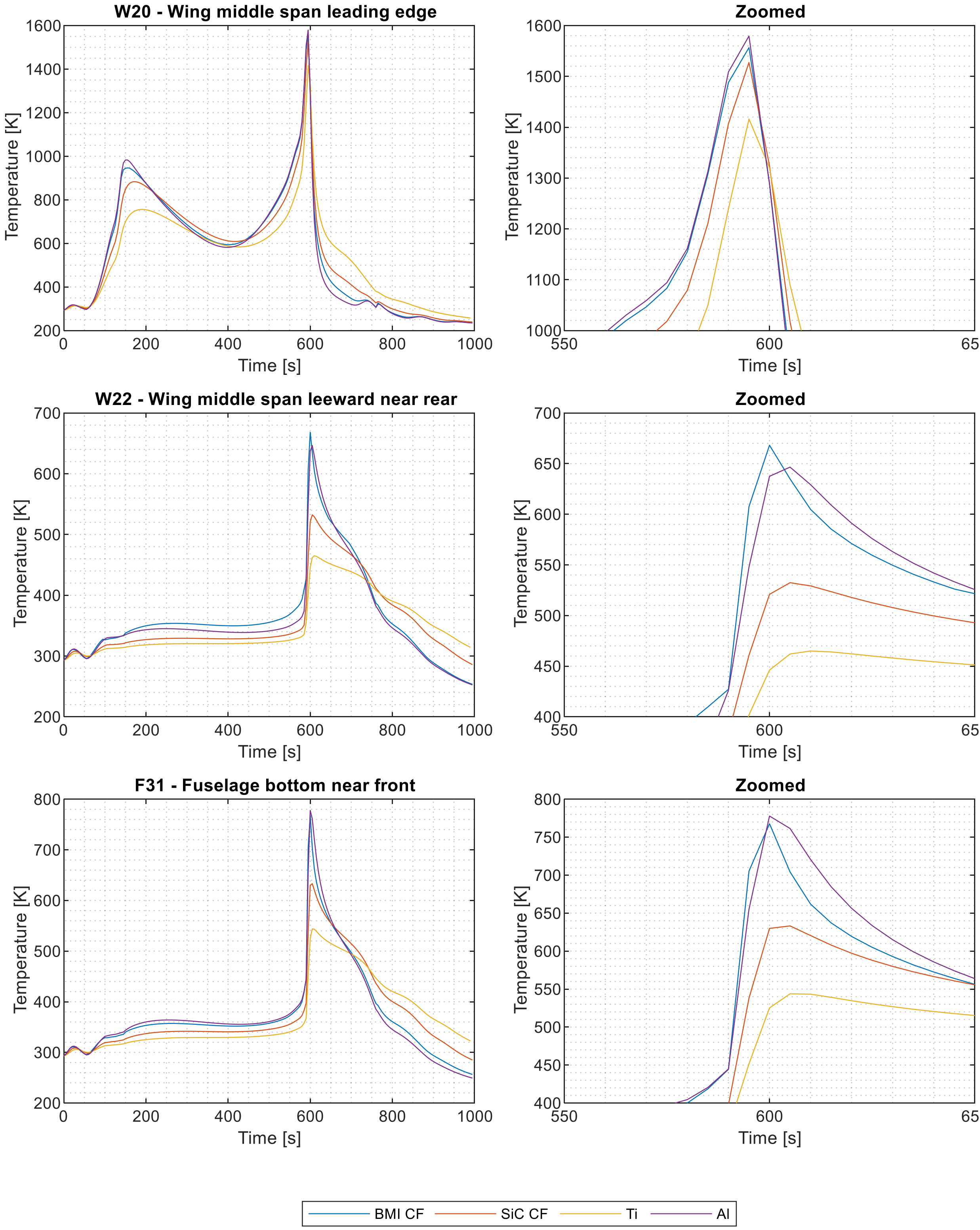

Figure C.24. BMI CF, SiC CF, titanium and aluminium temperature results for selected locations along the external surface of the vehicle for the Haex (2020) aeroturn high-energy trajectory.

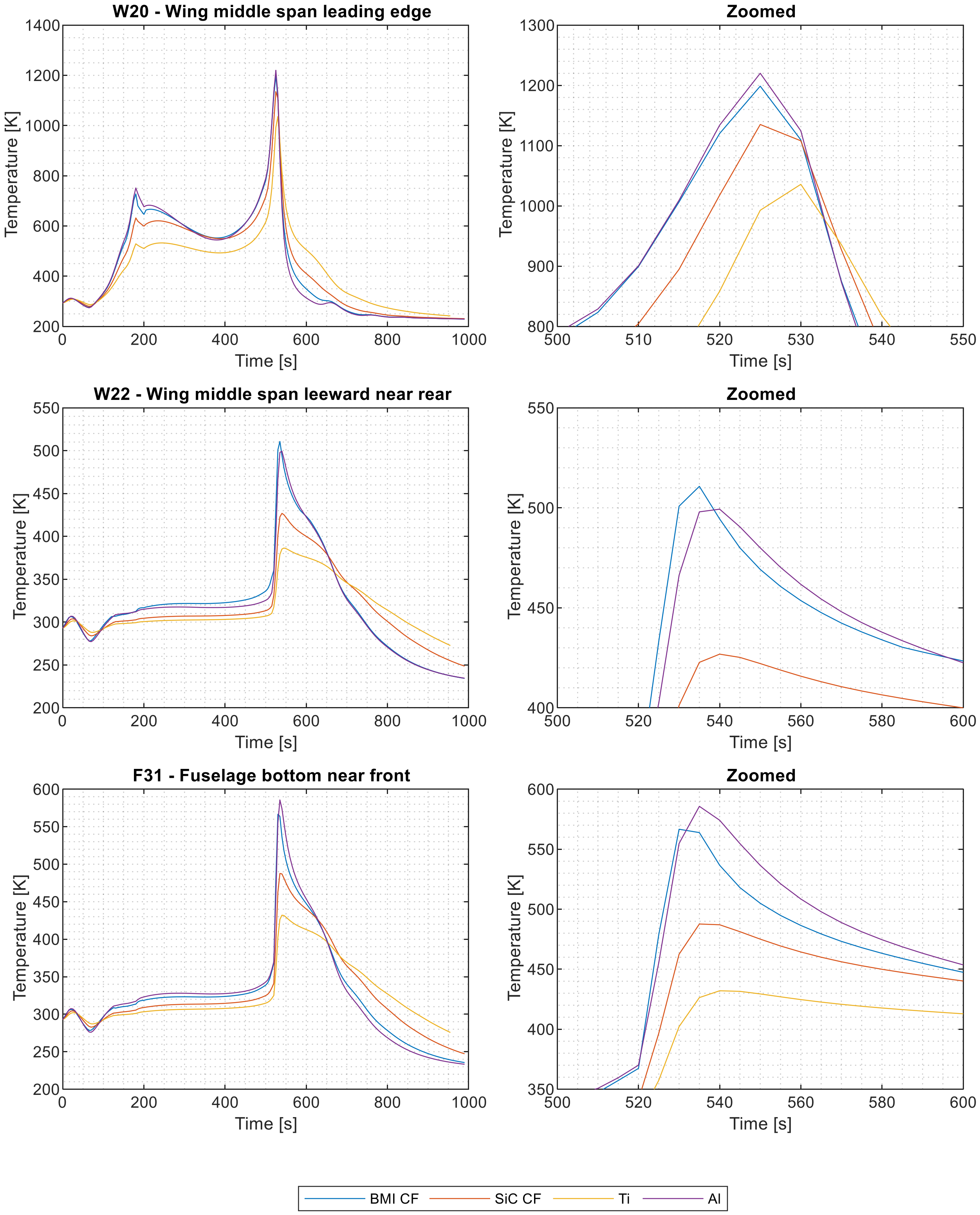

Figure C.25. BMI CF, SiC CF, titanium and aluminium temperature results for selected locations along the external surface of the vehicle for the Haex (2020) boostback low-energy trajectory.

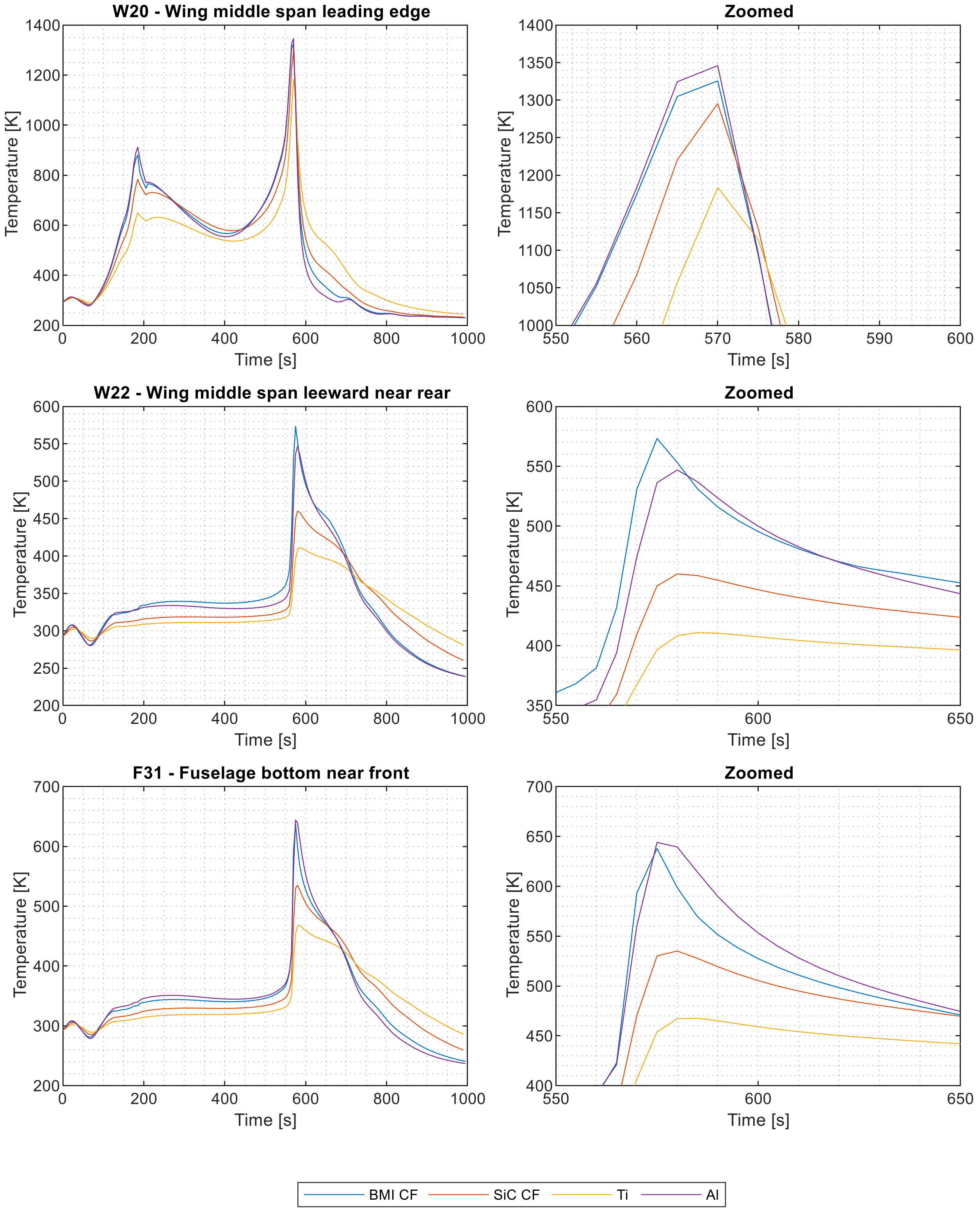

Figure C.26. BMI CF, SiC CF, titanium and aluminium temperature results for selected locations along the external surface of the vehicle for the Haex (2020) boostback mid-energy trajectory.

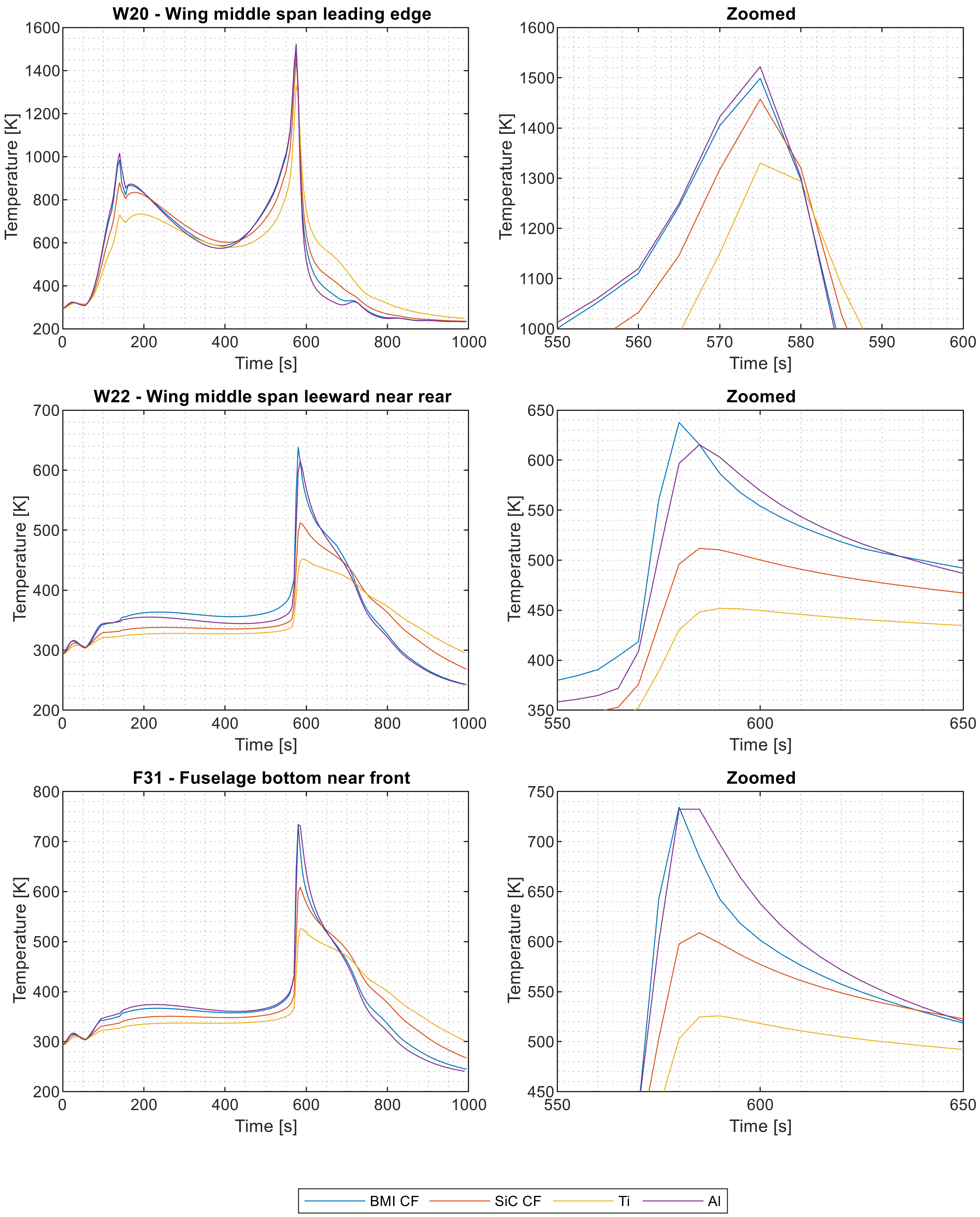

Figure C.27. BMI CF, SiC CF, titanium and aluminium temperature results for selected locations along the external surface of the vehicle for the Haex (2020) boostback high-energy trajectory.

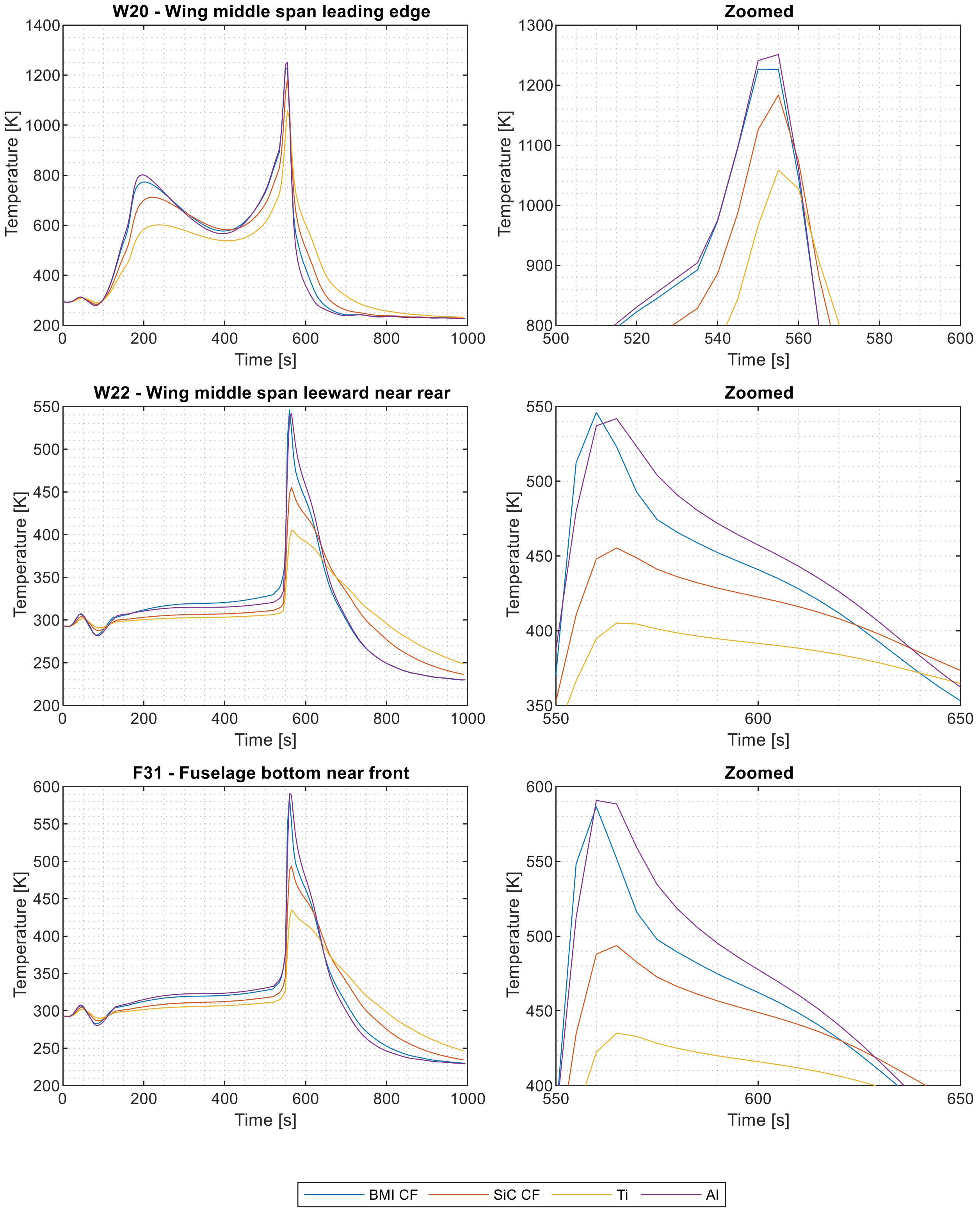

Figure C.28. BMI CF, SiC CF, titanium and aluminium temperature results for selected locations along the external surface of the vehicle for the Sonneveld (2021) low-energy trajectory.

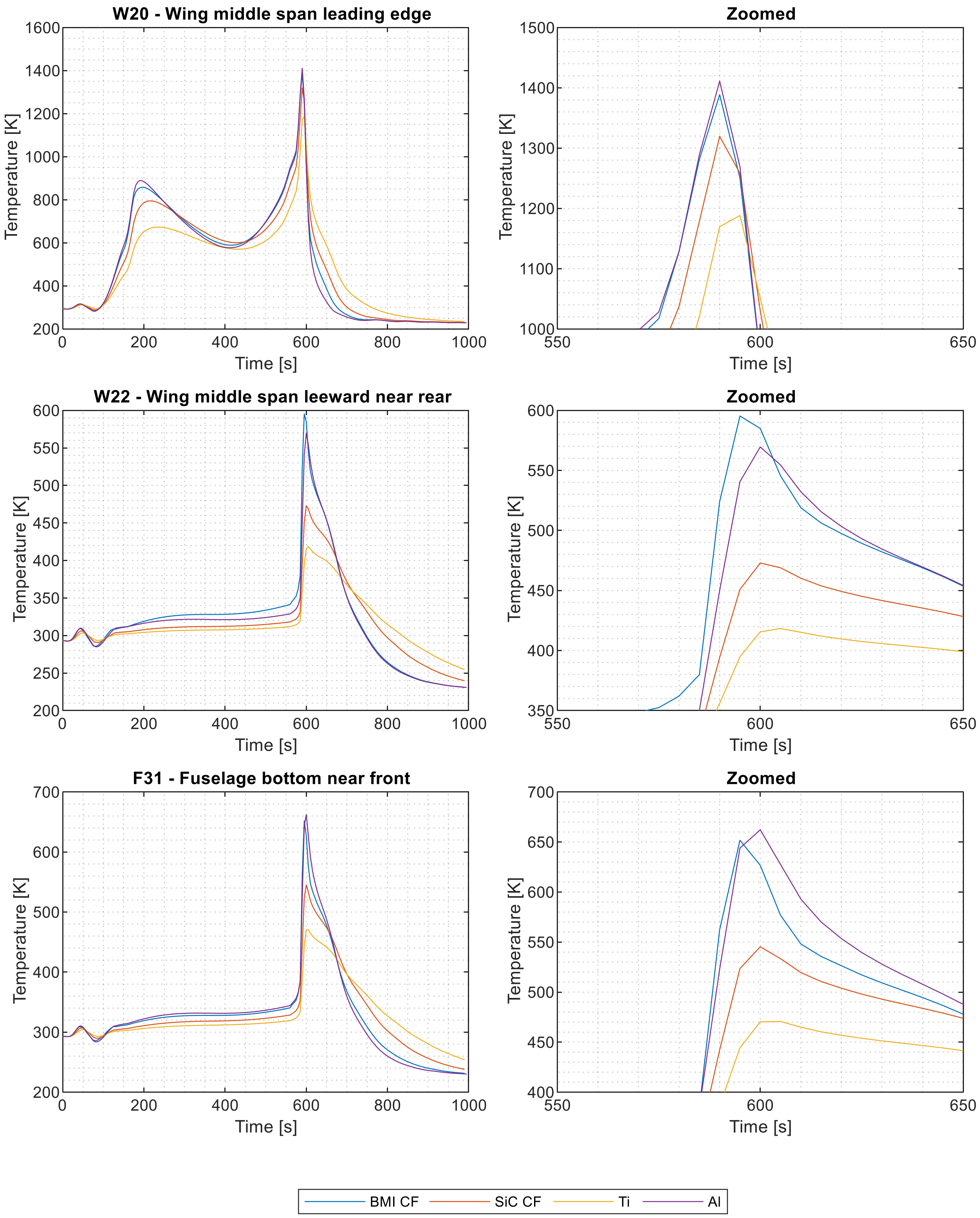

Figure C.29. BMI CF, SiC CF, titanium and aluminium temperature results for selected locations along the external surface of the vehicle for the Sonneveld (2021) mid-energy trajectory.

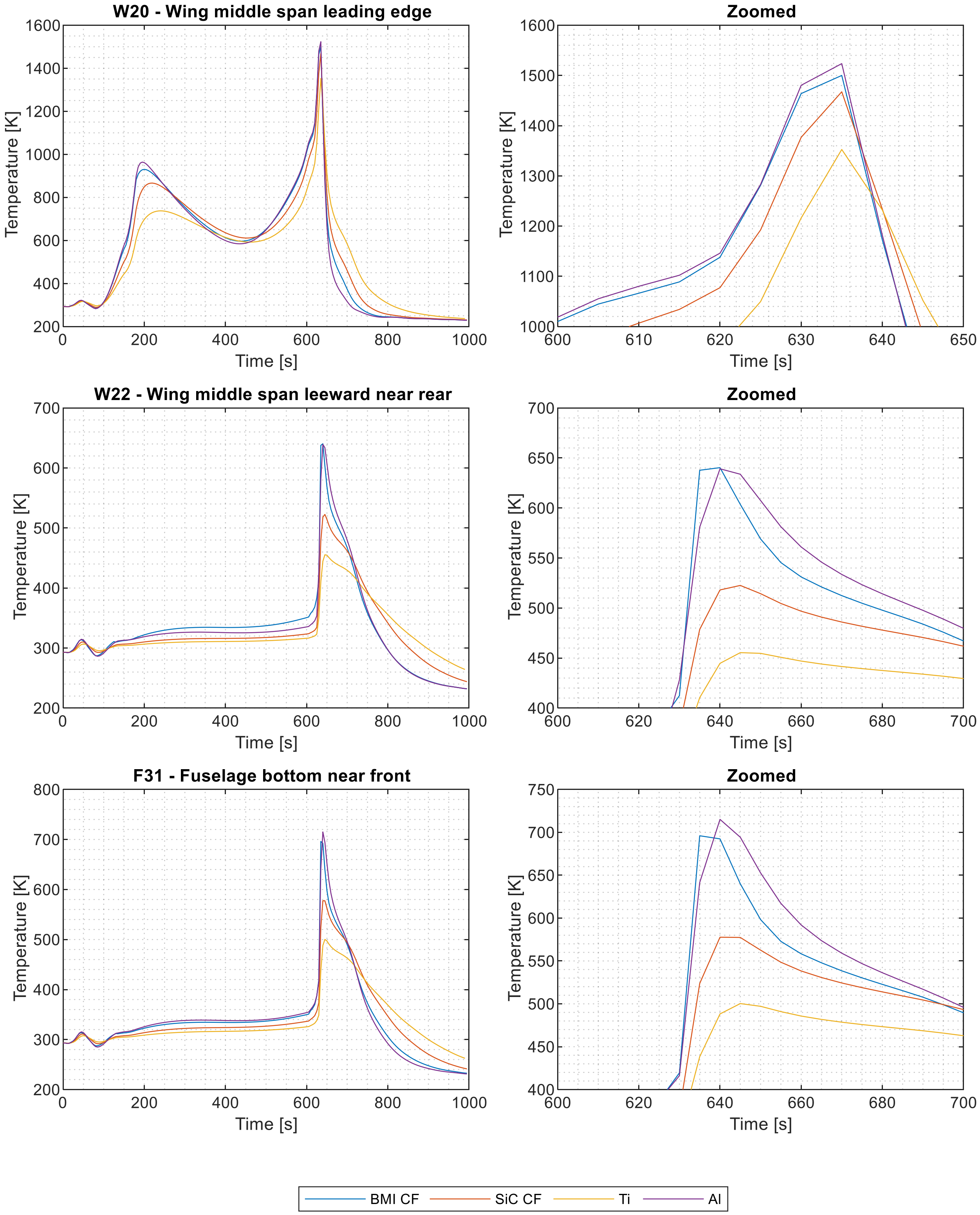

Figure C.30. BMI CF, SiC CF, titanium and aluminium temperature results for selected locations along the external surface of the vehicle for the Sonneveld (2021) high-energy trajectory.

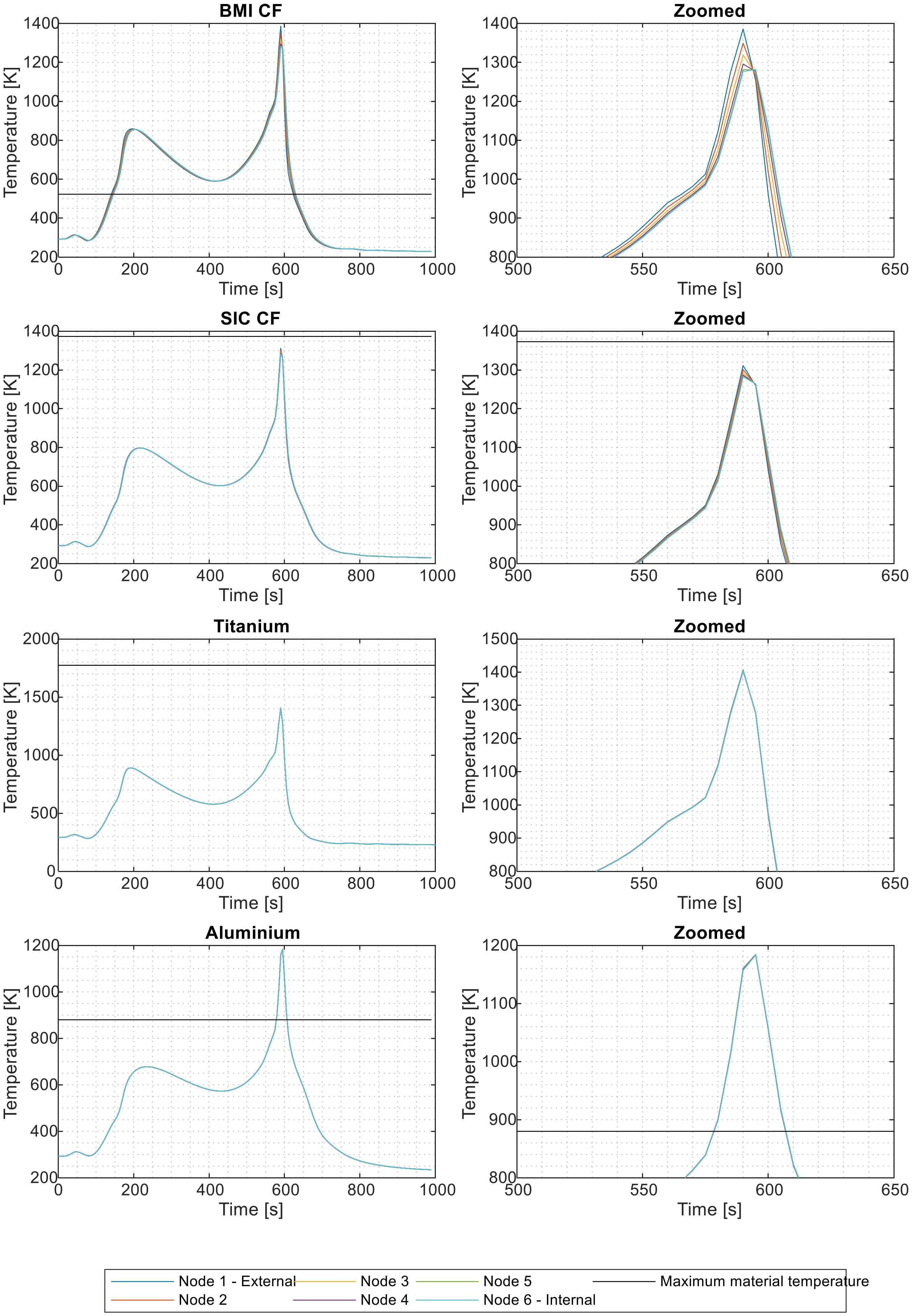

Figure C.31. BMI CF, SiC CF, titanium and aluminium node temperature results for W20 wing middle span leading edge location along the Sonneveld (2021) high-energy trajectory.

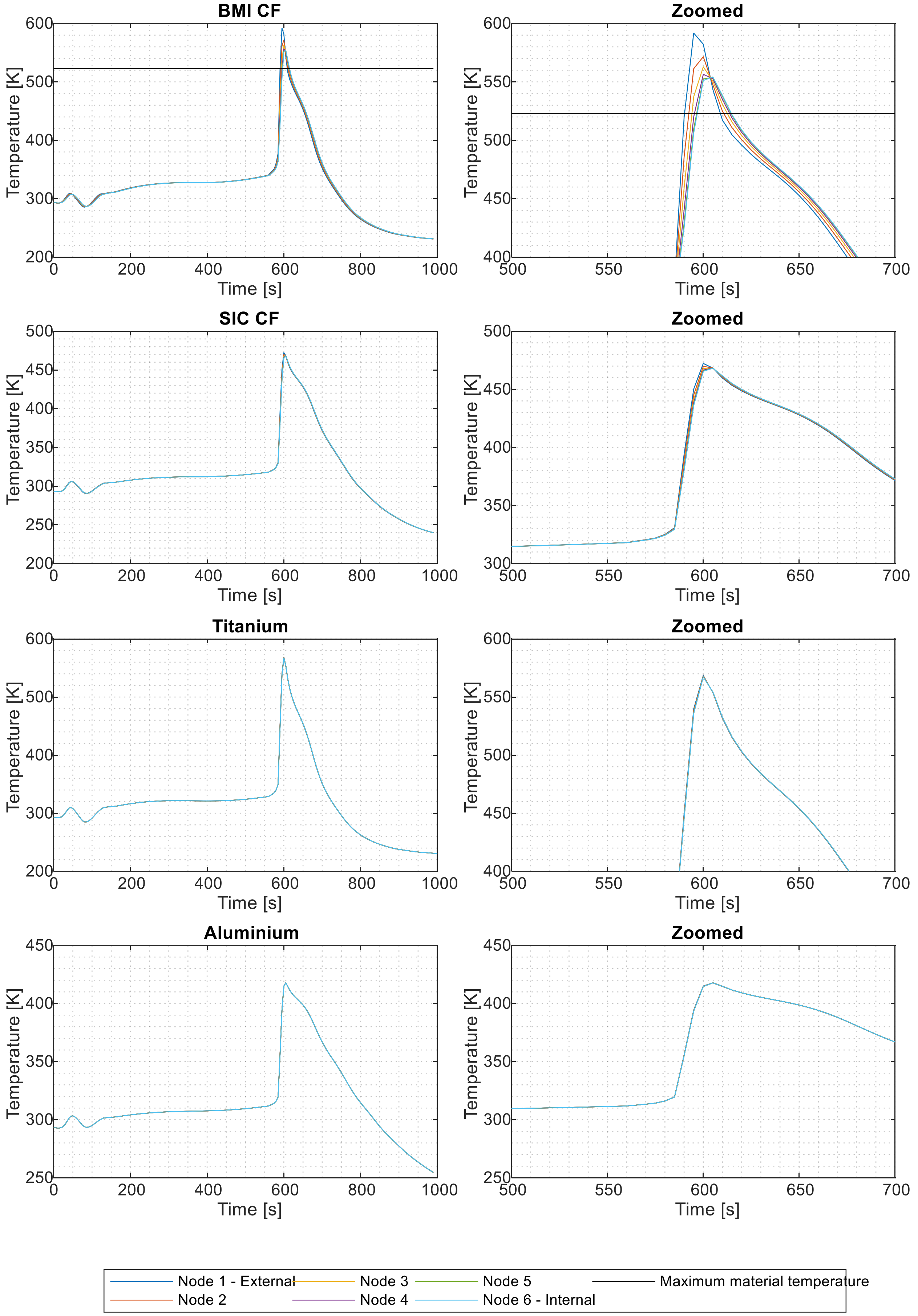

Figure C.32. BMI CF, SiC CF, titanium and aluminium node temperature results for W22 wing middle span leeward near rear location along the Sonneveld (2021) high-energy trajectory.

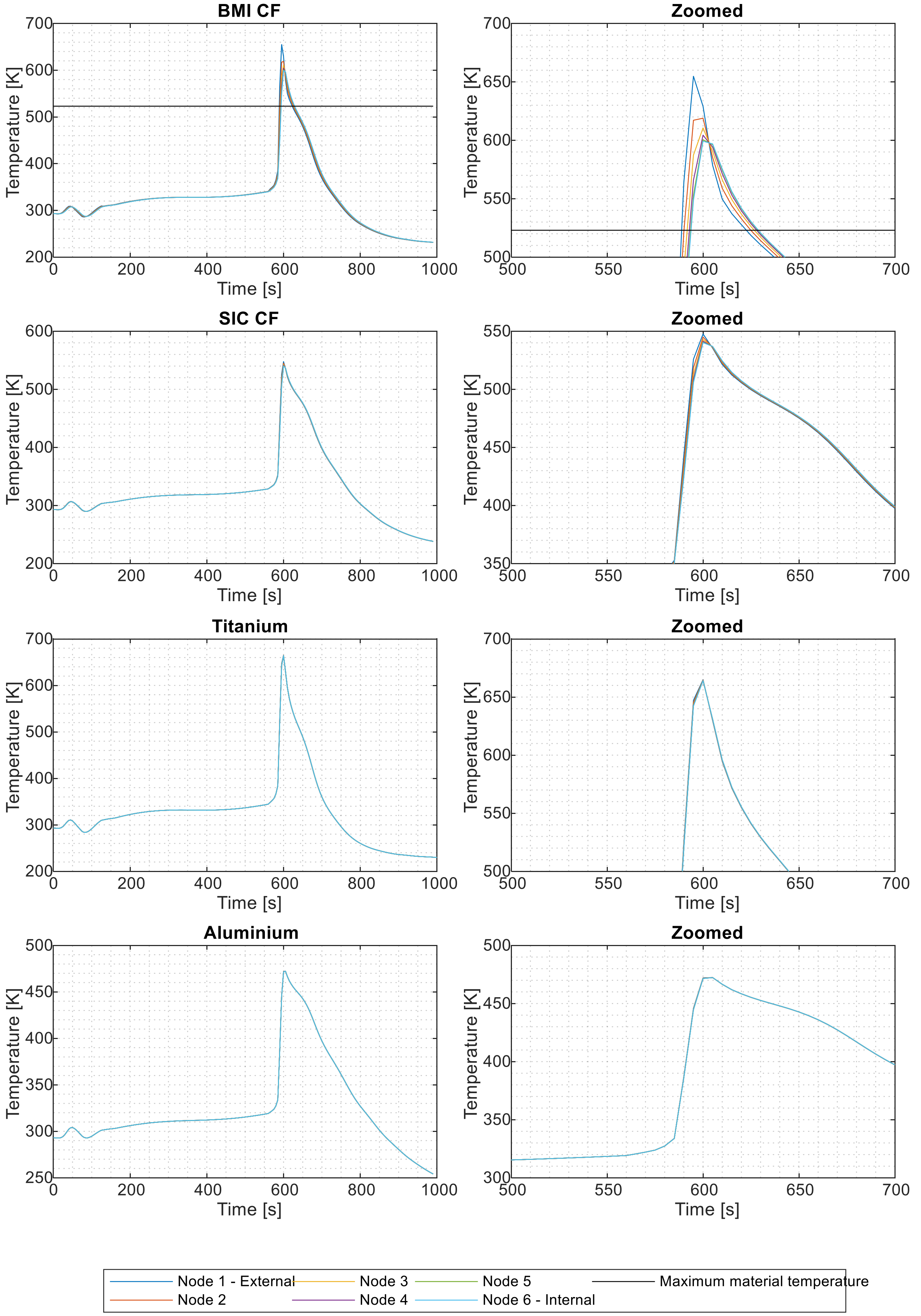

Figure C.33. BMI CF, SiC CF, titanium and aluminium node temperature results for F31 fuselage bottom near front edge location along the Sonneveld (2021) high-energy trajectory.

C.6. Active Cooling

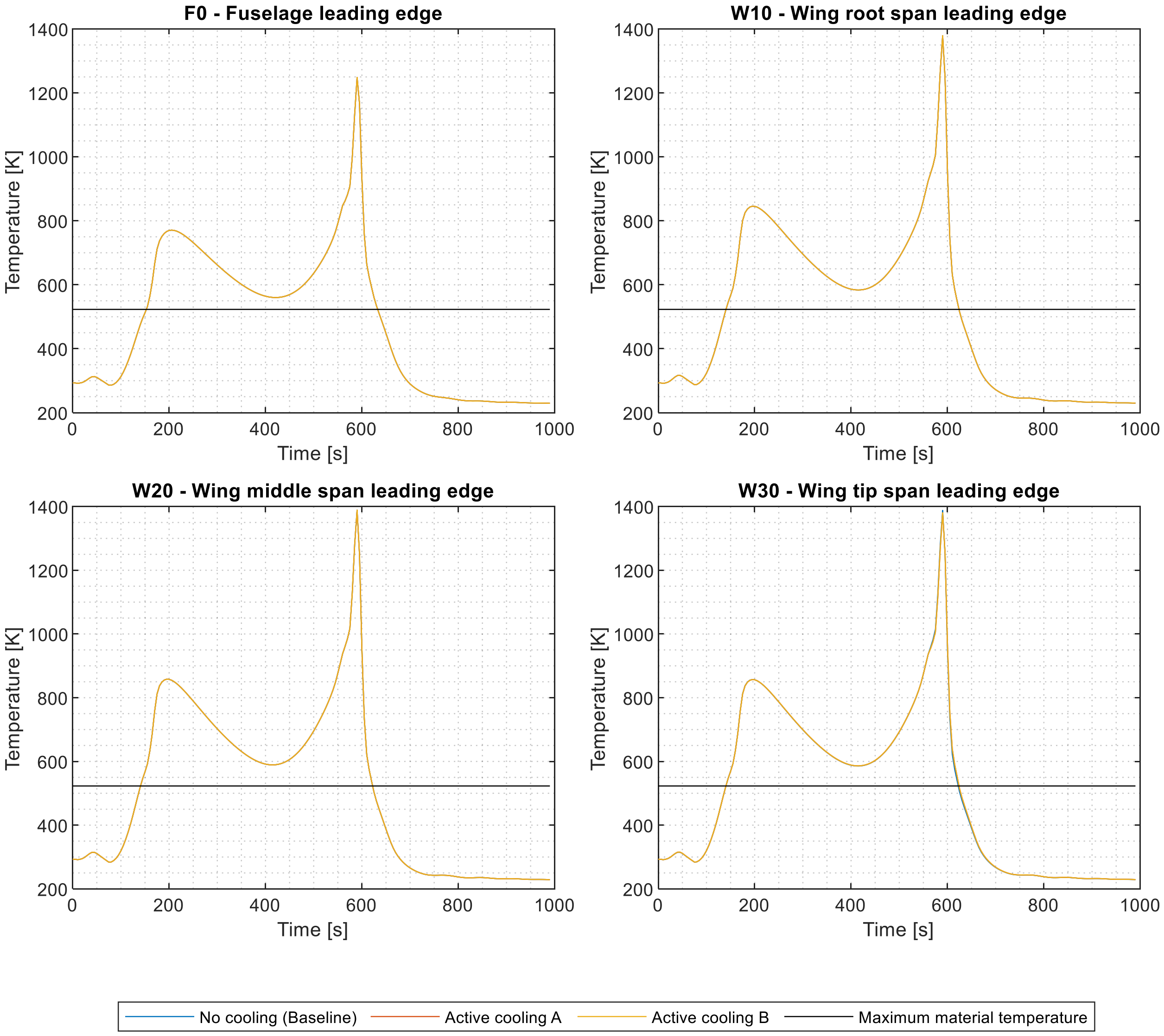

Figure C.34. BMI CF active cooling TPS temperature results for leading edge locations along the external surface of the vehicle along the Sonneveld (2021) mid-energy trajectory.

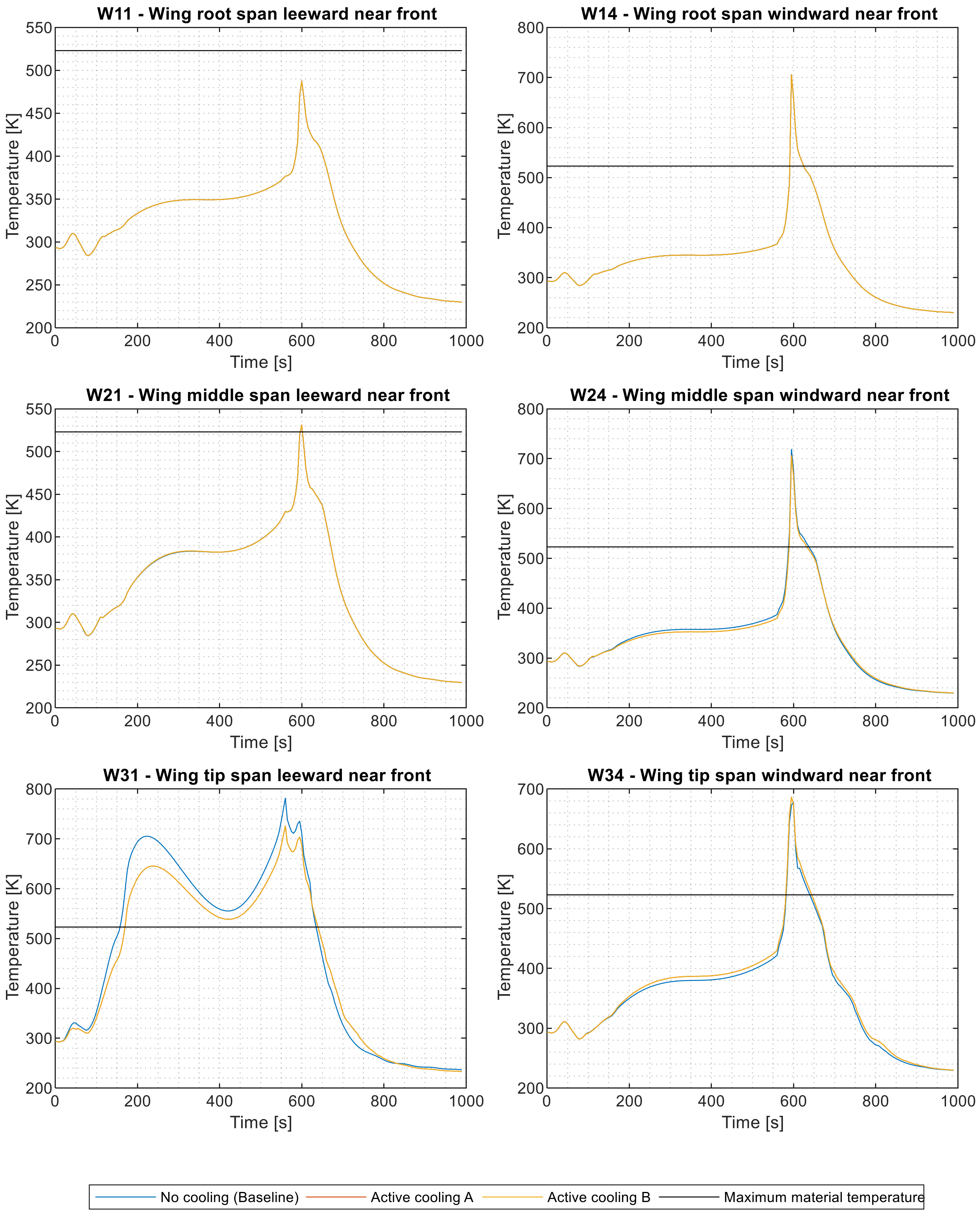

Figure C.35. BMI CF active cooling TPS temperature results for front wing locations along the external surface of the vehicle along the Sonneveld (2021) mid-energy trajectory.

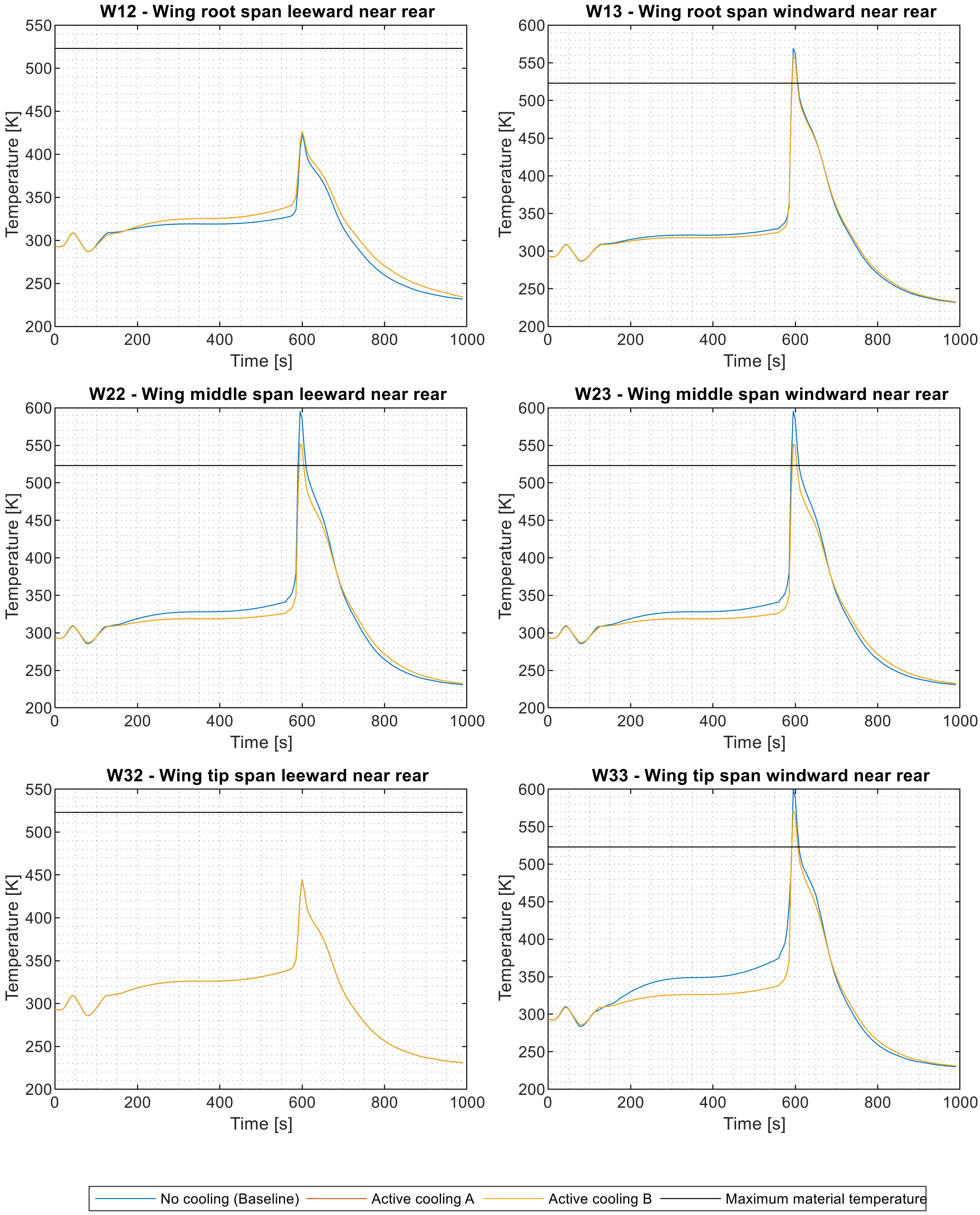

Figure C.36. BMI CF active cooling TPS temperature results for rear wing locations along the external surface of the vehicle along the Sonneveld (2021) mid-energy trajectory.

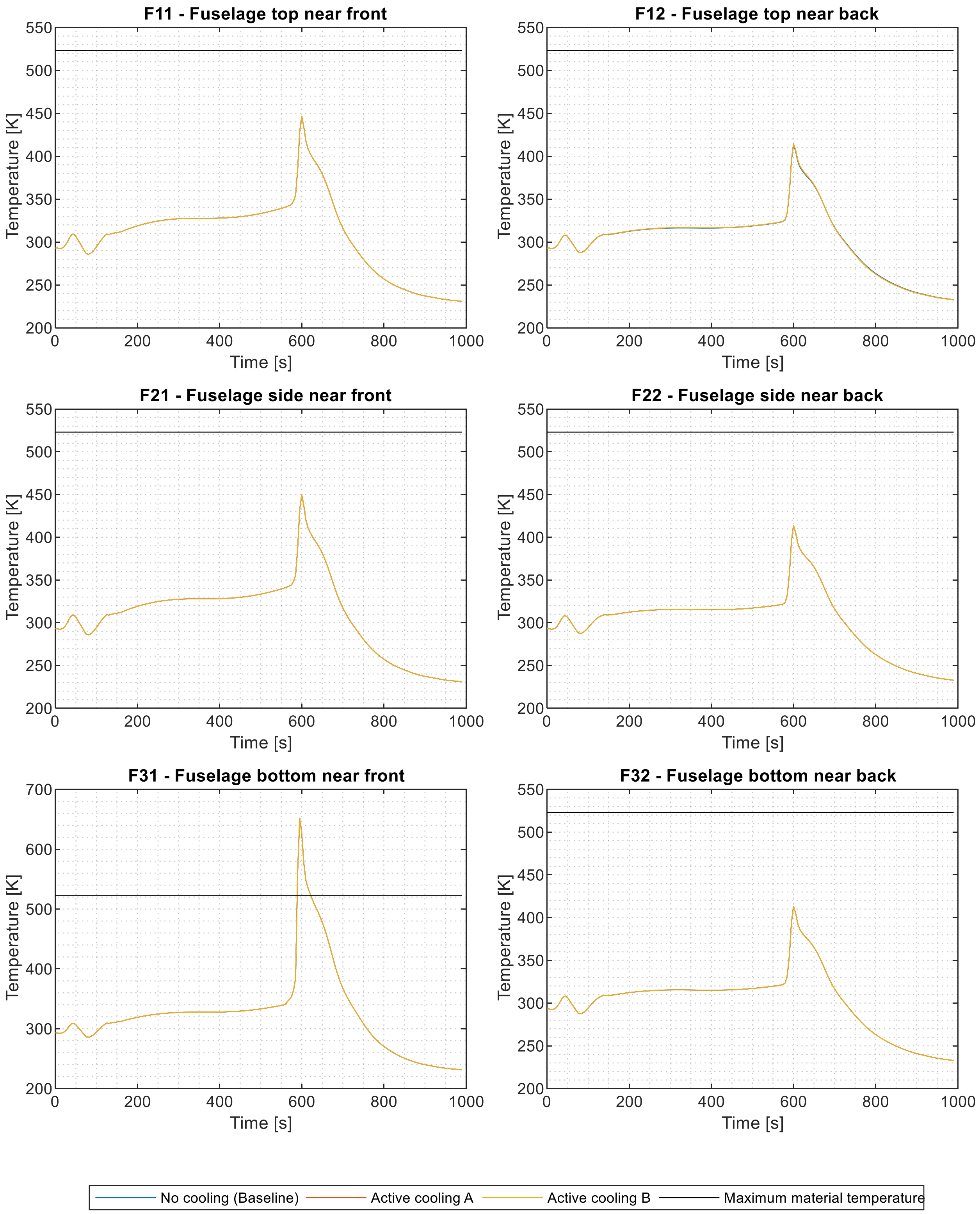

Figure C.37. BMI CF active cooling TPS temperature results for fuselage locations along the external surface of the vehicle along the Sonneveld (2021) mid-energy trajectory.

C.7. Radiation

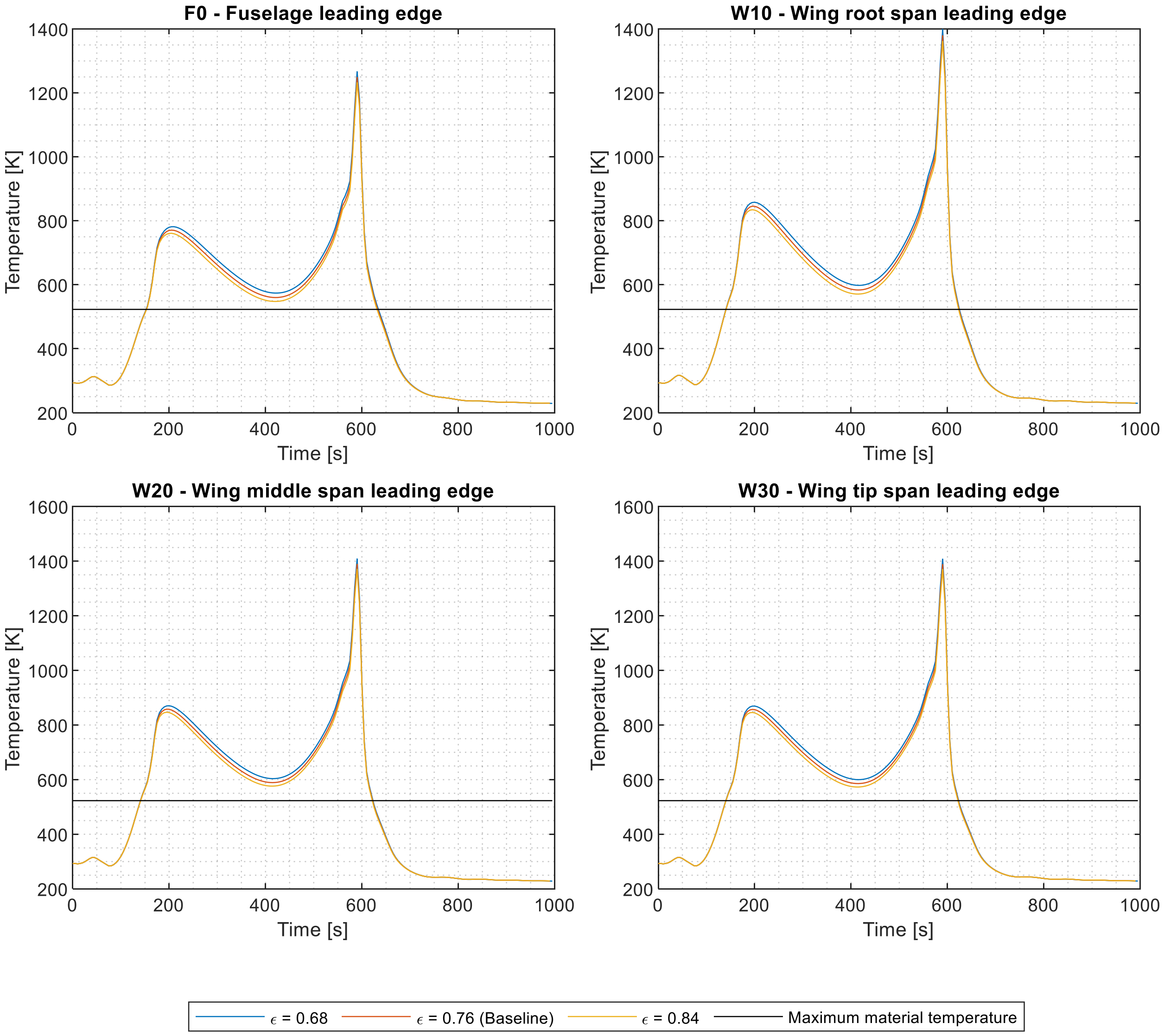

Figure C.38. BMI CF radiation TPS temperature results for leading edge locations along the external surface of the vehicle along the Sonneveld (2021) mid-energy trajectory.

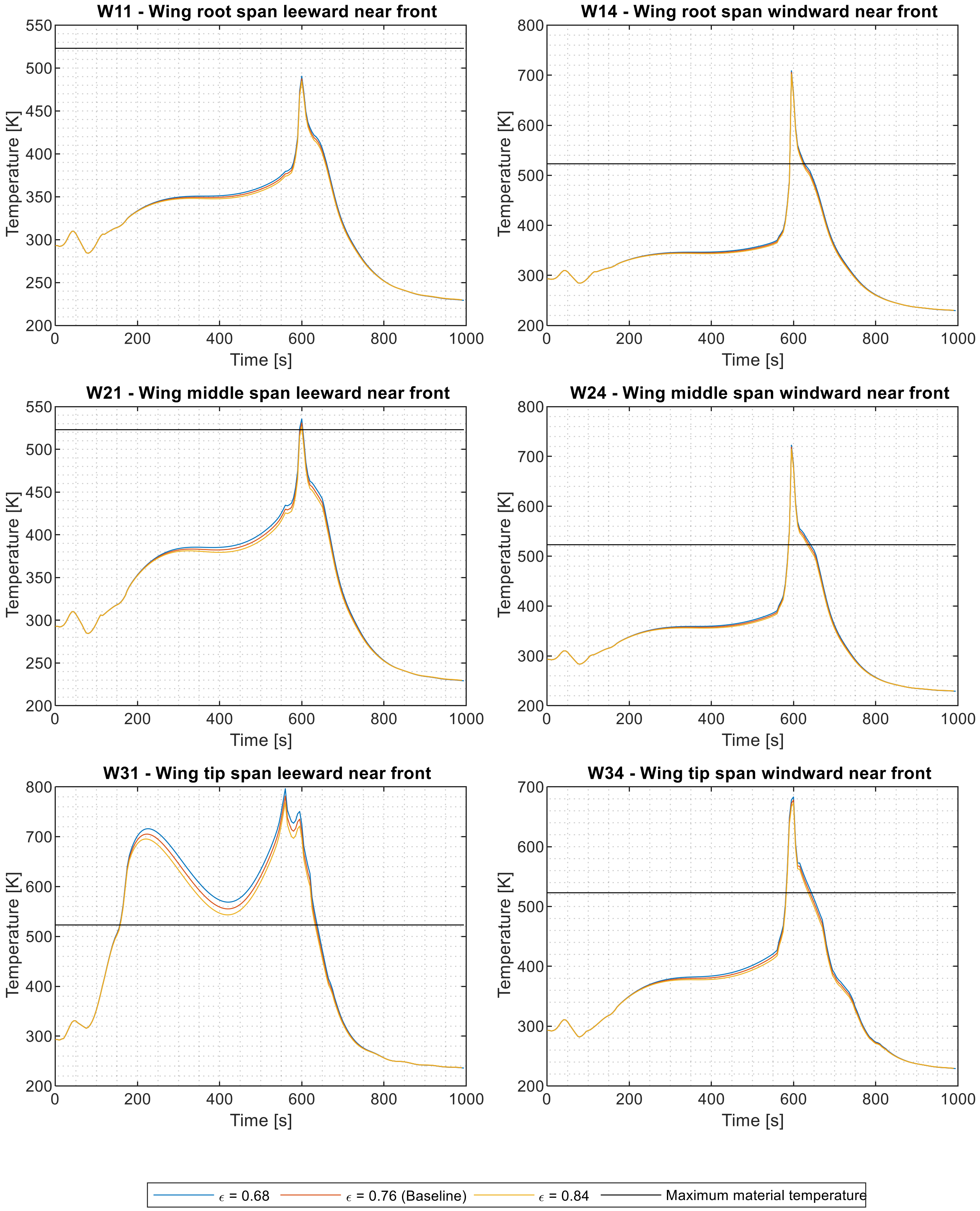

Figure C.39. BMI CF radiation TPS temperature results for front wing locations along the external surface of the vehicle along the Sonneveld (2021) mid-energy trajectory.

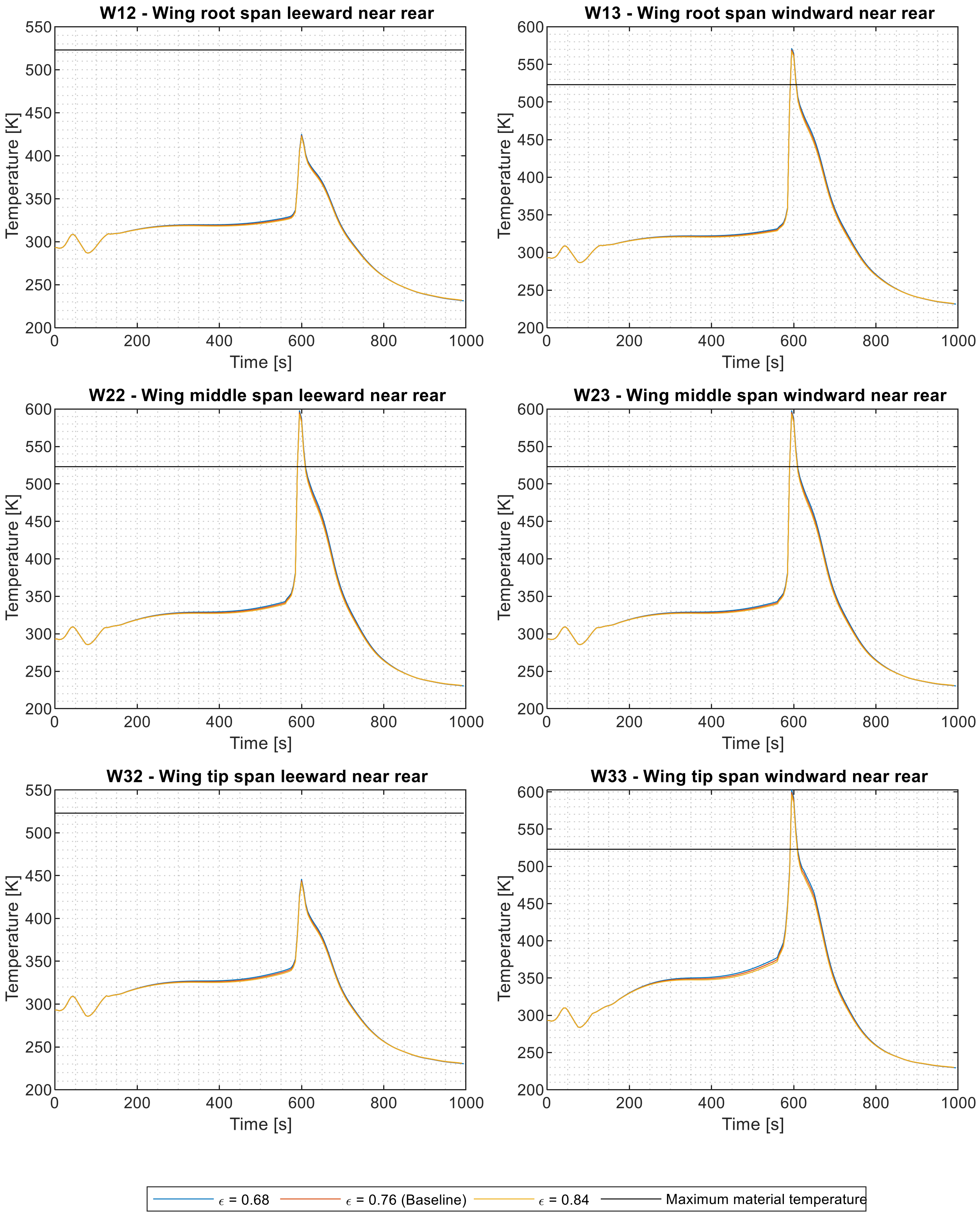

Figure C.40. BMI CF radiation TPS temperature results for rear wing locations along the external surface of the vehicle along the Sonneveld (2021) mid-energy trajectory.

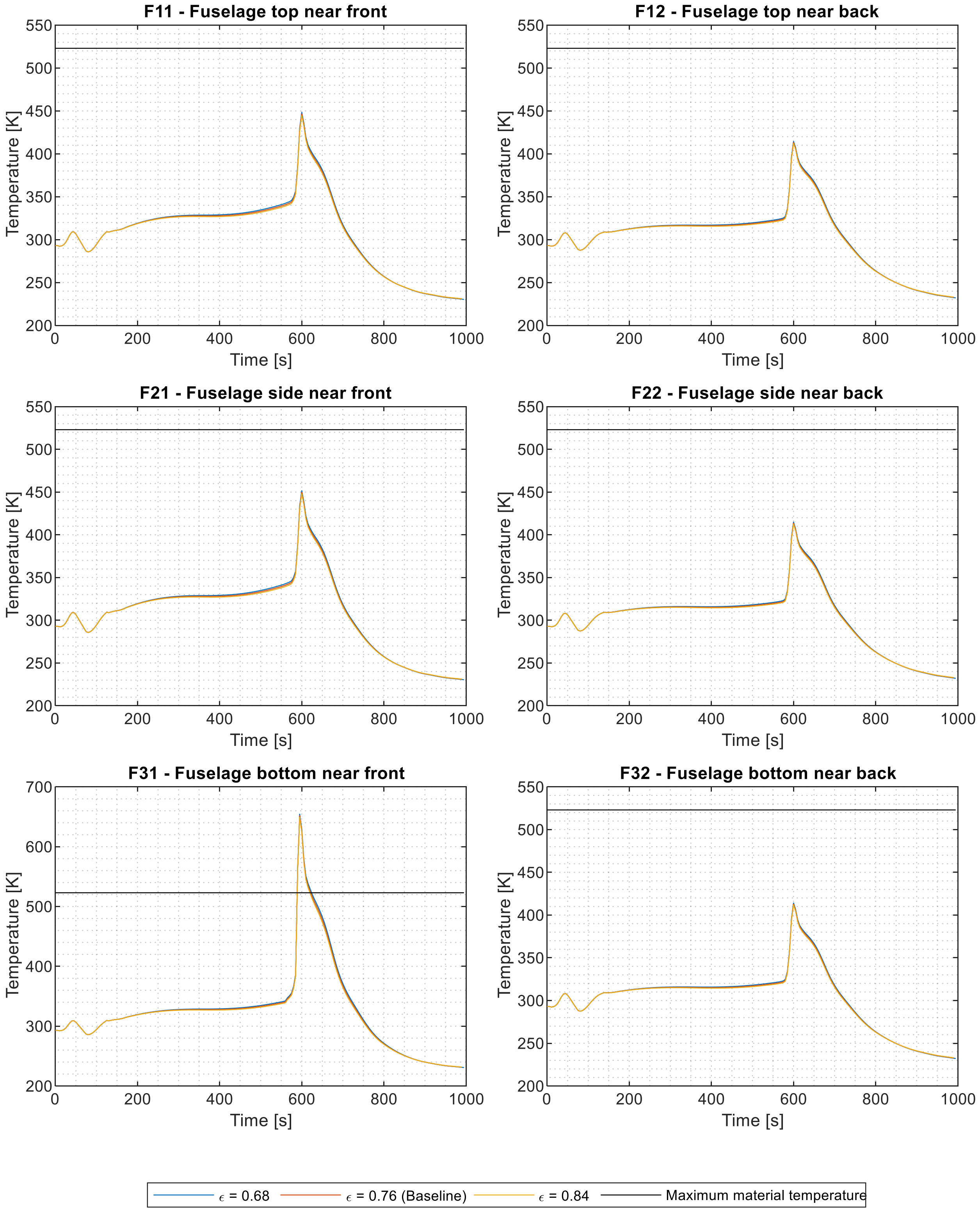

Figure C.41. BMI CF radiation TPS temperature results for fuselage locations along the external surface of the vehicle along the Sonneveld (2021) mid-energy trajectory.

C.8. Insulation

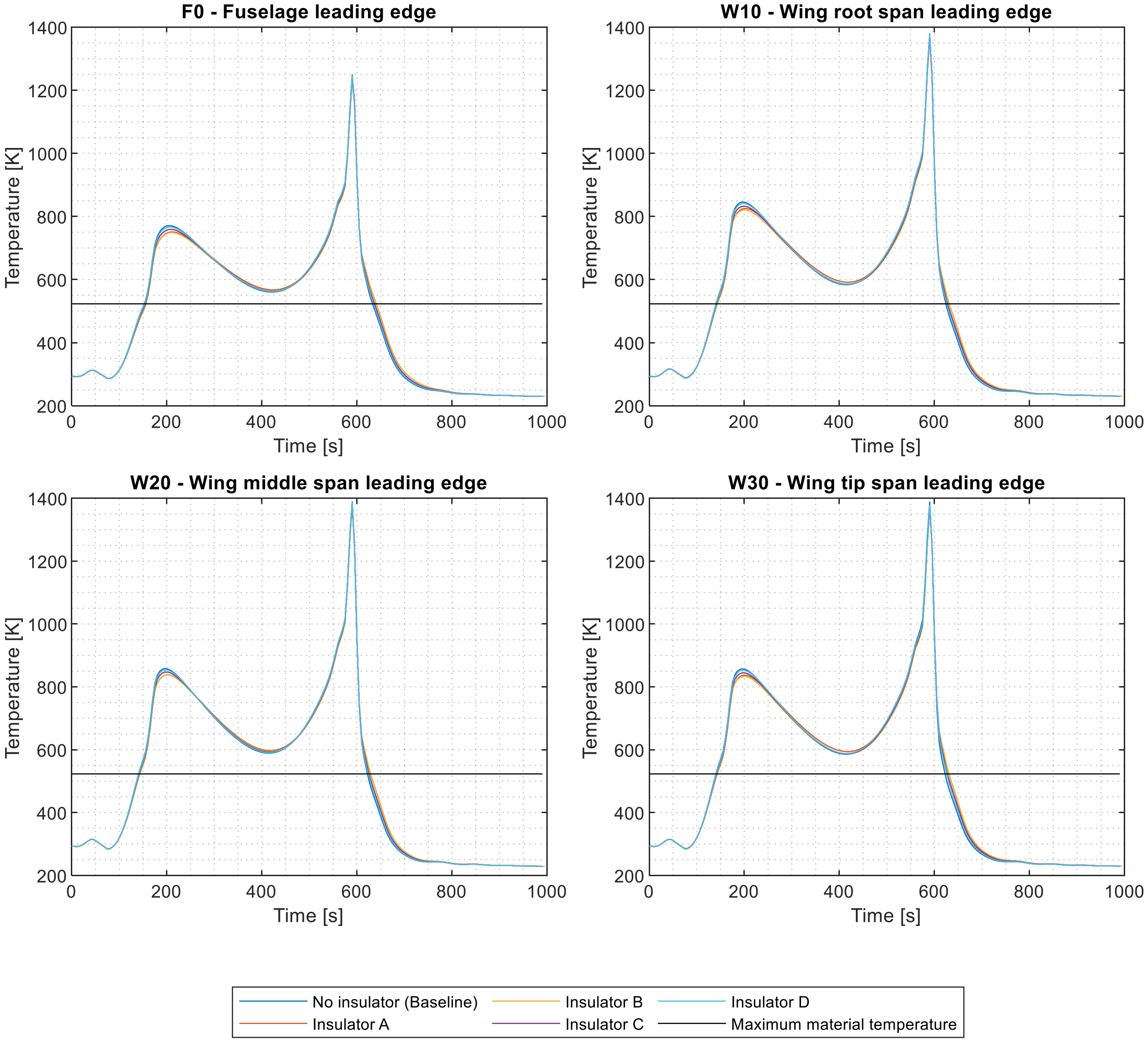

Figure C.42. BMI CF insulator layer TPS temperature results for leading edge locations along the external surface of the vehicle along the Sonneveld (2021) mid-energy trajectory.

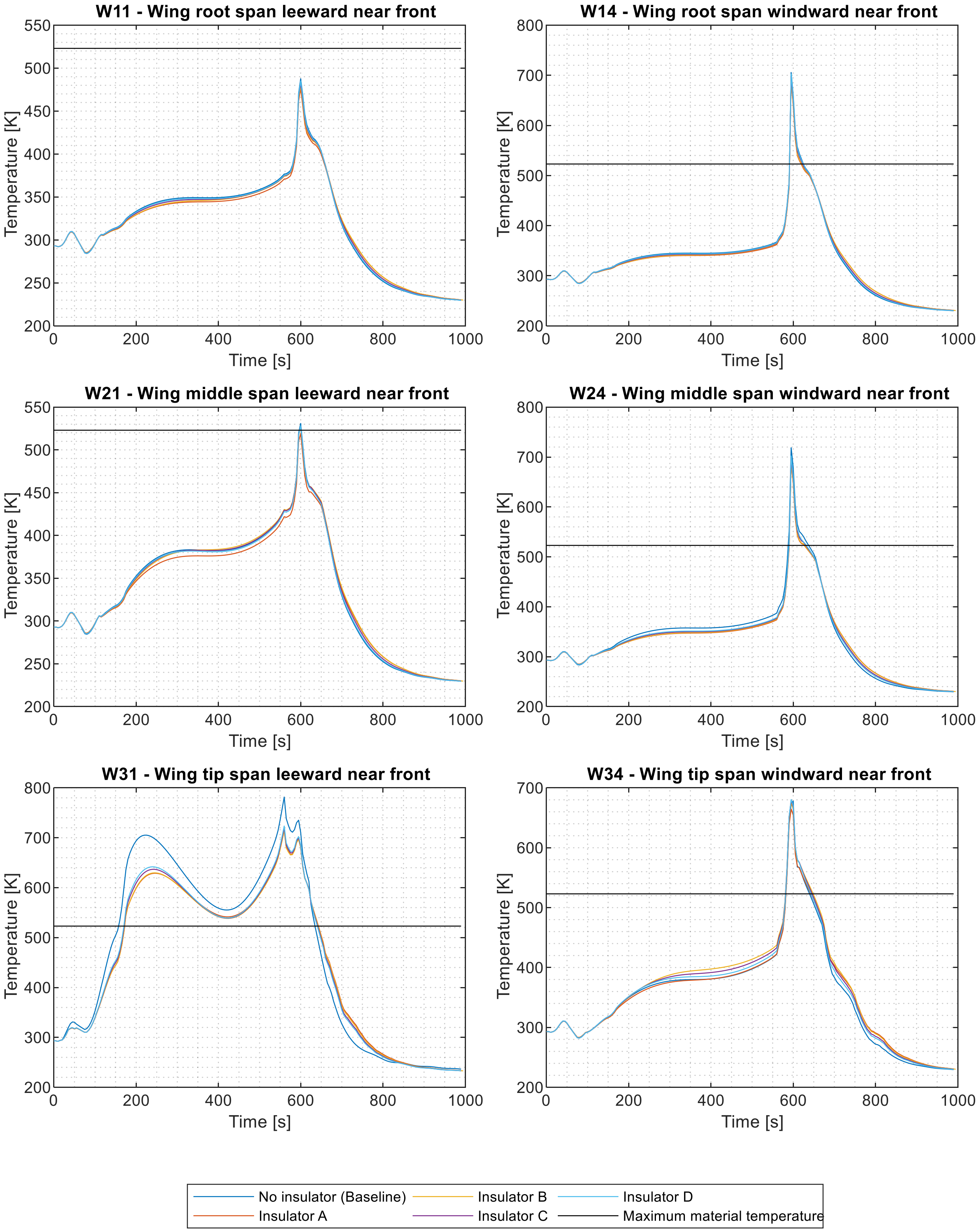

Figure C.43. BMI CF insulator layer TPS temperature results for front wing locations along the external surface of the vehicle along the Sonneveld (2021) mid-energy trajectory.

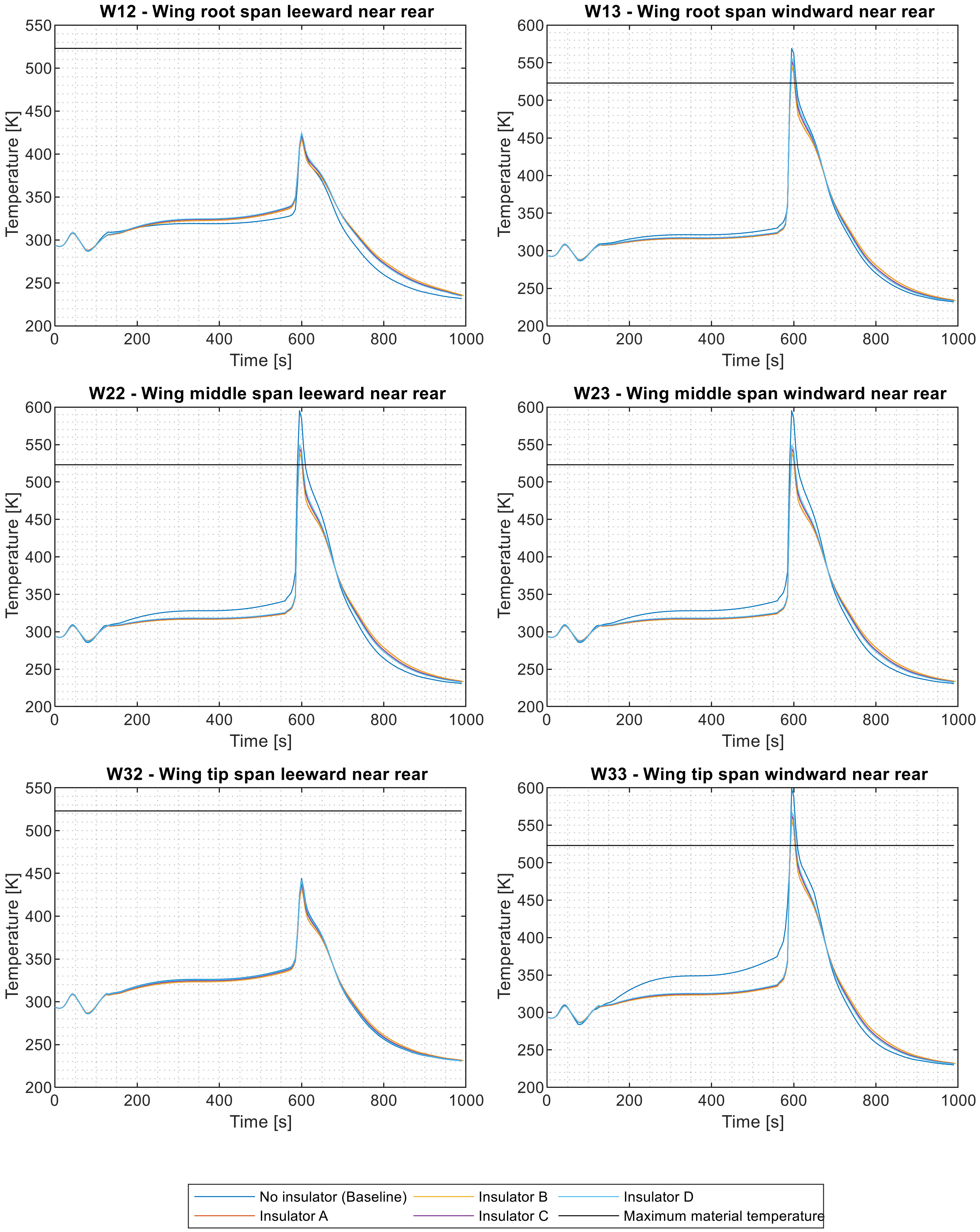

Figure C.44. BMI CF insulator layer TPS temperature results for rear wing locations along the external surface of the vehicle along the Sonneveld (2021) mid-energy trajectory.

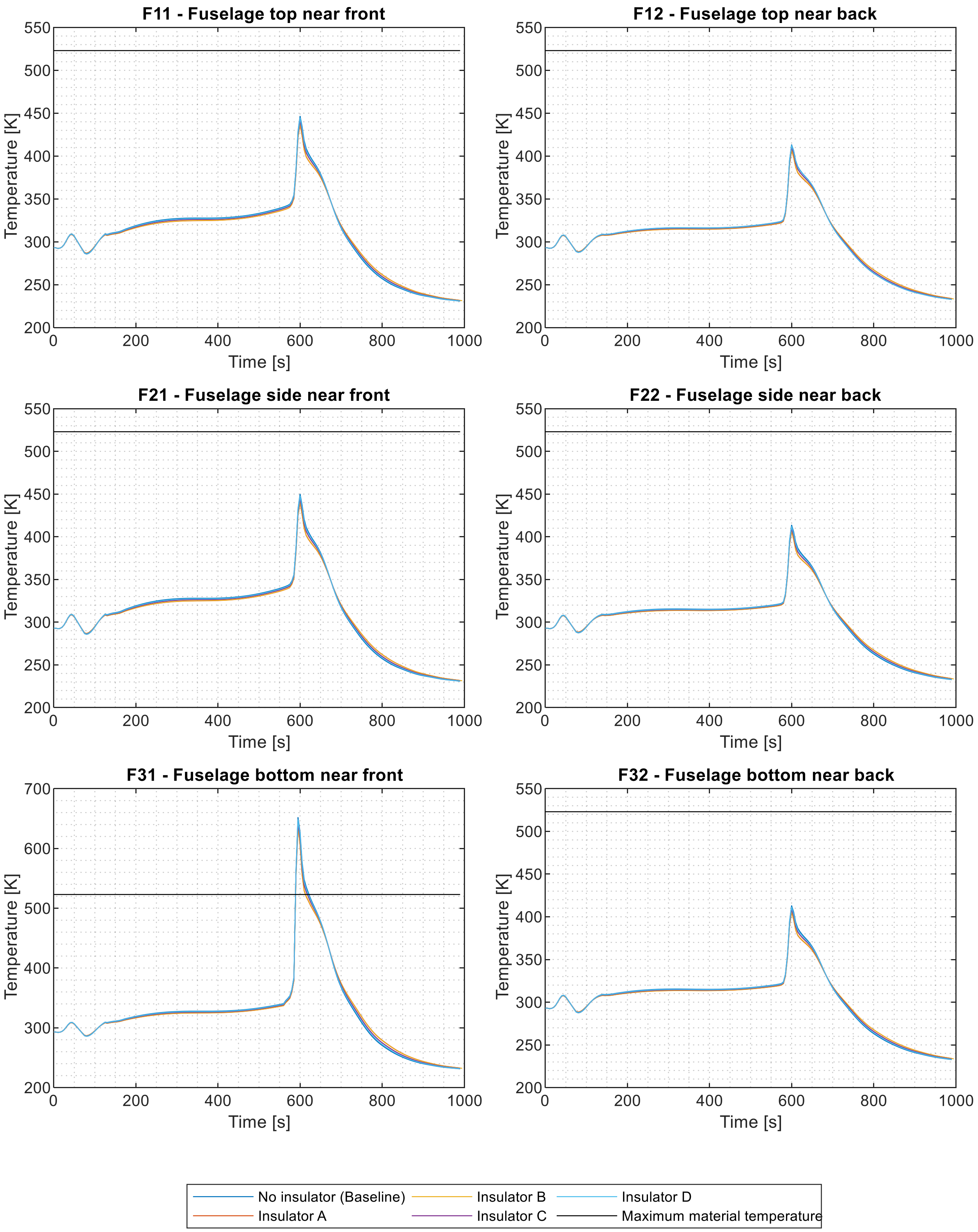

Figure C.45. BMI CF insulator layer TPS temperature results for fuselage locations along the external surface of the vehicle along the Sonneveld (2021) mid-energy trajectory.

C.9. Material Thickness

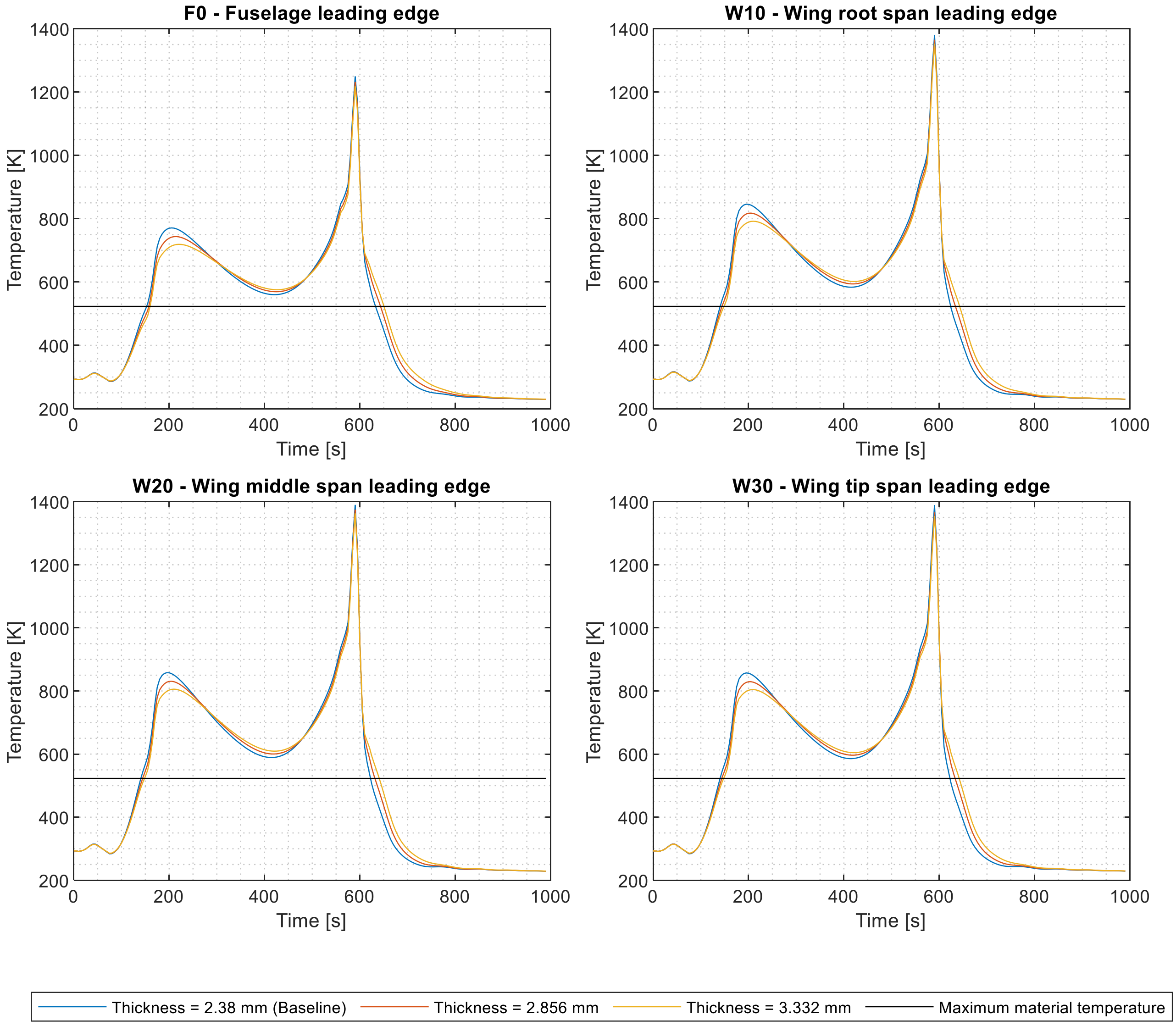

Figure C.46. BMI CF heat sink by material thickness TPS temperature results for leading edge locations along the external surface of the vehicle along the Sonneveld (2021) mid-energy trajectory.

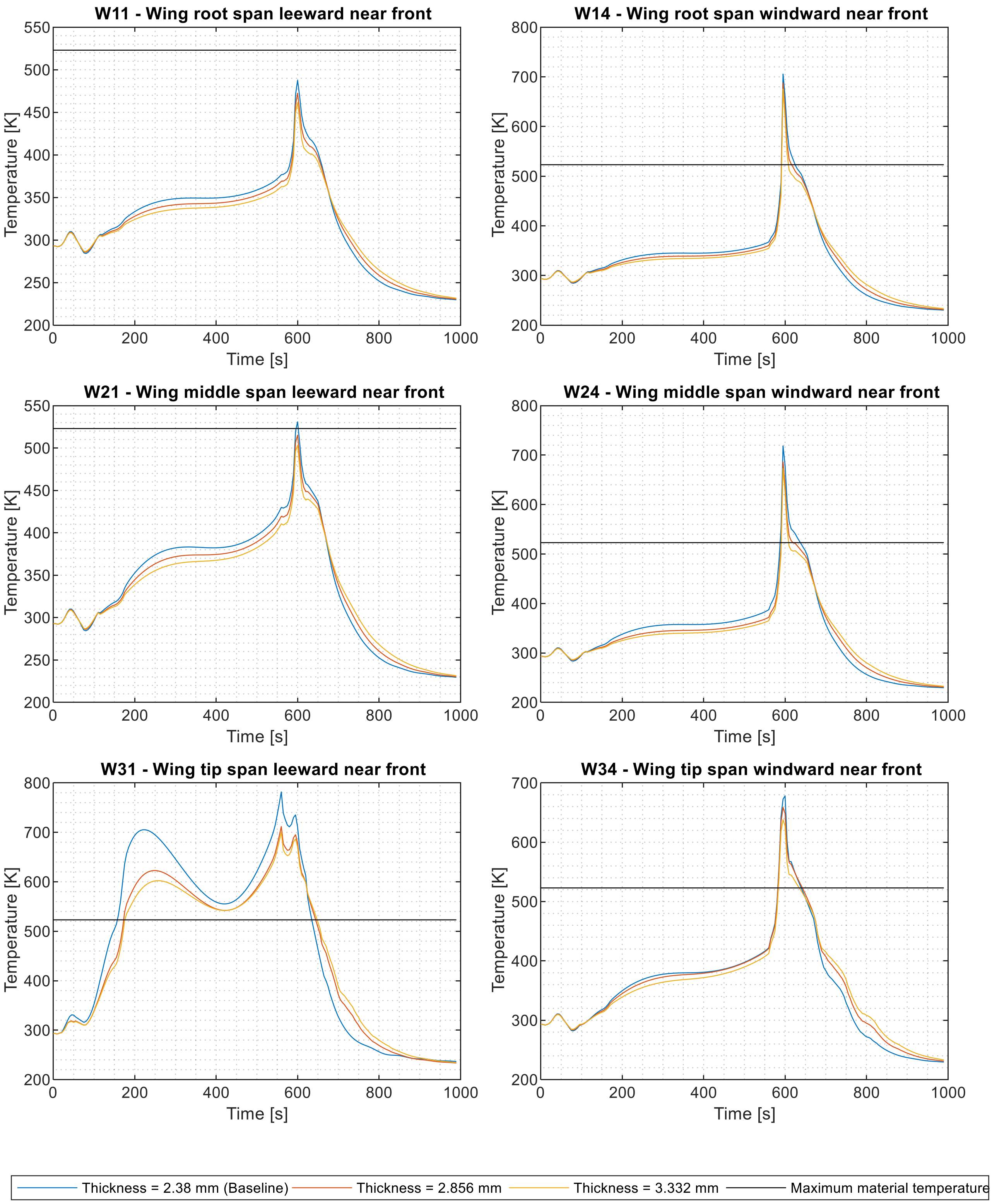

Figure C.47. BMI CF heat sink by material thickness TPS temperature results for front wing locations along the external surface of the vehicle along the Sonneveld (2021) mid-energy trajectory.

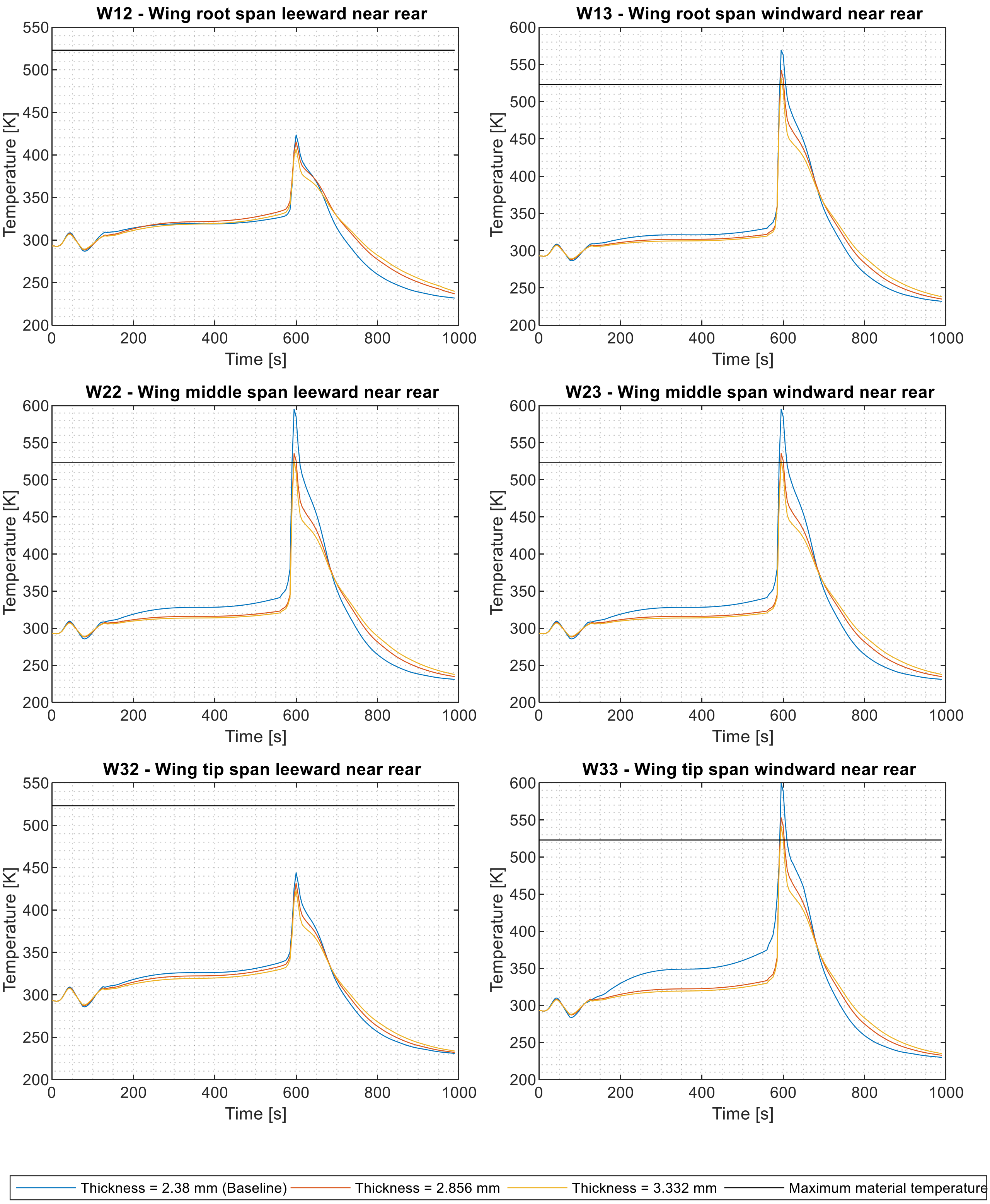

Figure C.48. BMI CF heat sink by material thickness TPS temperature results for rear wing locations along the external surface of the vehicle along the Sonneveld (2021) mid-energy trajectory.

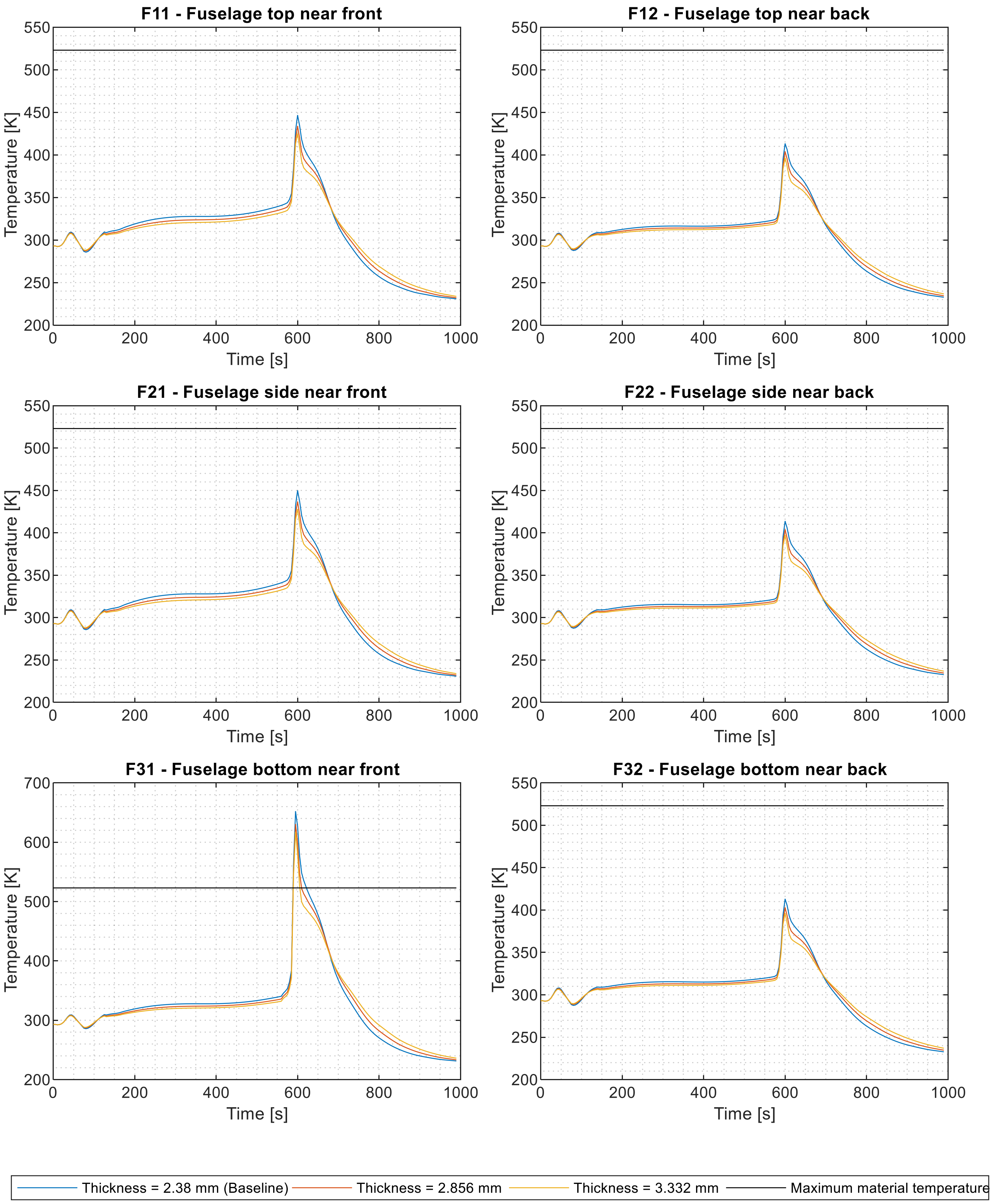

Figure C.49. BMI CF heat sink by material thickness TPS temperature results for fuselage locations along the external surface of the vehicle along the Sonneveld (2021) mid-energy trajectory.

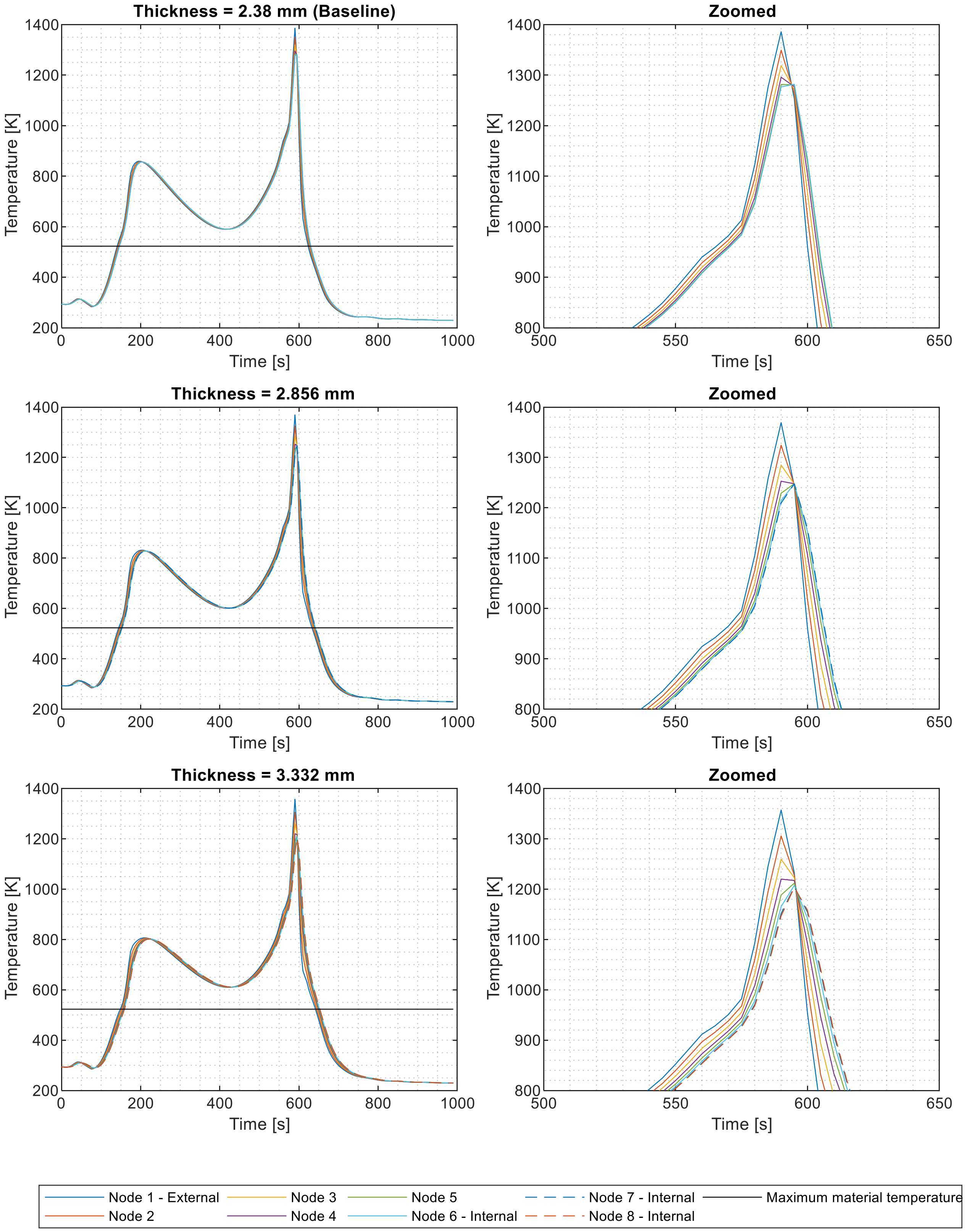

Figure C.50. BMI CF heat sink by material thickness TPS node temperature results for W20 wing middle span leading edge location along the Sonneveld (2021) mid-energy trajectory.

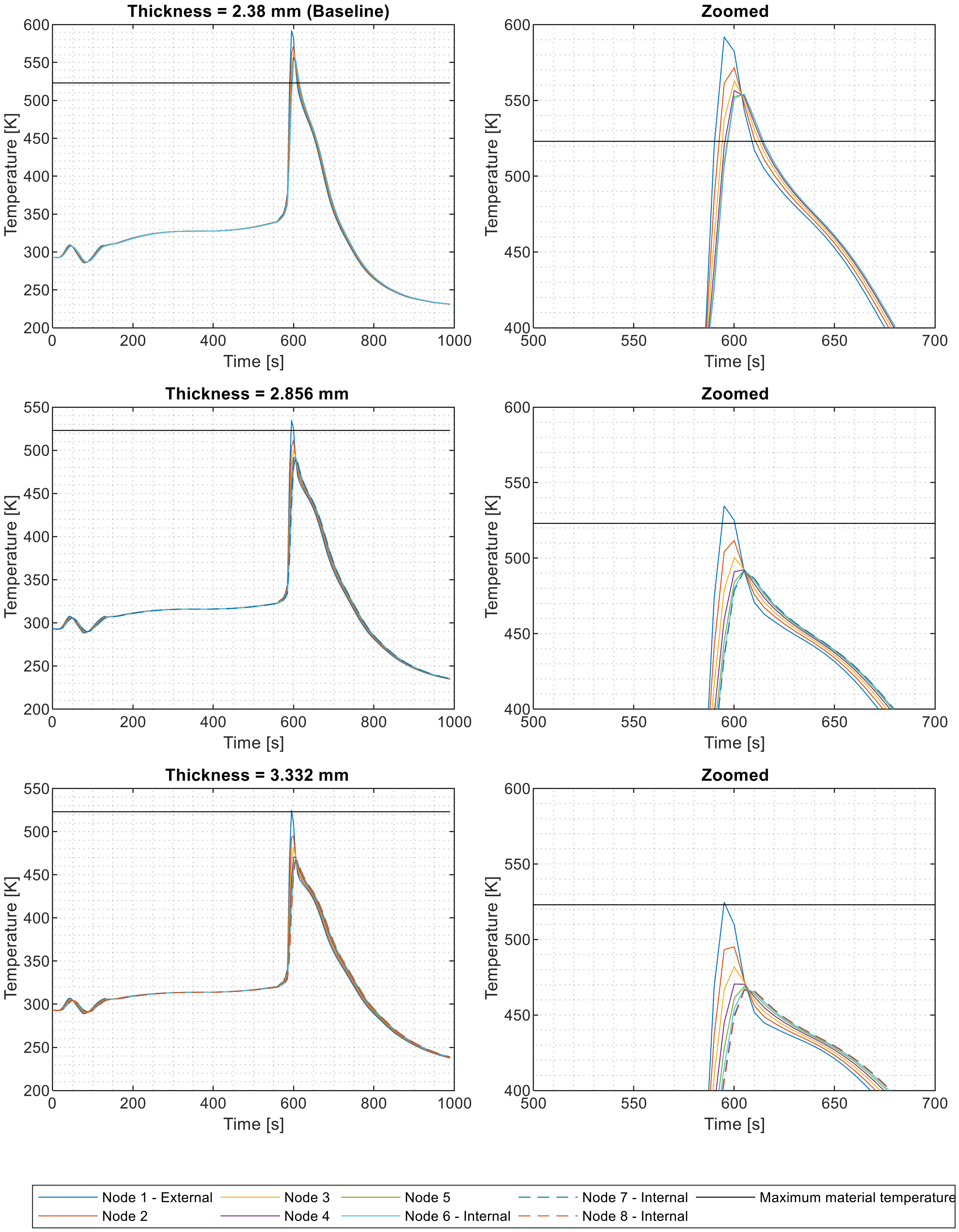

Figure C.51. BMI CF heat sink by material thickness TPS node temperature results for W22 wing middle span leeward near rear location along the Sonneveld (2021) mid-energy trajectory.

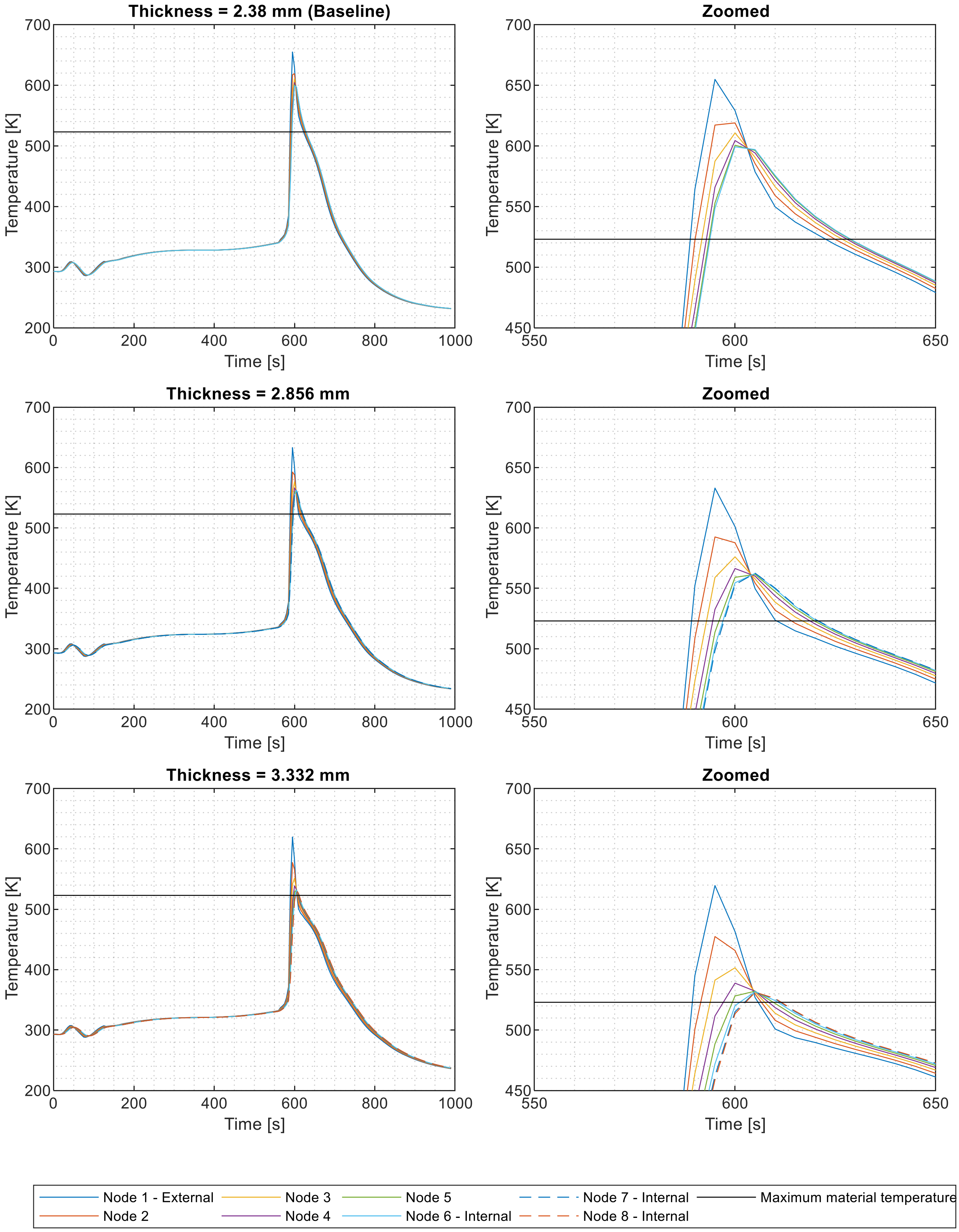

Figure C.52. BMI CF heat sink by material thickness TPS node temperature results for F31 fuselage bottom near front location along the Sonneveld (2021) mid-energy trajectory.